Synthesis, Characterisation and Photocatalytic Application of Rhodium-doped Oxides upon Irradiation with Visible Light

Thesis submitted in accordance with the requirements of the University of Liverpool for the degree of Doctor in Philosophy by

Borbala Kiss

October 2015

Abstract

As stated earlier in the title, the overall aim of the project has been to investigate "Synthesis, Characterisation and Photocatalytic Application of Rhodium-doped Oxides upon Irradiation with Visible Light".

The key considerations in photocatalyst design, assessment and challenges and energy requirements in application is reviewed in the Introduction chapter.

In the Discussion chapters, first, a simple one-step strategy was employed to produce a high surface area, phase pure metal oxide that is active in UV light. Various structures have been produced as parent phases such as $SrTiO_3$, $BaTiO_3$ and $Y_2Ti_2O_7$, and once the presence of phase pure material was confirmed, rhodium substitution was initiated by B site doping of structures by adding soluble Rh salts during phase formation. The idea of using rhodium was to provide active, new rhodium states within the band gap therefore induce e^- and h^+ transfer that will presumably facilitate photochemical reduction/oxidation reactions with a longer excited wavelength than 400 nm, visible light photons.

The series of nanoparticulate $SrTi_{1-x}Rh_xO_3$ and $BaTi_{1-x}Rh_xO_3$ materials with x = 0; 0.01; 0.025; 0.050; 0.075 and 0.1 rhodium content have been fully characterised. The functionality of well-known $SrTi_{1-x}Rh_xO_3$ H_2 generating p-type oxide was extended to be successfully applied in water remediation and disinfection with excellent performance in model Methyl Orange molecule degradation and reasonable efficiency in *E. coli* Gram-negative bacteria inactivation when exposed to visible light ($\lambda > 420$ mm). So far, of semiconductor oxides, nitrogen-doped titania in particular have demonstrated activity under visible light in all three functionalities mentioned above, making this new finding very encouraging in the application of $SrTi_{0.95}Rh_{0.05}O_3$ compound.

As the investigation of novel advanced materials is crucial in the field, following up on this, a novel stable visible-light-driven photocatalyst ($\lambda \geq 450$ nm) for water oxidation is reported. Rhodium substitution into the pyrochlore $Y_2Ti_2O_7$ is demonstrated by monitoring the Vegard's law evolution of the unit-cell parameters with changing rhodium content, to a maximum content of 3% dopant. Substitution renders the solid solutions visible-light active. The overall rate of oxygen evolution is

comparable to WO_3 but with superior light-harvesting and surface-area-normalized turnover rates, making $Y_2Ti_{1.94}Rh_{0.06}O_7$ an excellent candidate for use in a Z-scheme water splitting system and photoanode.

Acknowledgements

First and foremost I would like to thank my primary supervisor Prof. Matt Rosseinsky for giving me the opportunity to work with excellent scientists, for his continued guidance and his 'never settle for good enough' attitude guided by perfectionism. I would also like to thank Dr. John B. Claridge, my secondary supervisor for his advice and knowledge of synthetic inorganic chemistry. I would like to express my deep appreciation to Prof. Jim Darwent who contributed with his valuable input, support and advice throughout my PhD with the Wednesdays' meeting in his free time. Special thanks to Dr. Troy Manning for his fruitful discussions, for always having one minute for questions and also for making the project gratifying during challenging times.

I am very grateful to have the opportunity to work with past and present fellow members of the Photocatalysis sub-group Dr. Paul Boldrin, Dr. Rob Palgrave, Dr. Chris Ireland, Dr. Asif A. Tahir and Tim Johnson. Thanks particularly also to Matthew Dyer for his valuable DFT calculations. I thank Dr. Alex Katsoulidis for allowing me to benefit from his experience and knowledge and for always being available for valuable discussions. Most recently I am very grateful to Dr. Christophe Didier helping me in unit cell refinement discussions.

I would like to express huge and sincere thanks to Dr. Hongjun Niu, Dr. Marco Zanella, Mike Chatterton, Rob Clowes and George Miller for all the technical support and Jane Remmer our former PA.

I would like to thank to all our collaborators from various institutes and departments in Liverpool, Dr. Alex Cowan from the Stephenson Institute who provided much valuable input during meeting discussion and several GC related O_2 evolution measurements; Dr. David Hesp from the Stephenson Institute who carried out the XPS measurements; Dr. Heather Allison from the Institute of Integrative Biology for her valuable advice and her endless patience to train me how to work in a sterile environment in a microbiology lab; Dr. Arthur Taylor from the Institute of Translational Medicine for acquiring the Fluorescence Microscopy images; Dr. Simon Romani, Dr. Kerry Abrams from NiCaL for training me on TEM.

Thanks to the Marie Curie Programme and EPSRC for funding my research.

I cannot forget my friends, Oliver Wilcox, Wen Xu, Alex Katsoulidis, Jibreel Haddad, Zoe Taylor, Tom Mangnall, Tim Johnson, Noemie Perret, Alex Grigoropoulos, Daniel Munoz, Sebastian Sprick, Baltasar Bonillo Fernandez and Rachel Coulter in Liverpool. I thank Agnes Mahmoud and Judit Krajko from Szeged and my international friends Maike Potschulat and Natacha Lima Leite Ogando from elsewhere.

Additionally my huge thanks go to my family and Marci for being extremely supportive and being there in difficult times during my PhD and in particular during thesis writing.

Publication list

1. *"Photocatalytic Water Oxidation by a Pyrochlore Oxide upon Irradiation with Visible Light: Rhodium Substitution Into Yttrium Titanate";* B. Kiss, C. Didier, T. Johnson, T. D. Manning, M. S. Dyer, A. J. Cowan, J. B. Claridge, J. R. Darwent and M. J. Rosseinsky, *Angewandte Chemie International Edition*, 2014, **53**, 14480-14484.

2. *"Nano-structured rhodium doped $SrTiO_3$ – multifunctional visible light activated photocatalysis"*; B. Kiss, C. Didier, T. D. Manning, H. E. Allison, A. W. Taylor, J. B. Claridge, J. R. Darwent and M. J. Rosseinsky, *in preparation*, 2015.

Contents

1. Chapter 1: Introduction

The global situation with regards to climate change and the requirement for replacing the current energy supplies with alternative energy sources such as hydrogen has presented a grand challenge in the field of photocatalysis with major developments made in recent years. Hydrogen is considered as a high-energy density, renewable and clean energy carrier. Of the well-known energy storage materials, hydrogen stores over three times (142 MJ/kg) as much energy as gasoline (44 MJ/kg) or diesel (46 MJ/kg); and when recombined with oxygen in a fuel cell, electricity is generated and water is produced as the only by-product. However, until recently the most common method for producing molecular hydrogen has been Steam Reforming in a 2–step conversion of methane. This process emits large quantities of CO_2 into the atmosphere, contributing to the greenhouse effect, therefore removing the environmental appeal of hydrogen as a clean fuel. The average amount of solar energy absorbed by the Earth's atmosphere is 3,850 EJ annually. In comparison, our primary energy use is currently about 67 EJ per year. Thus, environmentally it is extremely appealing to utilize solar power, an essentially clean and inexhaustible alternative energy source as the driving force for chemical processes. Some of the disadvantages of solar energy is the intermittence, the seasonal variability and the low distributed density, hence, sun collectors and energy storage are crucial requirements for the utilization of solar energy.

It can be realised by applying hybrid processes such as Photovoltaic (PV) electrolysis where a solar cell powers the electrolyser. Besides this, Photoelectrolysis (PE) uses photocatalyst electrodes with an external bias to split water. Photocatalysis is a light harvesting mechanism in which photochemical reactions take place on the surface of

a light absorbing or sensitised material by photogenerated electrons and holes. Photocatalytic Water Splitting (PWS) is a method to split water into H_2 and O_2 and to effectively convert solar energy into chemical energy in a heterogeneous photocatalytic process. Moreover the combustion of H_2 fuel produces only pure water with a substantial heat release while avoiding the emission of CO_2, therefore provides a secure and sustainable energy supply on the long-term. In addition, photocatalysis has the ability to decompose organic pollutants, and to eliminate germs. Thus, the process can also be applied to detoxify waste water and to provide potable water.

This thesis focuses on solar energy conversion leading towards the above mentioned photocatalytic applications (water splitting, water remediation and water detoxification). When, a synthesised photocatalyst is added to pure water in the presence of sunlight, the evolved gases captured from the proceeding water splitting reaction can be used as alternative fuels. Alternatively, the photoactive material can be placed in contaminated water and the photocatalytic reaction drives the complete oxidation and/or mineralization of the pollutants. Whilst the application of such photocatalysts is extremely attractive, only a very limited numbers of catalysts are commercially available and used, *e.g.* TiO_2, ZnO, WO_3, thus further development is needed to make use of the potential in the process.

This introduction reviews the principal mechanisms and concepts of photocatalysis and provides an overview of its objectives, critical points, challenges and novel strategies for making successfully applied materials proposed in this work. This first chapter also exhibits strategies of band-gap energy engineering of UV activated compounds by narrowing their band gaps with dopants, in particular with rhodium, thus converting them to materials absorbing visible light. The chapter also explains methods for improving the photocatalytic activity by adding Platinum Group Metal

(PGM) based co-catalysts to extend the application of as-synthesised materials in alternative fuel generation, water remediation and water disinfection.

1.1. Photosynthesis

Photosynthesis is the process in green plants and cyanobacteria that uses sunlight to split water, generate oxygen and convert carbon dioxide into carbohydrate by using special chlorophyll species. It can be considered as a model process for artificial water splitting.

Plant photosynthesis occurs according to the following equation:

$$CO_2 + H_2O + 8h\nu \rightarrow \frac{1}{6} C_6H_{12}O_6 + O_2 \qquad \textbf{(Eq. 1.1)}$$

The entire cascade mechanism consists of the Z-scheme (Photosystem II. + I.) including the Photodissociation/Oxygen evolution in a light-dependent reaction, and the Calvin cycle in a light-independent reaction where CO_2 fixation occurs. In the Z-scheme reaction Photosystem II (P680) and Photosystem I (P700) are linked together through an electron transfer chain. Each photochemical reaction consists of one-electron transfer reaction through the thylakoid membrane of the chloroplast. In the overall process a minimum of eight photons are required for each oxygen molecule evolved.[1]

1.2. Photocatalysis

Recently, photocatalysis has become a key discipline involving the mutual combination of electrochemistry, radiochemistry, analytical chemistry, photochemistry, inorganic chemistry, material science, catalysis and surface science (**Fig. 1.1**).[2]

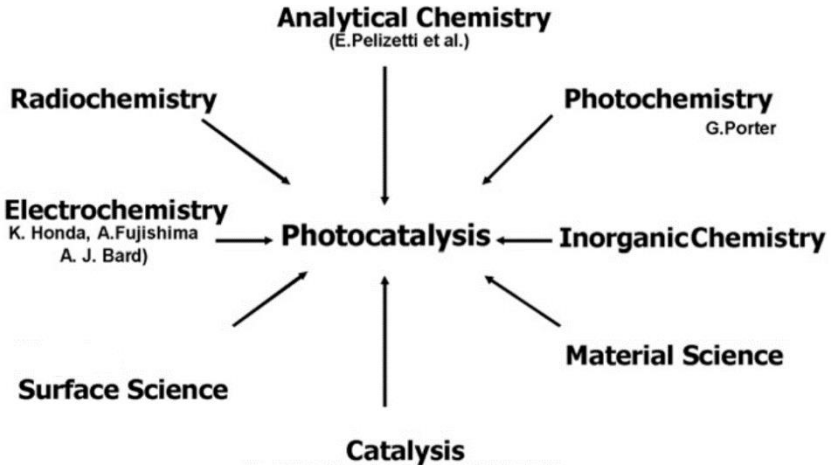

Fig.1.1 Photocatalysis as a multiple discipline[2]

Perhaps the earliest work for driving chemical reactions with sunlight was performed by J. H. Schulze who established the concept of silver-based black and white photography in 1717 when a slurry of silver nitrate, nitric acid and chalk was darkened on exposure to light. [3]

The first semi-permanent images were obtained in 1824 by N. Niepce, a French physicist, using glass plates coated with a dispersion of silver halides (AgBr and AgCl) in bitumen. [4]

Interestingly the earliest example of inorganic solids for photocatalytic water splitting was published in 1913 by a group in Liverpool: *"Synthesis by sunlight in relationship to the origin of life. Synthesis of Formaldehyde from Carbon Dioxide and Water by Inorganic Colloids Acting as Transformers of Light Energy"* [5]

In 1962, monoclinic WO_3 was first discovered as an oxygen generating photocatalyst from water by Krasnovsky and Brin. [6]

Since 1972, the concept of developing stable inorganic materials and using them for solar energy conversion has attracted substantial interest, when Honda and Fujishima had investigated water photolysis on a Pt-TiO_2 electrode arranged in an

electrochemical cell applying only UV irradiation without the application of any external voltage (**Fig. 1.2**).[7]

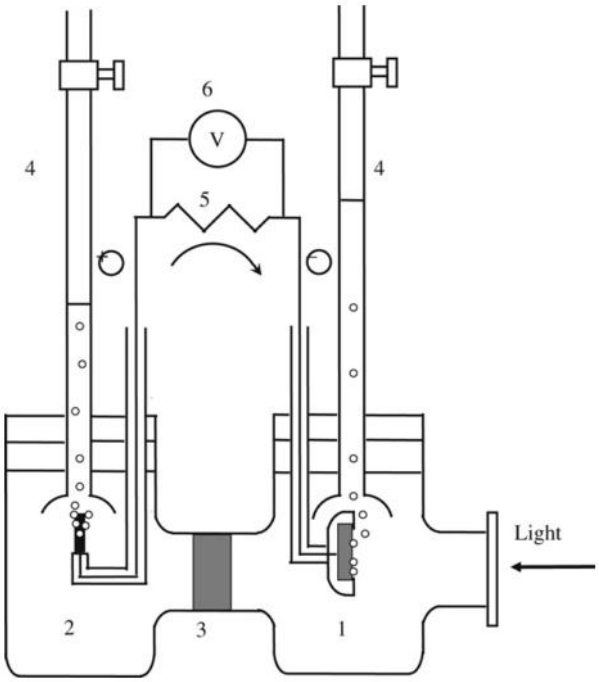

Fig. 1.2 The Honda cell for overall water splitting from 1972 contains the following compartments: (1) TiO_2 anode, (2) Pt cathode (3) Frit (4) Burette (5 – 6) External Circuit with (5) External Load and (6) External Voltage; Arrow shows the direction of current flow [8]

Since that decade, the potential of finding novel light harvesting compounds opened up new research directions using stable, non-toxic, industrially low-cost produced metal oxides. Photocatalysts that can be applied in the induction of water splitting are mainly semiconductor oxide materials.[9]

In 1973 W. H. Strehlow defined the electronic band structure as *"according to the band theory of solids, when atoms are brought together to form a crystal, the discrete electronic states of the isolated atoms merge into energy bands which represent the allowed energies for electrons in the crystal"*. [10] These bands can be separated by forbidden gaps or regions.[10] The atomic orbitals, however, form well-defined energy

levels. This electronic structure consists of the valence band (VB, the highest occupied band), the conduction band (CB, the lowest unoccupied band), and the energy difference between them is defined as the band gap energy (E_g). In conductors, the relative mobility of electrons is high in the conduction band, allowing the free electrons to easily migrate therefore to conduct electricity. For insulators, the CB does not contain electrons and in the VB these electrons are immobile thus the electron-flow is suppressed. Furthermore if the band gap is large (4-12 eV) the material is considered to be an insulator and if E_g is small (0-3 or 0-4 eV) these materials are classified as semiconductors. *"Semiconductor oxides have an electronic band structure such that the valence band, dominated by oxygen 2p orbitals, is full with the electrons immobile, and the higher energy conduction band, consisting predominantly of the metal ion d orbitals, empty of electrons."* [11] However, these materials can be electrically altered when electricity or heat or photons are applied. The energy of a photon depends on its wavelength (λ). Typically, electromagnetic waves are described by any of the following three physical properties: the frequency *f*, wavelength λ, or photon energy *E*. The equation between these properties is

$$E = \frac{hc}{\lambda} \qquad \textbf{(Eq. 1.2)}$$

By altering the semiconductor photocatalyst upon band gap irradiation with energy greater or equal than its band gap, the electrons (e^-) of the valence band (VB) are excited into the conduction band (CB) while the holes (h^+) are left in the VB. Electrons and holes which do not suffer re-combination, migrate toward the surface of the semiconductor where adsorbed species are either reduced by electrons and/or oxidised by holes. To summarise the photo-excitation processes the e^- can be used for the reduction of water to form hydrogen (water splitting half reaction or H_2 evolution) and

also for the reduction of O_2 to form superoxide radicals ($O_2^{\cdot -}$). The photo-hole excitation processes can involve the oxidation of water to form oxygen (water splitting half reaction or O_2 evolution), the oxidation of –OH groups from water for the formation of •OH radicals for microbial disinfection and the direct oxidation of organic matter such as azo-dyes and pollutants.

1.2.1.Requirements for Photocatalytic Water Splitting

In the Honda cell-type water splitting, H_2O is reduced by e^- and oxidised by h^+, forming H_2 and O_2 respectively:

$TiO_2 + 2h\nu \rightarrow 2e^- + 2h^+$ (excitation of TiO_2 by photons) **(Eq. 1.3)**

$2h^+ + H_2O \rightarrow \frac{1}{2}O_2 + 2H^+$ (at the TiO_2 electrode) **(Eq. 1.4)**

$2e^- + 2H^+ \rightarrow H_2$ (at the platinum electrode) **(Eq. 1.5)**

The overall reaction is following the scheme of:

$H_2O + TiO_2 + 2h\nu \rightarrow H_2 + \frac{1}{2}O_2$ **(Eq. 1.6)**

Although to achieve overall water splitting certain energy requirements are needed. One of the most important characteristics of the semiconductor photocatalysts are the absolute position of the conduction and valence bands and the width of the band gap. Band gaps can be measured by spectroscopic method. With regards to this more detail is given in **Section 2.4**. It is known that oxide semiconductors in general potentiate with H^+ or OH^- ions in solution, and the band edges at the interface consequently shift with the pH of the solution by 0.059 V per pH unit change in accordance with the Nernst equation. For H_2 generation the energy at the lower level of the conduction band must be more negative than the redox potential of H^+/H_2 of 0 V vs normal

hydrogen electrode (NHE) at pH = 0 (-0.41 V at pH = 7) (**Fig. 1.3**). For O_2 evolution the energy at the top level of the valence band must be more positive than the redox potential of O_2/H_2O of 1.23 V vs NHE at pH = 0 (+0.87 V at pH = 7).[12, 13] In other words, conduction band electrons are powerful reductants in the range of +0.5 to -1.5 V vs NHE, and valence band holes are good oxidants in the range of +1.0 to +3.5 V vs NHE depending on the semiconductor and the pH.[14]

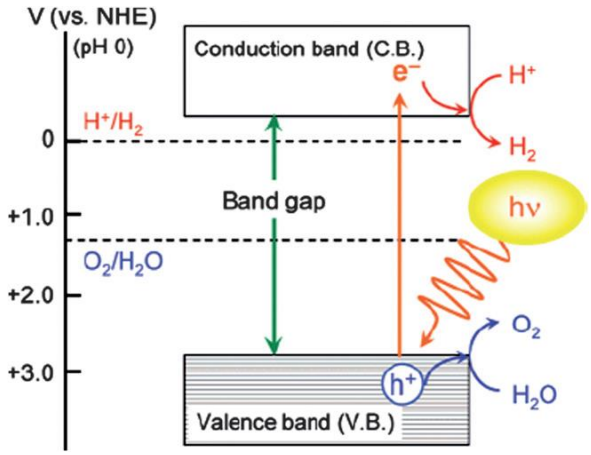

Fig. 1.3 Basic principle of overall water splitting on a heterogeneous photocatalyst [12]

Energetically the theoretical minimum band gap for water splitting is 1.23 eV, which corresponds to light of approximately 1010 nm, indicating that visible light is high enough energy for decomposition of water, however it has been considered that a band gap of ~2.0-2.2 eV is required due to kinetic limitations.[15] In fact, the energy of incoming photons must exceed the band gap energy.

J. R. Bolton explained this threshold wavelength for the photochemical reduction as

$$\lambda_{max} = \frac{nN_0hc\varepsilon}{\Delta G} \qquad \textbf{(Eq. 1.7)}$$

where n is the number of electrons transferred per molecule of fuel produced, ε is the fraction of the photon energy at λ_{max} which is converted to chemical free energy of the fuel, N_0 is the Avogadro's number, h is the Planck's constant in kilojoules, c is the

speed of light in meter per second, ΔG is the Gibbs free energy change in the fuel production reaction in kilojoule per mole of fuel produced. Furthermore, the energy requirement of water splitting reaction is ΔG^0 = + 237 kJ/mol and n = 2 (this example is represented in **Fig. 1.4**).[1]

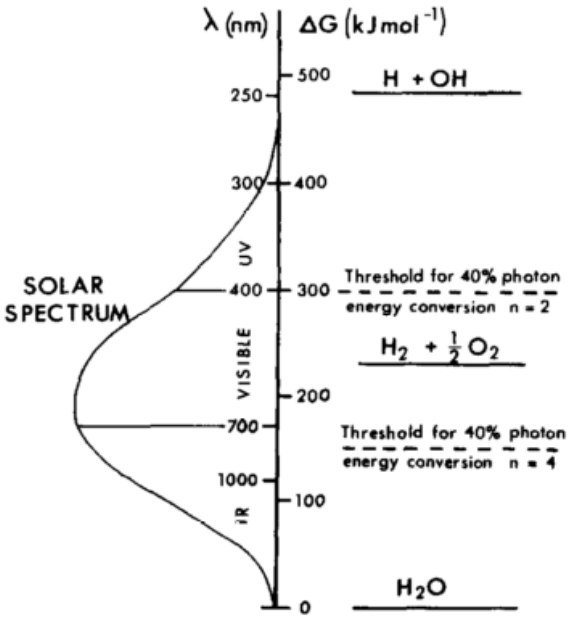

Fig. 1.4 Energy analysis for the reaction H_2O → H_2 + ½ O_2 compared to the solar spectrum. The threshold wavelength is determined by $\lambda_{max} = nN_0hc\varepsilon/\Delta G$ [1]

If we take n = 2 and ε is equal to 0.4 then λ_{max} becomes ~ 400 nm therefore it would not be possible to sensitize water photoreduction and generate H_2 only with visible light if only one photochemical step is applied. Therefore overall water splitting rather requires a cascade two photochemical electron transfer mechanism which will effectively double λ_{max}. This shows analogy to Z-scheme reaction existing in nature.

In contradiction with the Z-scheme reaction, a single visible photon activated photocatalyst was reported in 2006 in Domen's group in *Nature Communications*.[16] This solid solution of $(Ga_{1-x}Zn_x)(N_{1-x}O_x)$ is a yellow powder with an absorption edge at about 510 nm and can be typically synthesised by nitriding a mixture of Ga_2O_3 and

ZnO. According to the authors, DFT calculations indicated that the visible light response can be attributed to the contribution of Zn *3d* atomic orbitals to the valence band where bonding between Zn and N atoms is formed as a result of the formation of the solid solution.[17] When the synthesised particle is used alone, it has negligible photocatalytic activity. When impregnated with 10-20 nm $Rh_{2-y}Cr_yO_3$ nanoparticles (**Fig 1.5**), it shows high overall water splitting efficiency at pH 4 from aqueous H_2SO_4 solution with a ~2.5 % quantum yield at 420 – 440 nm. [16-18]

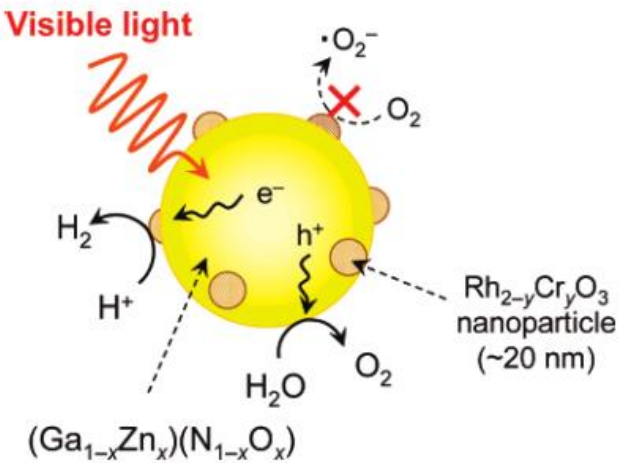

Fig. 1.5 Schematic illustration of mechanism of visible-light-driven overall water splitting on $Rh_{2-y}Cr_yO_3$ loaded $(Ga_{1-x}Zn_x)(N_{1-x}O_x)$ [17]

In more detail to the Z-scheme reaction analogy, Bolton and Hall have shown kinetic limitations on the conversion of light to stored chemical energy **(Fig. 1.6).** This study suggests that the bigger the activation energy the longer lifetime of the product is obtained in a first order kinetic reaction.[19]

In theory, every photon of light which absorbed will contribute toward the production of P from R, hence the quantum yield for the production of P will be assumed to be 100%. From a realistic point of view this number is likely to only represent a 15-16% maximum efficiency for a photochemical solar energy storage system considering the

loss of incomplete absorption of sunlight, internal conversion to the ground state, side reactions, etc.[1]

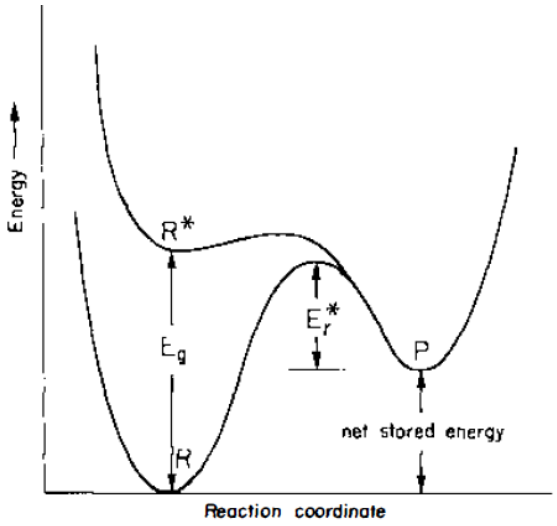

Fig. 1.6 Energy profile of photochemical reaction: R → R*. R denotes the ground state, E_g is the band gap corresponding to the minimum energy gap between the excited state (R*) and the R. E_r* is the activation energy for the back reaction: P → R*. The net stored energy is differential between P and R. [19]

The integrated energy distribution of solar spectrum indicates that only 5% of incoming photons can be accounted as effective UV irradiation and 43% and 52% light correlates to visible (Vis) and infrared (IR) photons respectively (**Fig. 1.7**).[5, 19] Thus, energetically and environmentally it is desirable to develop visible active materials and arrange them in a two-step reaction scheme.

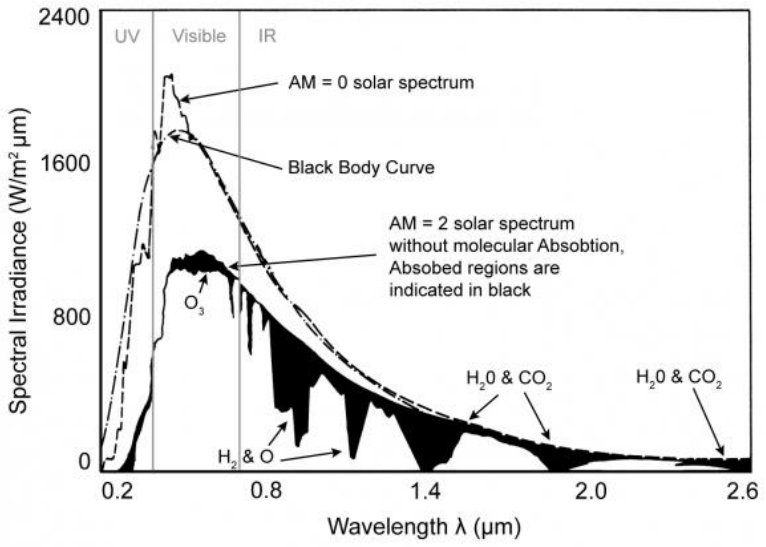

Fig. 1.7 Solar radiation spectrum, the UV, Vis and IR wavelength are labelled accordingly [5]

Once photons are absorbed and excitation occurs across the band gap, the charge separation (h^+ and e^-) takes place and the photoexcited charge carriers migrate to the surface ideally without recombination where the pre-adsorbed species are reduced and oxidised by the photoinduced electrons and holes to produce H_2 and O_2, respectively (**Fig. 1.8**). If the semiconductor surface remains intact the process will be continued with the condition that both substrate and photons are provided. However in competition several processes might take place.[20] Firstly, recombination of separated holes and electrons can occur in the bulk phase (*volume recombination*) or on the surface (*surface recombination*) with additional heat release. Secondly, a process called *back-donation* takes place when the adsorbed species transfer back the photoinduced species to the semiconductor without the chemical conversion of the substrate (H_3O^+ or OH^- molecules). Thirdly, the recombination of evolved H_2 and O_2 molecules can be defined as *surface back reaction* with the formation of H_2O in an exothermic reaction. Therefore, to kinetically suppress the back-reactions, extend the lifetime of charge carriers, enhance the photocatalytic activity and to reduce the

overvoltage, suitable addition of co-catalysts for water reduction and/or oxidation is a widely employed approach; more details will be given in **Section 1.2.2.6**.

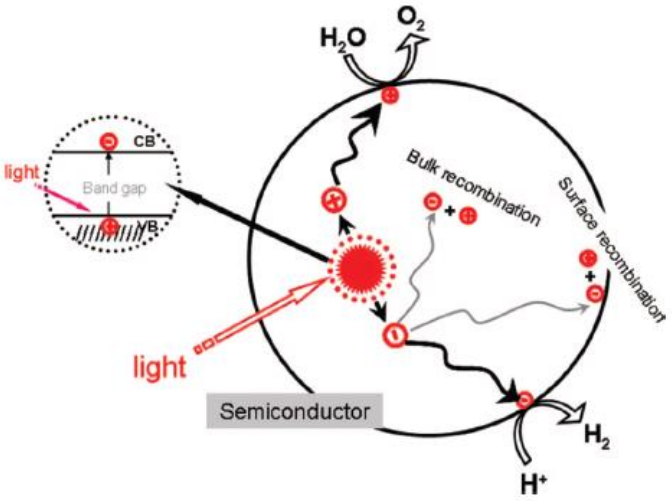

Fig. 1.8 The overall process of photocatalytic water splitting on a photocatalyst particle [20]

Transport of photoexcited carriers is determined by the conductivity, the crystal size, the crystalline structure, the nature and number of structural defects, the surface reaction sites and properties, as well as the morphology of the photocatalyst.

As a golden rule, highly crystalline compounds with high surface area, small particle size and well defined morphology involving low density of defects are considered as good photocatalyst attributes if it is combined with good electronic properties.[15, 21] Furthermore the ideal photocatalyst has to show chemical stability to corrosion and photo-corrosion in aqueous environments.[22] The recyclability and low cost of heterogeneous catalysts are essential in practise in order to design solid reusable photoactive particles.

1.2.2. UV and Visible Light Activated Compounds in Photocatalytic Water Splitting Reaction

1.2.2.1 Band Bending

When a semiconductor (SC) and an electrolyte are brought into contact, electrostatic equilibrium must be attained at the semiconductor-electrolyte interface by charge transfer between the two phases hence the Fermi levels become equal. [23, 24] This electrolyte acts as either an electron donor or acceptor when mobile charge carriers flow from bulk to the surface. For instance on an n-type semiconductor electrons will migrate (which becomes positively charged) to the electrolyte (which becomes negatively charged). Due to the excess charge on the surface, between the SC and the electrolyte a space-charge region must be formed and within the space-charge layer the valence and conduction bands are bent. *Band bending* can be defined as this change of the position of the valence and conduction bands of a semiconductor upon the generation of a space-charge region. This charge distribution is analogous to the *diffuse double layer* formed in solution. In the case of accumulation of positive charges (holes) in the space-charge region, the band tails of VB and CB bend downwards therefore facilitates the migration of h^+ toward the surface and e^- toward the bulk of the semiconductor (**Fig. 1.9a**). This situation is reversed when the space-charge region is negatively charged (accumulated electrons on the surface) and so the band tails bend upwards (**Fig. 1.9b**).[25] The resulting electric field in the space-charge region affects the local energy (electrochemical potential) of photoexcited electrons and holes. *Flat band potential* (E_{fb}) (**Fig. 1.9c**) refers to the definition of potential when no excess charge exists on the surface, thus the bands are not bent.[24, 26]

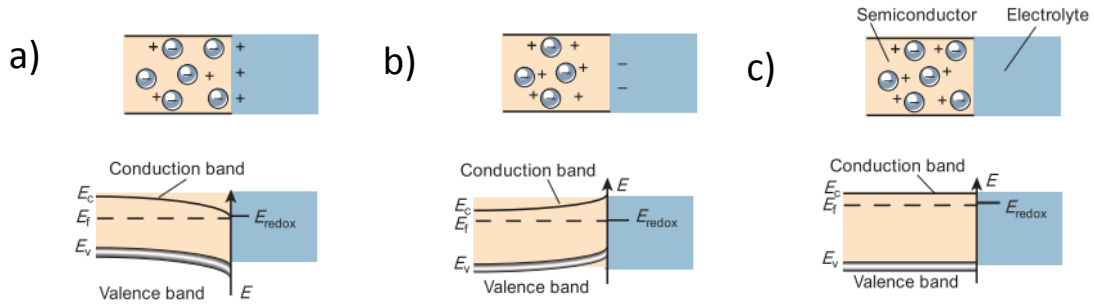

Fig. 1.9 Schematic representation of the electronic energy levels at the interface between an n-type semiconductor and an electrolyte containing a redox couple. The three cases indicated are: a) *accumulation layer*, where excess electrons have been injected into the solid producing a downward bending of the conduction and valence band towards the interface; b) *depletion layer*, where electrons have moved from the semiconductor to the electrolyte, producing an upward bending of the bands; c) *flat band potential*, where no space-charge layer exists in the semiconductor [23]

1.2.2.2 The Role of Electron and Hole Scavengers and Redox Mediators

Since the first revolutionising introduction of Pt-TiO_2 in 1972, many papers have been published on the basis of semiconductor oxides, nitrides, sulphides, phosphates, selenides applied in overall water splitting or in water splitting half reactions (O_2 evolution or H_2 evolution).[9, 27, 28] Some of these examples are represented in **Fig. 1.10**.[29]

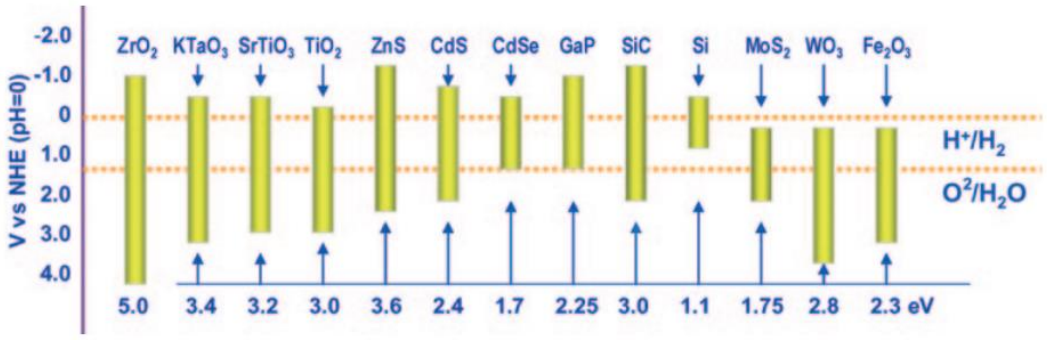

Fig. 1.10 Band gap energies and relative band positions of various semiconductors relative to the water oxidation/reduction potential (V vs NHE at pH = 0)

Even MOFs (Metal Organic Frameworks) are suitable compounds for H_2 generation with excellent gas evolving performance.[30, 31] In fact, in several publications, H_2 and O_2 generation reactions are studied separately using electron and hole scavengers. These studies are rather focused on presenting the suspended catalyst particles in the required sacrificial reagent than the application of potentially costly electrode connections and transparent conducting supports. Commonly used MeOH is a sacrificial electron mediator which mediates the flow of photoinduced electrons while oxidised by photoexcited holes. Similarly, $AgNO_3$ is a typical electron acceptor forming Ag^0 with photoexcited electrons. Although it has to be noted that as an often published misconception, sacrificial H_2 evolution or O_2 evolution half reaction is not equivalent to overall water splitting.[32, 33]

When MeOH oxidation occurs on the surface of TiO_2 photocatalyst, the reaction mechanism is following the scheme of: [34]

$$Ti^{4+} - O^{-}CH_3 + h^{+} \rightarrow Ti^{4+} - OC^{\bullet}H_3 \quad \textbf{(Eq. 1.8)}$$

$$Ti^{4+} - OC^{\bullet}H_3 \rightarrow Ti^{4+} - OC^{\bullet -}H_2 + H^{+} \quad \textbf{(Eq. 1.9)}$$

$$Ti^{4+} - OC^{\bullet -}H_2 \rightarrow Ti^{4+} - OCH_2 + e^{-} \quad \textbf{(Eq. 1.10)}$$

Reactions (**Eq. 1.8-1.10**) involve a two-electron oxidation process in which surface adsorbed methoxy groups are converted to $Ti^{4+}-OC^{\bullet-}H_2$ while protons are reduced by electrons and one molecule of H_2 is released. Evidence for the above reaction mechanism can be explained by "current doubling" given by N. Hykaway et *al.*[35] As a definition given, it can theoretically double the carrier generation by forming radicals in solution from that produced by photon absorption on TiO_2. This model involves both the interaction of holes and radicals produced by the holes, therefore the reaction mechanism and kinetics depend on the nature of the solution and the lifetime of the radicals produced. Authors also noticed that current doubling depends on the acidity of the solvent: the lower the donor number (more acidic) the higher the current doubling ratio.[35] In addition to methanol other organic solvents such as ethanol, 1-propanol, 2-propanol, 1-butanol, 2-butanol, formic acid have shown current doubling effect, however with *e.g.* acetone, ethyl acetate this affect has not been observed. This theory can be based on the theory of removal of the hydroxyl layer from TiO_2 surface with acidic solvents therefore leading to the modification of the inner Helmholtz layer. The other typically used sacrificial agent is silver nitrate. The Ag^+ reduction occurs according to the following mechanism: [36]

$$4Ag^+ + 2H_2O + 4h^+ + 4e^- \rightarrow 4Ag^0 + 4H^+ + O_2 \quad (E^0_{Ag+/Ag,} + 0.8V) \qquad \textbf{(Eq. 1.11)}$$

Although this O_2 evolving half of the water splitting process is more challenging since it typically involves a four-electron process and powerful oxidizing species which can lead to breakdown of the photocatalyst.

As it has been described before in any half or overall water splitting reactions the suitably chosen sacrificial agent or redox mediator is essential as it is moderating the

redox reactions taking place during photoreduction and/or oxidation, and also requires a good match with the CB and VB of the semiconductors. [37]

Some reagents are also suitable for repeated electron transfer and working as a non-sacrificial redox shuttle in the transfer of photoinduced h^+ and e^- **(Fig. 1.11)**.

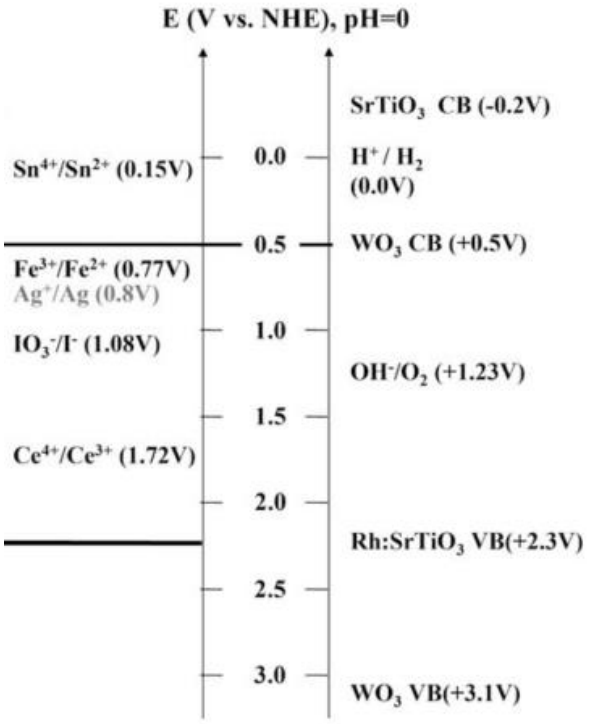

Fig. 1.11 Redox potential of Fe^{3+}/Fe^{2+}, IO^{3-}/I^- redox shuttles at pH = 0 with regards of absolute CB and VB positions of $SrTiO_3$, $SrTi_{1-x}Rh_xO_3$ and WO_3, respectively. [37]

For instance, the oxidation of ferrous ion requires one hole and for the reduction of ferric ion one electron is sufficient as described below:

$$Fe^{2+} + h^+ \rightarrow Fe^{3+} \qquad \textbf{(Eq. 1.12)}$$

$$Fe^{3+} + e^- \rightarrow Fe^{2+} \qquad \textbf{(Eq. 1.13)}$$

In contrast, the redox reaction of IO^{3-}/I^- requires six electrons and holes:

$$I^- + 6OH^- + 6h^+ \rightarrow IO_3^- + 3H_2O \qquad \textbf{(Eq. 1.14)}$$

$$IO_3^- + 3H_2O + 6e^- \rightarrow I^- + 6OH^-$$ **(Eq. 1.15)**

In order to make a proposed reaction work, the understanding of the possible photoinduced charge carrier pathways is essential along with the band structure of the photocatalyst particle.

1.2.2.3 Well-known UV Activated Materials

Much of the focus on the photocatalysis literature from the 70's was based on UV light activated materials such as TiO_2, $SrTiO_3$, ZnO, ZrO_2, $La_2Ti_2O_7$ semiconductor oxides. Of these materials, TiO_2 is one of the most studied classic examples and even recently a whole issue of Chem. Rev. was dedicated to TiO_2 nanomaterials considering a wide range of applications such as photocatalytic hydrogen generation, biomass reforming, photocatalytic reduction of CO_2 into fuels, water and air purification, antibacterial, anticorrosion, antifogging, self-cleaning, photovoltaic applications, gas sensors, biosensors and biomedical therapies. [38-59] P25 TiO_2 is the universal UV active standard for comparing activities of photocatalysts. This compound is a phase mixture of ~75% anatase and 25% rutile TiO_2 with a band gap of 3.1 eV and 25 nm particle size.

1.2.2.4 Crystal Structure Effects

To achieve overall water splitting mechanism the electronic structure of the compound has to be identified. **Fig. 1.12** shows the groups of elements which form suitable band gap structures of the corresponding oxide, oxynitride and nitride materials, and which have been successfully applied as photocatalysts for overall water splitting reactions.[12]

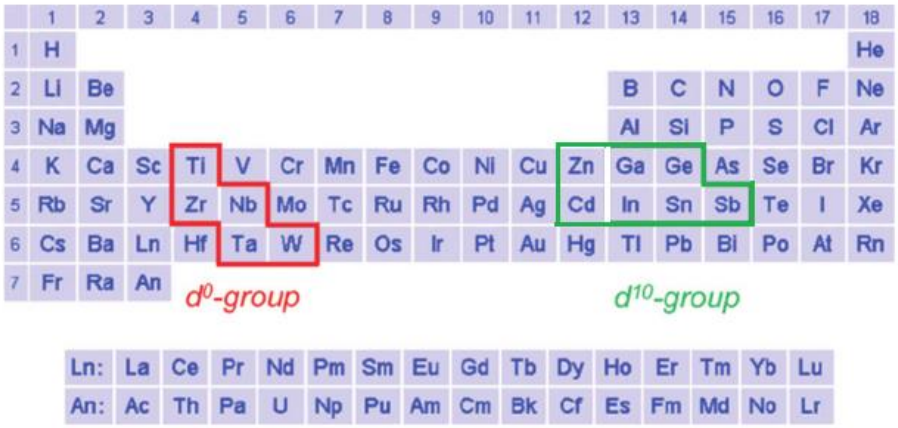

Fig. 1.12 Principal cation components for photocatalytic overall water splitting[12]

Photocatalysts based on transition-metal cations with empty *d* orbitals are defined as having a d^0 electronic configuration (red group). The metal cations which have d^{10} electronic configuration, with filled *d* orbitals are shown in the green group. The band gap structure of the above mentioned materials consist *s*, d^0 *and* d^{10} orbitals in the conduction band, which have more negative potential than 0 V vs NHE. The oxidation state of such elements are the highest, Ti^{4+}, Zr^{4+}, Nb^{5+}, Ta^{5+}, W^{6+}, in addition elements with d^{10} orbitals are Ga^{3+}, In^{3+}, Ge^{4+}, Sn^{4+} and Sb^{5+}.[12] It has to be also noted that some other reported suitable elements cannot be missed from these groups like Zn and Cd with d^{10} configuration, with Zn^{2+} and Cd^{2+} respectively.[27]

In this thesis, the main focus will be on titanates, such as single ($ATiO_3$, A: Mg^{2+}–Ba^{2+}) and lanthanide double perovskites ($A_2Ti_2O_7$, A: La^{3+}–Nd^{3+}), pyrochlore-type rare earth structures ($A_2Ti_2O_7$, A: Sm^{3+}−Yb^{3+}) and the A-site transition metal Y with a cubic pyrochlore $Y_2Ti_2O_7$ structure, therefore **Tab. 1.1** is used to represent some of the major crystallographic features of these structures beside the reported band gap energies. [7, 60-65]

	Ti-O distances (Å)	Octahedron distortion	Ti-Ti distances (Å)	Ti-O-Ti angle (º)	Connected octahedra	
$SrTiO_3$ perovskite (3.2eV)	1.9505 x 6	Perfect octahedron	3.901	180	6 corners	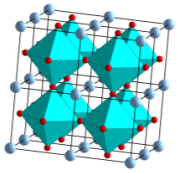
$Y_2Ti_2O_7$ pyrochlore (3.5eV)	1.9404 x 6	Perfect octahedron	3.5704	~135 ~70 ~57	6 corners	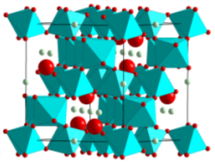
TiO_2 rutile (3eV)	1.9442 x 4 1.9770 x 2	Very small elongation of octahedra	2.9533 x 2 3.5622 x 8	~75 ~175 ~130	2 edges + 8 corners	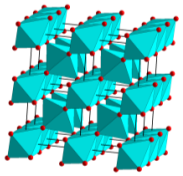
$La_2Ti_2O_7$ layered perovskite (3.8eV)	1.814 1.898 1.972 1.9914 2.02 2.1969	"5 coordination"	3.6901 3.8601 3.9400 3.9447 4.1329 4.1329	~145 ~139 ~75	6 corners	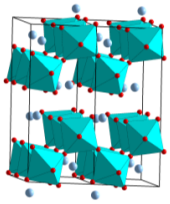

Tab. 1.1 Band gap and crystallographic features for various titanates

Importantly, as a common feature all of these materials are composed of a network of corner-sharing TiO_6 octahedra, in addition having the titanium in the coordination of 6, which most likely make them photocatalytically active compounds.[27, 61] In other words, having the feature of oxo-bridged metal ions in photocatalytically active compounds can facilitate an efficient charge separation and migration pathway.

1.2.2.5 Visible Light Activated Materials

Extended understanding of the above mentioned parent compounds (See **Section 1.2.2.3.** and **Section 1.2.2.4.**) has led the chemistry community to develop visible light activated materials. Visible light is defined from approximately 400 – 700 nm (3.10 eV – 1.77 eV). How can we design visible light active materials? In the literature the

most common method for approaching this is by modifying the electronic band structure. This process called band gap engineering by narrowing the band gap energy of the semiconductor either by forming a more positive donor level above the VB or pushing the CB into a more negative value (V vs NHE). Example for the earlier is $SrTiO_3$ doped with Rh cation[66] and for the latter WO_3 doped with Cs.[67] Band gap engineering can be achieved by metal and non-metal doping.

In the past decades, attention has been paid to doping titania with *3d* transition metals such as V, Cr, Mn, Fe, Co, Ni and Rh. It was found that *3d* metal doping created an occupied level either in the band gap (near the VB) or in the VB and this can be assigned to the t_{2g} state of the dopant. The charge transfer between this newly formed t_{2g} state and the CB of TiO_2 contributed to the photoexcitation being feasible under visible light.[9] Others have suggested the possibility of shifting the absorption edge of TiO_2 towards the visible light region.[68] Choi et *al.* investigated the electron configuration of the dopant when inserted into TiO_2 and found a good correlation between photoreactivity and charge carrier recombination dynamics.[69] Doping with Fe^{3+}, Mo^{5+}, Ru^{3+}, Os^{3+}, Re^{5+} V^{4+} and Rh^{3+} showed a significant increase in both photooxidation and reduction whereas Co^{3+}, Al^{3+} doping into TiO_2 resulted in detrimental effects. In 2007, Kudo and co-workers reported Ni^{3+}, Rh^{4+} and Cr^{6+} insertion into titania and measured negligible O_2 evolution rate using 0.05 M $AgNO_3$ solution under visible light while titania co-doped with Ta^{5+}, Nb^{5+} and Sb^{5+} resulted in Ni^{2+}, Rh^{3+} and Cr^{3+} charge-compensated cation distribution in the tetragonal TiO_2 rutile structure along with increased O_2 evolving capability upon visible light exposure.[70-72]

$SrTiO_3$ is also suitable for substitution on the B-site with various reported cations therefore visible light photocatalytic activity is achievable. In 2004, Kudo et *al.* reported Mn, Ru, Rh, Ir, Cr, Pd, Pt doping into cubic $SrTiO_3$ single perovskite. Pd gave difficulties in doping as impurity phases were formed and Pt did not show visible response upon irradiation, however Rh doping promoted excellent H_2 evolution capability from aq. methanol solution when loaded with Pt co-catalyst.[66, 73]

Lee and co-workers investigated the effect of cation insertion $La_2Ti_2O_7$ layered perovskite structure. It was reported that Fe and Cr doping into the monoclinic $La_2Ti_2O_7$ resulted in a visible light activated H_2 evolving photocatalyst, giving the explanation that the dopant B-site cation led to the formation of partially filled *3d* band within the band gap therefore playing a role as an electron donor level.[74] $La_2Ti_2O_7$ also became visible active for H_2 evolution when doped with Rh and loaded with Pt nanoparticles as a co-catalyst.[75]

Evidently, if we follow the series of lanthanides the next parent structure to look at is the pyrochlore-type $Fd\bar{3}m$ rare earth titanates ($RE_2Ti_2O_7$, RE: Yb^{3+}–Sm^{3+}), in addition the A-site transition metal Y exhibit a cubic $Fd\bar{3}m$ pyrochlore structure of $Y_2Ti_2O_7$.[61] In the literature the synthesis of Cr-doped $Y_2Ti_2O_7$ has been reported with Cr^{4+} present in the structure[76] although for the application this compound was only proposed as a SOFC electrolyte material. [77] Moreover, as described earlier, Rh seemed like a promising dopant into different pyrochlore structures which gave the idea for the synthesis of $Y_2Ti_{2-x}Rh_xO_7$.

1.2.2.6 The Role of Co-catalyst

Mainly noble metals or metal oxide alloys are used as co-catalysts due their electronic configurations. For instance Pt^0, Au^0, Ag^0, Ru^0, Rh^0, IrO_2, RuO_2, NiO_x, $Rh_{2-y}Cr_yO_3$ are widely applied co-catalysts.[9, 36] The role of the co-catalyst is to provide chemically active sites where relevant chemical transformations can take place with lower activation barriers than on the semiconductor itself. Furthermore, co-catalyst nanoparticles play a role to trap photoexcited e^- or h^+ and to extend the lifetime of energetic charge carriers that reach the surface of the semiconductor by enhancing the rates of electron–hole separation at the co-catalyst/semiconductor interface.[78] J. Yang et *al.* claimed the following: „noble metals with larger work function, thus lower Fermi level than that of a semiconductor oxide, should more rapidly trap electrons." [79] In other words, in the case of Pt^0, photo-extited elecrons can be transferred from the CB to metallic Pt particles deposited on TiO_2 surface.[80] The authors further claimed that H^+ reduction on the Pt^0 co-catalyst surface consists of two steps: 1. discharge step, 2. catalytic step. Hence, both electronic properties of suitably chosen co-catalyst and reaction pathways should be defined in redox reactions.

1.2.2.7 Action Spectrum, Apparent Quantum Efficiency and Turnover Numbers

In order to assess the visible light activity and photon excitation processes, Action Spectrum, Apparent Quantum Efficiency (AQE) and Turnover Rate (TOR) have been suggested as useful metrics between photocatalysts.[9, 81]

Action spectrum can be defined as the rate of activity of photocatalyst (for photcatalytic gas generation usually the units are µmol gas evolved or µmol gas

evolved/g catalyst) plotted against various wavelengths (nm). For these types of measurement either a monochromator or narrow band pass filters (for instance 400 ± 5 nm, 450 ± 5 nm, etc.) are used to produce the spectrum.

The AQE of photocatalytic systems is measured at a certain wavelength and defined as:

$$AQE = \frac{\mathrm{nX}}{\mathrm{F}} \qquad \textbf{(Eq. 1.16)}$$

where *n* is the number of electrons used in the photocatalytic process, *X* is the number of molecules formed or of substrate consumed and *F* is the number of incident photons or photon flux.[82]

For photocatalytic H_2 generation in methanol the AQE is defined as: [9]

$$AQE = \frac{2 * Number\ of\ H_2\ molecules}{number\ of\ incident\ photons} * 100\% \qquad \textbf{(Eq. 1.17)}$$

assuming 1 photon generates 1 electron and 2 electrons are required for H_2O reduction.

For photocatalytic O_2 evolution in $AgNO_3$ the AQE is defined as: [9]

$$AQE = \frac{4 * Number\ of\ O_2\ molecules}{number\ of\ incident\ photons} * 100\% \qquad \textbf{(Eq. 1.18)}$$

assuming 1 photon generates 1 hole and 4 holes are required for H_2O oxidation.

The TOR is calculated as following:

$$TOR = \frac{\mathrm{X}}{\mathrm{N}} \qquad \textbf{(Eq. 1.19)}$$

where X is the gas evolution rate, N denotes the site where the reaction takes place. Turnover rates/turnover frequency normalised to mass and surface area have been suggested to prove that a system is catalytic. [83]

The TOR units are defined as s^{-1}.

$$TOR_m = \frac{\text{Gas evolution rate}}{\text{catalyst mass}} \quad \textbf{(Eq. 1.20)}$$

$$TOR_s = \frac{\text{Gas evolution rate}}{\text{surface area}} \quad \textbf{(Eq. 1.21)}$$

Despite the simplicity of the above mentioned comparisons, in the photocatalysis literature we do not always find one or the other metrics therefore the direct comparisons of photocatalysts are difficult.

1.2.2.8 Current Best Photocatalysis Systems

1.2.2.8.1 Z-scheme (two-photon process)

Before discussing the current best Z-scheme systems, it is worth looking at **Tab. 1.2** that summarises some of the photocatalysts reported as UV light driven single compounds with an $E_g \geq 3.1$ eV with regards of their AQEs.[9] Nevertheless, many publications lack AQE numbers, a *Chemical Review* from 2010 published by Chen introduces numerous other examples to provide a general insight for UV active compounds with $\lambda \leq 400$ nm excitation wavelength. [9]

Tab. 1.2 Reported photocatalysts able to split pure water under UV light and their apparent quantum efficiencies.

Oxide(s)	Cocatalyst	Light Source	Solution	AQE / %	Ref.
TiO_2 (anatase) coated with NaOH	Rh	500 W-Hg	Water vapour	29 (340 nm)	84
P25 TiO_2	Pt	250 W-Hg	Pure water	1.4 (300-400 nm)	85
$SrTiO_3$	NiO_x	400 W-Hg	Water vapour	N/A	60, 86
$La_2Ti_2O_7$	NiO_x	450 W-Hg	Pure water	27 (N/A)	87
$Y_2Ti_2O_7$	NiO_x	400 W-Hg	Pure water	3 (313 nm)	88
$K_4Nb_6O_{17}$	NiO_x	450 W-Hg	Pure water	5.3 (330 nm)	89
$Ba_5Nb_4O_{15}$	NiO_x	400 W-Hg	Pure water	17 (270 nm)	90
$NaTaO_3$:La	NiO	400 W-Hg	Pure water	56 (270 nm)	91
$Sr_2Ta_2O_7$	NiO	400 W-Hg	Pure water	12 (270 nm)	92

From the above dataset in **Tab. 1.2** it is clear that direct comparison of Apparent Quantum Efficiency numbers of various UV activated compounds is challenging as authors published photocatalysts for overall water splitting using different band pass filters with wavelengths of 270 nm (UVC), 313 nm (UVB) and 330 nm UVA spectrum, respectively.

In the last two decades, major attention has been turned to investigate novel compounds in H_2/O_2 evolution upon visible light exposure. Some reported examples concerning H_2 evolution activity are shown in **Tab. 1.3**. Examples in particular are deficient in AQE quotations but compounds are structurally important to be mentioned in this section.

Tab. 1.3 Reported H_2 evolution photocatalysts able to generate hydrogen with a sacrificial electron donor (MeOH) under Vis light and their H_2 evolution activities.

Oxide(s)	Cocatalyst	Light Source	Aqueous Solution	H_2 activity ($\mu mol\ h^{-1}g^{-1}$)	AQE / %	Ref.
$SrTiO_3$:Ru	Pt	300 W-Xe ($\lambda > 440$ nm)	MeOH	5.7	N/A	[66]
$SrTiO_3$:Rh	Pt	300 W-Xe ($\lambda > 440$ nm)	MeOH	390	5.2 (420nm)	[66]
$SrTiO_3$:Sb,Cr	Pt	300 W-Xe ($\lambda > 420$ nm)	MeOH	156	N/A	[93]
$CaTiO_3$:Rh	Pt	300 W-Xe ($\lambda > 420$ nm)	MeOH	28.3	N/A	[94]
$La_2Ti_2O_7$:Cr	Pt	500 W-Hg ($\lambda > 420$ nm)	MeOH	30	N/A	[95]
$La_2Ti_2O_7$:Fe	Pt	500 W-Hg ($\lambda > 420$ nm)	MeOH	20	N/A	[95]
$La_2Ti_2O_7$:Rh		300 W-Xe ($\lambda > 420$ nm)	MeOH	8.3	N/A	[75]
$BiTaO_4$:Cu	RuO_2	350 W-Xe ($\lambda > 400$ nm)	MeOH	878	N/A	[96]
$SnNb_2O_6$	Pt	300 W-Xe ($\lambda > 420$ nm)	MeOH	60	N/A	[97, 98]
$K_4Nb_6O_{17}$:Ni	-	500 W-Hg ($\lambda > 400$ nm)	MeOH	144	N/A	[99]

Some visible light driven catalysts for O_2 evolution are reported in **Tab. 1.4**. These classic examples mostly exhibit AQE data in the visible light spectrum at various single wavelengths such as 420, 435, 450 and 480 nm, respectively following the compounds' absorption properties, hence comparison of materials is difficult but estimation can be made.

Tab. 1.4 Reported O_2 evolution photocatalysts able to generate oxygen with a sacrificial electron acceptor ($AgNO_3$) or redox mediator ($FeCl_3$) under Vis light and their apparent quantum efficiencies.

Oxide(s)	Cocatalyst	Light Source	Aqueous Solution	AQE / %	Ref.
WO_3	RuO_2	900 W-Xe ($\lambda > 410$ nm)	$AgNO_3$	N/A	100-102
WO_3:Cs	-	300 W-Xe ($\lambda > 420$ nm)	$FeCl_3 + H_2SO_4$	19 (420 nm)	67
TiO_2:Ru	-	500 W-Xe ($\lambda > 440$ nm)	$FeCl_3$	0.14 (435 nm)	103
TiO_2:Sb,Rh	-	300 W-Xe ($\lambda > 440$ nm)	$AgNO_3$	N/A	71
$BiVO_4$	-	300 W-Xe ($\lambda > 420$ nm)	$AgNO_3$	9 (450 nm)	104, 105
Bi_2MoO_6	-	300 W-Xe ($\lambda > 420$ nm)	$AgNO_3$	N/A	106
Ag_3PO_4	-	300 W-Xe ($\lambda > 400$ nm)	$AgNO_3$	80 (480 nm)	107

Tab. 1.5 shows some of the Z-scheme type reactions for overall water splitting when visible light activated H_2 and O_2 evolving catalysts are combined. Although the main focus of this thesis is not on tantalum oxynitrides compounds it is worth considering that with a suitably chosen redox mediator (IO_3^-/I^-) these materials work well when combined for instance with Pt-loaded WO_3. In this summary table among single perovskites, the highest gas generating activity was achieved when Pt-loaded $SrTiO_3$:Rh was combined with not commercialised Bi_2MoO_6, but the combination of

$Pt/SrTiO_3$:Cr,Ta and Pt/WO_3 exhibited the highest apparent quantum efficiency at 420 nm.

Tab. 1.5 Z-scheme type photocatalysts for water splitting under visible light irradiation [108]

H_2 photocatalyst	O_2 photocatalyst	Mediator	Activity (μmol $h^{-1}g^{-1}$)		AQE / %	Ref.
			H_2	O_2		
$Pt/SrTiO_3$:Cr,Ta	Pt/WO_3	IO_3^-/I^-	16	8	1 (420 nm)	[109, 110]
Pt/TaON	RuO_2/TaON	IO_3^-/I^-	3	1.5	0.1-0.2	[111]
$Pt/CaTaO_2N$	Pt/WO_3	IO_3^-/I^-	6.6	3.3	N/A	[112]
$Pt/BaTaO_2N$	Pt/WO_3	IO_3^-/I^-	4	2	N/A	[112]
Pt/TaON	Pt/WO_3	IO_3^-/I^-	24	12	0.4 (420 nm)	[113]
$Pt/SrTiO_3$:Rh	$BiVO_4$	Fe^{3+}/Fe^{2+}	15	7.2	0.3 (440 nm)	[114]
$Pt/SrTiO_3$:Rh	Bi_2MoO_6	Fe^{3+}/Fe^{2+}	19	8.9	0.2 (440 nm)	[114]
$Pt/SrTiO_3$:Rh	WO_3	Fe^{3+}/Fe^{2+}	7.8	4.0	0.2 (440 nm)	[114]

1.2.2.8.2 Single-photon Photocatalyst Systems

In **Section 1.2.1** the solid solution of gallium zinc oxynitride has been introduced as a single photon converting photocatalyst for overall water splitting. This compound, $Zn_{1.44}GeN_{2.08}O_{0.38}$ and nanoparticulate Co(II)O have been also investigated as such visible light activated catalysts (**Tab. 1.6)**. Interestingly, the former compound's reported AQE is doubled compared to the introduced best Z-scheme systems (**Tab. 1.5**) and goes against Bolton and Hall statement. [1, 19]

Tab. 1.6 Single-photon photocatalyst systems [108]

Single photocatalyst	Co-catalyst	Mediator	Activity (μmol $h^{-1}g^{-1}$)		AQE / %	Ref.
			H_2	O_2		
$(Ga_{0.88}Zn_{0.12})(N_{0.88}O_{1.02})$	$Rh_{2-x}Cr_xO_3$	H_2SO_4 (pH 4.5)[a]	800	400	2.5 (420 – 440 nm)	16-18
$Zn_{1.44}GeN_{2.08}O_{0.38}$	RuO_2	IO_3^-/I^- [a]	14.2	7.4	N/A	115
Nano Co(II)O	-	Pure water	[b]	[c]	5 [d]	116

[a] Light source: 450 W high-pressure mercury lamp; Reaction cell type: inner irradiation cell, made of pyrex; Incident light: λ > 400 nm, pyrex cell filled with aqueous $NaNO_2$ solution as a filter
[b] ~920 mL $h^{-1}g^{-1}$ H_2 and [c] ~430 mL $h^{-1}g^{-1}$ O_2 with incident laser beam at λ > 532 nm and at the power of 900 mW; Reaction cell type: 33 mL high vacuum chamber; no reported data for injected GC volume and reactor headspace
[d] with AM1.5G simulated sunlight (100 mW cm^{-2})

1.2.2.8.3 Dye-sensitisation

There has been extensive work on the development of dye-sensitised solar cells (DSSC), since the publication of the famous 1991 *Nature* paper by O'Regan and Grätzel.[117] The use of a mesoporous semiconductor electrode with high internal surface area when combined with a photon-excited Ru-complex photosensitiser has led to enormous improvement of the field of photovoltaics and photochemistry. **Fig. 1.13** shows the process of visible light photocatalytic H_2 evolution over a wide band gap semiconductor sensitised by an adsorbed dye molecule.

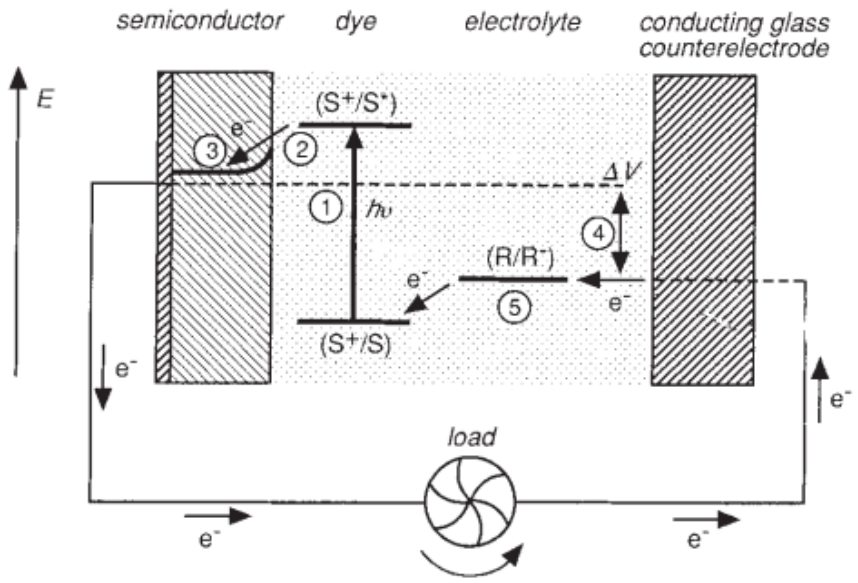

Fig.1.13 Schematic representation of the principle of the dye-sensitised photovoltaic cell to indicate the electron energy level in the different phases. The cell voltage observed under illumination corresponds to the difference, ΔV, between the quasi-Fermi level of TiO_2 under illumination and the electrochemical potential of the electrolyte. The latter is equal to the Nerst potential of the redox couple (R/R^-) used to mediate charge transfer between the electrodes. S, sensitiser, S*, electronically excited sensitiser, S^+, oxidised sensitiser [117]

Under visible light, band gap excitation of n-type TiO_2 wide band gap semiconductor is not possible, but instead it is feasible with the aid of the adsorbed dye that is excited upon irradiation. The excited dye is then able to inject an electron into the conduction band of the semiconductor, resulting in the oxidised state of the dye. The conduction band e^- is then able to reduce adsorbed species such as H^+ to generate H_2; although the e^- can also recombine with the oxidised dye, similarly to the undesired electron-hole recombination in conventional band gap excitation mechanisms. If recombination is avoided, the oxidised dye is reduced by a donor, which may be sacrificial (*e.g.* EDTA) or non-sacrificial (*e.g.* I^-), maintaining the adsorbed dye concentration. No valence band h^+ is formed in this mechanism. The classic example for the dye is $Ru(bpy)_3^{2+}$

but several derivatives can be found in a 2010 *Chemical Review* paper published by Hagfeldt et *al.* [118]

1.2.2.9 Methyl Orange Model Compound

Before choosing a model pollutant for photocatalytic testing, the origin and type of chemicals present in waste water have to be identified. Azo dyes can be classified as synthetic dyes, produced by textile industry as waste.

In 1999, A. Mills and J. Wang proposed an interesting concept on TiO_2 sensitised decolourisation of Methylene Blue (MB) with UV light which up to that date was a widely used test molecule. They revealed that MB undergoes photobleacing in the presence and absence of oxygen when sensitised by TiO_2 particles. They investigated that MB in the absence of oxygen and in the presence of an electron acceptor and TiO_2 catalyst, is reduced to its colourless leuco form. Oxidation process led by oxygen quickly regenerates MB at high partial pressure, at high concentration of dissolved oxygen and in non-acidic solution. [119]

Following upon this, Ohtani and co-workers published a paper questioning '*Is methylene blue an appropriate substrate for a photocatalytic activity test? A study with visible-light responsive titania.'* [120] Authors examined the dye photoabsorption in various regions, such as region I (290-400 nm), region II (400-540 nm) and region III (540-680 nm) and compared the efficacy of the visible light activated S-TiO_2 and the UV absorber TiO_2 particles in aerated aqueous solution on photobleacing of MB (**Fig. 1.14**).

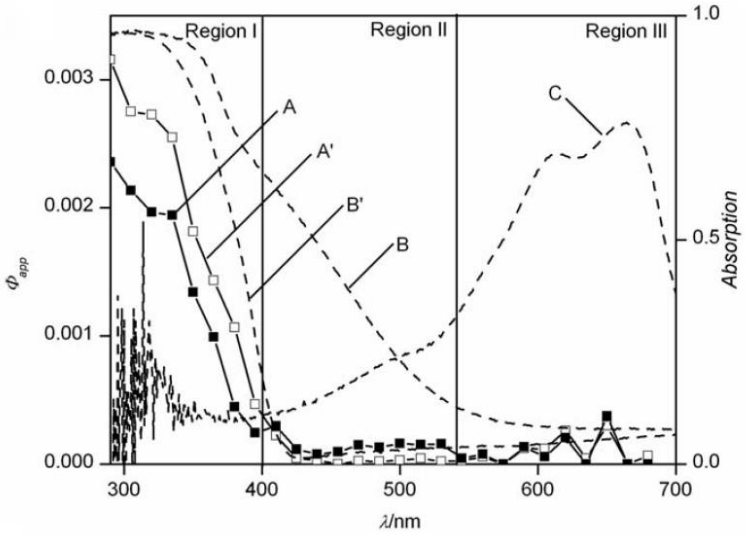

Fig. 1.14 Action spectra of MB decomposition on (A) S–TiO_2 and (A') P-25 in overall region; DR spectra of (B) S–TiO_2 and (B') P-25; (C) DR spectrum of adsorbed MB. [120]

As explained, in region I, the MB decomposition was attributable to the band gap photoexcitation of titania particles where the absorption coefficient of MB is negligible. This reaction mechanism seems ambiguous and can be easily influenced by the reaction conditions as introduced above by Mills.

In region II, only the S-TiO_2 particles have visible light absorption and this can probably contribute to the higher rate of MB decomposition which tails off in this region. The overall degradation rate remains low with both catalysts.

In region III, where none of the photocatalysts have absorption, some of the MB decomposes due to photosensitisation. The mechanism is explained as follows: electrons are injected from the photoexcited MB molecules to the titanate particles, the reduced molecular oxygen results in the oxidative decomposition of electron deficient MB dye. Therefore this mechanism cannot be seen as real photocatalytic activity.

Due to this ambiguity of such dye decomposition it is required to prove that a catalyst is photocatalytically active *e.g.* in acetic acid decomposition, 4-chlorophenol

demineralisation or in *E. coli* inactivation reactions. Also the detailed analysis of the by-products or mineralised products could affirm what reaction takes place.

Methyl Orange (MO) (**Fig. 1.15**) is one of the most studied and commonly used model dyes in photocatalytic reactions, with almost 9,000 published papers considering its photo-degradation [121], partly because its concentration can be easily monitored using a spectrometer. Additionally, MO shows stability under visible light, opposed to another popular dye molecule, Methylene Blue (MB) which suffers self-degradation.[120]

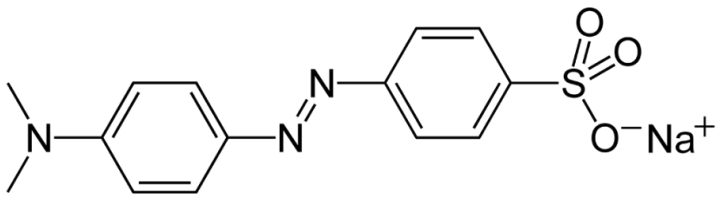

Fig. 1.15 Skeletal structural formula of Methyl Orange

If complete mineralisation of MO occurs the following products should be formed:

$$C_{14}H_{14}N_3NaO_3S + catalyst + hv + \ 21.5\ O_2 \ \rightarrow \ H_2SO_4 + 3\ HNO_3 + 14CO_2 + \\ + 4\ H_2O + \ NaOH \qquad \textbf{(Eq. 1.22)}$$

It has to be noted that **Eq. 1.22** does not describe the formation of by-products.

1.2.2.10 Antimicrobial Disinfection

Disinfection of surfaces with various chemicals are less effective over time due to increasing levels of resistance. Disinfectants have chemical origins, which possess the risk of being toxic and producing allergic reactions. In water treatment applications,

chlorination has many disadvantages, associated with the generation of toxic products (*e.g.* trihalomethanes: chloroform, dibromochlormethane). As an alternative method to disinfect surfaces, heterogeneous photocatalyst particles could be used, which are semiconductor materials that can be activated upon light exposure and can produce reactive oxygen species (ROS).

1.2.2.10.1 Metallic Nanoparticles and Semiconductor oxides in Disinfection

Synthetic nanomaterials and particularly silver nanoparticles (Ag-NPs) have been widely demonstrated to exhibit anti-microbial activity against a broad range of microorganisms, including bacteria, fungi and viruses. [122]

The bactericidal action of a semiconductor (TiO_2) (**Fig. 1.16**) can be explained by the damage caused to cell membrane via an oxidative attack on the cellular components, and subsequent loss of membrane permeability (**Fig. 1.17**). [123]

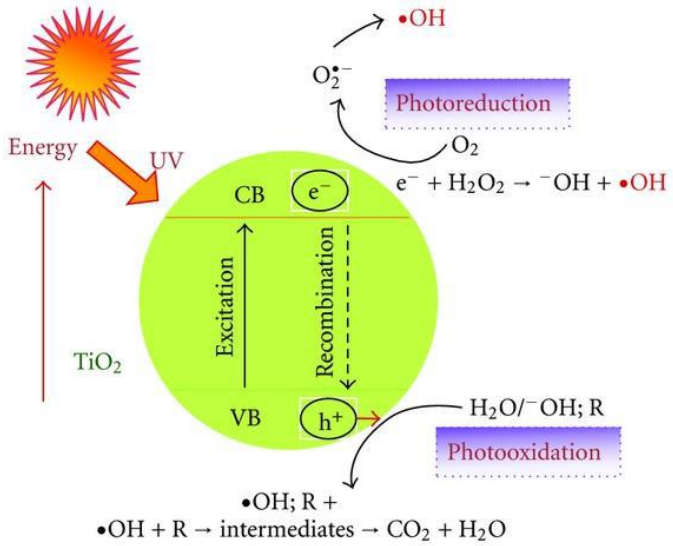

Fig. 1.16 Schematic diagram of photocatalytic degradation of organic matter in photo-reduction and photo-oxidation reactions with oxygen free-radicals [124] (Note reaction mechanism works for organic dye as well)

Studies on the cellular components and their interaction with ROS indicated that degradation of the cellular membrane is followed by the leakage of the intracellular components (RNA, proteins, and cations) from the cells.[125]

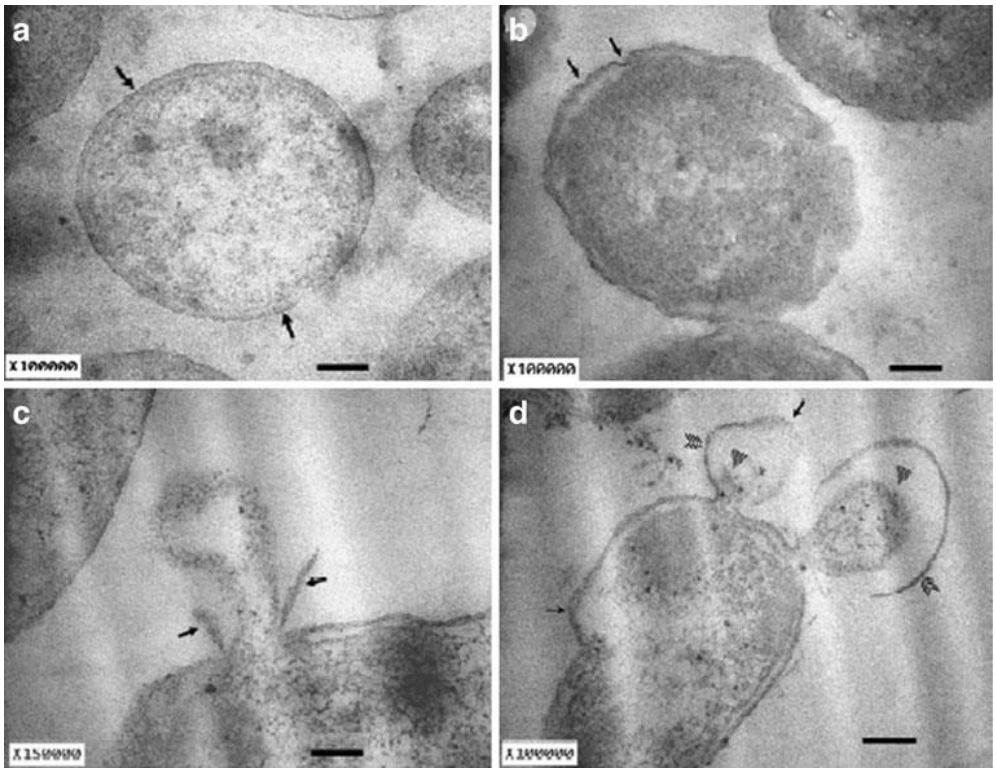

Fig. 1.17 Transmission electron micrographs of photocatalytically treated P. aeruginosa. (a) Untreated cells transverse section showing normal thickness and shape cell wall (arrows). b–d Cells after 240 min treatment showing abnormal wavy cell wall (arrows), (c) cytoplasmic material escaping from the cell with damaged cell wall (arrows) and (d) cell showing two "bubbles" of cellular material with cell wall (arrows). Catalyst TiO_2 thin film. Bar marker = 200 nm. [123]

In **Section 4.1** there will be a detailed introduction to the use of semiconductor materials in Methyl Orange degradation and *E. coli* inactivation.

1.3. Conclusion and Future Prospects

The approach of designing inorganic solar light harvesting systems has been introduced as an analogy to green plant photosynthesis. Energetic considerations for solar to hydrogen conversion and cost-effective use of semiconductors have been discussed. For developing novel and complex metal oxide based systems, the understanding of their crystal structure, conductivity, surface reaction and recombination sites is determined to be a crucial step. Hence, co-catalyst loading on the catalyst surface has been considered as a widely employed manipulation technique for the enhancement of charge separation. The assistance of suitably chosen electron and hole scavengers and redox mediators has been explained to facilitate favourable irreversible or reversible photochemical reactions taking place. The pH of the chemical environment during photoreaction is also essential as it can cause catalyst stability issues if not considered but can also positively drive the photooxidation and –reduction processes. Several UV-activated (*e.g.* TiO_2, $SrTiO_3$, ZnO, ZrO_2, $La_2Ti_2O_7$, $Y_2Ti_2O_7$ compounds have been discussed, in particular those titanate structures that are composed of a network of corner-sharing TiO_6 octahedrons. Attention has also been paid to review the existing dopants, particularly rhodium for visible light incorporation into likely to be photocatalytically active oxide materials. A short overview was also written to introduce the current best photosynthesis systems upon excitation with UV and visible light and comparison was made according to their AQEs.

Importantly, besides water splitting application, water remediation and water disinfection could greatly benefit society and the environment when reusable photocatalysts are designed.

1.4. References

1. J. R. Bolton, *Journal of Solid State Chemistry*, 1977, **22**, 3-8.
2. J. M. Herrmann, *J. Photochem. Photobiol. A Chem.*, 2010, **216**, 85-93.
3. L. D. Stroebel and R. D. Zakia, *The Focal encyclopedia of photography*, 3rd edn., Focal Press, 1993.
4. W. Baatz, *Photography: An illustrated historical overview*, New York: Barron's, 1997.
5. B. Moore and T. A. Webster, *Proc. R. Soc. Lond. B* 1913, **87**, 163-176.
6. A. A. Krasnovsky and G. P. Brin, *Dokl. Akad. Nauk SSSR*, 1962, **147**, 656–659.
7. A. Fujishima and K. Honda, *Nature*, 1972, **238**, 37-38.
8. A. Fujishima, X. Zhang and D. A. Tryk, *Surface Science Reports*, 2008, **63**, 515-582.
9. X. B. Chen, S. H. Shen, L. J. Guo and S. S. Mao, *Chem. Rev.*, 2010, **110**, 6503-6570.
10. W. H. Strehlow and E. L. Cook, *Journal of Physical and Chemical Reference Data*, 1973, **2**, 163-200.
11. I. Christopher, *Niobium oxide based material for visible light photocatalysis, PhD Thesis*, University of Liverpool, 2012.
12. M. Kitano and M. Hara, *J. Mater. Chem.*, 2010, **20**, 627-641.
13. L. A. Harris and R. H. Wilson, *Annual Review of Materials Science*, 1978, **8**, 99-134.
14. M. R. Hoffmann, S. T. Martin, W. Y. Choi and D. W. Bahnemann, *Chemical Reviews*, 1995, **95**, 69-96.
15. R. M. Navarro, M. C. Alvarez-Galván, J. A. Villoria De La Mano, S. M. Al-Zahrani and J. L. G. Fierro, *Energy Environ. Sci.*, 2010, **3**, 1865-1882.
16. K. Maeda, K. Teramura, D. Lu, T. Takata, N. Saito, Y. Inoue and K. Domen, *Nature*, 2006, **440**, 295.
17. K. Maeda and K. Domen, *The Journal of Physical Chemistry C*, 2007, **111**, 7851-7861.
18. K. Maeda, K. Teramura and K. Domen, *Journal of Catalysis*, 2008, **254**, 198-204.
19. J. R. Bolton and D. O. Hall, *Annual Review of Energy*, 1979, **4**, 353-401.
20. A. L. Linsebigler, G. Lu and J. T. Yates Jr, *Chemical Reviews*, 1995, **95**, 735-758.
21. K. Maeda, A. Xiong, T. Yoshinaga, T. Ikeda, N. Sakamoto, T. Hisatomi, M. Takashima, D. Lu, M. Kanehara, T. Setoyama, T. Teranishi, K. Domen, K. Maeda, A. Xiong, T. Yoshinaga, T. Ikeda, N. Sakamoto, T. Hisatomi, M. Takashima, D. Lu, M. Kanehara, T. Setoyama, T. Teranishi and K. Domen, *Angewandte Chemie International Edition*, 2010, **49**, 4096-4099.
22. H. Maruska, H. P. Maruska and A. K. Ghosh, *Solar Energy*, 1978, **20**, 443-458.
23. M. Gratzel, *Nature*, 2001, **414**, 338-344.
24. A. J. Bard and L. R. Faulkner, *Electrochemical methods: Fundamentals and Applications*, 2nd edn., Wiley, 2001.
25. Z. Zhang and J. T. Yates, *Chemical Reviews*, 2012, **112**, 5520-5551.
26. A. Hagfeld and M. Grätzel, *Chemical Reviews*, 1995, **95**, 49-68.
27. F. E. Osterloh, *Chem. Mater.*, 2008, **20**, 35-54.
28. F. E. Osterloh, *Chem. Soc. Rev.*, 2013, **42**, 2294-2320.
29. R. M. Navarro Yerga, M. Consuelo Álvarez Galván, F. del Valle, J. A. Villoria de la Mano and J. L. Fierro, *ChemSusChem*, 2009, **2**, 471-485.
30. A. Fateeva, P. A. Chater, C. P. Ireland, A. A. Tahir, Y. Z. Khimyak, P. V. Wiper, J. R. Darwent and M. J. Rosseinsky, *Angew. Chem. Int. Ed.*, 2012, **51**, 7440-7444.
31. T. Zhang and W. Lin, *Chem. Soc. Rev.*, 2014, **43**, 5982-5993.
32. Z. Chen, T. F. Jaramillo, T. G. Deutsch, A. Kleiman-Shwarsctein, A. J. Forman, N. Gaillard, R. Garland, K. Takanabe, C. Heske, M. Sunkara, E. W. McFarland, K. Domen, E. L. Milled and H. N. Dinh, *J Mater Res*, 2010, **25**, 3-16.
33. J. M. Buriak, P. V. Kamat and K. S. Schanze, *ACS Applied Materials and Interfaces*, 2014, **6**, 11815-11816.

34. D. A. Panayotov, S. P. Burrows and J. R. Morris, *J. Phys. Chem. C*, 2012, **116**, 6623-6635.
35. N. Hykaway, W. M. Sears, H. Morisaki and S. R. Morrison, *Journal of Physical Chemistry*, 1986, **90**, 6663-6667.
36. T. Hisatomi, J. Kubota and K. Domen, *Chem. Soc. Rev.*, 2014, **43**, 6470-6471.
37. S. W. Bae, S. M. Ji, S. J. Hong, J. W. Jang and J. S. Lee, *Int J Hydrogen Energy*, 2009, **34**, 3243-3249.
38. X. Chen and A. Selloni, *Chemical Reviews*, 2014, **114**, 9281-9282.
39. L. X. Sang, Y. X. Zhao and C. Burda, *Chemical Reviews*, 2014, **114**, 9283-9318.
40. M. Cargnello, T. R. Gordon and C. B. Murray, *Chemical Reviews*, 2014, **114**, 9319-9345.
41. X. D. Wang, Z. D. Li, J. Shi and Y. H. Yu, *Chemical Reviews*, 2014, **114**, 9346-9384.
42. K. Lee, A. Mazare and P. Schmuki, *Chemical Reviews*, 2014, **114**, 9385-9454.
43. L. Z. Wang and T. Sasaki, *Chemical Reviews*, 2014, **114**, 9455-9486.
44. D. Fattakhova-Rohlfing, A. Zaleska and T. Bein, *Chemical Reviews*, 2014, **114**, 9487-9558.
45. G. Liu, H. G. Yang, J. Pan, Y. Q. Yang, G. Q. Lu and H.-M. Cheng, *Chemical Reviews*, 2014, **114**, 9559-9612.
46. H. Zhang and J. F. Banfield, *Chemical Reviews*, 2014, **114**, 9613-9644.
47. P. Coppens, Y. Chen and E. Trzop, *Chemical Reviews*, 2014, **114**, 9645-9661.
48. M. Kapilashrami, Y. Zhang, Y.-S. Liu, A. Hagfeldt and J. Guo, *Chemical Reviews*, 2014, **114**, 9662-9707.
49. F. De Angelis, C. Di Valentin, S. Fantacci, A. Vittadini and A. Selloni, *Chemical Reviews*, 2014, **114**, 9708-9753.
50. K. Bourikas, C. Kordulis and A. Lycourghiotis, *Chemical Reviews*, 2014, **114**, 9754-9823.
51. R. Asahi, T. Morikawa, H. Irie and T. Ohwaki, *Chemical Reviews*, 2014, **114**, 9824-9852.
52. M. Dahl, Y. Liu and Y. Yin, *Chemical Reviews*, 2014, **114**, 9853-9889.
53. L. Liu and X. Chen, *Chemical Reviews*, 2014, **114**, 9890-9918.
54. J. Schneider, M. Matsuoka, M. Takeuchi, J. Zhang, Y. Horiuchi, M. Anpo and D. W. Bahnemann, *Chemical Reviews*, 2014, **114**, 9919-9986.
55. Y. Ma, X. Wang, Y. Jia, X. Chen, H. Han and C. Li, *Chemical Reviews*, 2014, **114**, 9987-10043.
56. K. Liu, M. Cao, A. Fujishima and L. Jiang, *Chemical Reviews*, 2014, **114**, 10044-10094.
57. Y. Bai, I. Mora-Seró, F. De Angelis, J. Bisquert and P. Wang, *Chemical Reviews*, 2014, **114**, 10095-10130.
58. J. Bai and B. Zhou, *Chemical Reviews*, 2014, **114**, 10131-10176.
59. T. Rajh, N. M. Dimitrijevic, M. Bissonnette, T. Koritarov and V. Konda, *Chemical Reviews*, 2014, **114**, 10177-10216.
60. K. Domen, S. Naito, T. Onishi, K. Tamaru and M. Soma, *Journal of Physical Chemistry*, 1982, **86**, 3657-3661.
61. R. Abe, M. Higashi, K. Sayama, Y. Abe and H. Sugihara, *The Journal of Physical Chemistry B*, 2006, **110**, 2219-2226.
62. M. A. Subramanian, G. Aravamudan and G. V. Subba Rao, *Prog. Solid State Chem.*, 1983, **15**, 55-143.
63. J. K. Burdett, T. Hughbanks, G. J. Miller, J. W. Richardson and J. V. Smith, *J. Amer. Chem. Soc.*, 1987, **109**, 3639-3646.
64. U. Diebold, *Surface Science Reports*, 2003, **48**, 53-229.
65. Y. A. Abramov, V. G. Tsirelson, V. E. Zavodnik, S. A. Ivanov and I. D. Brown, *Acta Crystallographica Section B*, 1995, **51**, 942-951.

66. R. Konta, T. Ishii, H. Kato and A. Kudo, *The Journal of Physical Chemistry B*, 2004, **108**, 8992-8995.
67. Y. Miseki, H. Kusama, H. Sugihara and K. Sayama, *Journal of Physical Chemistry Letters*, 2010, **1**, 1196-1200.
68. T. Nishikawa, Y. Shinohara, T. Nakajima, M. Fujita and S. Mishima, *Chemistry Letters*, 1999, 1133-1134.
69. W. Choi, A. Termin and M. R. Hoffmann, *Journal of Physical Chemistry*, 1994, **98**, 13669-13679.
70. R. Niishiro, H. Kato and A. Kudo, *Physical Chemistry Chemical Physics*, 2005, **7**, 2241-2245.
71. R. Niishiro, R. Konta, H. Kato, W.-J. Chun, K. Asakura and A. Kudo, *The Journal of Physical Chemistry C*, 2007, **111**, 17420-17426.
72. T. Ikeda, T. Nomoto, K. Eda, Y. Mizutani, H. Kato, A. Kudo and H. Onishi, *J. Phys. Chem. C*, 2008, **112**, 1167-1173.
73. A. Kudo, R. Niishiro, A. Iwase and H. Kato, *Chem. Phys.*, 2007, **339**, 104-110.
74. D. W. Hwang, H. G. Kim, J. S. Jang, S. W. Bae, S. M. Ji and J. S. Lee, *Catal Today*, 2004, **93-95**, 845-850.
75. Q. Wang, T. Hisatomi, Y. Moriya, K. Maeda and K. Domen, *Catalysis Science & Technology*, 2013, **3**, 2098-2103.
76. F. Matteucci, G. Cruciani, M. Dondi, G. Baldi and A. Barzanti, *Acta Mater*, 2007, **55**, 2229-2238.
77. H. E. Hung, C. K. Hao and C. S. Lee, *ECS Transactions*, 2013, **58**, 175-184.
78. S. Linic, P. Christopher and D. B. Ingram, *Nature Materials*, 2011, **10**, 911-921.
79. J. Yang, D. Wang, H. Han and C. Li, *Accounts of Chemical Research*, 2013, **46**, 1900-1909.
80. M. Ni, M. K. H. Leung, D. Y. C. Leung and K. Sumathy, *Renewable and Sustainable Energy Reviews*, 2007, **11**, 401-425.
81. M. Boudart, *Chemical Reviews*, 1995, **95**, 661-666.
82. M. D. Archer and A. J. Nozik, *Nanostructured and Photoelectrochemical Systems for Solar Photon Conversion*, Imperial College, 2008.
83. I. E. Wachs, S. P. Phivilay and C. A. Roberts, *ACS Catalysis*, 2013, **3**, 2606-2611.
84. K. Yamaguti and S. Sato, *Journal of the Chemical Society, Faraday Transactions 1: Physical Chemistry in Condensed Phases*, 1985, **81**, 1237-1246.
85. S. Tabata, H. Nishida, Y. Masaki and K. Tabata, *Catal Lett*, 1995, **34**, 245-249.
86. K. Domen, S. Naito, M. Soma, T. Onishi and K. Tamaru, *Journal of the Chemical Society, Chemical Communications*, 1980, 543-544.
87. H. G. Kim, D. W. Hwang, S. W. Bae, J. H. Jung and J. S. Lee, *Catal Lett*, 2003, **91**, 193-198.
88. R. Abe, M. Higashi, Z. Zou, K. Sayama and Y. Abe, *Chemistry Letters*, 2004, **33**, 954-955.
89. K. Sayama, H. Arakawa and K. Domen, *Catalysis Today*, 1996, **28**, 175-182.
90. Y. Miseki, H. Kato and A. Kudo, *Energy Environ. Sci.*, 2009, **2**, 306-314.
91. H. Kato, K. Asakura and A. Kudo, *J. Amer. Chem. Soc.*, 2003, **125**, 3082-3089.
92. A. Kudo, H. Kato and S. Nakagawa, *J Phys Chem B*, 2000, **104**, 571-575.
93. H. Kato and A. Kudo, *J Phys Chem B*, 2002, **106**, 5029-5034.
94. S. Nishimoto, M. Matsuda and M. Miyake, *Chemistry Letters*, 2006, **35**, 308-309.
95. D. W. Hwang, H. G. Kim, J. S. Lee, J. Kim, W. Li and S. H. Oh, *The Journal of Physical Chemistry B*, 2005, **109**, 2093-2102.
96. H. Zhang, G. Chen, X. Li and Q. Wang, *Int J Hydrogen Energy*, 2009, **34**, 3631-3638.
97. Y. Hosogi, K. Tanabe, H. Kato, H. Kobayashi and A. Kudo, *Chemistry Letters*, 2004, **33**, 28-29.
98. Y. Hosogi, H. Kato and A. Kudo, *Chemistry Letters*, 2006, **35**, 578-579.

99. H.-Y. Lin, T.-H. Lee and C.-Y. Sie, *Int J Hydrogen Energy*, 2008, **33**, 4055-4063.
100. J. R. Darwent and A. Mills, *J. Chem. Soc., Faraday Trans. 2*, 1982, **78**, 359-367.
101. W. Erbs, J. Desilvestro, E. Borgarello and M. Graetzel, *The Journal of Physical Chemistry*, 1984, **88**, 4001-4006.
102. S. J. Hong, H. Jun, P. H. Borse and J. S. Lee, *Int J Hydrogen Energy*, 2009, **34**, 3234-3242.
103. T. Ohno, F. Tanigawa, K. Fujihara, S. Izumi and M. Matsumura, *J. Photochem. Photobiol. A Chem.*, 1999, **127**, 107-110.
104. A. Kudo, K. Ueda, H. Kato and I. Mikami, *Catal Lett*, 1998, **53**, 229-230.
105. A. Kudo, K. Omori and H. Kato, *J. Amer. Chem. Soc.*, 1999, **121**, 11459-11467.
106. Y. Shimodaira, H. Kato, H. Kobayashi and A. Kudo, *J Phys Chem B*, 2006, **110**, 17790-17797.
107. Z. Yi, J. Ye, N. Kikugawa, T. Kako, S. Ouyang, H. Stuart-Williams, H. Yang, J. Cao, W. Luo, Z. Li, Y. Liu and R. L. Withers, *Nature Materials*, 2010, **9**, 559-564.
108. A. Kudo and Y. Miseki, *Chem. Soc. Rev.*, 2009, **38**, 253-278.
109. K. Sayama, K. Mukasa, R. Abe, Y. Abe and H. Arakawa, *Chemical Communications*, 2001, 2416-2417.
110. R. Abe, K. Sayama and H. Sugihara, *The Journal of Physical Chemistry B*, 2005, **109**, 16052-16061.
111. M. Higashi, R. Abe, A. Ishikawa, T. Takata, B. Ohtani and K. Domen, *Chemistry Letters*, 2008, **37**, 138-139.
112. M. Higashi, R. Abe, K. Teramura, T. Takata, B. Ohtani and K. Domen, *Chemical Physics Letters*, 2008, **452**, 120-123.
113. R. Abe, T. Takata, H. Sugihara and K. Domen, *Chemical Communications*, 2005, 3829-3831.
114. H. Kato, M. Hori, R. Konta, Y. Shimodaira and A. Kudo, *Chemistry Letters*, 2004, **33**, 1348-1349.
115. Y. Lee, H. Terashima, Y. Shimodaira, K. Teramura, M. Hara, H. Kobayashi, K. Domen and M. Yashima, *The Journal of Physical Chemistry C*, 2007, **111**, 1042-1048.
116. L. Liao, Q. Zhang, Z. Su, Z. Zhao, Y. Wang, Y. Li, X. Lu, D. Wei, G. Feng, Q. Yu, X. Cai, J. Zhao, Z. Ren, H. Fang, F. Robles-Hernandez, S. Baldelli and J. Bao, *Nat Nano*, 2014, **9**, 69-73.
117. B. O'Regan and M. Gratzel, *Nature*, 1991, **353**, 737-740.
118. A. Hagfeldt, G. Boschloo, L. Sun, L. Kloo and H. Pettersson, *Chemical Reviews*, 2010, **110**, 6595-6663.
119. A. Mills and J. Wang, *Journal of Photochemistry and Photobiology A: Chemistry*, 1999, **127,** 123–134.
120. X. Yan, T. Ohno, K. Nishijima, R. Abe and B. Ohtani, *Chemical Physics Letters*, 2006, **429**, 606-610.
121. *Web of Knowledge*, Thomson Reuters, 2015.
122. I. Sondi and B. Salopek-Sondi, *Journal of Colloid and Interface Science*, 2004, **275**, 177-182.
123. P. Amézaga-Madrid, R. Silveyra-Morales, L. Córdoba-Fierro, G. V. Nevárez-Moorillón, M. Miki-Yoshida, E. Orrantia-Borunda, Solı, amp, x and F. J. s, *Journal of Photochemistry and Photobiology B: Biology*, 2003, **70**, 45-50.
124. S. Ahmed, M. G. Rasul, W. N. Martens, R. Brown and M. A. Hashib, *Desalination*, 2010, **261**, 3-18.
125. H. A. Foster, I. B. Ditta, S. Varghese and A. Steele, *Appl. Microbiol. Biotechnol.*, 2011, **90**, 1847-1868.

2. Chapter 2: Experimental Methods

2.1 Synthetic Methods

2.1.1 Standard Solid State Synthesis

Solid state synthesis is one of the methods used in this thesis. Typically, it involves mixing and grinding of appropriate quantities of solid starting materials using an agate mortar and pestle, followed by a subsequent reaction at high temperature in the absence of solvent. Grinding is one of the crucial steps of the synthesis as it increases the homogeneity within the samples, reduces the particle size and facilitates the thermodynamic reactions taking place with an increased reaction rate.[1] For synthesising solid state compounds, the required amount of binary metal oxides or carbonates were weighed out and mixed until a homogenous powder was obtained. All starting materials were heated before weighing in an oven at 200 ºC, or in a furnace at 950 ºC for lanthanide oxides and Y_2O_3, due to highly hygroscopic properties. All samples were prepared on a 1.0 g scale. High reaction temperature (often ~1400 ºC) is required to overcome kinetic barriers such as ion diffusion, resulting in long timescales (hours - days) due to the slow rate of diffusion in several cases.[1] In order to minimise the reaction time and maximise the contact between individual particles, powders were pressed into pellets (d = 10 mm, p = 5 tonnes). The pellets were then placed into inert alumina crucibles for the appropriate reaction time and fired in a programme controlled electric box furnace under static air. Additional grinding and annealing cycles were carried out until the reaction reached completion, indicated by Powder X-ray Diffraction (PXRD) measurements. Reaction was completed when the PXRD patterns stopped changing and all starting materials and impurity phases disappeared. Details

of reaction temperature and time, heating and cooling rates, atmospheres are described in the appropriate chapters.

2.1.2 Hydrothermal Synthesis

Hydrothermal synthesis is referred to a synthesis technique for forming crystalline materials from its salts at high temperature and pressure in the presence of aqueous solvent. The formation of the product is dependent on the synthesis time, temperature and pressure, the solubility of the precursors and the pH of the solution during reaction.[2] The crystal growth is performed in a stainless steel pressure vessel (**Fig. 2.1**) supplied by Parr Instrument Company.

Fig. 2.1 Stainless steel autoclave suitable for hydrothermal synthesis

The 125 mL volume stainless steel body, used in synthesis, contains a removable PTFE cup and lid which are sealed on the top of the body's screw cap with six crap crews. An expandable wave spring maintains continuous pressure on the seal during the cooling cycle when PTFE parts might otherwise relax and leak. Stirring can be provided with magnetic stirrer bars when mixing precursors. For safe operation, the pressure in these vessels should never exceed 1900 psi and a maximum temperature of 250 ºC based on the *pT* diagram of water which is primarily determined by the degree

of autoclave fill.[2] The autoclave is generally placed into a programmable electric oven where crystallisation occurred during synthesis.

The method is particularly suitable for the growth of high surface area, good quality crystals while maintaining appropriate control over their compositions.[2] In addition, in relatively low temperature range (160 – 240 ºC) the formation of a new material is feasible compared to the classic solid state method.

Reaction temperature and time, heating and cooling rate parameters are described in the appropriate chapters.

2.1.3 Sol-gel Synthesis

Sol-gel process is a multi-step wet-chemical technique used for the fabrication of inorganic oxides.[3] Typically it involves mixing of metal ions on an atomic level; in solution providing improved homogeneity, lower synthesis temperature and beneficial size and morphology. This technique allows us to synthesise nanoparticulate metal oxide particles in comparison with the solid state synthesised micron scale grain size.

Sol-gel process generally involves the formation of amorphous transition metal-oxo complex (M-O-M) from metal salts and organometallic precursors (*e.g.* metal alkoxides). First, the hydrolysis of alkoxide precursor occurs, followed by condensation reaction while the polymeric gel network is being formed. In the Pechini method,[4] complexing agents are added such as Ethylene glycol and a buffering agent, Citric acid to assist the gel formation and facilitate the formation of an integrated network as an intermediate product. The polycondensation of Ethylene glycol and Citric acid starts above 100 ºC. When the heating temperature exceeds 400 ºC, oxidation and pyrolysis begin with the formation of a dry amorphous

oxynitrate/oxycarbonate complex. Upon further firing this intermediate product in air, crystalline solid oxide products are formed with a high degree of homogeneity.

2.2 Powder Diffraction Techniques

2.2.1 Powder X-ray Diffraction (PXRD)

Powder diffraction is a powerful technique for acquiring information about crystal structures of crystalline solids. This approach has been widely employed in this thesis. The basics and terminology of crystal structure determination will be discussed below.

2.2.1.1 Crystal Symmetry and Diffraction

A crystal structure [1, 5] consists of regular arrangements and coordination of atoms in a three dimensional space. This regular uniformity can be represented by the periodic repeat of identical unit cells; the unit cell is defined as the smallest repeating unit in a crystal structure. Crystal lattices can be categorised in seven major crystal/lattice systems, in line with relation between the unit cell length (*a, b, c*) and the relation between the angles (α, β, γ) (**Tab. 2.1**).[1]

Crystals form lattice planes; these are described by the three Miller indices (*h*, *k* and *l*) which converge the unit cell axes at *a/h*, *b/k* and *c/l*, respectively. The definition of lattice planes is made to provide a reference grid to which the atoms in the crystal structure may be referred; it can be correspondent to and coincides with layers of atoms.[1] Nevertheless, one atom (or lattice point) can belong to more than one unit cell depending on the centering type, which if combined with any of the seven possible lattice systems makes 14 possible Bravais lattice types. When the possible Bravais

lattice types are combined with the internal symmetry operators for the unit cells, 230 space groups are defined in total.[6]

Table 2.1 The seven crystal systems and the typical features of the lattice [1]

Crystal system	Unit cell edges	Unit cell angles
Triclinic	a≠b≠c	α≠β≠γ
Monoclinic	a≠b≠c	α=γ= 90°, β≠90°
Orthorhombic	a≠b≠c	α=β=γ= 90°
Tetragonal	a=b≠c	α=β=γ= 90°
Hexagonal	a=b≠c	α=β= 90°, γ= 120°
Trigonal	a=b=c	α=β=γ≠ 90°
Cubic	a=b=c	α=β=γ= 90°

Powder diffraction can provide information about the space group that a crystalline solid adopts and its lattice characteristics, namely the length of lattice edges (usually referred as lattice parameters) and lattice angles. In particular, it is a common technique in solid state chemistry, as it is rapid and non-destructive. In this thesis, X-rays are used for crystal structure diffraction studies. Besides this, neutrons and electrons sources are also prevalent radiation types but will not be discussed further.

2.2.1.2 Fundamentals of Diffraction

When a radiation beam of wavelength λ encounters a solid crystalline material, diffraction occurs due to the 'reflection' by the lattice planes within the crystal structure. In fact, diffraction can be only observed when the scattered beam from one lattice plane is in phase with the scattered beam from other lattice planes and by combining they form an enhanced scattered beam (*constructive interference*, **Fig. 2.2** [7]). If the generated scattered beams are out of phase, then *destructive interference* arises, therefore diffracted beams eliminate each other. [1, 6]

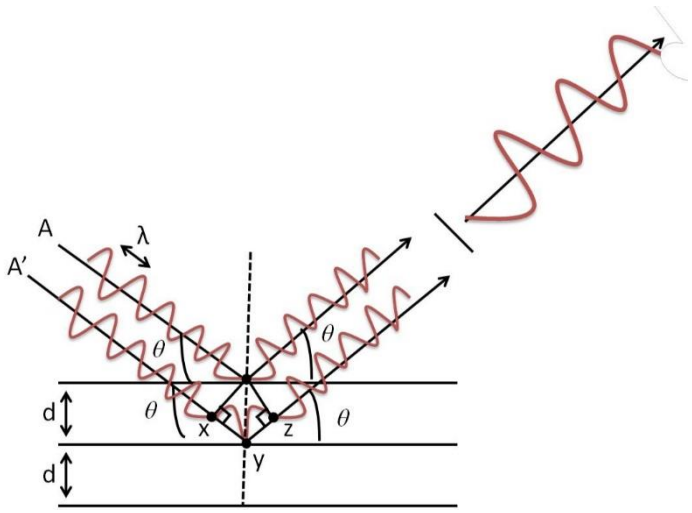

Fig. 2.2 Bragg reflection of monochromatic radiation beams A and A', with wavelength λ and incident angle θ, from adjacent crystal lattice planes regularly spaced by d. The labelled distances and points are used to construct the Bragg equation (Eq. 2.1).

According to **Fig. 2.2**, constructive interference occurs when the difference in path lengths ($xyz = xy + yz$, and from trigonometry $xy = yz = d\ sin\theta$) for the beams *A* and *A'* is equal to an integer number of wavelengths, $n\lambda$; this is known as the Bragg's law [6, 8] (**Eq. 2.1**). Moreover, when the Bragg's law is not satisfied, destructive interference will occur.

Bragg's law:

$$n\lambda = 2d\ sin\theta \qquad \textbf{(Eq. 2.1)}$$

where n is an integer number, λ is the radiation beam wavelength, θ is the angle relative to the incident beam at which constructive interference occurs and d is the interplanar distance of the lattice planes, defined by the three Miller indices (h, k and l).[9]

Therefore, for a monochromatic beam with a constant wavelength λ, the diffracted beam can only be observed at discrete θ values, which are called Bragg angles and are associated with the interplanar spacing d according to the Bragg's law. As mentioned above, the interplanar spacing d depends on the lattice characteristics (lattice parameters and angles) of the crystal and the Miller indices (h, k, l) of the planes. The exact relation differs for each of the seven crystal systems in **Table 2.1***;* the example for the cubic crystal system, for which $a = b = c$ and $\alpha = \beta = \gamma = 90^o$, is presented in **Eq. 2.2**. [1, 6]

$$\frac{1}{d^2} = \frac{h^2}{a^2} + \frac{k^2}{b^2} + \frac{l^2}{c^2} = \frac{h^2 + k^2 + l^2}{a^2} \qquad \textbf{(Eq. 2.2)}$$

Because the atomic structure is a key characteristic of each crystalline material, it diffracts X-rays according to a unique characteristic diffraction pattern, showing peaks (Bragg reflections) for each of the allowed Bragg angles. The diffraction pattern can be analysed based on the peak positions, which corresponds to the spacing of the lattice planes. By assigning Miller indices to each observed reflection (a process known 'as indexing' of the diffraction pattern) it is possible to precisely identify the crystal system.[6] Moreover, the lack of systematic reflection can also provide information to the space group determination based on phenomena of destructive interference.

Moreover, not only the position but the intensity of each Bragg reflections can give information about the position of atoms within the crystal. For a perfect crystal, the intensity I_{hkl} of a reflection [10] with assigned Miller indices *h, k, l* is described by **Eq. 2.3**.

$$I_{hkl} = s\ L\ p\ |F_{hkl}|^2 \qquad \textbf{(Eq. 2.3)}$$

where *s* is a scale factor (accounting for factors such as data acquisition time), *L* is the Lorentz factor (dependent on instrument geometry) and *p* is the polarisation correction. The factor F_{hkl} is the 'structure factor', which is in correlation with the structure of the crystal and dominates in the intensity equation.

2.2.1.3 X-ray Radiation Source for Diffraction

X-rays are electromagnetic radiation with wavelength of about 1Å.[1] They can be generated either by laboratory or synchrotron sources via different processes, but in both cases monochromatic X-rays are required for XRD measurements.[11] In PXRD experiments, the intensity of the diffracted beam is measured as a function of 2θ.

2.2.1.3.1 Radiation Sources for Diffraction Generation of Laboratory X-rays

In laboratory diffractometers, a beam of electrons emitted from a metal filament (usually tungsten) is accelerated across a potential difference in order to bombard a metal anode. Various anode materials are available, including cobalt, copper and molybdenum. The bombardment of high energy electrons results in ionisation at the inner K-shell (n = 1) of the target anode. Electrons from higher orbitals fall into the

vacancies: in doing so X-rays are emitted with energies corresponding to the energy gap between the two electronic states. Electrons rising from the L-shell (n = 2) cause K_α radiation, and electrons from the M-shell (n = 3) generate K_β radiation. Moreover, both K_α and K_β consist of two components: $K_{\alpha1}$ and $K_{\alpha2}$, and $K_{\beta1}$ and $K_{\beta2}$, respectively. The absorption edge of an element with atomic number (Z-1) lies between K_α and K_β of element Z. Hence, an iron filter removes K_β radiation from e.g. copper anode. $K_{\alpha2}$ radiation can be removed with the use of a suitable monochromator. The generation of X-rays in this way generates a considerable amount of heat at the anode; the capability to absorb this heat by continuous water cooling is a main factor in moderating the flux of laboratory sources.[12, 13]

2.2.1.3.1.1 PANalytical X'Pert Pro Diffractometer

The Panalytical X'pert Pro powder X-ray diffractometer generated X-rays from a cobalt anode operating at 40 kV and 40 mA. $K_{\alpha2}$ radiation was removed using a germanium monochromator. Diffracted intensities were detected and collected using an X'Celerator X-ray detector, which uses Real Time Multiple Strip (RTMS) technology. The use of soller slits (collimator) helps to reduce air scattering resulting in improved resolution. The diffractometer was set up in Bragg-Brentano geometry using Co-$K_{\alpha1}$ radiation (λ = 1.7890 Å). Prior to analysis, the samples were suspended in acetone and then mounted into the sample holder, which was rotated at approximately 60 rpm during data collection.

2.2.1.3.1.2 Cu Bruker Diffractometer

Some Powder X-ray diffraction (PXRD) patterns were also recorded on Bruker diffractometer, with Cu-$K_{\alpha 1}$ as radiation source (λ = 1.540596 Å.) Powder samples were suspended in acetone prior to measurement.

2.2.2 Crystallite Size Determination, The Scherrer Equation

In order to determine what 'size' means in crystallography, the terminology of crystallite size, particle size, agglomerated particle and aggregated particle has to be identified.

Crystallite size relates to the width (L) (see **Eq. 2.4**) of the diffracted line while diffraction/reflection occurs.

Particle size refers to the dimension of several crystallites compose of a particle. In case of nanoparticles, crystallite size which is determined by PXRD can be in a good agreement with particle size obtained by electron microscopy.

Particle agglomeration: the sticking of particles to one other or to solid surface. Size enlargement through agglomeration is done to obtain a product with larger particle dimensions. The resulting entity is only apparently a new unit.

Particle aggregation: those solid particles that form compressive stress resistant entities in a composite material.

The average crystalline size can be estimated from its powder X-ray diffraction pattern,[14] with the assumption of spherical morphology, the Scherrer equation is given as,

$$B = \frac{K\lambda}{L\cos\theta} \qquad \textbf{(Eq. 2.4)}$$

where B is the full width half maximum (FWHM) of the reflection, L is the linear dimension of the grain, θ is the Bragg angle, K is equal to $2\left(\frac{\ln 2}{\pi}\right)^{1/2} = 0.93$. This relation assumes matters with spherical morphology and does not take into consideration strain broadening contributions to peak widths.

2.2.3 Unit Cell Refinement

Sample powders were mixed with LaB_6 (S.G: $Pm\bar{3}m$; a = 4.15700 Å) as an internal standard for the precise measurement of lattice spacing. The whole pattern fitting was performed with the Le Bail method[15] using the JANA2006 software.[16] For all compositions, the refined parameters were: background (fitted with Legendre polynomials, 5 parameters), height displacement 2θ shift, cell parameter of the pyrochlore material (S.G: $Fd\bar{3}m$; a ≅ 10.098 Å), pseudo-Voigt peak shape parameters [17] and instrumental asymmetry correction.[18] The cell parameter of LaB_6 was fixed. Estimated standard deviations (e.s.d.) obtained from the refinement procedure have been multiplied by Berar's factor to produce more realistic values.[19] The factor reduces the underestimation of e.s.d. values due to unaccounted-for background oscillations and possible inadequacies of the peak shape profiles.[19] As a result, the corrected e.s.d. from data sets collected under different conditions become comparable.

The unit cell refinement of the $Y_2Ti_{2-x}Rh_xO_7$ was made by Dr Christophe Didier.

2.3 X-ray Photoelectron Spectroscopy (XPS)

X-ray photoelectron spectroscopy (XPS) is a surface-sensitive quantitative spectroscopic technique that provides information of the elemental composition of the surface of a material and the oxidation state of the elements.[20] The basic setup of a conventional XPS analysis is shown in **Fig. 2.3**.

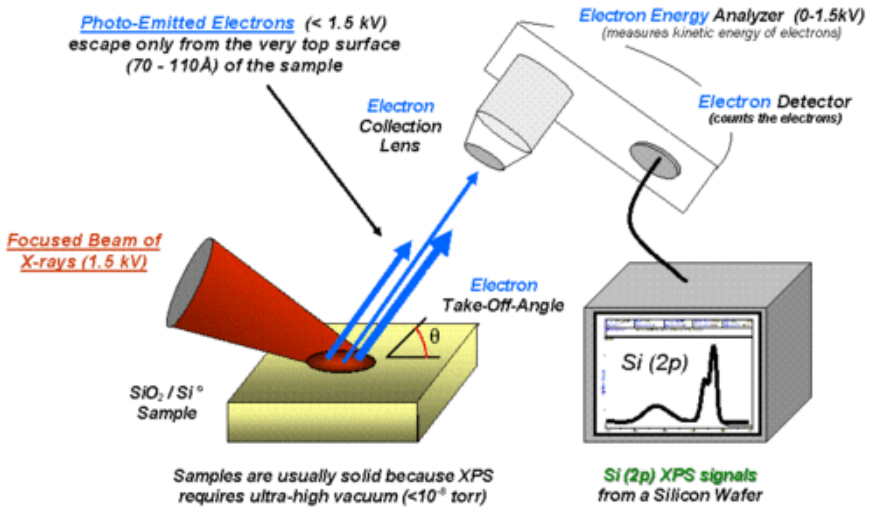

Fig. 2.3 Schematic diagram for the experimental XPS setup

XPS spectra can be obtained by irradiating a material with a focused high-energy X-ray beam and thus photoelectrons from atoms will be emitted. The kinetic energy of the ejected photoelectrons can be detected by electron detector and translated to form a representative signal (cps vs electron binding energy) by the electron energy analyser.

The electron orbitals of an atom have different binding energies. These orbital energies also differ depending on what element of the sample atom is composed of. The electron biding energy is measure of the energy that is required to free electrons from their atomic orbits.

As the energy of the incident X-ray at a particular wavelength is determined (E_{photon} = 1486.6 eV for *Al* K_α) and because the kinetic energy of emitted electrons ($E_{kinetic}$) are being measured, the electron binding energy ($E_{binding}$) of each of the emitted electrons can be calculated based on the work conducted by Rutherford in 1914. The relation is realised as follows:

$$E_{binding} = E_{photon} - (E_{kinetic} + \varphi) \quad \textbf{(Eq. 2.5)}$$

where φ is the work function of the spectrometer.

The XPS method is a surface chemical analysis techniques as photo-emitted electrons escape only from the top surface of the material up to 10 nm depth, therefore does not necessarily contain information of the bulk material.[20] Measurements are performed under ultra high vacuum (UHV) conditions.

The characteristic set of binding energies from each element generate a characteristic set of XPS peaks, hence this method can be used to identify the elements present at the surface of a material and peak areas can be used to determine the chemical composition.[21] The shape and position of each peak are influenced by the chemical state of the emitting atom, hence, XPS can provide information about the chemical bonding and the electronic band structures of complex materials.[20]

The composition and valence state of Rh in the samples were analysed by X-ray Photoelectron Spectroscopy (XPS) using PSP Hemispherical Electron Analyser with a Mg K_α (1253.6 eV) DUEL anode X-ray source and using PSP vacuum chamber ($1*10^{-10}$ bar, 16 hrs sample collection, room temperature). For XPS data analysis CasaXPS software [20, 22] was applied using a Shirley type background [23] and the peaks were fitted with 70% Lorentzian and 30% Gaussian function line shapes. Area was adjusted for each elements according to the *j* values, for example for Rh 3d spectra *j*

will be 3/2 and 5/2. The area ratio for the two spin orbit peaks $3d_{3/2}$: $3d_{5/2}$ was given as 2 : 3. For Ti 2p spectra, $2p_{1/2}$: $2p_{3/2}$ was correspondent to the area of 1 : 2. For O 1s subshell the *j* value is ½ therefore no area adjustment was needed.[21] All spin orbit peaks were given equal FWHM. The charge shift was adjusted to give the Ti $2p_{3/2}$ core level peak at 458.5 eV which is assigned to the Ti^{4+} state in $SrTiO_3$. The binding energies for the Rh $3d_{5/2}$ peaks were referenced to standard materials, Rh^0 (rhodium foil, GoodFellow) measured at 307.4 eV (**Fig. 2.4**, **Tab. 2.2**) and Rh^{3+} (Rh_2O_3, Sigma Aldrich) measured at 308.4 eV (**Fig. 2.5**, **Tab. 2.3**).

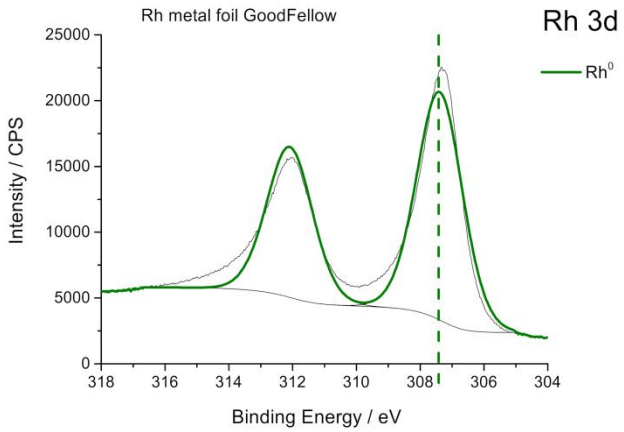

Fig. 2.4 XPS data of metallic rhodium foil purchased from GoodFellow

Tab. 2.2 XPS binding energies of Rh 3d 3/2 and 5/2 for metallic rhodium foil purchased from GoodFellow

	Rh $3d_{3/2}$	**Rh $3d_{5/2}$**
B. E. / eV	312.09	307.38

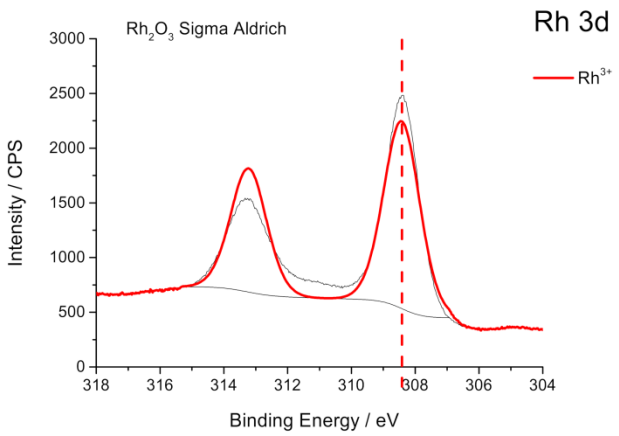

Fig. 2.5 XPS data of Rh_2O_3 purchased from Sigma Aldrich

Tab. 2.3 XPS binding energies of Rh 3d 3/2 and 5/2 for Rh_2O_3 purchased from Sigma Aldrich

	Rh $3d_{3/2}$	**Rh $3d_{5/2}$**
B. E. / eV	313.22	308.42

The calibration of the XPS instrument and the XPS measurements were carried out by Dr. David Hesp from the Stephenson Institute who also helped me to understand the data analysis. The data fitting after all was made by me.

2.4 Band Gap Determination from UV-Vis Diffuse Reflectance Spectroscopy (DRS)

In solid-state physics, the electronic band structure of a solid describes those ranges of energy that an electron within the solid may have (called *energy bands*, *allowed bands*) and ranges of energy that it may not have (called *band gaps* or *forbidden bands*). The density of states in various types of materials at equilibrium is shown in **Fig. 2.6**.

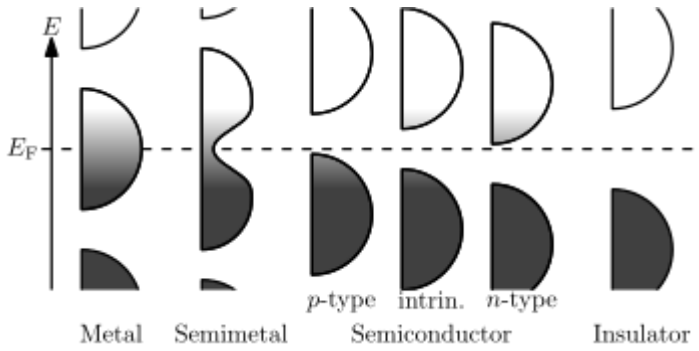

Fig. 2.6 Energy vs density of states in materials listed (Metal; Semimetal; Semiconductors; Insulator)

The optical absorption measurement of a material is a principal characterisation method which provides information whether solid powder is able to absorb light in the UV, visible or infrared region of the electromagnetic spectrum.

This optical absorption spectrum of a semiconductor provides information on its band structure. The fundamental absorption, which is distinct itself by a rapid rise in adsorption, refers to band-to-band transitions, i.e. the excitation of an electron from the valence to the conduction band, hence can be used to determine the band gap energy value of a semiconductor. Transitions are classed as either *direct* or *indirect* (**Fig. 2.7**). *Direct transition* require a change in energy, provided by an incident photon, whereas *indirect transition* require a change in both energy and momentum: momentum is conserved by a phonon interaction.[24]

It is not unusual for an indirect transition to occur at slightly lower photon energy than a corresponding direct transition: this may become obvious as a shoulder on a sharp absorption edge, or the combination of transitions may result in a curved appearance to the absorption edge.

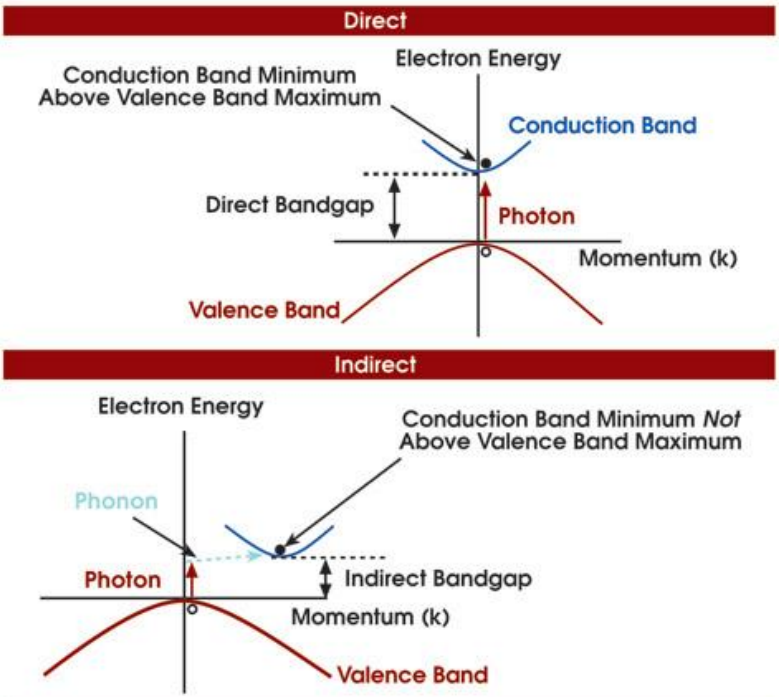

Fig 2.7 Band structure of direct and indirect band gap semiconductors in energy-momentum space.

The variation in absorption coefficient, $\alpha(E)$, of the semiconductor as a function of photon energy, *E*, can be fitted to a power law relationship of the following equation:

$$E\alpha(E) = B(E - E_g)^n, E \geq E_g \qquad \textbf{(Eq. 2.6)}$$

where *B* is a constant, E_g is the band gap energy, and *n* takes on a value that depends on the nature of above mentioned transitions; values of n = ½ and n = 2 result in a linear fit for direct and indirect transitions.[24, 25] As explained above, **Eq. 2.6** is valid for photon energies greater than or equal to the band gap energy. Thus a plot of $(E\alpha(E))^{1/n}$ vs *E* (called *Tauc plot*) is linear and intercepts the x axis at $E = E_g$.

Optical transmission in bulk powder samples can be very low, and thus the absorption coefficient may not be directly measured. Nevertheless, the diffuse reflectance spectrum of a sample also includes information on the absorption of the material.[26]

The Kubelka-Munk function F(*R*) relates the reflectivity, *R*, of a sample to an absorption coefficient α and a scattering coefficient, *s*, as described in **Eq. 2.7**:

$$F(R) = \frac{(1-R)^2}{2R} = \frac{\alpha}{s} \quad \textbf{(Eq. 2.7)}$$

Assuming a constant scattering coefficient *s*, F(*R*) is identified to be proportional to α and thus produces the absorbance of the measured material. This presumption is usually made in the study of powder's optical properties.[27] Therefore a plot of $(F(R)\times E)^{1/n}$ against *E* should be linear and can be extrapolated to the x axis to give the band gap energy.

In the literature, it is a fairly common practise to simply extrapolate a plot of F(R) vs *E* to find E_g, [28] and this method usually gives results similar to that summarised above. However, it is rather an approximation, and may be inadequate in some cases, such as where direct and indirect gaps must be accurately identified.

UV/Vis diffuse reflectance spectroscopy (DRS) and absorption measurements were taken on Shimadzu UV-2550 UV/Vis spectrometer, equipped with a Labsphere integrating sphere over the spectral range of 300-1400 nm (4.13–0.86 eV), using $BaSO_4$ standard for 100% reflectance. Prior to measurement, the powdered sample was ground, then placed in a solid sample holder with a quartz glass window, and placed in the UV/Vis spectrometer. Collected reflectance data was converted to absorbance using the Kubelka-Munk function, and the values of direct and indirect transitions were extrapolated as described earlier.

2.5 Fourier Transform Infrared Spectroscopy (FTIR)

Fourier Transform Infrared Spectroscopes[29] are used to detect, collect and process information in the infrared spectrum of a solid, liquid or gas. This technique uses infrared (IR) radiation which is partly absorbed and partially transmitted by the sample. The resulted infrared spectrum represents a unique fingerprint of a sample with absorption or transmission peaks which correspond to the frequencies of vibrations between the bonds of the atoms existing in material.

FTIR spectra were recorded on powder samples using a Bruker Tensor 27 Spectrometer.

2.6 Inductively Coupled Plasma Atomic Emission Spectroscopy (ICP-AES)

Inductively Coupled Plasma Atomic Emission Spectroscopy (ICP-AES) or Inductively Coupled Plasma Optical Emission Spectroscopy (ICP-OES) is used as an analytical technique for the detection of trace (ppm) metals in solution.[30] This type of electron spectroscopy uses the inductively coupled plasma to produce excited atoms and ions which can emit electromagnetic radiation at certain wavelengths specific for the detected elements. The applied flame temperature for ionisation is in the range of 6000 – 10000 K.[30] The intensity of measured emission is indicative of the concentration of the element within the sample.

Sample measurements were performed utilising a Spectro Ciros ICP-AES radial view instrument. The machine set up is comprised of cross flow nebuliser, cyclonic spray chamber and peristaltic pump. The required elemental lines were selected for their intensity and lack of interferences before being calibrated with certified standards,

matrix matched and within a previously established concentration range via a 3 point calibration curve. Each peak then being maximised with background compensation applied before final recalculation of the method and with a correlation coefficient > 0.9993. Instrument parameters from optimisation were, plasma power 1400 W with a nebulising flow of 0.82 L/min, coolant flow of 12.0 L/min and auxiliary flow of 1.0 L/min. Line selection for each element was, Rh 343.489 nm, Rh 233.477 nm and Sr 421.552 and Sr 460.733 nm. Typical RSD values were between 1-2 % indicating a stable plasma with consistent sample injection and aspiration.

The ICP-AES analysis of the samples was carried out by George Miller.

2.7 Electron Microscopy Techniques

2.7.1 General Electron Microscopy

Electron microscopy uses a beam of accelerated high voltage electrons as a source of illumination. This beam will then illuminate the sample and produce an image from secondary or back scattered electrons. The technique works at much higher magnification and resolving power compared to an optical microscope.

The first prototype of an electron microscope was developed by Hungarian scientists Dennis Gabor and Leo Szilard in 1928 with the contribution of Hans Busch, although the patent failed in the same year.

Three years later, the German physicist, Ernst Ruska and the electrical engineer, Max Knoll constructed another prototype. [31] This apparatus was the first demonstration of the principles of electron microscopy (**Fig. 2.8**).

Fig. 2.8 Electron microscope constructed by Ernst Ruska and Max Knoll in 1933 [31]

Electron microscopes use electrostatic and electromagnetic lenses to control the incident electron beam in order to focus it and form the image.

2.7.2 Transmission Electron Microscopy (TEM)

Transmission Electron Microscopy (TEM)[31, 32] is an electron microscopic technique using a focused, high voltage electron beam which is interacting with an ultra-thin specimen (TEM grid). The partially transmitted electrons will induce the signal which will be translated to an image after being magnified and focused on a fluorescent screen and can be visualised on a photographic film or be detected by a CCD camera (**Fig. 2.9**).

In this thesis, work has been carried out using a JEOL 2000FXII TEM in the Nanoinvestigation Centre at Liverpool (NiCaL), operating with a tungsten electron source operated at 200 keV. All powder samples were prepared onto carbon coated Cu grids by suspending the samples in MeOH which was applied dropwise onto the TEM grid using a glass pipette in a dust free environment. The grids were dried before loading them into the specimen holder.

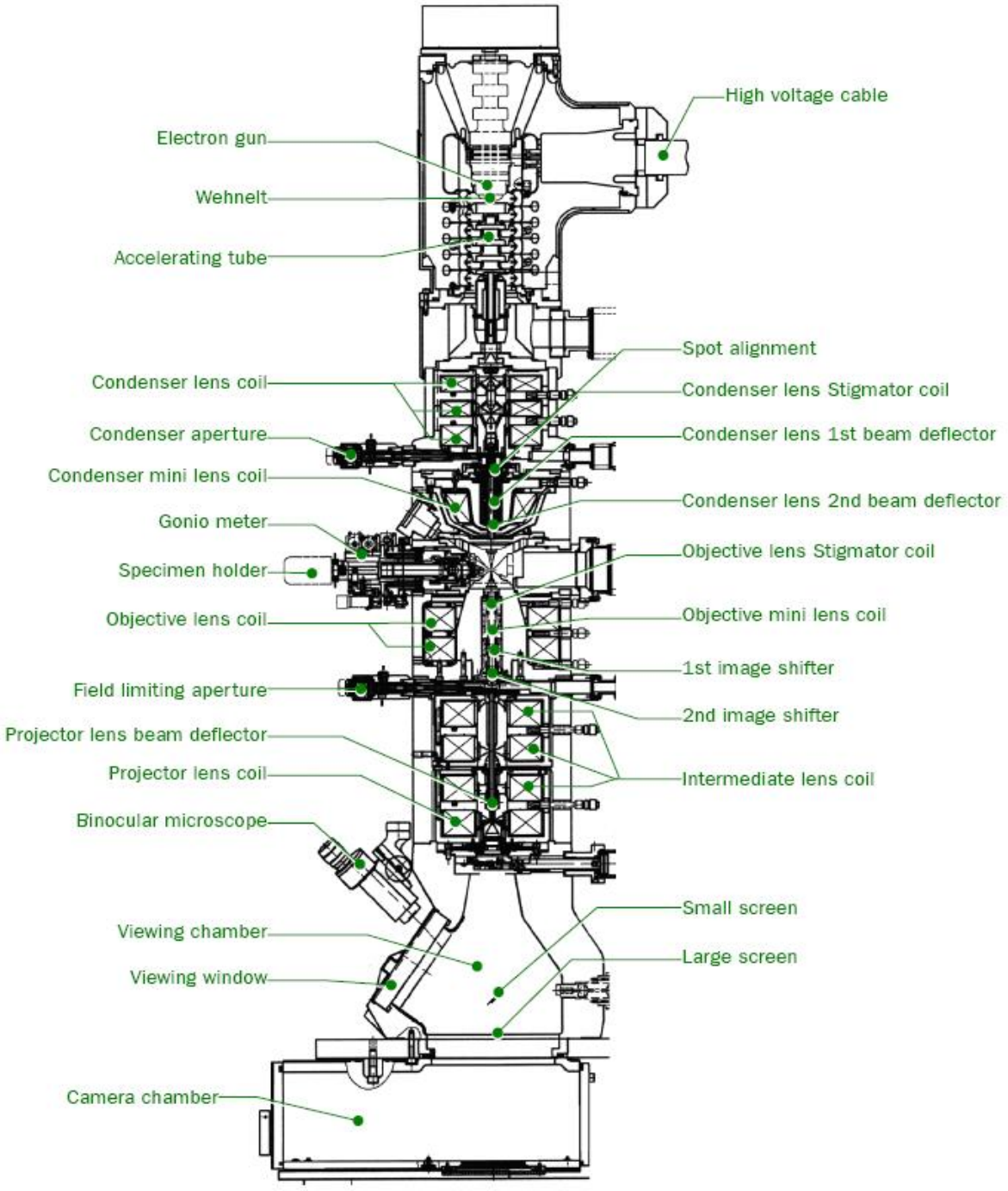

Fig. 2.9 Schematic representation of JEOL 2X00 Series TEM in Cross-Section

The TEM analysis of the samples was carried out by Dr Marco Zanella.

2.7.3 Energy Dispersive X-ray Spectroscopy (TEM – EDX)

When the ionising electron radiation interact with the TEM specimen, the emission of X-rays can also occur with regards to specific energy characteristic of the chemical elements in the sample. The number and energy of the emitted X-rays can be measured by an energy-dispersive spectrometer.[33] This analytical technique gives information on accurate elemental analysis and chemical composition of the specimen.

Measurements were carried out using a JEOL 2000FXII Transmission Electron Microscope with an EDAX Genesis 4000 EDX detector. The instrument was calibrated for Yttrium (L), Titanium (K) and Rhodium (L) shells respectively. The TEM-EDX analysis of the samples was carried out by Dr Marco Zanella.

2.7.4 Scanning Electron Microscopy (SEM)

SEMs [34] produce images through the detection of backscattered electrons and emitted secondary electrons which are ejected from the surface of the sample due to primary high voltage electron beam excitation. Therefore, SEM provides information on the material's surface topology.

SEM imaging and EDX were performed in the Centre for Materials Discovery (CMD) at Liverpool University, using Hitachi S-4800 Field-Emission Scanning Electron Microscope with an Energy Dispersive X-ray detector (Oxford Instruments). Analysis of the samples was carried out using 3 kV electron beam. The samples were prepared by distributing a few mg of powder onto a carbon tab, placed on a SEM sample holder. The prepared sample holder was then coated with gold using splutter deposition, depositing 5 – 10 nm gold layer. The SEM analysis of the samples was carried out by Dr Marco Zanella.

2.8 BET Surface Area Measurement

One of the fundamental characterisation techniques used in catalysis is the determination of the surface area of synthesised material, which can be directly applied using the BET method published in 1938, and named after the authors, Stephen Brunauer (HUN), Paul. H. Emmet (US) and Edward Teller (HUN). This theory is an extension of the classical Langmuir monolayer adsorption theory with the additional assumption: gas molecules physically adsorb on a solid in layers infinitely, with the lack of interaction between each adsorption layer, and thus Langmuir theory can be applied to each layer.[35] The limiting reason of an infinite number of adsorbate layers, which provides a reasonable approximation for multilayer adsorbates with more than four layers,[36] yields the expression of **Eq. 2.8**:

$$\frac{p}{v(p_0 - p)} = \frac{1}{v_m c} + \frac{c-1}{v_m c}.\frac{p}{p_0} \qquad \textbf{(Eq. 2.8)}$$

where v_m is the volume of gas adsorbed for monolayer coverage, p_0 is the saturation pressure of the adsorptive gas, and c is the BET constant.

A plot of $\frac{p}{v(p_0 - p)}$ against $\frac{p}{p_0}$ should be linear with a y intercept of $\frac{1}{v_m c}$ and gradient $\frac{(c-1)}{v_m c}$. Therefore, the values of v_m and c can be calculated from the intercept and gradient of this plot. The BET constant c can be expressed as a function of thermodynamic parameters:

$$c = \exp\left(E_1 - \frac{E_L}{RT}\right) \qquad \textbf{(Eq. 2.9)}$$

where E_1 is the heat of adsorption of the first layer and E_L is the heat of adsorption for the second and higher layers, which is equal to the heat of condensation. R is the gas constant and T is the temperature in Kelvin. The value of c must always be positive.

The BET isotherm provides a standardised method to determine the specific surface area of non-porous or macroporous (pore diameter > 50 nm) solids, where only the linear region of the isotherm ($0.05 < \frac{p}{p_0} \leq 0.35$) is used:

$$S_{Total} = \frac{v_m N s}{V} \quad \textbf{(Eq. 2.10)}$$

$$S_{BET} = \frac{S_{Total}}{a} \quad \textbf{(Eq. 2.11)}$$

where N is Avagadro's number, s is the adsorption cross section of the adsorbing species, V is the molar volume of the adsorbate gas and a is the mass of adsorbent.

The high number of active sites is a principal requirement for a catalyst where the catalytic reactions can take place. The determined surface area is a good indication of the amount of active sites available, with the surface area usually quoted in meters squared per gram ($m^2\ g^{-1}$).

5 point BET surface area was analysed on a Quantachrome Nova gas sorption analyser. Samples' surface was previously degassed at 110-120 °C overnight under vacuum. After degassing, the sample holder containing the sample was placed in the sorption analyzer, with nitrogen as the sorption gas, and the BET isotherm measured at 5 points along the linear section of the full adsorbance isotherm (p/p_0 = 0.05 to 0.35) with the assumption of spherical particle morphology.

2.9 Thermogravimetric Analysis (TGA)

Thermogravimetric Analysis (TGA) measures weight changes as a function of temperature and time.[1] When a material undergoes heating, a change of mass can occur due to dehydration, oxidation, reduction, phase transition, etc.

In this thesis, TGA measurements were performed using a TA Instruments Q600 thermal analyser. Typically, 100 – 200 mg samples were places in a Al crucible and heated in the range of 25 – 1200 ºC under constant, 80-100 ml per minute air flow (10% N_2 and 90% compressed air, instrument standard). The heating and cooling rates were set as 5 ºC per minute.

2.10 Photocatalysis Testing

In all hydrogen and oxygen evolution tests, MO degradation and E.coli inactivation reactions a 300 W Xenon lamp with a 420 nm cut-off filter was used as the source of visible light. In addition, an inserted water filter mounted at the light source was applied to avoid the thermal effect of IR radiation.

2.10.1 H_2 evolution

A Varian 4000 Gas Chromatograph with a thermal conductivity detector and with argon (supplier: BOC, UN1006) as the carrier gas was used to monitor the amount of hydrogen evolved during the photocatalytic testing. The GC was calibrated using high purity calibrant gas (1% H_2, 2% O_2 in N_2, supplier: BOC, UN1956). During calibration 0, 50, 100, 150, 200, 250 μL of calibrant gas were injected 10 times to ensure consistency, with a lockable gas-tight syringe and the peak areas indicative of H_2, O_2 and N_2 was recorded. The average of the 10 area values was used to provide the

gradient for each gases used in calculations. In further measurements, this calibration curve was used to convert the detected peak areas into amount of hydrogen, oxygen and nitrogen.

The H_2 generation reactions were all carried out following identical protocol described below. For H_2 evolving test reactions, 70 mg of catalyst was dispersed in 35 mL of 1 : 3 MeOH : H_2O or in 0.02 M EDTA solution.[37] The reactor was sealed with a septum and covered in aluminium foil prior to irradiation. With the septum in place, the total volume of the photoreactor including both the liquid and gas phase was 45 mL, hence the total gas phase was 10 mL. The suspensions were purged with nitrogen flow to remove dissolved oxygen. For sampling the headspace, a lockable gas-tight syringe was used to take 250 μL of the gas.

Using the calibration curve described above, the area of the peak of injected samples can be converted to actual evolved gas amount. This evolved gas was scaled up according to the reactor vessel headspace. To convert the volume to moles, the ideal gas law was used:

$$n = \frac{pV}{RT} \qquad \textbf{(Eq. 2.12)}$$

with R = 0.08206 L atm mol^{-1} K^{-1}, p = 1 atm and T = 293 K. In the literature, the value is usually given in μmol is referred to the evolved gas amount in the gas phase of the reactor at a certain point in the reaction.

2.10.2 O_2 evolution

The oxygen evolution behaviour of the materials was measured with three different protocols using a Clark electrode, a gas chromatograph [38] and a Fospor probe.

Oxygen evolution was measured using a Clark electrode (The Rank Brothers Oxygen Electrode, **Fig. 2.10**). This device allows us to measure the partial pressure of oxygen dissolved preferably in solution.

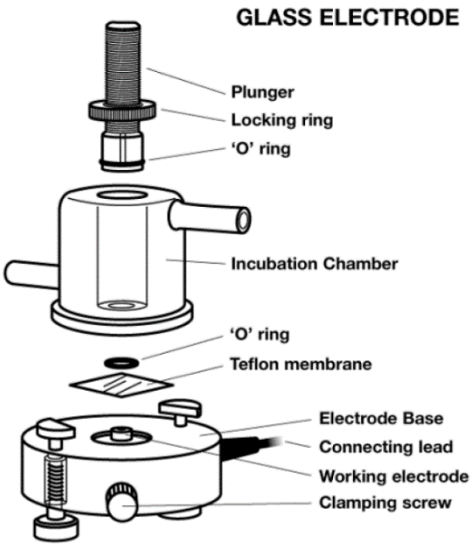

Fig. 2.10 Schematic representation of Clark electrode supplied by the Rank Brothers

The setup consists of an electrochemical cell with a platinum working electrode and a silver reference electrode. Conduction between these electrodes is achieved by 3 M potassium chloride solution. On top of this is placed a permeable Teflon membrane which is permeable to molecular oxygen but impermeable to ions. The membrane in the incubation chamber is sealed with a silicone rubber 'O' ring.

The controller supplied by Rank Brothers applies a voltage (-0.6 V) to the central platinum electrode that is sufficiently negative, with respect to the silver electrode, that all the oxygen diffusing through the membrane and reaching this electrode is reduced. The resultant current which flows between the two electrodes is proportional to the

oxygen partial pressure in the test system, $P(O_2)$. The controller converts this current directly into a voltage and depending on the model will display this in units of percentage saturation.

Thus the overall electrochemical process that occurs in an Oxygen Electrode is as follows:

$$4\,Ag + O_2 + 2\,H_2O + 4\,Cl^- \rightarrow 4\,AgCl + 4\,OH^- \qquad \textbf{(Eq. 2.13)}$$

As the oxygen electrode is repeatedly used, the bright silver ring electrode rapidly becomes coated with brown silver chloride. The presence of this silver chloride layer is desirable as it stabilises the overall behaviour of the electrode.

Prior to measurements, the voltage read on the electrode (sensitivity) was calibrated by saturating the water solution with air to give a display reading of 100.0 (100% saturation) or until a chart recorder gives a full-scale reading; then the solution was purged with N_2 gas to remove dissolved O_2 from solution to give 0 volt.

Samples were tested under visible light ($\lambda > 420$ nm) using aqueous $AgNO_3$ solution as an electron acceptor. In the reaction cell, 0.1 g of sample was suspended in 20 mL of 0.05 M $AgNO_{3(aq)}$ solution, covered in aluminium foil. To ensure that the electrode is working fine, the suspensions were saturated with air and then with N_2 in the dark. To perform the photocatalytic measurement, the suspension was stirred, the reaction cell was sealed and the temperature was maintained at 20 ºC using a water cooling jacket around the reaction cell. For comparison, the O_2 evolution rate of WO_3 (Sigma Aldrich, 100 nm, monoclinic, BET surface area 9.1 m^2/g) was also measured.

The Oxygen evolving capability of the solid state synthesised $Y_2Ti_{2-x}Rh_xO_7$ samples was mostly measured by Timothy Johnson using the Clark electrode.

100% air saturation is the maximum and equilibrium point for dissolved gases in water. Gas molecules continuously diffuse between the atmosphere and the water's surface. According to Henry's law, the dissolved oxygen content of water (partial pressure) is proportional to the percentage of oxygen in the air above it (ambient oxygen level). The oxygen in the atmosphere is about 20.9%, the partial pressure of oxygen at sea level is 0.209 atm.

For the calculation of the O_2 rate the following dissolved O_2 concentration was used:

For 100% air saturated water $[O_2] = 2.4 \times 10^{-4}$ M.

$n_{O2} = 2.4 \times 10^{-4}$ M $\times 2 \times 10^{-2}$ L = 4.8 μmol. The gradient of the linear section of the $[O_2]$/time course was taken and the reaction rate was calculated for 250 s period of time.

To confirm the presence of oxygen, photocatalytic tests were reproduced using a custom quartz cuvette (10 mm) with B24 adaptor and a septa adaptor. 5 mL of $AgNO_3$ (0.05 M) and 25 mg of photocatalyst were stirred under a N_2 flow for 1 hour prior to photocatalysis experiments using a 150 W Xe lamp with stacked Schott glass KG1 filters and a 400 nm band pass filter. The gas headspace (20 mL) was sampled prior to and during the exposure to light and analysed using an Agilent 6890 GC with a 5 Å molecular sieve column (ValcoPLOT, 30 m length, 0.53 mm ID) and a pulsed discharge detector (D-3-I-HP, Valco Vici) with Helium (N6.0) as the carrier gas. The oxygen evolution measurements when using a GC was carried out by Dr Alex Cowan.

Thirdly, some of the oxygen generating measurements were carried out by using an optical oxygen sensor. On irradiation, dye molecules at their absorption maxima emit radiation at longer wavelengths (fluorescence). The excited state of the luminescent dye can be quenched by an energy transfer mechanism upon collision with free oxygen molecules. [39]

Fluorescence: $L^* \rightarrow L + hv$ (**Eq. 2.14**)

Quencing: $L^* + O_2 \rightarrow L + O_2^*$ (**Eq. 2.15**)

As a result, the intensity of the luminescence is reduced along with the lifetime and the degree of quenching is proportional to the oxygen concentration. **Fig. 2.11** shows a schematic diagram of an optical oxygen sensor. The active components of the sensor are the luminescence dye encapsulated in a polymer medium, a light source (typically a LED or a laser) for exciting the dye at a particular wavelength (commonly 550 - 800 nm), a photodiode to detect the fluorescent radiation and an optical fiber for the light transmission.

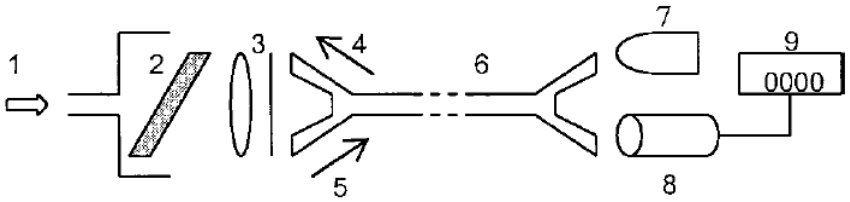

Fig 2.11 Schematic diagram of an optical oxygen sensor. (1) gas or liquid path, (2) lumophore dispersed on oxygen permeable membrane, (3) lens and filter, (4) exciting radiation, (5) fluorescent radiation, (6) optical fiber, (7) LED/laser, (8) photodiode and (9) display. [39]

The quenching of the luminescence can be described with the Stern-Volmer equation:

$\frac{I_0}{I} = 1 + K_{sv} * P_{O2}$ (**Eq. 2.16**)

where I_0 and I are the luminescence intensities in the presence and absence of oxygen, P_{O2} is the oxygen partial pressure and K_{sv} is the quenching constant which determines the sensitivity of the optical sensor.

O_2 evolution measurements of the sol-gel synthesised $Y_2Ti_{2-x}Rh_xO_7$ samples were also carried out using a Fospor oxygen sensor (OR125 series, stainless steel, 1000 μm fiber core diameter, 3.15 mm outer diameter, 63.5 mm length) supplied by OceanOptics. This optically based sensor (optrode) works by coming into equilibrium with its environment. Oxygen diffuses into the sensor coating, where it alters the nature of the fluorescence of an indicator material (**Fig 2.12**).

Fig. 2.12 Fospor sensor where the indicator material is coated on the tip

The Fospor probe uses a very sensitive platinum-porphyrin complex embedded in polymer matrix as its indicator. Similarly to the well-known ruthenium fluorescence quenching of the platinum complex at about 650 nm can be directly related to the partial pressure of dissolved or gaseous oxygen.

The advantage of this probe in particular is that it is able to detect molecular oxygen in gas and in liquid phases across wide ranges of temperature and concentration. It eliminates interference from sample colour and turbidity. The oxygen level can be accurately determined as it does not consume oxygen. These types of sensors can resolve to 0.004% oxygen at 1 atm and stay chemically inert. For calibrating the sensor, the τ value (normalised decay time) should be in the 20-30 μsec range at 0% oxygen when calibrated in constant nitrogen flow (oxygen-free N_2, supplier: BOC, UN1066),

and in the 9-13 µsec range in air (synthetic air, supplier: BOC, UN1002), following this the NeoFox software gives valid readings for further measurements. For O_2 evolving test reactions, 0.1 g of sample was suspended in 20 mL of 0.05 M $AgNO_{3(aq)}$ solution, covered in aluminium foil. The reactor was sealed with a septum and the suspension was fully purged with N_2 gas to remove dissolved O_2 in the suspension.

2.10.3 Methyl Orange Photooxidation

The photocatalytic degradation of Methyl-Orange (MO) (**Section 1.2.2.9**) dye solution was carried out under visible light irradiation. The reaction suspensions were prepared by adding the catalyst (0.1 g) to 100 mL of 0.02 g/L MO solution (6.1×10^{-5} M). The as-made suspension was purged with air during the whole reaction. The suspension was stirred in the dark overnight to ensure adsorption/desorption equilibrium of the dye had been attained on the surface of the catalyst prior to irradiation. During irradiation, 4 mL of the suspension was removed at 15 minute intervals for subsequent MO concentration analysis followed by filtering by a 0.2 µm syringe filter.[37, 40] The absorption spectra of the aliquots were recorded in the range of 240 - 720 nm to determine the MO concentration and the degradation rate was calculated. The pH of the MO solution remained constant throughout the reaction time during the decomposition process (pH 7.2-7.7), no further adjustment was needed. [37]

2.10.4 Colony Counting Method of Gram-negative *E. coli* Bacteria

For water disinfection with semiconductor oxides, *E. coli*, Gram-negative bacteria have been studied as one model organism. **Fig 2.13a-b** show the schematic representation and the SEM image of E. coli.

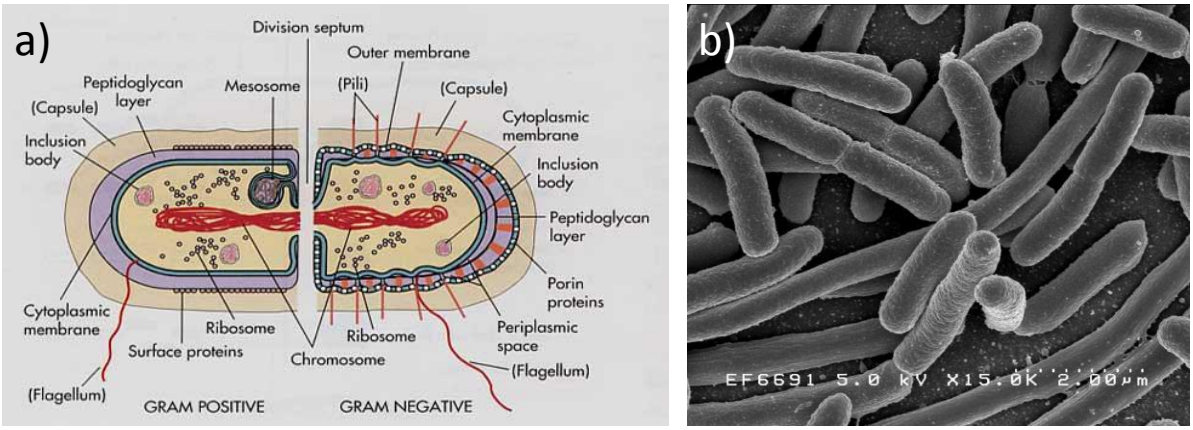

Fig. 2.13(a) Schematic representation of Gram positive and gram negative bacteria (b) Scanning Electron Microscopic image of *E. coli* bacteria

Microbiological studies were carried out as follows. A series of stock suspensions (0 % w/V, 0.01 % w/V, 0.05 % w/V, 0.1 % w/V) were made by dispersing 0 g, 0.003 g, 0.015 g, 0.03 g $SrTi_{0.95}Rh_{0.05}O_3$ photocatalysts in 30 mL aq. PBS (Phosphate Buffered Saline) solution. The suspensions were kept in the dark by covering with aluminium foil and stirred overnight with magnetic stirrer bars in order to get a fine suspension of the catalyst.

Bacterial overnight cultures were set up by transferring a single bacterial colony from a streak plate to 10 mL Luria-Bertani (LB) broth for *E. coli* (MC1061 strain [41]) and incubated at 37 ^{o}C overnight on a rotary table. The overnight bacterial cultures were then sub-cultured and 250 µL was transferred to 10 mL fresh LB broth. Once again incubated at 37 ^{o}C to get the bacterial cells into a mid-log growth phase, where 1000 µL samples were transferred to cuvettes to measure the optical density (OD) at 600 nm with a spectrophotometer. When an OD of *E. coli* in LB broth was measured 0.4 – 0.5, 5 µL of the sub-cultures were transferred to the 5 mL of pre-autoclaved photocatalyst suspensions in aq. PBS. 4 types of suspensions containing the catalyst as well as the *E. coli* sub-culture were made: light (*L),* dark *(D),* control light *(CL),* control dark *(CD*). The *L* experiment is described as follows: 5 µL of *E. coli* sub-

cultures were transferred to 5 mL PBS containing 0.1 % w/V sterilised photocatalyst and exposed to a visible light source ($\lambda > 420$ nm). The suspension of the *D* experiment was prepared identically but during the photo-disinfection reaction, kept in dark by covering with aluminium foil. The *CL* and *CD* suspensions contained no added photocatalyst, only *E. coli*, and were exposed to either visible light (*CL*) or were kept in dark (*CD*). Each sample was prepared in duplicate with biological replicates. During the reaction, the cells in the photocatalyst suspensions were stirred with magnetic stirrer bars. 100 µL samples were taken at 0 min, 120 min, 240 min and 360 min and diluted in 900 µL aq. PBS in a dilution series from 10^0 to 10^{-5}. In order to make up the cell dilutions in PBS and also to make the dilution series representative for plating, the harvested samples were vortexed. 20 µL of each dilution was spot plated in duplicate on LB agar plates and incubated overnight at 37 ^oC. [42] The bacterial colonies were then counted and colony forming units (CFU) mL^{-1} was calculated. The absolute density (CFU mL^{-1}) of cell population was plotted over time; standard deviation was calculated.[37]

2.10.5 Fluorescent Microscopy

The basic Fluorescent Microscope refers to a certain type of optical microscope where the specimen is illuminated with a high-intensity light source which is absorbed by the fluorophores[1], inducing them to emit fluorescence.[43] By completely filtering out the exciting light for image generation, it is feasible to only see those objects that are fluorescent. This fluorescent emission occurs within nanoseconds. The LIVE/DEAD BacLight Bacterial Viability Kit utilizes the mixtures of the SYTO®9 green-

[1] Fluorophores typically contain several combined aromatic groups or cyclic groups with with several π electrons.

fluorescent nucleic acid stain and the red-fluorescent nucleic acid stain, propidium iodide. These stains differ both in their spectral characteristics and in their ability to penetrate into healthy bacterial cells. When both dyes (green-fluorescent SYTO®9 and red-fluorescent propidium iodide) are pre-mixed and added together to the cell culture, propidium iodide penetrates only into bacteria with damaged membranes, causing a reduction in the SYTO®9 stain fluorescence and stains the cells red.

Fluorescent Microscopy was used to visualize *E.coli* bacteria and the possible cell death during photocatalytic inactivation processes. In this thesis, a Leica DM2500 fluorescence microscope coupled to a Leica DFC420C camera. All images were acquired with a 40x objective. ImageJ software was used to display, edit, analyse and process the digital images. The image acquisition was carried out by Dr Arthur Taylor who also taught me to understand how to further process and overlay the images.

2.10.6 Photodiode and Chemical Actinometry

For the Apparent Quantum Efficiency (AQE) determination (**Section 1.2.2.7**), the number of incident photons emitted by the ozone-free Xenon 300 W lamp supplied with 400(±5) nm, 450(± 5) nm band pass filters was determined with two comparable means[38] namely chemical actinometry [44] and with a photodiode device using physical photon flux absorption determination.

A photodiode is a semiconductor device which is able to convert light into current. The photon flux at 400(±5) nm, 450(± 5) nm was determined with a S120VC photodiode attached to a PM100D (Thor) unit.

Secondly, the actinometry measurement was performed applying potassium ferrioxalate actinometry.[44, 45] In this process, the ferrioxalate complex absorbs a photon

of light (photoreduction) and subsequently decomposes to form $Fe(C_2O_4)_2^{2-}$ and CO_2. The iron centre is reduced (gains an electron) from the +3 to the +2 oxidation state while an oxalate ion is oxidised to carbon dioxide:

$$2\,[Fe(C_2O_4)_3]^{3-} + h\nu \rightarrow 2\,Fe^{2+}\,[Fe(C_2O_4)_2]^{2-} + 2\,CO_2 + \,C_2O_4^{2-} \qquad \textbf{(Eq. 2.17)}$$

This technique involves the initial preparation of three solutions. Solution A was prepared using 16.1g $Fe(NO_3)_3$ and 5.5 cm^3 H_2SO_4, made up to 100 cm^3 with H_2O. Solution B contained 19.9 g $K_2C_2O_4$ in 100 cm^3 H_2O. Solution C contained 0.025 g phenanthroline, 5.625 g $NaOAc{\cdot}3H_2O$, and 1.22 cm^3 H_2SO_4 diluted to 25 cm^3 with H_2O. 12.5 cm^3 of solution A was added to 12.5 ml of solution B and made up to 250 cm^3 with H_2O, forming solution D. 20 cm^3 of solution D was placed into the photo-reactor to be irradiated, and another 20 cm^3 was placed in another reactor and kept in the dark. After irradiation time *t*, 1 cm^3 of the irradiated solution D was added to 2 cm^3 of solution C and diluted to 10 cm^3 with H_2O; the same was performed with the 1 cm^3 of solution D that was kept in the dark. The absorbance of this 10 cm^3 solution at 510 nm was measured and allowed for the amount of Fe^{2+} (in moles) generated from photochemical reaction to be calculated using the formula:

$$Fe^{2+} = \frac{V_1 V_3 \Delta A}{10^3 V_2 l \varepsilon} \qquad \textbf{(Eq. 2.18)}$$

where V_1 is the irradiated volume (20 cm^3), V_2 is the volume of the sample taken for measurement (1 cm^3), V_3 is the final volume used for measurement (10 cm^3), l is the optical pathlength (1 cm), ΔA is the difference in absorbance at 510 nm with and without irradiation (i.e. between the dark and irradiated sample), and ε is the absorbance coefficient of Fe^{2+} with a value of 11100 L mol^{-1} cm^{-1}. From the amount of Fe^{2+}, the photon flux (*Nhv*) at a given wavelength was calculated using the formula:

$$\frac{Nh\nu}{t} = \frac{Fe^{2+}}{\phi_\gamma t F} \qquad \textbf{(Eq. 2.19)}$$

where ϕ_γ is the known quantum yield for Fe^{2+} production at a given wavelength,[46] t is the irradiation time in seconds, F is the mean fraction of light absorbed which is assumed to be equal to 1. It is very important to note that these solutions must be handled as much as possible in the dark under red light, as any light source other than that being characterised will interfere with the experiment.

This technique allows for the determination of the photon flux entering a reactor, and avoids the need to correct for any influences of light reflections. The same reactor and light source as for the photocatalytic reactions was used. The light source was fitted with 400 nm and 450 nm ± 5 nm band pass filters. The change in the absorption spectra of the complex before (Dark meas.) and after irradiation is shown in **Fig. 2.14a-b**. Samples were prepared in duplicates (e.g. 400 nm Meas. A and B), and the photon flux value was calculated based on the mean values.

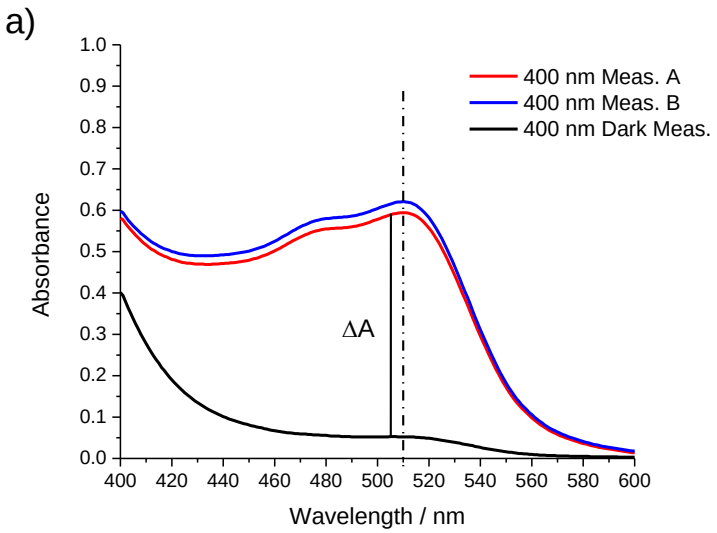

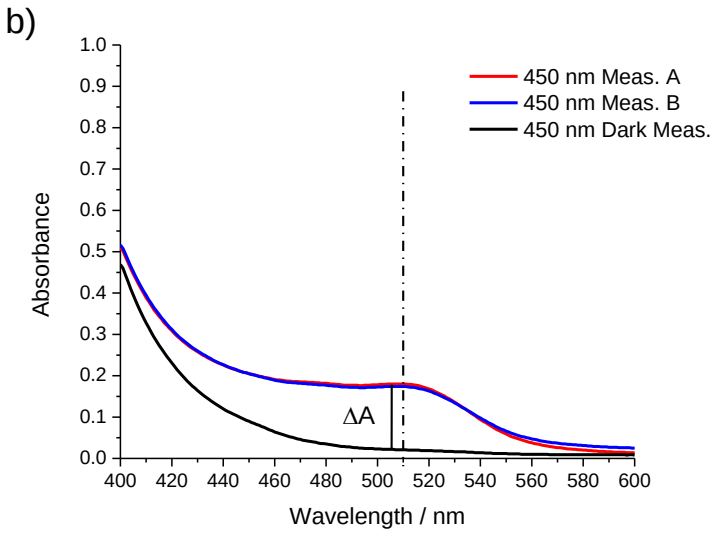

Fig. 2.14 Change in the absorption spectra of Fe^{2+} - oxalate – phenanthroline complex in duplicated measurements (red line and blue line) upon irradiation with a Xenon lamp source fitted with an a) 400 nm ± 5 nm and b) 450 nm ± 5 nm band pass filters. The graphs show the dark absorbance of the complex for comparison (black line).

The summary tables of photon flux measurement with two different methods (actinometry and photodiode devices) is shown in **Tab. 2.4**.[38] and **Tab.2.5.**

Tab. 2.4 Measured light intensity of 300 W Xenon lamp

Band pass filter wavelength (±5 nm)	Intensity measured on the photodiode (W/m^2)[a]	Photodiode[a,c] (photons/h)	Actinometry[b,c] (photons/h)
400	6.16	$3.12x10^{19}$	$3.17x10^{19}$
450	9.43	$5.38x10^{19}$	$4.53x10^{19}$

[a] S120VC photodiode attached to a PM100D (Thor) unit

[b] ferric oxalate actinometry[14]

[c] Illuminated area 7 cm^2, side irradiation of a 50 mL bore glass incubation chamber assembly, 50 mm x 100 mm x 50 mm approx.

As a conclusion it is clear that the two types of measurement confirmed the same order of magnitude of the number of incident photons per hour.

Tab. 2.5 Additional data to light intensities of 300 W Xenon lamp measured by 2 different photodiodes using a 400 ± 5 nm band pass filter

	Photodiode 1	Photodiode 2
Irradiated area of disc (cm^2)	0.70	1.13
$P_{measured}$ (mW) 29/04/14	0.432	N/A
$P_{measured}$ (mW) 15/05/14/	0.407	N/A
$P_{measured}$ (mW) 20/05/14/	0.330	0.550
$P_{measured}$ (mW/ cm^2) 20/05/14/	0.471	0.487

Again, the data show the same order of magnitude of the emitted light when measured with Photodiode 1 and 2. The measurement was carried out by Dr. Troy Manning and Dr. Alex Cowan. This is in a good agreement with the chemical actinometry light intensity results at 400 ± 5 nm. Moreover the data show the accuracy of all techniques for comparison.

2.11 References

1. A. R. West, *Basic Solid State Chemistry*, 2nd edn., John Wiley & Sons, 1996.
2. A. Rabenau, *Angewandte Chemie International Edition in English*, 1985, **24**, 1026-1040.
3. *The Sol-Gel Handbook: Synthesis, Characterisation and Application, 3-Volume Set, Synthesis and Processing*, Wiley, 2015.
4. P. M. Pechini, Ceramic Dielectric Materials, U.S. Patent 3330697, Editon edn., 1967.
5. *Powder Diffraction & Rietveld School*, Durham University, 2010.
6. V. K. Pecharsky and P. Y. Zavalij, *Fundamentals of Powder Diffraction and Structural Characterisation of Materials*, 2nd edn., Springer, 2009.
7. M. A. Tsiamtsouri, *Structure and Properties of (Ba, Sr)(Co,Fe, Mo)O3 perovskite oxides, PhD Thesis*, University of Liverpool, 2012.
8. W. H. Bragg and W. L. Bragg, *Proceedings of the Royal Society of London A: Mathematical, Physical and Engineering Sciences*, 1913, **88**, 428-438.
9. W. H. Miller, *A Treatise on Crystallography, https://archive.org/details/treatiseoncrysta00millrich*, Cambridge, For J. & J. J. Deighton, 1839.
10. M. Ladd and R. Palmer, *Structure Determination by X-ray Crystallography*, 5th edn., Springer, 1985.
11. *Generation of X-rays*, http://pd.chem.ucl.ac.uk/pdnn/inst1/xrays.htm.
12. W. Clegg, *Crystal Structure Determination*, Oxford University Press, 1998.
13. M. Weller, *Inorganic Materials Chemistry*, 3rd edn., Oxford University Press, 1994.
14. A. L. Patterson, *Physical Review*, 1939, **56**, 972-977.
15. A. Le Bail, H. Duroy and J. L. Fourquet, *Mater. Res. Bull.*, 1988, **23**, 447-452.
16. V. Petříček, M. Dušek and L. Palatinus, *Z. Kristallogr.*, 2014, **229**, 345-352.
17. P. Thompson, D. E. Cox and J. B. Hastings, *J. Appl. Crystallogr.*, 1987, **20**, 79-83.
18. C. Howard, *J. Appl. Crystallogr.*, 1982, **15**, 615-620.
19. J. F. Berar and P. Lelann, *J. Appl. Crystallogr.*, 1991, **24**, 1-5.
20. N. Fairley and A. Carrick, *The Casa Cookbook, Part 1: Recipes for XPS Data Processing*, Acolyte Science, 2005.
21. *XPS database*, http://www.lasurface.com/xps/.
22. *CasaXPS Software*, http://www.casaxps.com/.
23. J. Végh, *Journal of Electron Spectroscopy and Related Phenomena*, 1988, **46**, 411-417.
24. N. Serpone, D. Lawless and R. Khairutdinov, *The Journal of Physical Chemistry*, 1995, **99**, 16646-16654.
25. R. A. Smith, *Semiconductors*, 2nd edn., Cambridge University Press, 1978.
26. P. A. Cox, *Electronic Structure and Chemistry of Solids*, Oxford University Press, 1987.
27. H. Deng and J. M. Hossenlopp, *The Journal of Physical Chemistry B*, 2005, **109**, 66-73.
28. G. Pang, S. Chen, Y. Koltypin, A. Zaban, S. Feng and A. Gedanken, *Nano Letters*, 2001, **1**, 723-726.
29. P. R. Griffiths and J. A. de-Haseth, *Fourier Transform Infrared Spectrometry*, 2nd edn., John Wiley & Sons, 2007.
30. G. L. Moore, *Introduction to Inductively Coupled Plasma Atomic Emission Spectrometry*, Elsevier, Amsterdam, 1989.
31. D. B. Williams and C. B. Carter, *Transmission Electron Microscopy, A Textbook for Materials Science*, 2nd edn., Springer, 1996.
32. D. B. Williams and C. B. Carter, *Transmission Electron Microscopy, I - Basics*, Plenum Press, New York, 1996.

33. D. B. Williams and C. B. Carter, *Transmission Electron Microscopy, IV - Spectrometry*, Plenum Press, New York, 1996.
34. J. I. Goldstein, D. E. Newbury, P. Echlin, D. C. Joy, A. D. Romig, C. E. Lyman, C. Fiori and E. Lifshin, *Scanning Electron Microscopy and X-ray Microanalysis, A Text for Biologists, Materials Scientists and Geologists*, 2nd edn., 1992.
35. S. Brunauer, P. H. Emmett and E. Teller, *Journal of the American Chemical Society*, 1938, **60**, 309-319.
36. J. U. Keller and R. Staudt, *Gas Adsorption Equilibria: Experimental Methods and Adsorptive Isotherms*, Springer, 2005.
37. B. Kiss, C. Didier, T. D. Manning, H. E. Allison, A. W. Taylor, J. B. Claridge, J. R. Darwent and M. J. Rosseinsky, *in preparation*, 2015.
38. B. Kiss, C. Didier, T. Johnson, T. D. Manning, M. S. Dyer, A. J. Cowan, J. B. Claridge, J. R. Darwent and M. J. Rosseinsky, *Angewandte Chemie International Edition*, 2014, **53**, 14480-14484.
39. R. Ramamoorthy, P.K. Dutta, S. A. Akbar, *Journal of Materials Science*, 2003, **38**, 4271-4282.
40. J. H. Clark, M. S. Dyer, R. G. Palgrave, C. P. Ireland, J. R. Darwent, J. B. Claridge and M. J. Rosseinsky, *Journal of the American Chemical Society*, 2011, **133**, 1016-1032.
41. M. J. Casadaban and S. N. Cohen, *Journal of Molecular Biology*, 1980, **138**, 179-207.
42. A. A. Miles, S. S. Misra and J. O. Irwin, *Epidemiology & Infection*, 1938, **38**, 732-749.
43. J. W. Lichtman and J.-A. Conchello, *Nat Meth*, 2005, **2**, 910-919.
44. H. J. Kuhn, S. E. Braslavsky and R. Schmidt, *Pure Appl. Chem.*, 2004, **76**, 2105-2146.
45. C. G. Hatchard and C. A. Parker, *Proceedings of the Royal Society of London A: Mathematical, Physical and Engineering Sciences*, 1956, **235**, 518-536.
46. M. Montalti, A. Credi, L. Prodi and M. T. Gandolfi, *Handbook of Photochemistry*, 3rd edn., CRC Press, 2006.

3. Chapter 3: Synthesis, Characterisation of $BaTi_{1-x}Rh_xO_3$ and $SrTi_{1-x}Rh_xO_3$ Single Perovskites

3.1. Introduction

Since the 1970's photocatalysis has remained an area of very active research, initially with the focus on solar energy conversion for alternative H_2 fuel and more recently for environmental clean-up by the photodestruction of organic contaminants and bacteria in water. The most widely studied material has been TiO_2 which is restricted to activity with UV light.[1] At neutral pH, the calculated conduction band position of anatase TiO_2 is determined to be ca. -0.6 V vs. NHE, and for rutile these values are less negative, the conduction band energy would be ca. -0.4 V.[2] In 1976, J. Bolts and Mark S. Wrighton measured the position of the rutile TiO_2's CB vs. SCE (Saturated Calomel Electrode) at pH 13.[3] They claim that value is given -1.05 V vs. SCE at pH 13 [3] which can be correlated to -0.45 V vs. NHE at neutral pH. Moreover, for anatase this value was published to be -1.2 V vs. SCE at pH 13 [4], hence -0.6 V vs. NHE at pH 7. It is clear, that calculated and measured potential values are matching very well. In addition, for both titanate phases it is indicative, that the CB energy is more negative than or equal to the redox potential of H^+/H_2 of -0.41 V vs. NHE at neutral pH, therefore proton reduction for instance with photo-generated electrons is possible.[2] Alternative non-oxide semiconductors (CdS, E_g = 2.4 eV and CdSe, E_g = 1.7 eV)[5] can also be effective photocatalysts with visible light but generally undergo photocorrosion when used in water without the approach of stabilization of photoelectrodes.[6] Semiconductor oxides have been extensively studied considering their stability, efficiency and their photo-electrochemical properties. Of those, ABO_3 structure has been investigated exhaustively since the discovery of its paraelectric and

ferroelectric properties.[7] At room T or above it has a classic cubic perovskite structure with Mg^{2+}, Ca^{2+}, Sr^{2+}, Ba^{2+} on the A site and Ti^{4+} as B. This is a centrosymmetric cubic structure with A at the corners, B at the centre and oxygen atoms at the face centres. The $BaTiO_3$ $Pm\bar{3}m$ cubic phase (**Fig. 3.1**) at 393 K undergoes a paraelectric to ferroelectric transition while forming a tetragonal structure with the space group of *P4mm* (**Fig. 3.2**).

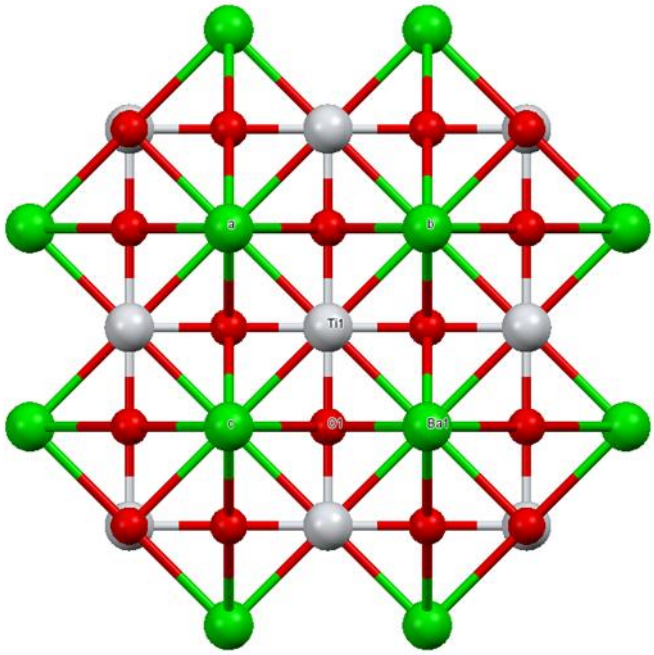

Fig. 3.1 Structural display of $BaTiO_3$ cubic $Pm\bar{3}m$ phase; green colour labels Ba atoms, Ti atoms displayed in white and O atoms are red.

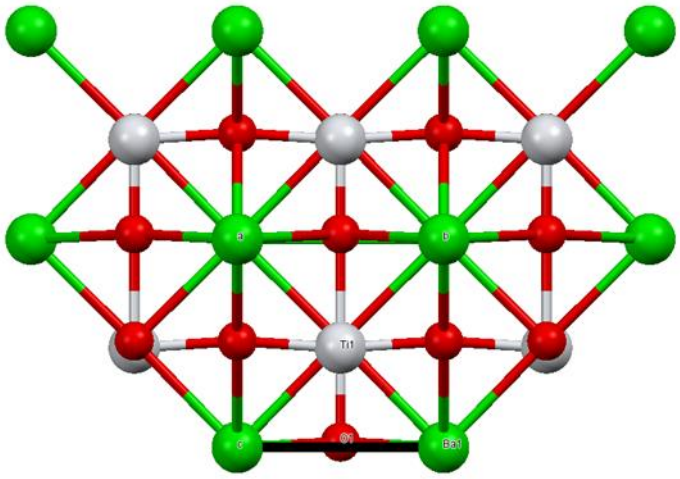

Fig. 3.2 Structural display of $BaTiO_3$ tetragonal *P4mm* phase; green colour labels Ba atoms, Ti atoms displayed in white and O atoms are red.

It becomes orthorhombic between 278 and 183 K, and finally it is rhombohedral below 183 K.[8, 9] Although, the calculated absolute CB position of the parent phase $BaTiO_3$ lies at -1.24 V vs. NHE [10] at neutral pH (original paper includes -0.83 V vs. NHE at pH = 0), it is not a widely published photocatalyst, perhaps due to the fact that some of the barium compounds are toxic to humans. Nevertheless, the reported band gap of this white reflecting compound is 3.14 eV [10], therefore the overall potential gap is still adequate and would make it a suitable material for overall water splitting.

The cubic perovskite $SrTiO_3$ has shown excellent activity in water splitting reaction. [11-13] At 293 K, $SrTiO_3$ crystallizes as a cubic structure (**Fig. 3.3**) with the space group of $Pm\bar{3}m$ where Ti ions are octahedrally coordinated to 6 oxygen atoms (TiO_6) exhibiting ferroelectric properties.

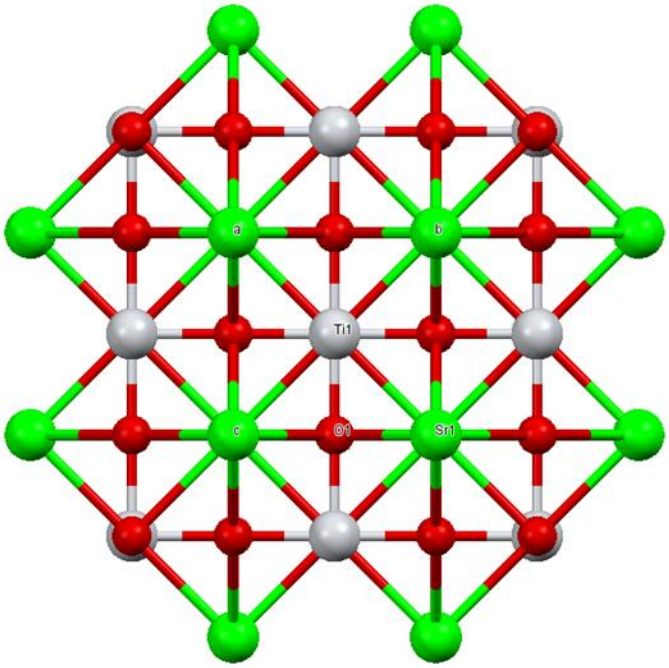

Fig. 3.3 Structural display of $SrTiO_3$ cubic $Pm\bar{3}m$ phase; green colour labels Sr atoms, Ti atoms displayed in white and O atoms are red.

At 105 K this phase undergoes an antiferro-distortive phase transition to tetragonal with the space group of $I4/mcm$. On further cooling down to about 50 K, there is a weak ferroelectric transition again and at 0 K $SrTiO_3$ shows a so-called quantum paraelectric feature.[14] In **Section 1.2.2.4** cubic $SrTiO_3$ has been introduced with regard to its band gap energy and crystallographic features (**Tab. 1.1**). The measured conduction band of $SrTiO_3$ reported by Jeffrey M. Bolts and Mark S. Wrighton is situated at -0.8 V vs. NHE at pH = 7 (original paper includes -1.4 V vs SCE at pH = 13) [3] and the measured band gap energy is 3.2 eV.[3, 4, 15] In cubic $SrTiO_3$, the octahedral distortion describes a perfect octahedron order and the Ti-O-Ti angle is regular with an approximate value of 180°. Hence the given crystallographic features, the position of the conduction and valence band edges and the material stability promote an excellent UV activated material for overall water splitting reaction.[11-13] However, to

utilise solar light for this particular application the need of designing visible activated stable oxides is urgent.

A wide range of studies have shown that oxides such as TiO_2 and $SrTiO_3$ can be activated to visible light by substitutional doping. In most cases the dopants lead to reduced photoactivity but Rh and N are notable exceptions and can be used to create stable visible light photocatalysts.[15-17] One of the most efficient photocatalytic activities utilizing visible light in H_2 evolution was found when Rh is substituted for Ti^{4+} ions on the B-site of the $SrTiO_3$ perovskite.[18] In the literature, when designing a new material, the most accepted primary synthesis method is the conventional Solid-State reaction route for preparation of high purity polycrystalline solids (**Section 2.1.1.**). Moreover the advantage of using this, the as-produced highly crystalline compound leads to good electronic properties. Alternatively, hydrothermal synthesis (**Section 2.1.2.**) and sol-gel methods (**Section 2.1.3**) provide high surface area, small particle size and well specified morphology materials.

In 2004, the Kudo group initiated research in the area of solid state synthesised $SrTi_{1-x}Rh_xO_3$ and showed that it can be an effective photocatalyst for hydrogen generation with visible light from water using methanol as a sacrificial electron donor. The photocatalytic H_2 generation activity of $SrTi_{1-x}Rh_xO_3$ was shown to depend on the valence state of the Rh dopant, $SrTi_{1-x}Rh(IV)_xO_3$ being photocatalytically less active with Rh^{4+} giving photocatalytically inactive interband states, while $SrTi_{1-x}Rh(III)_xO_3$ is active in H_2 evolution reactions having Rh^{3+} states at the bottom of the conduction band.[16] The Rh valence shift is visually detectable as a colour change from purple $SrTi_{1-x}Rh(IV)_xO_3$ to yellow $SrTi_{1-x}Rh(III)_xO_3$ and the optical absorption appears at 580 nm and 420 nm, respectively.[19] In 2008 W. Bae and co-workers synthesised $SrTi_{1-x}Rh_xO_3$ hydrothermally using a Rh^{3+} precursor although as a second step, a high

temperature calcination (1000 °C) in air was applied therefore most likely the Rh^{3+} in the lattice was oxidised to Rh^{4+}.[20] In 2014 Kudo et al. confirmed the Rh state in the lattice with EPR technique when $SrTi_{1-x}Rh_xO_3$ was synthesised hydrothermally and thereafter threated at 1000 °C in air, and found an EPR active Rh^{4+} sample after post high temperature heat treatment due to an oxidation process.[21] W. Bae et al. directly compared the key features of solid state synthesised and hydrothermally made compounds and created an argument how the crystal size, the surface area and H_2 evolution activity was dissimilar depending on the synthesis routes.[20] As expected the parent solid state (SS) $SrTiO_3$ sample synthesised at 1000 °C showed the lowest BET surface area with 0.79 m^2/g. As a comparison the same measure for hydrothermally (HT) made samples even after firing at either 800 °C or 1000 °C showed 5.50 m^2/g or 3.42 m^2/g respectively. The authors related the H_2 evolution capability to the surface area and measured 670 µmol/g/h H_2 gas on a HT-synthesised Pt cocatalyst loaded $SrTiO_3$ sample under UV light whereas the solid state sample showed only 460 µmol/g/h H_2 evolution from 10 mM NaOH.[20] Interestingly, direct comparison is difficult with the literature values as authors used NaOH solution instead of MeOH, a commonly used sacrificial hole scavenger.

In a very recent publication from 2014, R. Niisiro and co-workers showed that hydrothermally synthesised and thereafter at 1000 °C air calcined $SrTi_{0.98}Rh_{0.02}O_3$ (Rh^{4+}) and $SrTi_{0.96}Rh_{0.02}Sb_{0.02}O_3$ (Rh^{3+}/Sb^{5+}) compounds showed H_2 generation activity from aq. MeOH solution under visible light when loaded with Pt cocatalyst.[21] Based on several publications from the previous years[15, 16], they expected that material with Rh^{3+} oxidation state would perform better when stabilised with a higher oxidation state cation (M^{5+}) than the one with Rh^{4+} in the lattice. However, in measurements, the single doped $SrTi_{0.98}Rh_{0.02}O_3$ compound demonstrated better performance, 330

µmol/g/h in H_2 evolution compared to the co-doped sample, showing less, 170 µmol/g/h H_2 in aq. MeOH; owing to the explanation that antimony introduced undesirable recombination sites. The authors further claimed that, samples made by HT synthesis exhibited better performance when tested in H_2 generation reaction than the samples synthesised by SS route. However, direct information for the BET surface area and actual H_2 evolution activity as a comparison is not found.[21]

Another way of synthesising inorganic crystalline metal alkoxides, for instance $ATiO_3$ (A = Mg, Ca, Sr, Ba) at reduced temperature is the sol-gel/Pechini-method developed as a patent in the US in 1967.[22] In a very recent article, published in 2014, K. Maeda reported visible light activated sol-gel $BaTi_{1-x}Rh_xO_3$ compounds for H_2 evolution with a BET surface area of approximately 3.0 - 6.4 m^2/g. As a comparison, the SS – samples were less active in the same reaction when 2.0 m^2/g specific surface area was measured.[23] For making nanoparticulate $ATiO_3$ (A = Sr, Ba) and $ATi_{1-x}Rh_xO_3$ (A = Sr, Ba) compounds, first the synthesis of the parent phase has to be optimised in order to obtain the phase pure material. Nanostructured $SrTiO_3$ particles can be synthesized hydrothermally at temperature between 100 – 200 °C by reacting nanoparticulate TiO_2 particles with alkaline solution (pH > 12) of $Sr(OH)_2$.[20, 24] Also reducing the number of steps during material synthesis is crucial to enhance repeatability. Therefore work done by Y. Wang and co-workers provide a good route for the synthesis.[24] In their publication they reported a one-step HT process to form crystalline cubic $SrTiO_3$ and $BaTiO_3$ nanoparticles from crystalline TiO_2 spheres. The PXRD pattern and the SEM images of the pre-synthesised TiO_2 particles suggested the formation of nanoparticles. As a conclusion, using commercially available TiO_2 nanopowder as a replacement of as-made TiO_2 particles [24] as starting material is a significant step forward to provide

nanoparticulate $SrTiO_3$ and $BaTiO_3$ single perovskite under well-controlled synthesis condition in a one-step synthesis.

Similarly, cubic phase $BaTiO_3$ can be synthesised at the temperature range of 80 – 240 °C by reacting fine TiO_2 particles in alkaline $Ba(OH)_2$ solution under pressure.[24, 25] In the latter publication [25], E. Ciftci and co-workers investigated the cubic to tetragonal phase composition as the function of synthesis temperature vs reaction time and confirmed the results by Rietveld structure refinement. They have found that after 24 hours, if the HT synthesis temperature was in the range of 80 – 120 °C, three phases were formed, predominantly (88 – 95 %) cubic $BaTiO_3$, some secondary (1 – 5 %) tetragonal $BaTiO_3$ and some unreacted (2 – 9 %) TiO_2. Furthermore, the optimised temperature range was found between 140 and 160 °C when the TiO_2 starting material was fully reacted and the $BaTiO_3$ phase ratio was 95 % cubic to 5 % tetragonal. Increasing the temperature up to 240 °C, 71 % of the cubic and 29 % of the tetragonal phases were found after refinement. The authors also studied the reaction time at 150 °C and found that phase-pure cubic structure was formed after 12 h. They have reported that at high temperature (240 °C) the obtained material changed with reaction time and after 96 hours the phase composition was 59 to 41 % cubic to tetragonal.[25]

In HT synthesis after reaction, washing the slurry with an organic acid (formic acid, acetic acid) is a general method for removing the residual $SrCO_3$ or $BaCO_3$.[24, 26]

To summarise the **Introduction** to **Chapter 3**, there has been a detailed discussion about suitable UV-light activated parent structures ($SrTiO_3$ and $BaTiO_3$) and some of the visible-light activated rhodium doped single perovskites ($SrTi_{1-x}Rh_xO_3$ and $BaTi_{1-x}Rh_xO_3$) in relation to addressing the various synthesis methods, the crystal structure,

the oxidation state of the dopant and the compounds' surface area associated with photocatalytic performance.

In this chapter, studies of hydrothermally made undoped and rhodium doped barium titanates were extended to produce phase pure cubic compounds for photocatalytic application using novel synthesis routes.

A further investigation was carried out to use hydrothermal synthesis to produce and fully characterise high surface area nanostructured $SrTi_{1-x}Rh_xO_3$ with cubic phase and a maximum Rh doping level was identified as x = 0.05 with conventional solid state as well as with hydrothermal methods.

Moreover, a second step calcination was not applied in any HT synthesis reactions therefore providing a compound with ready synthesised Rh^{3+} in the lattice as well as with increased surface area to facilitate enhanced photoactivity.

3.2. Synthesis

3.2.1. Hydrothermal synthesis of $BaTi_{1-x}Rh_xO_3$

For the HT synthesis of parent $BaTiO_3$, 7.5 mmol of Aeroxide® TiO_2 P25 (Sigma Aldrich, 99.5 %) and excess amount of 7.7 mmol of $Ba(OH) \cdot 8\ H_2O$ (Sigma Aldrich, 98 %) was used. $Ba(OH)_2 \cdot 8\ H_2O$ was dissolved in 30 mL preheated (80 °C) distilled water. During dissolution, N_2 gas was purged through the solution to remove dissolved CO_2. TiO_2 was added under N_2 purging and stirring, thereafter the suspension was made up to 35 mL. The 125 mL Teflon-coated reactor was sealed and the hydrothermal reaction was carried out in an oven at 150 °C for 12 h, 5 °C/min heating and cooling rates. The synthesized oxides were washed twice with 30 mL 1 M acetic acid and then

twice with 30 mL distilled water. The suspension was dried at 60 °C in air. The yield of the product was 1.35 g, when 7.5 mmol of starting materials were used.

Accordingly, for preparing the doped $BaTi_{1-x}Rh_xO_3$ (x = 0.01; 0.025; 0.050; 0.1), the precursor of $RhCl_3 \cdot xH_2O$ (Sigma Aldrich, Rh 38-40 %) was added last and the following steps were identical to the synthesis of parent compound. The powder of the undoped sample is colourless and the doped samples have yellow colour.

3.2.2. Hydrothermal synthesis of $SrTi_{1-x}Rh_xO_3$

$SrTi_{1-x}Rh_xO_3$ (x = 0; 0.01; 0.025; 0.050; 0.075; 0.1) were prepared hydrothermally by the replacement of Ti^{4+} ions at the B-site of the perovskite structure. The starting materials, Aeroxide® TiO_2 P25 (Sigma Aldrich, 99.5 %), $Sr(OH)_2 \cdot 8\,H_2O$ (Sigma Aldrich, 95 %), and $RhCl_3 \cdot xH_2O$ (Sigma Aldrich, Rh 38-40 %) were mixed in 60 mL of distilled water at room temperature, using 2 % excess of $Sr(OH)_2 \cdot 8\,H_2O$. The hydrothermal reaction was carried out in a 125 mL Teflon-coated reactor, at 180 °C for 12 h, 5°C/min heating rate, 2°C/min cooling rate. The synthesized oxides were washed twice with 1 M acetic acid and then twice with distilled water. The suspension was dried at 60 °C in air. The yield of the product was 1.2 g, 44 % when 7.5 mmol of starting materials were used. The parent phase is colourless and the Rh-doped compounds show the colour of yellow to brownish-yellow depending on the dopant concentration.[27]

3.2.3. Solid State Synthesis of $SrTi_{1-x}Rh_xO_3$

In order to compare hydrothermally synthesised and solid state products, samples of $SrTi_{1-x}Rh_xO_3$ with Rh content of x = 0; 0.01; 0.02; 0.03; 0.04; 0.05, 0.06, 0.07, 0.08,

0.09, 0.1) were prepared by solid state reaction using a stochiometric mixture of TiO_2 (Sigma Aldrich, nano anatase, 99.7%), $SrCO_3$ (Alfa Aesar, 99.994%) and Rh_2O_3 (Sigma Aldrich, 99.8%) precursors, according to the reaction:

$$SrCO_3 + (1-x)TiO_2 + \frac{x}{2}Rh_2O_3 \rightarrow SrTi_{1-x}Rh_xO_3 + CO_2 \qquad \textbf{(Eq. 3.1)}$$

Before weighing out, the powders were dried overnight at 200 °C. The reagents were carefully mixed with a mortar and pestle and pressed into a pellet and fired at 1400 °C for 12 h with 5 °C/min heating and 5 °C/min cooling rates. The obtained samples were re ground, pelletized and annealed for a second time at 1400 °C for 24 h with the same rates. The powder of the undoped sample is colourless and the doped samples have greyish purple colour.[27]

3.3. Discussion 1 – Characterisation of $BaTi_{1-x}Rh_xO_3$

As mentioned in the Introduction (**3.1.**) the synthesis of hydrothermally made phase pure cubic $BaTi_{1-x}Rh_xO_3$ is only possible at a narrow range of temperature and reaction time.[24, 25] Following the synthesis steps reported by Y. Wang et. *al*, 180 °C for 12 hours [24], the doping limit of Rh into $BaTiO_3$ was examined. **Fig. 3.4** demonstrates the powder XRD patterns of synthesised samples. At the undoped (x = 0) and at low Rh dopant concentration (x = 0.01) the PXRD pattern of the samples showed phase pure cubic structure with the space group of $Pm\bar{3}m$ $BaTiO_3$ and $BaTi_{0.99}Rh_{0.01}O_3$ compounds, however at x > 0.01 of Rh, a secondary phase of the tetragonal $I4_1/amd$ TiO_2 anatase [101] appeared at 25.3° 2 theta. In addition, it has to be also noted that the sample synthesised with x = 0.1 Rh also shows a significant [200] anatase impurity peak at

48.1° 2 theta, suggesting that the unit cell cannot be further expanded which results in the lack of Rh to Ti replacement.

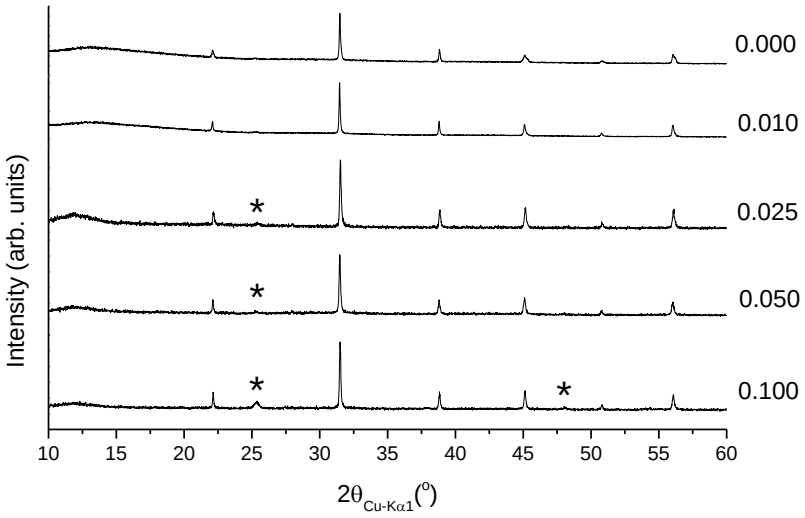

Fig. 3.4 Powder XRD patterns of $BaTi_{1-x}Rh_xO_3$ with $0 \leq x \leq 0.1$, synthesised at 180 °C, 12 hours showing impurities for $x > 0.01$. The main peaks denote the phase-pure cubic structure. TiO_2 anatase impurity is indicated for $x > 0.01$ samples marked with *.

The BET surface area of the as-synthesised phase pure samples was 19.8 ± 1.4 m^2/g.

To verify the $BaTiO_3$ compositional tunability, another preparation method published by E. Ciftci et al. is used to synthesise phase pure cubic $BaTi_{1-x}Rh_xO_3$ compounds (**Section 3.2.1.**). This detailed study of the parent compound explains the cubic to tetragonal phase transition depending on the synthesis temperature.[25] The samples synthesised at 150 °C for 12 hours are shown in **Fig. 3.5** in comparison to the commercially available (Inframat®, Advanced Materials™) $BaTiO_3$ tetragonal structure with the space group of *P4mm*.

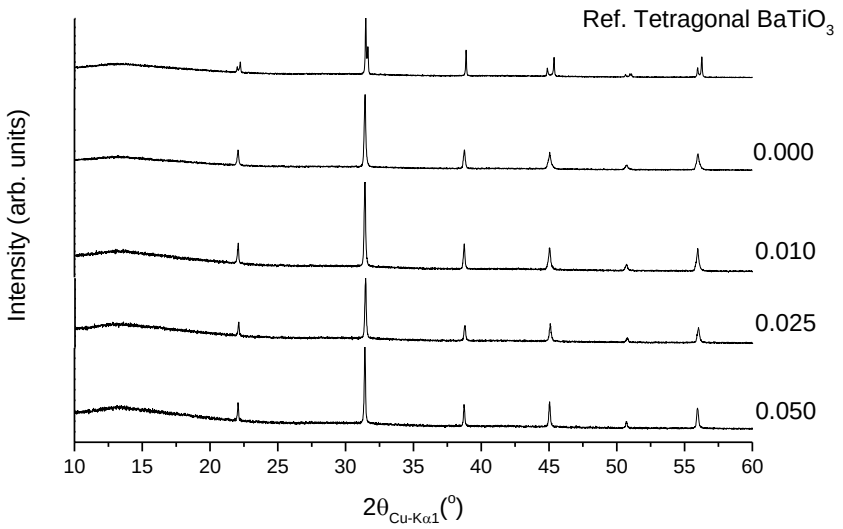

Fig. 3.5 Powder XRD patterns of $BaTi_{1-x}Rh_xO_3$ with $0 \leq x \leq 0.05$, synthesised at 150 °C, 12 hours showing no impurities. The main peaks denote the phase-pure cubic structure. The top layer of the graph indicates the reference pattern of tetragonal $BaTiO_3$.

The enlargement of Power X-ray diffraction patterns of **Fig. 3.5** at the base of peak intensities is shown in **Fig. 3.6**. At finer examination of these patterns it is noticeable that the peak shape of the as-synthesised samples is symmetric and no division of the peaks can be observed, therefore indicating the presence of a single $Pm\bar{3}m$ cubic structure after doped with rhodium ($0 \leq x \leq 0.05$). In comparison, the reference $BaTiO_3$ tetragonal pattern shows the splitting of the peaks at higher 2 theta angles (45°, 51° and 56°) hence indicating a lower structural symmetry than the synthesised cubic structure.

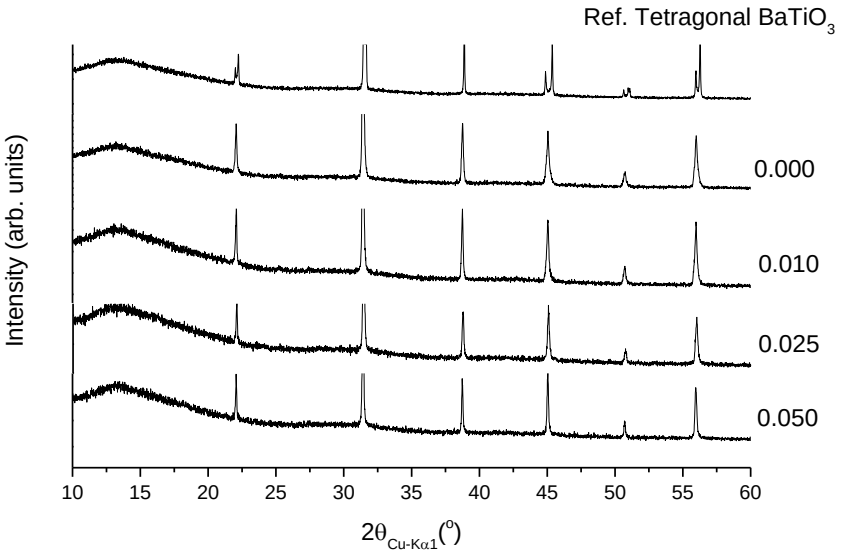

Fig. 3.6 Enlargement of the PXRD patterns of $BaTi_{1-x}Rh_xO_3$ with $0 \leq x \leq 0.05$, synthesised at 150 °C, 12 hours showing no impurities only cubic structure of barium titanate compounds. The top layer of the graph denotes the reference pattern of tetragonal $BaTiO_3$ with typical split peaks.

The UV-Vis spectrum of $BaTi_{1-x}Rh_xO_3$ with $0 \leq x \leq 0.05$ using the synthesis temperature of 150 °C for 12 h is presented in **Fig. 3.7**. For the sample containing no rhodium (x = 0), a UV light absorption was obtained, and the colourless powder sample reflected high percentage of incident photons during spectroscopic measurement. This sample showed a calculated indirect band gap of 3.17 eV (~ 390 nm), and its fundamental absorption edge is in line with the literature value of 3.15 eV.[28] The rhodium doped samples showed a pronounced absorption band at a photon energy of 3.1 - 2.75 eV (400 - 450 nm), confirming the titanium cation substitution in the lattice by the rhodium(III) oxidation state cations and resulting in visible light absorbing materials. As expected, the colours of samples have changed from colourless to yellow upon doping (**Fig. 3.8**). In addition, an absorption band at the position of about 580

nm, which is typically attributed to Rh^{4+} cations, was not obtained for the doped samples (**Fig. 3.7**).

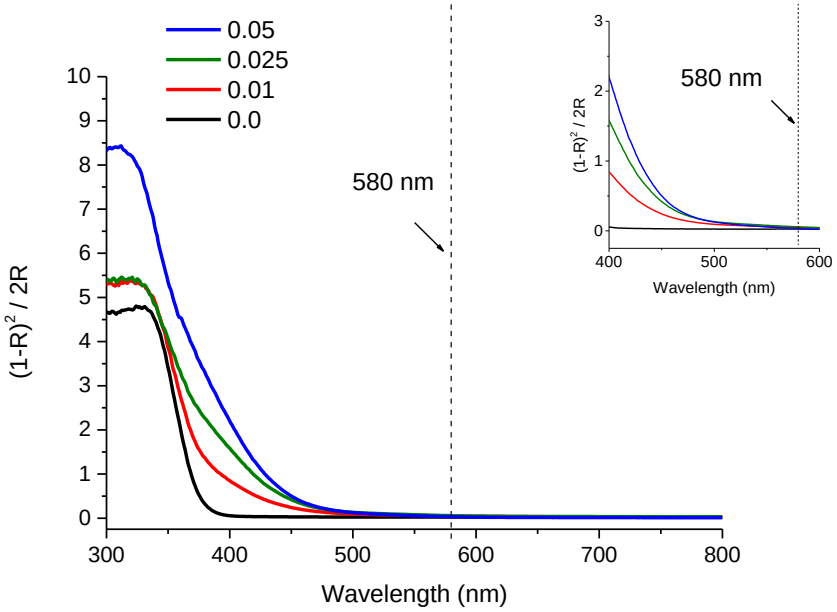

Fig. 3.7 Kubelka-Munk function of $BaTi_{1-x}Rh_xO_3$ with $0 \leq x \leq 0.05$ rhodium, synthesised at 150 °C for 12 hours.

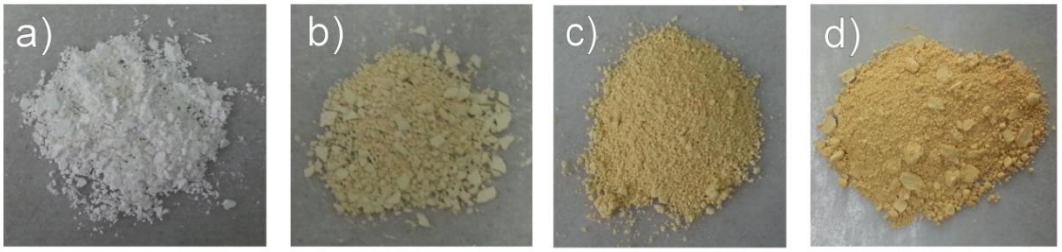

Fig. 3.8 Images of powder $BaTi_{1-x}Rh_xO_3$ samples with Rh content of (a) 0, (b) 0.01, (c) 0.025, (d) 0.050, synthesised at 150 °C for 12 hours.

SEM morphology study was performed on samples without and with rhodium doping into cubic $BaTiO_3$ and the results are shown in **Fig. 3.9.**

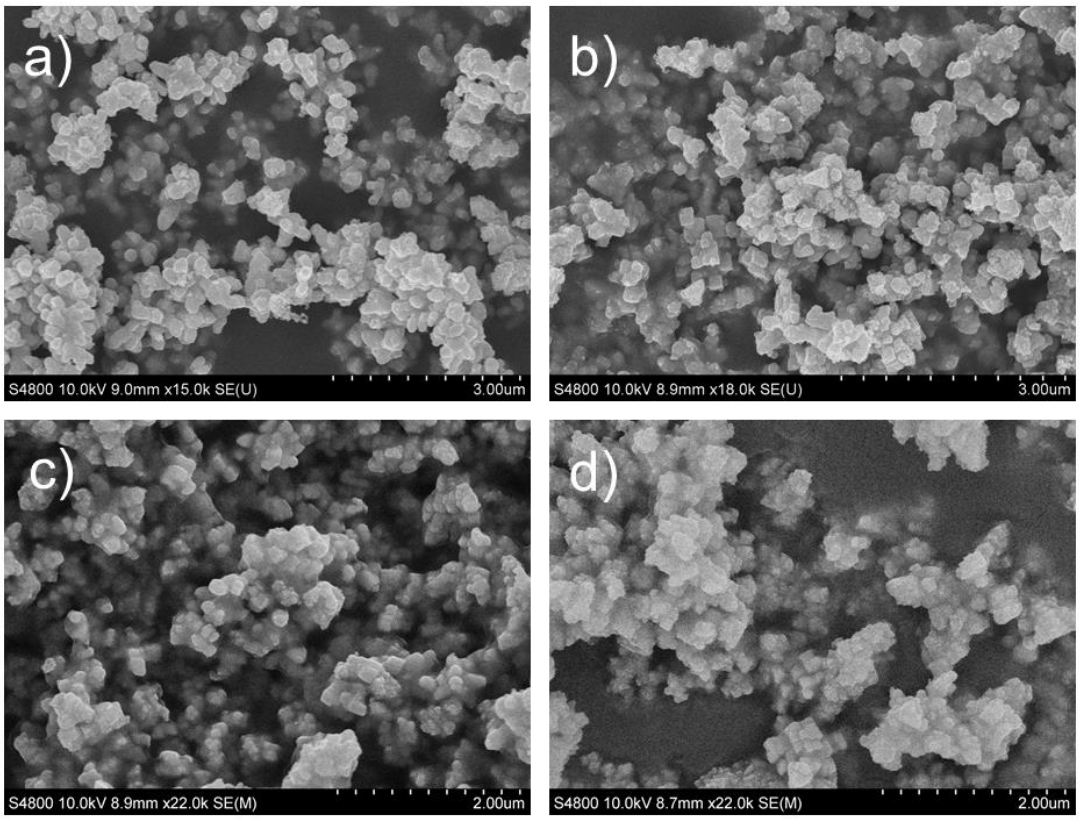

Fig. 3.9 SEM images of powder $BaTi_{1-x}Rh_xO_3$ samples with Rh content of (a) 0, (b) 0.01, (c) 0.025, (d) 0.050, synthesised at 150 °C for 12 hours.

Samples showed approximately 200 - 300 nm particle size distribution for particles for all dopant levels. The primary particle size calculated from Powder XRD data after precise peak fitting and using the Scherrer equation, was 75-81 nm. Upon doping evident deviation in morphology did not appear.

The Brunauer-Emmett-Teller surface area of the 150 °C synthesised samples was 6.8 - 7.5 m^2/g.

To further prove the oxidation state of dopant after synthesis at 150 °C for 12 h , the sample containing x = 0.05 Rh was treated overnight at room temperature in H_2/N_2 atmosphere (**Fig. 3.10**). After reduction the absorption band around 580 nm remained

constant suggesting that Rh^{3+} was formed during HT synthesis and no further reduction possible.

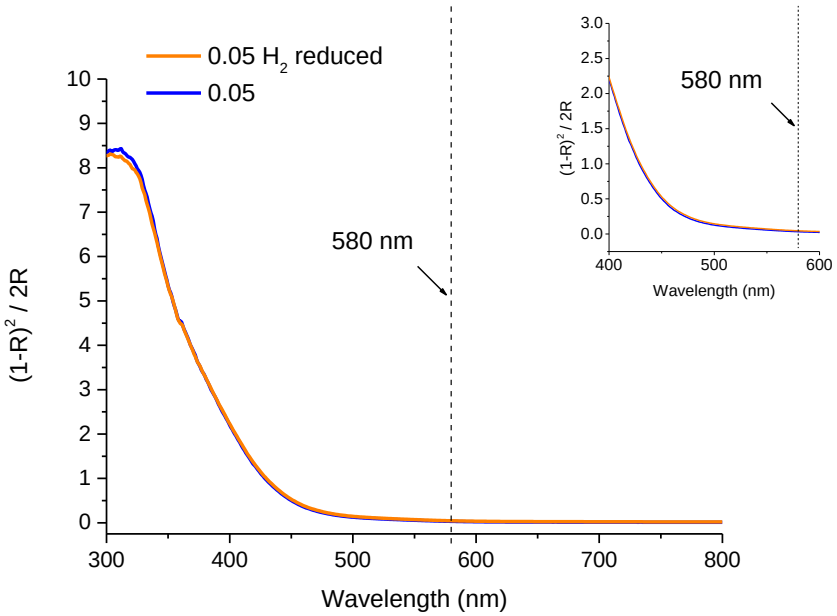

Fig. 3.10 Kubelka-Munk function of as-synthesised $BaTi_{0.95}Rh_{0.05}O_3$ and $BaTi_{0.95}Rh_{0.05}O_3$ reduced overnight at room temperature under H_2 atm.

3.4. Discussion 2 – Characterisation of $SrTi_{1-x}Rh_xO_3$

To ensure any residual amount of $SrCO_3$ was successfully removed from the samples by acetic acid washing FTIR measurement was carried out. Following the hydrothermal synthesis using the same batch of the suspension half of the sample was washed twice with 1 M acetic acid and then twice with distilled water (AA) and the other half of the slurry was only washed 2 times with distilled water (DW). The FTIR measurement indicated the presence of CO_3^{2-} in DW sample and also confirmed that after treating the sample with 1 M acetic acid the $SrCO_3$ content was completely removed (1468 cm^{-1} assigned peak)[29] (**Fig. 3.11**). Only the purified materials were used in this study.[27]

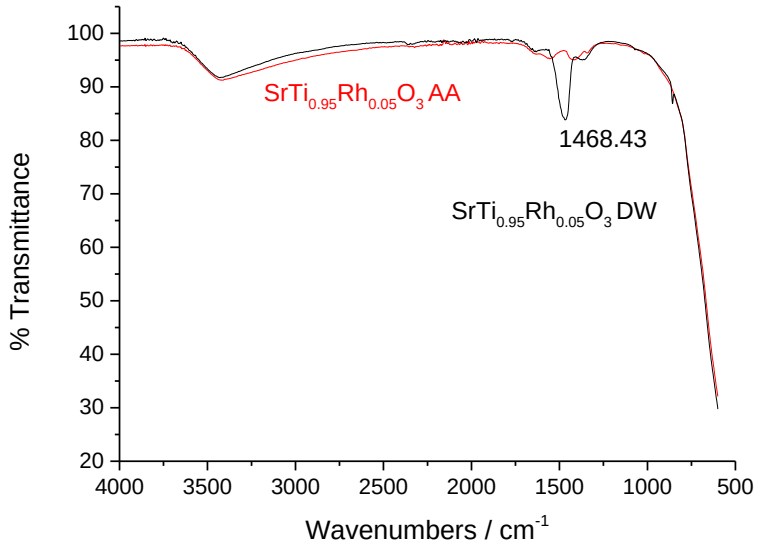

Fig. 3.11 FTIR data of $SrTi_{0.95}Rh_{0.05}O_3$ AA and DW washed samples

XRD data of hydrothermally synthesised $SrTi_{1-x}Rh_xO_3$ samples can be indexed to a cubic unit cell with space group of $Pm\bar{3}m$. A small amount of TiO_2 anatase (29.3 2θ) was found by the XRD to be present as an impurity phase when x = 0.075 and x = 0.1 (**Fig. 3.12**). Data also show extensive tunability of cubic structure upon doping with Rh up to $x \leq 0.05$.

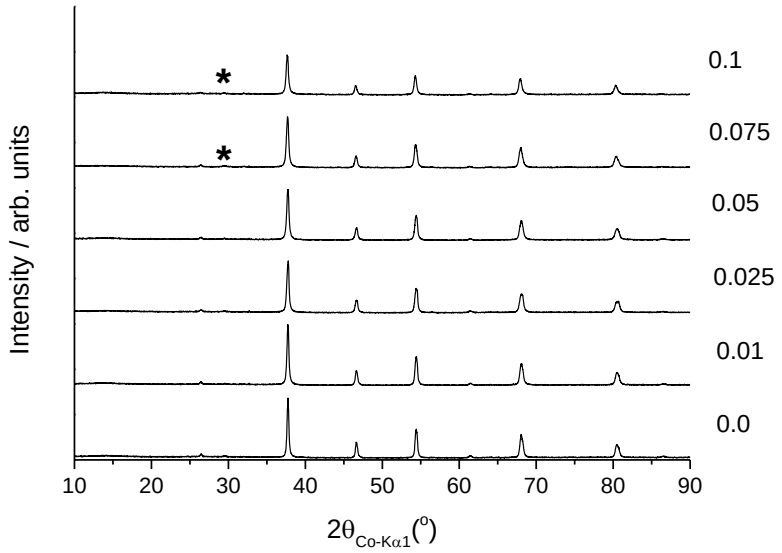

Fig 3.12 PXRD pattern of hydrothermally made $SrTi_{1-x}Rh_xO_3$ samples with increasing Rh doping level (x = 0.0; 0.01; 0.025; 0.05; 0.075; 0.1). * anatase TiO_2.

As a comparison of perovskite tunability, Rh insertion was also investigated by solid-state synthesis. Phase pure sample composition was found up to x = 0.06 Rh content. **Fig. 3.13** shows the x = 0.1 Rh containing samples along with the typical impurity phases of Rh_3Ti and $Sr_4Ti_3O_{10}$. The impurities are formed according to the equation of

$$SrTi_{0.9}Rh_{0.1}O_3 \rightarrow 0.69\ SrTi_{0.94}Rh_{0.06}O_3 + 0.02\ Rh_3Ti + 0.08\ Sr_4Ti_3O_{10}$$

(**Eq. 3.2**)

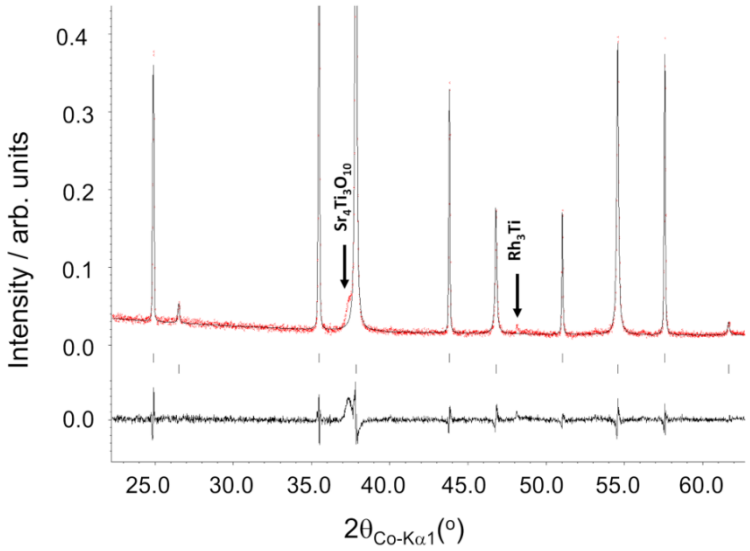

Fig. 3.13 Profile matching PXRD pattern of solid state synthesised $SrTi_{1-x}Rh_xO_3$ sample with x = 0.1, the arrows index the impurities of $Sr_4Ti_3O_7$ and Rh_3Ti, all other peaks are referred to the cubic perovskite structure

XPS was used to determine the oxidation state of rhodium on the surface of hydrothermally synthesised $SrTi_{1-x}Rh_xO_3$ where x = 0.01, 0.05 and 0.1. The Rh $3d_{5/2}$ XPS for x = 0.01 showed a symmetrical peak shape and a binding energy of 308.5 eV (*c.f.* Rh $3d_{5/2}$ in Rh_2O_3 at 308.4 eV, **Fig. 2.4, Table 2.3**), indicating the presence of the photocatalytically active Rh^{3+} (**Fig. 3.14a**). For x = 0.05 and 0.1 an asymmetric Rh $3d_{5/2}$ peak shape was observed which could be deconvoluted into two peaks at 308.4 eV and 309.8 eV assigned to Rh^{3+} and Rh^{4+} species respectively (**Fig. 3.14a**), again confirming the presence of the photoactive Rh^{3+} species in the material. Fitting parameters for Rh XPS are given in **Table 3.1, Table 3.2, Fig. 3.15**. The doping limit of Rh into $SrTiO_3$ determined from solid-state and HT synthesis was at ~ 6 %, hence the presence of RhO_2 is not unexpected in the higher Rh content for examined HT samples though may be detrimental to photocatalytic activity. Some surface oxidation may also occur forming Rh^{4+} species. All Rh measured binding energies match well with literature values [30-34] and standard materials (**Fig. 2.5, Table 2.3**).[27]

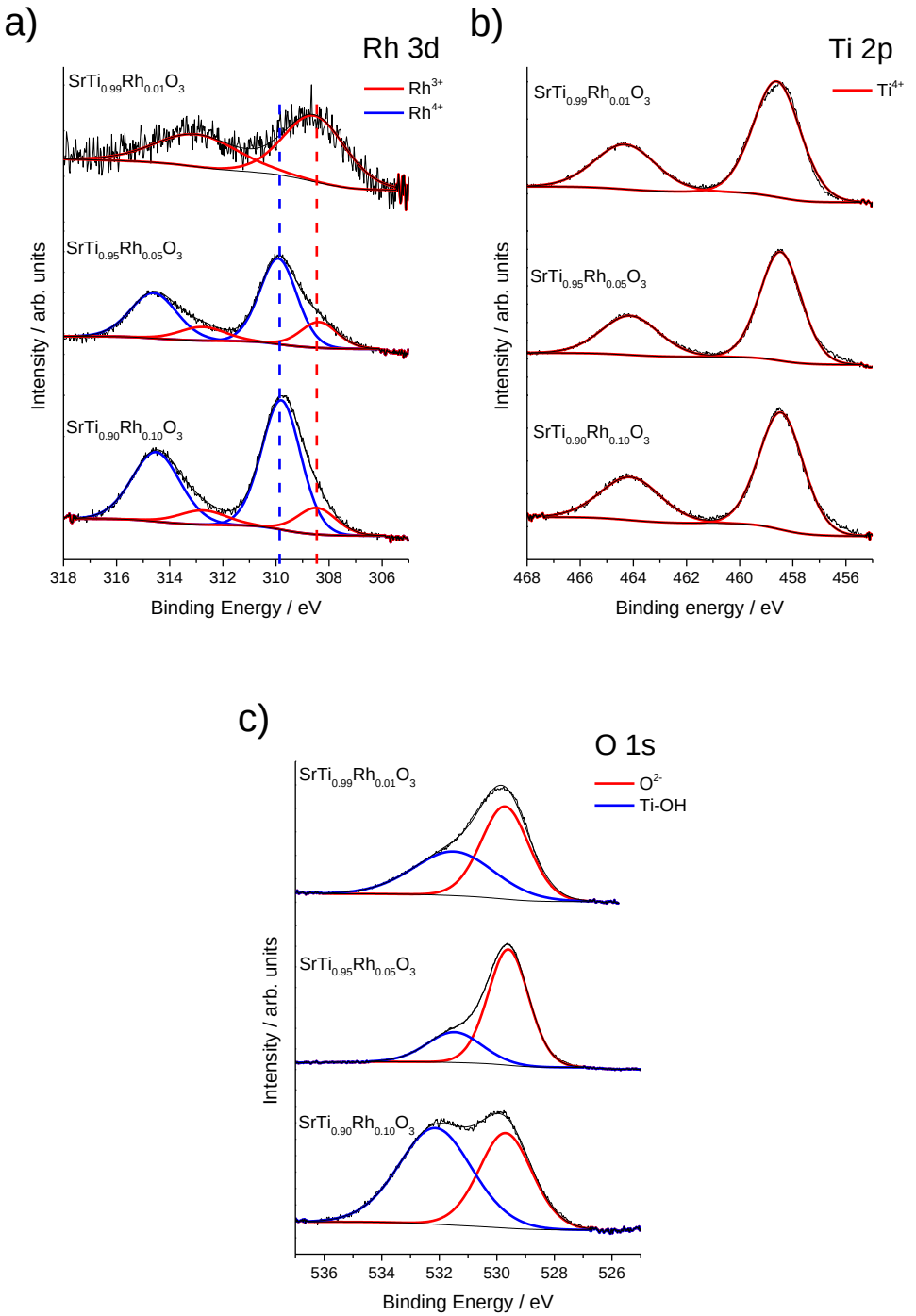

Fig. 3.14 (a) Fitted Rh 3d XPS spectrum of $SrTi_{0.99}Rh_{0.01}O_3$; $SrTi_{0.95}Rh_{0.05}O_3$ and $SrTi_{0.9}Rh_{0.1}O_3$ samples (Black line is the original data, red line is the Rh^{3+} fit and blue line is the Rh^{4+} fit (b) Fitted Ti 2p XPS spectrum of $SrTi_{0.99}Rh_{0.01}O_3$; $SrTi_{0.95}Rh_{0.05}O_3$ and $SrTi_{0.9}Rh_{0.1}O_3$ samples (Black line is the original data, red curve is the Ti^{4+} fit) (c) Fitted O 1s XPS spectrum of $SrTi_{0.99}Rh_{0.01}O_3$; $SrTi_{0.95}Rh_{0.05}O_3$ and $SrTi_{0.9}Rh_{0.1}O_3$ samples (Black line denotes the experimental data which is the superposition of O^{2-} species as red line and the -OH components as blue curve)

Tab. 3.1 XPS binding energies of Rh^{4+} and Rh^{3+} 3d 3/2 and 5/2 spin orbit peaks for hydrothermally synthesised $SrTi_{1-x}Rh_xO_3$ samples with x = 0.01, x = 0.05, x = 0.10 contents

Sample Composition	B. E. / eV		B. E. / eV	
	Rh^{4+} 3d 3/2	Rh^{4+} 3d 5/2	Rh^{3+} 3d 3/2	Rh^{3+} 3d 5/2
$SrTi_{0.99}Rh_{0.01}O_3$	-	-	312.96	308.54
$SrTi_{0.95}Rh_{0.05}O_3$	314.61	309.91	312.76	308.38
$SrTi_{0.90}Rh_{0.10}O_3$	314.51	309.80	312.75	308.46

Tab. 3.2 XPS areas of Rh^{4+} and Rh^{3+} 3d 3/2 and 5/2 spin orbit peaks for hydrothermally synthesised $SrTi_{1-x}Rh_xO_3$ samples with x = 0.01, x = 0.05, x = 0.10 contents

Sample Composition	Area		Area	
	Rh^{4+} 3d 3/2	Rh^{4+} 3d 5/2	Rh^{3+} 3d 3/2	Rh^{3+} 3d 5/2
$SrTi_{0.99}Rh_{0.01}O_3$	-	-	35.4	53.6
$SrTi_{0.95}Rh_{0.05}O_3$	122.5	185.7	36.9	56.0
$SrTi_{0.90}Rh_{0.10}O_3$	195.0	295.5	39.9	60.5

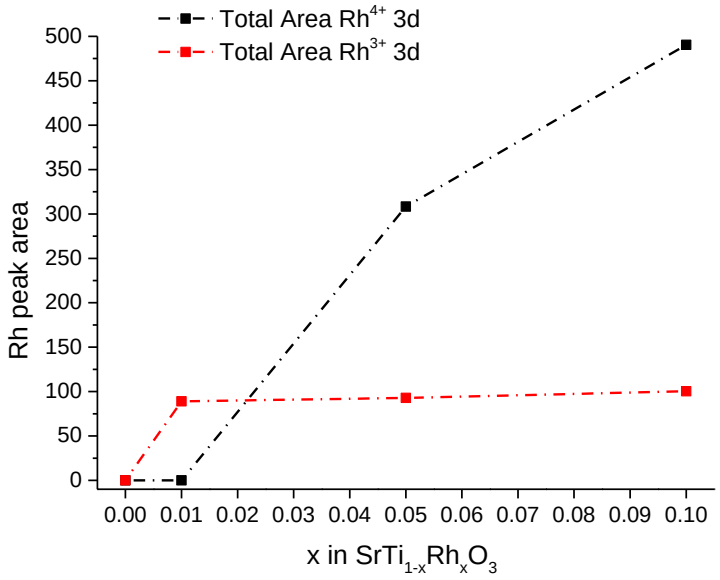

Fig. 3.15 Calculated XPS Total Rh area of Rh^{4+} and Rh^{3+} 3d species for hydrothermally synthesised $SrTi_{1-x}Rh_xO_3$ samples with x = 0.01, x = 0.05, x = 0.10 contents

In the Ti 2p XPS spectral region (**Fig. 3.14b**), there are 2 symmetrical peaks at 464.2 eV and 458.5 eV binding energies which can be attributed to Ti $2p_{1/2}$ and Ti $2p_{3/2}$ levels of Ti^{4+}.[35] No other Ti species were detected**.**

In the O 1s spectra the asymmetric peak is assigned to the O^{2-} species at 529.7 eV binding energy characteristic of oxide materials.[36] The shoulder observed at 531.5 eV can be attributed to the Ti-OH species [36] (**Fig. 3.14c**). Furthermore the ester oxygen in carboxyl groups gives a O 1s peak at ~533 eV [36] which is not observed, indicating that the acetic acid used to remove unreacted $SrCO_3$, is completely removed after distilled water washing, confirming the FTIR measurement (**Fig. 3.11**). [27]

XPS did not show any Cl $2p_{3/2}$ at 199.1 eV binding energy even at x = 0.1 Rh concentration, indicating that no unreacted $RhCl_3$ or chloride contamination was present in the samples.[37]

Diffuse reflection measurements gave optical band gaps of 3.2 eV for x = 0 and 2.0 – 2.1 eV for all levels of rhodium doping (**Fig 3.16a-b**) which is consistent with literature values after Rh^{4+} to Rh^{3+} photoreduction reported by Kudo.[16]

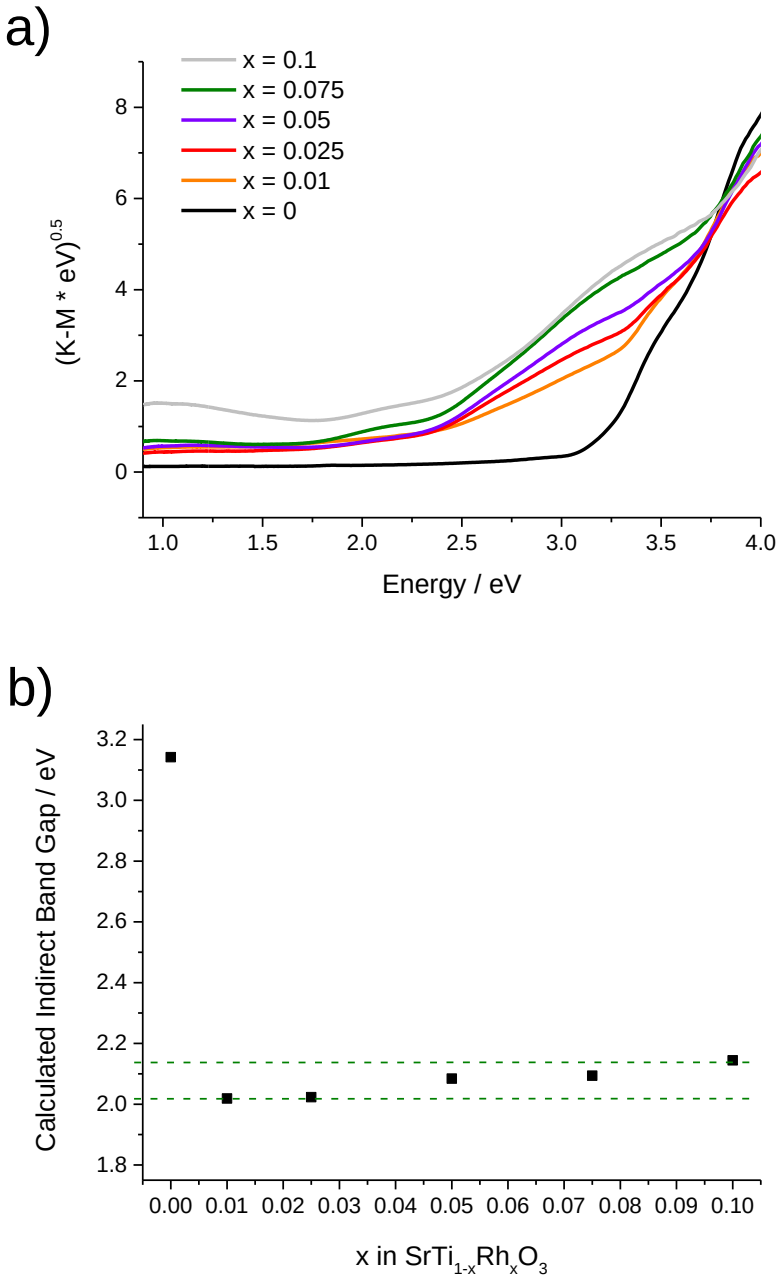

Fig. 3.16 (a) Indirect Band Gap vs Energy plots of $SrTi_{1-x}Rh_xO_3$ with increasing Rh doping level (x = 0.0; 0.01; 0.025; 0.05; 0.075; 0.1), (b) Calculated Indirect band gap remains constant upon doping with rhodium

In addition, the colour change from colourless to yellow indicated the formation of Rh^{3+} donor level and also the substitution of Ti^{4+} ions (**Fig 3.17a-b).**

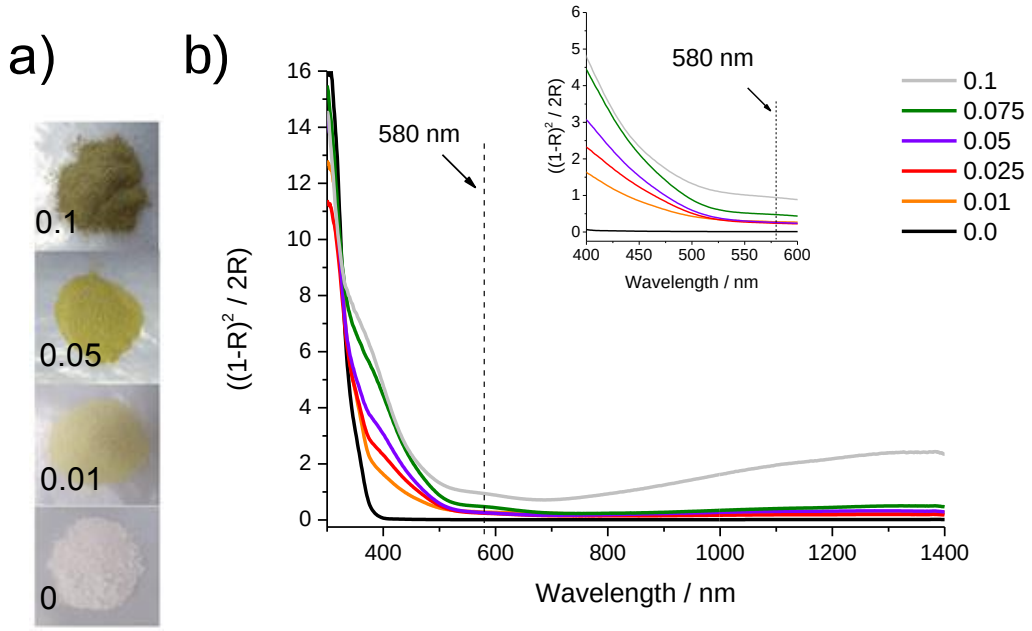

Fig. 3.17 (a) Colour change of $SrTi_{1-x}Rh_xO_3$ samples upon Rh doping level x = 0; 0.01; 0.05; 0.1 and (b) Kubelka-Munk function of as-made samples for x = 0; 0.01; 0.025; 0.05; 0.075; 0.1 Rh

The samples at the doping level of x = 0.01; 0.025 and 0.05 Rh showed a yellow colour resulting from a broad peak centred around 450 nm. At higher concentrations of Rh ($x \geq 0.075$ there was a second absorption band around 580 nm and a broad peak stretching into the near infrared with a maximum at 1300 nm attributable to Rh^{4+} d-d transitions.[15] The diffuse reflectance measurement of the $x \leq 0.05$ sample shows limited absorption at this region, indicating predominantly Rh^{3+} in the structure in a good agreement with the XPS results.

Low magnification SEM images of the hydrothermally made STO materials show large (10's μm), non-uniform particles with some apparent porosity (**Fig. 3.18a-b**).

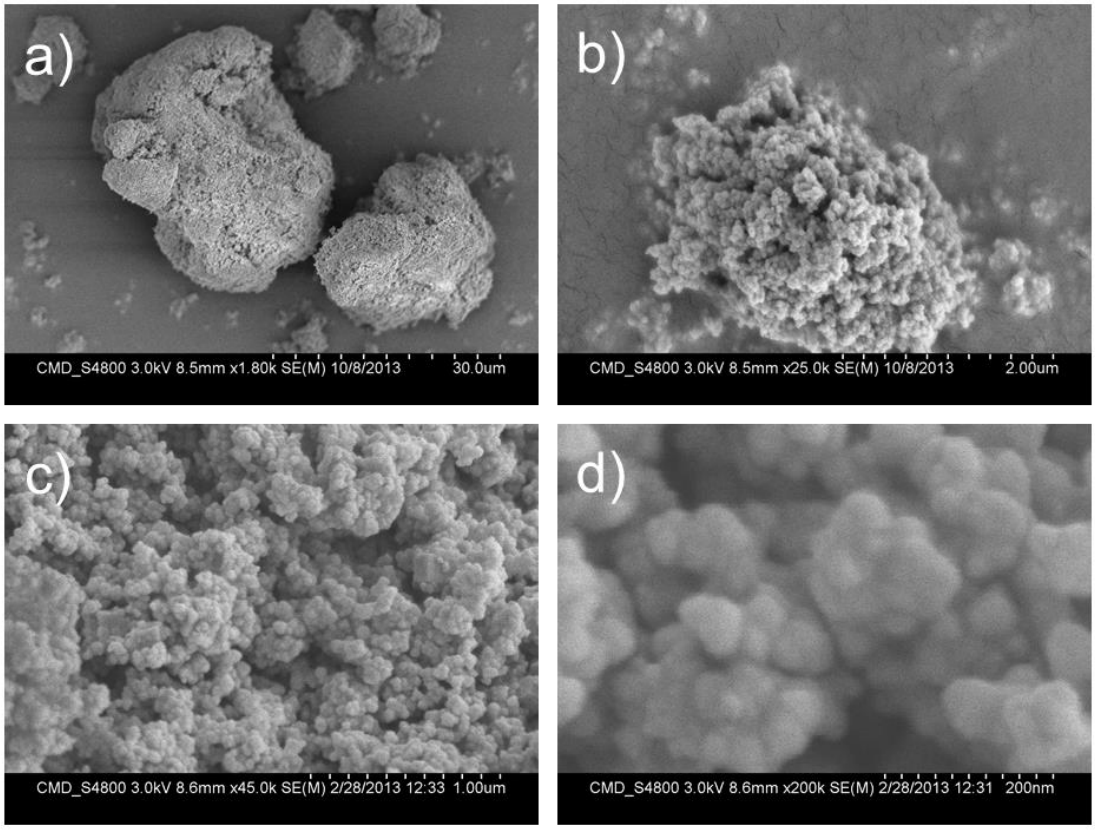

Fig. 3.18 SEM images of $SrTiO_3$ (a, b) and $SrTi_{0.95}Rh_{0.05}O_3$ (c, d) samples

At higher magnification these large particles can be resolved to be clusters of small particles with a size range of 50-100 nm (**Fig. 18c-d**), concurring with the primary particle size calculated from the PXRD data using the Scherrer equation (29-35 nm) and TEM images (**Fig. 3.19a-b**). [27]

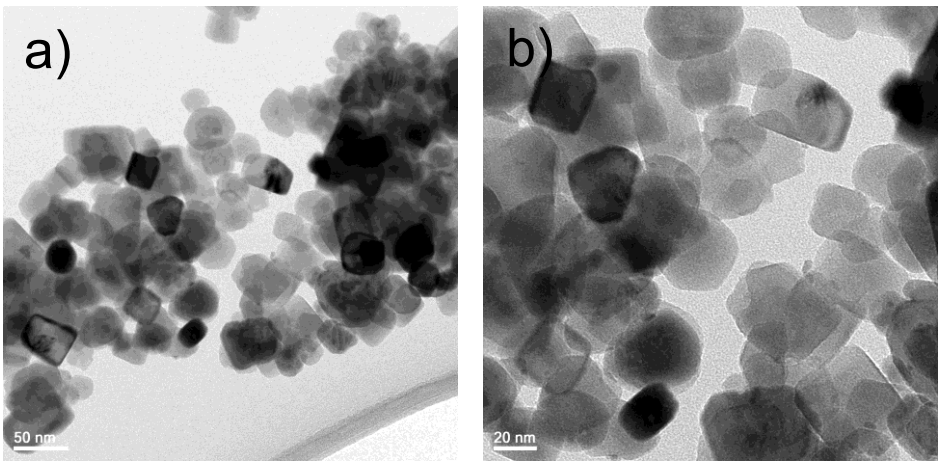

Fig. 3.19a-b TEM images of $SrTi_{0.95}Rh_{0.05}O_3$ samples

The individual particles appear to be fused to form a porous structure in the larger clusters (**Fig. 3.18d**). The morphology is consistent throughout the range of doping investigated (**Fig 3.18a-d, Fig.3.20a-c**).

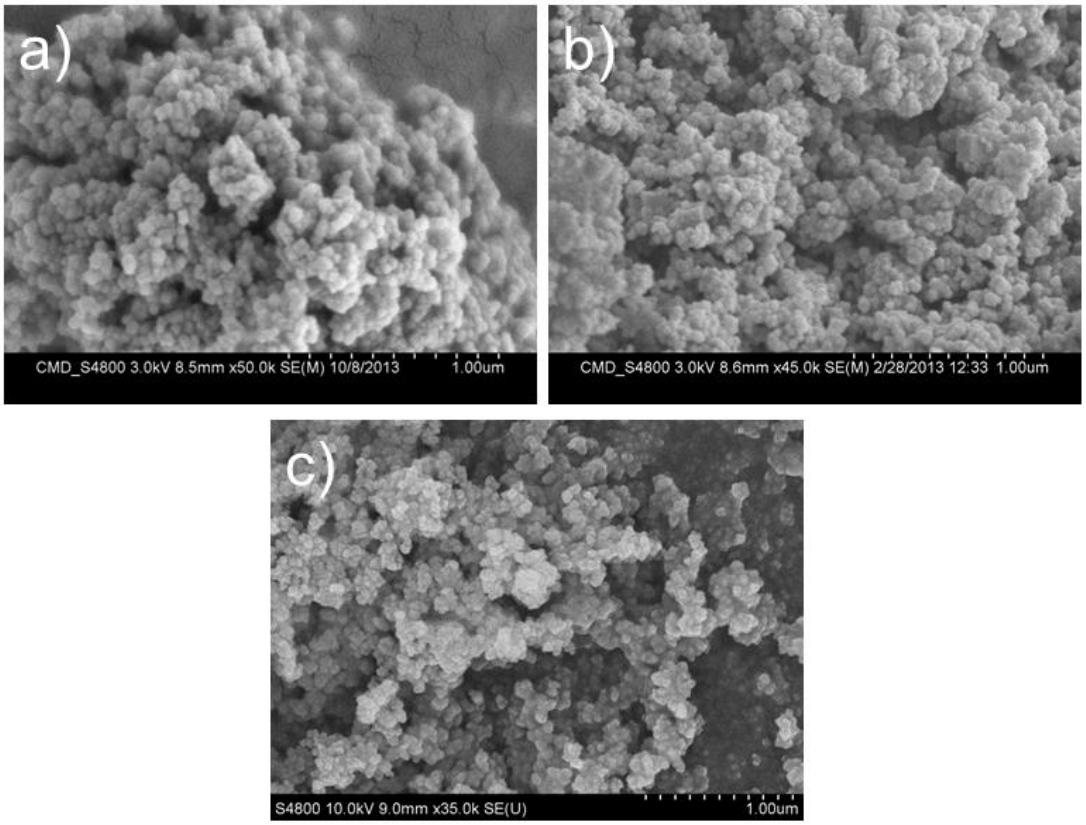

Fig. 3.20a-c SEM images of (a) $SrTiO_3$, (b) $SrTi_{0.95}Rh_{0.05}O_3$, (c) $SrTi_{0.9}Rh_{0.1}O_3$ samples

BET surface area of the samples was measured to be 37 ± 3 m^2/g, a reduced from 50 m^2/g for the P25 starting material.

3.5. Conclusion

A novel synthsis way of producing $BaTi_{1-x}Rh_xO_3$ was described in this chapter. A hydrothermal synthesis route was optimised to confirm $BaTiO_3$ tunability upon doping with rhodium at 150 °C. UV-Vis data confirmed the Rh^{3+} state in samples which was

further confirmed by reduction reactions. HT synthesis resulted in 200-300 nm clusters with 75-81 nm primary particle size and with approx. 7 m^2/g BET surface area.

Moreover, a hydrothermal synthesis at 180 °C was used, without high temperature calcination, to produce high surface area nanostructured, cubic $SrTi_{1-x}Rh_xO_3$. Using Powder XRD, an optimum level of Rh was identified at x = 0.05 in $SrTi_{1-x}Rh_xO_3$. Furthermore, avoiding the high temperature calcination in air prevented oxidation of Rh^{3+} to Rh^{4+} as well as as maintaining the high surface area required for enhancing photoactivity.

The rhodium oxidation state was identified in the lattice for both Ba^{2+} and Sr^{2+} perovskie family compounds. The role of Rh in the photocatalysis processes will be investigated in **Chapter 4**.

3.6. References

1. K. Liu, M. Cao, A. Fujishima and L. Jiang, *Chemical Reviews*, 2014, **114**, 10044-10094.
2. A. Fujishima, X. Zhang and D. A. Tryk, *Surface Science Reports*, 2008, **63**, 515-582.
3. J. M. Bolts and M. S. Wrighton, *Journal of Physical Chemistry*, 1976, **80**, 2641-2645.
4. S. Burnside, J.-E. Moser, K. Brooks, M. Grätzel and D. Cahen, *J. Phys. Chem. B*, 1999, **103**, 9328-9332.
5. X. Yong and M. A. A. Schoonen, *Am. Mineral.*, 2000, **85**, 543-556.
6. A. B. Ellis, S. W. Kaiser and M. S. Wrighton, *Journal of the American Chemical Society*, 1976, **98**, 1635-1637.
7. B. Wul and J. M. Goldman, *C. R. Acad. Sci URSS*, 1946, **51**, 21-27.
8. G. H. Kwei, A. C. Lawson, S. J. L. Billinge and S. W. Cheong, *Journal of Physical Chemistry*, 1993, **97**, 2368-2377.
9. A. Mahmoud, A. Erba, K. E. El-Kelany, M. Rérat and R. Orlando, *Phys. Rev. B Condens. Matter Mater. Phys.*, 2014, **89**.
10. X. Lin, J. Xing, W. Wang, Z. Shan, F. Xu and F. Huang, *J. Phys. Chem. C*, 2007, **111**, 18288-18293.
11. K. Domen, S. Naito, M. Soma, T. Onishi and K. Tamaru, *Journal of the Chemical Society, Chemical Communications*, 1980, 543-544.
12. K. Domen, S. Naito, T. Onishi, K. Tamaru and M. Soma, *Journal of Physical Chemistry*, 1982, **86**, 3657-3661.
13. K. Domen, A. Kudo, T. Onishi, N. Kosugi and H. Kuroda, *Journal of Physical Chemistry*, 1986, **90**, 292-295.
14. A. Erba, K. E. El-Kelany, M. Ferrero, I. Baraille and M. Rérat, *Phys. Rev. B Condens. Matter Mater. Phys.*, 2013, **88**.
15. R. Konta, T. Ishii, H. Kato and A. Kudo, *J. Phys. Chem. B*, 2004, **108**, 8992-8995.
16. A. Kudo, R. Niishiro, A. Iwase and H. Kato, *Chem. Phys.*, 2007, **339**, 104-110.
17. R. Asahi, T. Morikawa, T. Ohwaki, K. Aoki and Y. Taga, *Science*, 2001, **293**, 269-271.
18. X. B. Chen, S. H. Shen, L. J. Guo and S. S. Mao, *Chem. Rev.*, 2010, **110**, 6503-6570.
19. S. Kawasaki, K. Akagi, K. Nakatsuji, S. Yamamoto, I. Matsuda, Y. Harada, J. Yoshinobu, F. Komori, R. Takahashi, M. Lippmaa, C. Sakai, H. Niwa, M. Oshima, K. Iwashina and A. Kudo, *J. Phys. Chem. C*, 2012, **116**, 24445-24448.
20. S. W. Bae, P. H. Borse and J. S. Lee, *Applied Physics Letters*, 2008, **92**, 104107.
21. R. Niishiro, S. Tanaka and A. Kudo, *Applied Catalysis B: Environmental*, 2014, **150–151**, 187-196.
22. P. M. Pechini, Ceramic Dielectric Materials, U.S. Patent 3330697, Editon edn., 1967.
23. K. Maeda, *ACS Applied Materials & Interfaces*, 2014, **6**, 2167-2173.
24. Y. Wang, H. Xu, X. Wang, X. Zhang, H. Jia, L. Zhang and J. Qiu, *J Phys Chem B*, 2006, **110**, 13835-13840.
25. E. Ciftci, M. N. Rahaman and M. Shumsky, *J Mater Sci*, 2001, **36**, 4875-4882.
26. I. J. Clark, T. Takeuchi, N. Ohtori and D. C. Sinclair, *Journal of Materials Chemistry*, 1999, **9**, 83-91.
27. B. Kiss, C. Didier, T. D. Manning, H. E. Allison, A. W. Taylor, J. B. Claridge, J. R. Darwent and M. J. Rosseinsky, *in preparation*, 2015.
28. M. Cardona, *Physical Review*, 1965, **140**, A651-A655.
29. S. M. Teleb, D. El-Sayed Nassr and E. M. Nour, *Bull Mater Sci*, 2004, **27**, 483-485.
30. Z. Weng-Sieh, R. Gronsky and A. T. Bell, *J. Catal.*, 1997, **170**, 62-74.
31. T. L. Barr, *Journal of Physical Chemistry*, 1978, **82**, 1801-1810.
32. J. S. Brinen and A. Melera, *Journal of Physical Chemistry*, 1972, **76**, 2525-2526.
33. K. Maeda, K. Teramura, D. Lu, T. Takata, N. Saito, Y. Inoue and K. Domen, *J Phys Chem B*, 2006, **110**, 13753-13758.

34. M. Zimowska, J. B. Wagner, J. Dziedzic, J. Camra, B. Borzęcka-Prokop and M. Najbar, *Chem. Phys. Lett.*, 2006, **417**, 137-142.
35. X. Chen, L. Liu, P. Y. Yu and S. S. Mao, *Science*, 2011, **331**, 746-750.
36. E. McCafferty and J. P. Wightman, *Surface and Interface Analysis*, 1998, **26**, 549-564.
37. H. J. Borg, L. C. A. van den Oetelaar and J. W. Niemantsverdriet, *Catal Lett*, 1993, **17**, 81-95.

4. Chapter 4: Photocatalytic Application of $BaTi_{1-x}Rh_xO_3$ and $SrTi_{1-x}Rh_xO_3$ Single Perovskites

4.1. Introduction

It is clear that water is vital for all known forms of life. Safe drinking water is essential to humans and other life-forms even though it provides no calories or organic nutrients. It has been estimated that by 2025 more than half of the world population will be facing water-based vulnerability. From the 23rd - 28th August 2015, the World Water Week was held in Stockholm, Sweden. From this event UNICEF quoted the following:

"In 2015, 663 million worldwide still do not have access to improved drinking water sources although the global target for safe drinking water was met in 2010 – well ahead of the Millennium Development Goal (MDG) to reduce by half the proportion of the population without safe drinking water and basic sanitation by 2015. Over 90 per cent of the world's population now has access to improved sources of drinking water. However, 2.4 billion still lack improved sanitation facilities and 946 million still practise open defecation. Access to safe water and sanitation is a human right, and water and sanitation are fundamental to human development and well-being, as well as critical to achieving other development objectives. The world has made significant progress in water and sanitation but challenges persist, and much remains to be done to ensure that everyone is reached. Inequalities in access to drinking water and sanitation exist, including between rural and urban areas and the rich and the poor, and also include the gender burden of water collection; and the persistent exclusion of the poor from water and sanitation services." [1]

In addition, water also plays an important role in the world economy, as it functions as a solvent for a wide variety of chemical industrial processes and reactions and facilitates industrial cooling and transportation.

In this regard when water is used in energy related processes, a milestone article published by Krasnovsky and Brin from 1962 has to be noted; WO_3 was used first for catalytic oxygen generation from water.[2] In addition, redox reaction of overall water splitting can be driven by UV light and light harvesting compounds, hence the interest in giving functions to semiconductor oxides as photoelectrodes extensively exists since the 70's when n-type rutile TiO_2 was arranged in a photo-electrochemical cell as an anode material and metallic Pt was used as the cathode material published in *Nature*.[3]

In addition, considering these arranged electrodes, several designs have been published so far for the easy gas separation when O_2 and H_2 are generated from water and pros and cons exist considering price, effectiveness and possibility to scale up such systems. In **Fig. 4.1a-b** photochemical cell design shows two types where the anode and cathode materials are arranged in either two (**Fig. 4.1a**) or one-compartment cells (**Fig. 4.1b**).[4] The former is separated by a frit to prevent diffusion of 1N H_2SO_4 electrolyte on the Pt side and the 1M NaOH on the TiO_2 side. The latter cell design uses either NaOH, $NaClO_4$ or H_2SO_4 as an aqueous electrolyte where photo-generated H_2 and O_2 are in the same compartment thus recombination to form water molecules is more likely.

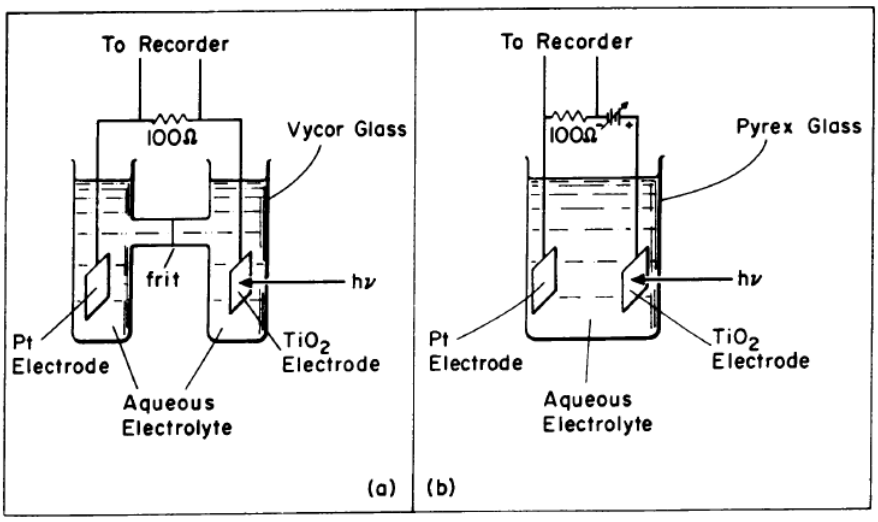

Fig. 4.1 Photochemical cells with (a) two electrode compartments (b) one electrode compartment used for the photo-electrolysis of water [4]

Following up on the *Nature* paper from 1972, the authors also noted that it might be possible that electrochemical photolysis of water may occur more effectively if a p-type semiconductor electrode is used instead of the platinum electrode.[3] Interestingly, this has been further investigated and confirmed since then, when researchers combined n-type anode material WO_3 catalyst for water oxidation and p-type cathode material $Pt/SrTi_{1-x}Rh_xO_3$ for water reduction upon visible light irradiation along with $Fe^{3+/}Fe^{2+}$ redox mediator.[5, 6] More examples for p- and n-heterojunctions are given in a review article published by K. Maeda in 2011.[7] These examples besides showing reasonable performance, have also shown a significant direction towards a cheap application as avoiding high-priced electrode connections by simply having the p- and n-type catalysts suspended in the same solution using an artificial Z-scheme.[7]

In the literature, we can also find an example for an as-called "twin reactor system" where gas separation is feasible in suspension when separation of the two compartments is realised through a proton exchange membrane (**Fig. 4.2**). Evidently,

this leads to a better water splitting performance when in this particular example solid state WO_3 and $Pt/SrTi_{1-x}Rh_xO_3$ were combined.[8]

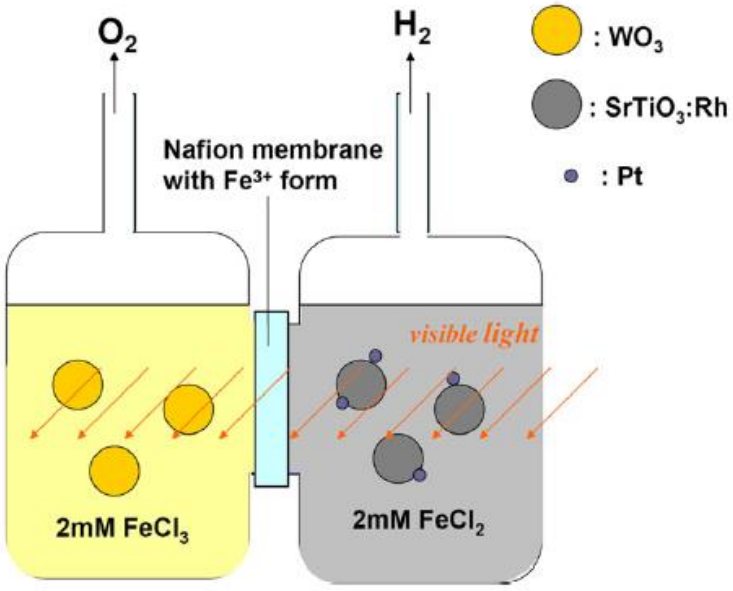

Fig. 4.2 Schematic diagram of a twin reactor system with a proton exchange membrane [8]

Evolved gases can be evacuated and securely stored afterwards for instance in carbon nanotubes (CNTs) or metal organic frameworks (MOFs).

Certainly, before designing any photochemical cells/photoreactors or artificial Z-scheme systems, both of the water splitting half reactions have to be understood by conducting test reactions especially when synthesising novel compounds. Therefore the initial step forward for testing new materials has to occur in the presence of electron/hole scavengers earlier described in **1.2.2.2** and perhaps with the need of co-catalysts explained in **1.2.2.6** sections.

In the investigation of visible light absorbing novel compound design, in the past few years, research groups in Japan were pioneers when examining single perovskites.[9-11] $SrTi_{1-x}Rh_xO_3$ and $BaTi_{1-x}Rh_xO_3$ compounds have been published as H_2 generating photocatalyst in the presence of aq. MeOH [9, 11], compounds were also successfully

arranged in Z-scheme photocatalysis [10, 11] and then were considered as p-type photocathode materials [6, 11]. However, other functionality of such oxides has not been investigated until now, such as photocatalytic degradation of contaminants (azo dyes (**Section 1.2.2.9**) and bacteria (**Section 1.2.2.10.**) in waste water supplies.

Several materials have been published for photocatalytic elimination of pollutants with photoinduced charge carriers. Photo-oxidation of Methyl-Orange (MO) by TiO_2 under UV [12] has been extensively studied via its kinetic reaction rate and products, in comparison with UV/H_2O_2 combined treatment.[13-15] Besides photo-oxidation of MO, Darwent et *al.* also elucidated the possible reaction mechanism for MO photo-reduction with TiO_2 [16] and for photo-oxidation over ZnO under UV light.[17]

In 1987, Mills and Williams proved that MO was photoreduced by CdS particles in the presence of EDTA solution, where CdS suspension was used to photosensitise the reduction of dye and the latter worked as an electron donor. Complete MO photobleacing was observed at pH = 4.4 at the wavelength greater than 320 nm within 15 min. The authors also showed that Cd^{2+} ions were liberated into solution as a function of irradiation time, indicating the subsequent corrosion of CdS in water. [18]

Several UV-activated compounds have been proven as successful photocatalysts in dye degradation, and many publications have reported visible light active materials for the same application (**Table 4.1**).

Table 4.1 Summary of visible light active photocatalysts in Methyl Orange degradation *

Visible Active Photocatalyst	MO Degradation	Lamp Type	Comments	Ref.
g-C_3N_4	5 h	250 W Xenon, $\lambda > 420$ nm	With CoO_4 co-catalyst degradation was achieved in 3 hour	19
carbon-QDs/Ag/Ag_3PO_4	10 min	150 W Xenon, $\lambda > 420$ nm + IR filter	Showed dark degradation of the dye resulting in 20 % disappearance. Unanswered whether it is due to thermal oxidation on Ag_3PO_4 particles or to dye adsorption	20
Pt/WO_3	4 h	300 W Xenon, $\lambda > 420$ nm + IR filter	Unloaded WO_3 itself results in no photo-oxidation	21
AgBr/WO_3	3 h	500 W Xenon, $\lambda > 420$ nm + IR filter	AgBr decomposes; Br_2 could thermally oxidise dye	22
N-doped anatase TiO_2	3 h	300 W Xenon, $\lambda > 420$ nm	Mixture of anatase and rutile exhibited 80 % decomposition after 5 hours	23
Fe-doped anatase TiO_2	6 h	Halogen-Tungsten lamp with visible light filter **	Only 72 %	24
Pt/$CaCu_3Ti_4O_{12}$	20 h	300 W Xenon, $\lambda > 420$ nm + IR filter	Only 60 %	25

*Given MO degradation times are not directly comparable due to various mass of catalysts in suspensions, light intensities, undesirable dark degradation processes

**No quote for wavelength

Among latter compounds, polymeric graphitic carbon nitrate (g-C_3N_4) completely degraded MO in 5 hours.[19, 26] Boron-modified g-C_3N_4 sample showed less effective performance as after 5 hours of visible light irradiation only 70% of MO was converted.[26] When Co_3O_4 co-catalyst was impregnated to a g-C_3N_4 sample, it showed an improved degradation rate by shortening the complete degradation to 3 hours.[19]

In 2012, H. Zhang and co-workers claimed the material stability and MO degradation efficiency over carbon quantum dots/Ag/Ag_3PO_4 system.[20] It has to be noted, this complex photocatalyst system showed dark degradation of the dye resulting in 20 % disappearance prior to visible light irradiation ($\lambda > 420$ nm), although question remains unanswered whether it is due to thermal oxidation on Ag_3PO_4 particles or dye adsorption on the photocatalyst. Upon light irradiation the rest of the organic dye was decomposed within 10 minutes. This excellent performance was confirmed in recyclability tests and after the 10th run of the dye decomposition experiment, the sample did not exhibit significant loss in photocatalytic performance, nor stability issues. On the other hand, pure Ag_3PO_4 sample showed complete MO photo-oxidation in 55 minutes, but after the 10th recyclability run, the sample exhibited Ag bleaching confirmed by PXRD.[20] The authors further claim that the insoluble and photo-induced electron transfer properties of carbon quantum dots (CQDs) can effectively protect the Ag_3PO_4 from dissolution and photo-corrosion. In addition, the existence of Ag accompanied by surface plasmon resonance (SPR) can further facilitate the utilization of sunlight and formation of electron/hole pairs.[20]

Of n-type semiconductor oxides, in 2011, U. A. Joshi et al. published Pt nanoparticles photo-deposited on to monoclinic WO_3 as an effective catalyst for complete MO photo-oxidaton within 4 hours under visible light ($\lambda > 420$ nm).[21] The authors also note that Pt in particular is essential in the enhancement of photo-induced decomposition

reaction as on the un-loaded catalyst no photo-oxidation of MO was observed.[21] The explanation is given as follows: Pt facilitates a multi-electron process with either two electrons or four electrons to reduce molecular oxygen while organic matter is oxidised by photogenerated holes.

$AgBr/WO_3$ composite was synthesised by a deposition-precipitation method on WO_3 substrate using $AgNO_3$, NaBr in ammonium hydroxide solution.[22] A sample with 0.30 Ag/W molar ratio was able to effectively degrade MO within 3 hours using visible light as the light source. Not surprisingly, in recyclability tests some of the AgBr itself was decomposed and was converted to metallic silver resulting in restriction of the degradation rate. It has to be emphasized that Br_2 is known to thermally oxidise MO, therefore the formation of Br_2 may be involved in "photo-oxidation" defined by the authors. Hence, further experiments should be carried out to improve the stability of $AgBr/WO_3$.[22]

Well-known N-doped TiO_2, containing only the anatase phase performed complete MO degradation under 3 hours of visible light exposure.[23] Interestingly, doped compound containing the mixture of anatase and rutile phases exhibited 80% decomposition of MO after irradiation for 5 hours with a visible light source.[23]

0.2% Fe-doped anatase TiO_2 exhibited visible light photoactivity by converting 72% of the MO dye within 6 hours.[24] Chemical stability of $Ti_{1-x}Fe_xO_2$ is expected but a direct recyclability test is not performed in this publication.[24]

Another titanate compound, $Pt/CaCu_3Ti_4O_{12}$ synthesised in the Rosseinsky group, showed 60 % of MO conversion after 20 hours visible light irradiation. Although MO dye decomposition reaction rate is slow, photo-oxidised products are entirely analysed by Mass Spectrometry.[25]

A third but equally relevant application, besides water splitting and waste water purification, is water disinfection. For water sterilisation with semiconductor oxides, *E. coli*, Gram-negative bacteria have been studied as one model organism (**Section 2.10.4**).

As reported earlier, by using platinised rutile TiO_2, photo-oxidation of various substrates can be realised such as water [27], acetic acid [28] and methyl-orange [15]. In 1985, T. Matsunaga and co-workers reported the first revolutionising concept of photo-electrochemically killing various bacteria (*S. cerevisiae*, *E. coli*, *L. acidophilus*) with Pt-loaded TiO_2 powder, where the synergistic effect of UV light and Pt/TiO_2 was reported.[29] Since then, this pioneering research opened up a new field for antibacterial sterilisation by substituting the typical heat and UV irradiation methods to some extent. In this early study, the authors proposed the possible application of semiconductor powders in the direct oxidation of Coenzyme-A (CoA) in microbial cells and as a result, the inhibition of respiratory activity and loss of viability occured.[29] Authors also claimed that pH of solution did not change during deactivation, suggesting that any bactericidal effects of toxic substances such as H_2O_2 and free radicals formed by electrolysis were not possible.

The development of visible light excited compounds is vital, to extend the usability of photocatalysis to bactericidal activity (**Table 4.2**).

Table 4.2 Summary of visible light active photocatalysts in *E. coli* deactivation

Visible Active Photocatalyst	Lamp Type	Comments	Ref.
N-doped TiO_2	60 W, Classictone incandescent lamp*	It is not clear in the publication whether the photocatalyst was anatase or rutile ***	30
PdO/N-doped TiO_2	Metal halogen desk lamp with glass filter $\lambda > 400$ nm	Post-illumination catalytic "memory" on metallic Pd ***	31
CdS-coated TiO_2	Xenon lamp*	Small applied external potential; CdS could produce toxic by-products ***	32
$Ag/AgBr/WO_3$	300 W Xenon, $\lambda > 400$ nm + ice/water cooling	Nanoparticulate Ag is reported as an antimicrobial agent ***	33, 34
$BiVO_4$	300 W Xenon, $\lambda > 400$ nm	TEM confirms cell damage	35
ZnS	15 W fluorescent tube + $NaNO_3$ liquid filter	Effect of photo-generated electrons; TEM confirms cell damage	36
Pd/N-doped TiO_2	Visible light source**	Fluorescent Microscopy, SEM and TEM visualisation confirm cell damage	37

* No quote for wavelength

** No quote for wavelength and for light source type

***No microscopic visualisation

M. S. Wong et *al.* demonstrated that nitrogen-doped TiO_2 substrates have superior visible-light-induced bactericidal activity on *E. coli* compared to pure TiO_2 and carbon-doped TiO_2.[30] Although, these authors did not make that clear whether anatase or rutile phase was used in deactivation.

More interestingly, Q. Li and co-workers reported accelerated photocatalytic *E. coli* disinfection activity when PdO/TiON fibers were tested under visible light due to PdO-promoted charge carrier separation. The authors also observed a post-illumination catalytic "memory" which could be attributed to the optoelectronic coupling effect between reduced metallic Pd nanoparticles and TiON semiconductor.[31]

S. C. Hayden et *al.* reported highly efficient CdS-coated TiO_2 nanotube arrays in disinfection of *E. coli*.[32] CdS nanocrystals were used to increase the sensitivity of TiO_2 nanotubes towards visible light. Although in this communication a small applied potential was also used in order to allow record short time bacteria destruction. It can be questioned, whether unstable CdS produces toxic breakdown products, such as Cd^{2+}, S^{2-} and SO_3^{2-}, as this is not discussed in the paper.

In 2014, Zhang et *al.* investigated perovskite $SrTi_{1-x}Fe_xO_3$ for *E. coli* inactivation under visible light at 0.1 w/V% suspension concentration. Under reaction conditions used, a significant amount (~ 49 ppm) of Sr^{2+} was detected in the supernatant.[38] This high concentration of Sr^{2+} showed equally significant harmful effect under both visible light and dark conditions resulting in the complete but toxic inactivation of studied *E. coli* Gram negative bacteria.

$Ag/AgBr/WO_3 \bullet H_2O$ composite system showed effective visible light driven photo-destruction ability for *E. coli* and photo-oxidation of Methyl Orange.[33] In addition, metallic silver resulted in a surface plasmon resonance effect with promoted photocatalytic performance. In addition, nanoparticulate Ag is widely used and highly effective as an antimicrobial agent [34], therefore it is not surprising that disinfection occurred.

The above listed papers do lack the direct microscopic evidence of inactivated *E. coli* bacteria therefore weakening the impact of the published reports.

Visible light driven $BiVO_4$ nanotubes were also successfully used for inactivation of *E. coli* K-12.[35] The mechanism was also investigated and was found that photo-induced h^+ and reactive oxidative species derived from h^+, such as $\bullet OH_{ads}$, H_2O_2, and $\bullet HO_2/\bullet O_2^-$ were the major radicals in inactivating bacteria. Finding was also supported by TEM microscopy for cell damage.[35]

Another non-oxide sulphide mineral, the naturally occurring ZnS sphalerite was used cost-effectively for photocatalytic bacterial disinfection upon visible light irradiation on *E. coli* K-12 strain.[36] Interestingly, authors claim that •OH is not the primary attacking agent which caused cell damage but photo-generated e^- or as H_2O_2 that has a much longer life time and can diffuse through the cell membrane. As a result, in TEM images the leakage of the intracellular components is observed after treatment.[36]

P. Wu et a. showed Fluorescent Microscopy, SEM and TEM evidence for *E. coli* disinfection on palladium-modified N-doped TiO_2 under visible light. [37]

In fact, not many research groups have published microscopic visualisation evidence for bacteria damage. Although to exclude the toxicity effect under dark condition and to get a closer insight of the degradation of cellular membrane via oxygen free radicals, it is vital.

In short summary of **Introduction** to **Chapter 4**, a limited number of stable, visible active compounds have been reported so far (**Table 4.1 and Table 4.2**). Of semiconductor oxides, nitrogen-doped titania in particular have demonstrated activity under visible light in all three functionalities (H_2 generation, dye decomposition and antibacterial properties).[23, 30, 39, 40]

In this chapter, HT synthesised high surface area titanates were studied in water reduction reaction under visible light and the application of $BaTi_{1-x}Rh_xO_3$ compounds was demonstrated in water splitting half reaction with various co-catalyst loading.

In addition, the functionality of $SrTi_{1-x}Rh_xO_3$ beyond water reduction has been extended to the effective treatment of dyes and bacteria in water. Hydrothermal synthesis was used without high temperature calcination, to produce high surface area nanostructured, cubic $SrTi_{1-x}Rh_xO_3$. An optimum level of Rh at x = 0.05 was identified and the role of Rh in the photocatalysis processes was investigated. Moreover avoiding the high temperature calcination prevented oxidation of Rh^{3+} to Rh^{4+} enhancing photoactivity. A triple function of this particular compound was demonstrated using photogenerated electrons in a photoreduction reaction (H_2 generation) and photoexcited holes in photooxidation reactions (*e.g.* dye oxidation and bacteria killing with •OH radicals).

4.2. Application

4.2.1. Discussion 1 – Photocatalytic application of $BaTi_{1-x}Rh_xO_3$

4.2.1.1. Addition of co-catalyst to $BaTi_{1-x}Rh_xO_3$

In order to investigate the influence of co-catalyst addition, rhodium barium titanates were loaded with various co-catalysts and thereafter tested in photocatalytic reactions.

For Ru metal, $BaTi_{0.99}Rh_{0.01}O_3$ was loaded with 1 wt % Ru by photodeposition. 0.4 g of catalyst and 0.0082 g $RuCl_3 \bullet x\ H_2O$ (Sigma Aldrich) were dissolved in 400 mL 10 % aq. MeOH solution. The suspension was then purged with nitrogen under stirring for 30 minutes to remove all oxygen from the solution. Following this, the solution was placed under a UV lamp for 5 hours. The photodeposited samples were centrifuged and dried at 60ºC in an electric oven. According to M. I. Litter there might be a concern that the photoreduction of $RuCl_3 \bullet x\ H_2O$ into Ru metal is not possible and perhaps RuO_2 is formed instead. [41]

For Pt metal, $BaTi_{0.99}Rh_{0.01}O_3$ was loaded with 1 wt % Pt by photodeposition. 0.4 g of catalyst and 0.1050 g H_2PtCl_6 (8wt % Pt – Sigma Aldrich) were dissolved in 400 mL 10 % aq. MeOH solution. The suspension was then purged with nitrogen under stirring for 30 minutes to remove all oxygen from the solution. Following this, the solution was placed under a UV lamp for 5 hours. The photodeposited samples were centrifuged and dried at 60ºC in an electric oven. [42]

1 wt % of Au was deposited from aqueous solution of $HAuCl_4$ onto $BaTi_{0.99}Rh_{0.01}O_3$ surface. 0.0100 g $HAuCl_4 \bullet 3\ H_2O$ (Sigma Aldrich) was dissolved in 100 ml Milli-Q water. The pH of the solution was adjusted to 5.7 by 0.2 M NaOH. After the pH was

stable, the Chloroauric Acid solution was slowly heated up to 70 °C. While both conditions (pH and temperature) were maintained, the precipitation-deposition procedure was started by adding 0.5 g $BaTi_{0.99}Rh_{0.01}O_3$ to the aq. $HAuCl_4$ solution under stirring. The suspension was further stirred for 2 hours at 70 °C. Finally the resulting suspension was left to cool down to room temperature and stirred overnight. The $Au/BaTi_{0.99}Rh_{0.01}O_3$ sample was centrifuged, washed with Milli-Q water and dried at 60 °C under air for 4 hours in an electric oven. The dried sample was further calcined at 300 °C in an electric furnace under static air for 3 hr, with 5ºC/min heating and cooling rates. [43]

For Ni metal, $BaTi_{0.99}Rh_{0.01}O_3$ was loaded with 1 wt % Ni by photodeposition. 0.4 g of catalyst and 0.0198 g $Ni(NO_3)_2 \cdot 6\ H_2O$ (Sigma Aldrich) were dissolved in 400 mL 10 % aq. MeOH solution. The suspension was then purged with nitrogen under stirring for 30 minutes to remove all oxygen from the solution. Following this, the solution was placed under a UV lamp for 5 hours. The photodeposited samples were centrifuged and dried at 60ºC in an electric oven.

For NiO loading, the impregnation method was used. Both $BaTi_{0.99}Rh_{0.01}O_3$ and $BaTi_{0.95}Rh_{0.05}O_3$ were loaded separately with 1 wt % NiO (the calculation was made for 1 wt % Ni metal content). 0.0248 g $Ni(NO_3)_2 \cdot 6\ H_2O$ (Sigma Aldrich) was dissolved in 4 mL MeOH solution. 0.5 g of catalyst was added to this solution and carefully mixed with a mortar and pestle. At 110ºC, atmospheric pressure and vigorous stirring the MeOH was evaporated and the powder was annealed in air at either 200ºC or 300ºC or 400ºC for 3 hr, with 5ºC/min heating and cooling rates. [44]

4.2.1.2. H_2 evolution Under Visible Light

Phase pure $BaTi_{1-x}Rh_xO_3$ samples synthesised hydrothermally at 150 ºC for 12 hours with x = 0.01 and x = 0.05 Rh content were tested in H_2 generation reaction upon visible light irradiation ($\lambda > 420$ nm) using EDTA solution as a sacrificial reagent and the results are shown in **Table 4.3** and **Table 4.4**). First, sample with x = 0.01 was analysed without and with various co-catalyst loading (**Table 4.3**). Details for additional metals (Ru^0, Pt^0, Au^0 and Ni^0) or metal-oxide (NiO_x) loading onto the surface of the catalyst are given in **Chapter 4.2.1.1**.

Table 4.3 H_2 generation of $BaTi_{0.99}Rh_{0.01}O_3$ samples synthesised at 150 °C for 12 hours and thereafter unloaded and loaded with 1 wt % various co-catalysts; Reaction conditions: Visible light (300 W Xenon lamp ($\lambda > 420$ nm)); $m_{catalyst}$ = 68 mg; Sacrificial reagent: Calcium Disodium EDTA solution, c = 0.02 M, V = 34 ml, pH = 6 adjusted with 1M NaOH prior test

Catalyst	Co-catalyst	Co-catalyst loading / Treatment	Evolved H_2 (µmol/g/h)
$BaTi_{0.99}Rh_{0.01}O_3$	-	-	0.69
	Ru^0	Photodeposition	trace
	Pt^0	Photodeposition	1.30
	Au^0	Precipitation & Deposition + 300 ºC in air	2.82
	Ni^0	Photodeposition	0.73
	NiO_x	Impregnation + 200 ºC in air	0.21
	NiO_x	Impregnation + 300 ºC in air	2.91

The as-synthesised un-loaded compound produced ~0.7 µmol/g/h H_2, similar to the Ni^0 photodeposited sample, which did not extensively facilitate H_2 production. Nevertheless, this performance was further improved, when the compound was loaded with metallic Pt and Au particles. For the latter, most likely the SPR gold effect (**Fig.**

4.3) was predominant [43] resulting in metallic Au nanoparticles acting as primary photo-induced electron trap-sites and leading to the phenomena that these trapped electrons might have migrated to the CB of $BaTi_{0.99}Rh_{0.01}O_3$ hence reducing water molecules and oxidation reaction of EDTA can occur on Au NPs. [43] According to the paper published by Silva et *al.*, the estimated average gold particle size synthesised at pH ~ 6 and then calcined in static air, is in the range of 3 - 4 nm. [43]

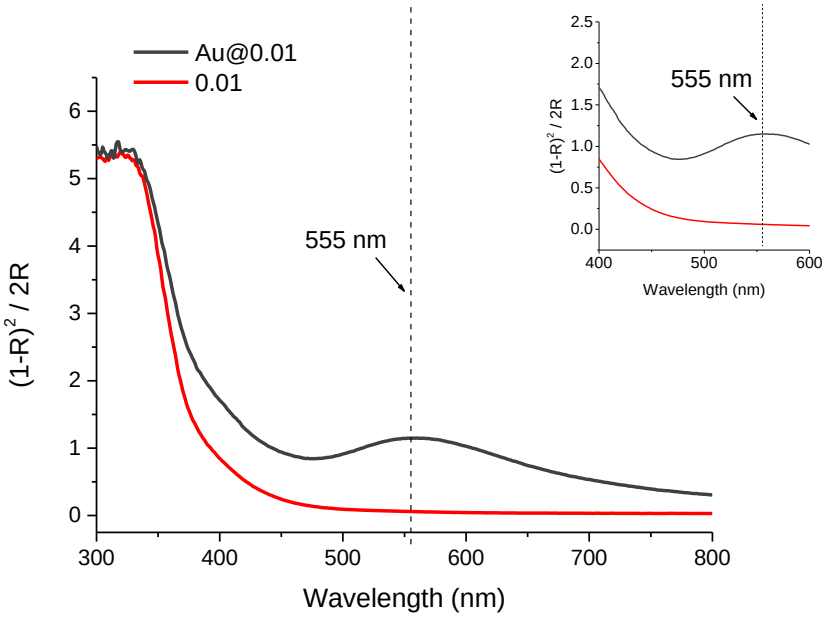

Fig. 4.3 Kubelka-Munk function of as-synthesised $Au/BaTi_{0.99}Rh_{0.01}O_3$ and $BaTi_{0.99}Rh_{0.01}O_3$. Absorbance peak at 555 nm indicates the surface plasmon resonance associated with surface loaded gold nanoparticles

Interestingly, in this particular sample Ru^0 exhibited a detrimental effect of a complete lack of H_2 evolution efficiency. Loaded NiO_x particles when calcined at 300 ºC showed the highest performance of tested co-catalysts.

Barium titanate single perovskite compound containing x = 0.05 Rh showed a slightly improved H_2 evolution performance compared to the x = 0.01 sample when the unloaded sample was tested (~1.1 µmol/g/h H_2 – see results in **Table 4.3** and **Table**

4.4 as comparison). In order to investigate if the heat treatment or in fact the NiO_x loading helped to facilitate water reduction, samples were either calcined at 400 °C in air or first impregnated with $Ni(NO_3)_2 \bullet 6\ H_2O$ salt then calcined at 400 ºC in air. From the measured data it is evident that NiO_x plays a role in enhanced H_2 generation activity and heat treatment largely reduces the activity.

Table 4.4 H_2 generation of $BaTi_{0.95}Rh_{0.05}O_3$ samples synthesised at 150 °C for 12 hours and thereafter unloaded and loaded with 1 wt % NiO co-catalyst; Reaction conditions: Visible light (300 W Xenon lamp (λ > 420 nm)); $m_{catalyst}$ = 68 mg; Sacrificial reagent: Calcium Disodium EDTA solution, c = 0.02 M, V = 34 ml, pH = 6 adjusted with 1M NaOH prior test

Catalyst	Co-catalyst	Co-catalyst loading / Treatment	Evolved H_2 (µmol/g/h)
$BaTi_{0.95}Rh_{0.05}O_3$	-		1.08
	-	400 ºC in air	0.16
	NiO_x	Impregnation + 400 ºC in air	2.75

It is also interesting that K. Maeda did not conduct any work on various co-catalyst loading when in 2014, he published this compound first for water reduction under visible light [11], but synthesised the material with conventional solid-state and sol-gel methods and loaded them only with photodeposited Pt. In principal, in his paper, the enhanced photo-response and photo-activity was attributed to the increased BET surface area when rhodium doped barium titanates were synthesised with sol-gel method (3.0 – 4.6 m^2/g) in comparison with solid state method (2.0 m^2/g).[11] It is possible that our synthesis method with a two-fold increased surface area (6.8 – 7.5 m^2/g) compound might further improve water reduction on hydrothermally synthesised samples compered to Maeda's synthesis methods.

4.2.1.3. Methyl Orange Degradation

Barium titanate doped with x = 0.01 Rh, synthesised at 150 ºC for 12 hours, was tested in MO degradation upon visible light (**Fig. 4.4**). Results indicate that sample in particular shows very slow photo-oxidation rate. After 120 min only 3% of the organic matter was converted. As a result this material was not used for antibacterial testing.

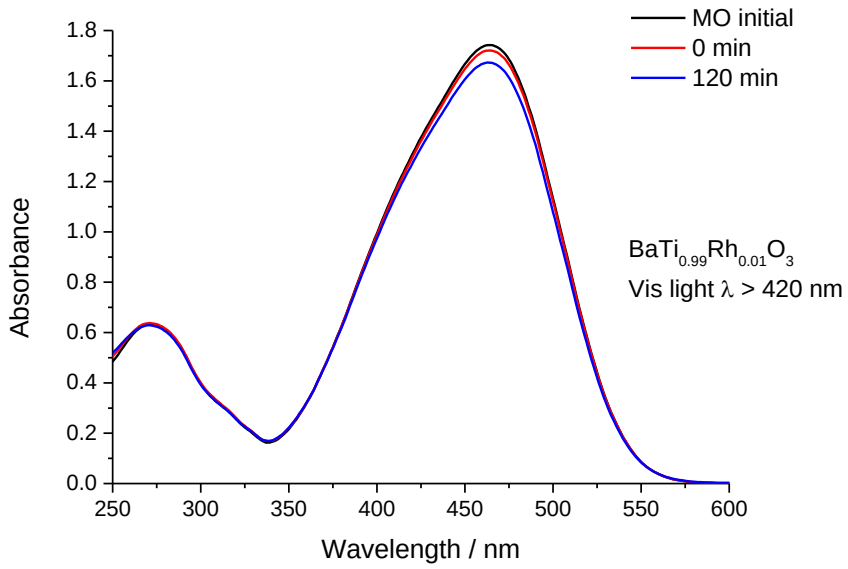

Fig. 4.4 MO degradation with a sample of $BaTi_{0.99}Rh_{0.01}O_3$ under visible light (λ > 420 nm) reaction (*MO initial* denotes the dye UV-Vis spectra prior to catalyst added; *0 min* is the absorbance spectra of dye after overnight stirring in dark with catalyst added; *120 min* are the UV/Vis spectra of the dye during destruction.

4.2.2. Discussion 2 – Photocatalytic application of $SrTi_{1-x}Rh_xO_3$

4.2.2.1. Addition of co-catalyst to $SrTi_{1-x}Rh_xO_3$

For Pt metal loading, photodeposition was used. $SrTi_{0.95}Rh_{0.05}O_3$ was loaded with 0.5 wt% Pt. 0.5 g of catalyst and 0.066 g H_2PtCl_6 (8 wt % Pt – Sigma Aldrich) were dissolved in 400 mL 10 % aq. MeOH solution. The suspension was then purged with nitrogen under stirring for 30 minutes to remove all oxygen from the solution. Following this, the solution was placed under a UV lamp for 5 hours. The photodeposited samples were centrifuged and dried at 60 °C in an electric oven.[42]

For Ru metal loading, photodeposition was used. $SrTi_{0.95}Rh_{0.05}O_3$ was loaded with 0.5 wt% Ru. 0.5 g of catalyst and 0.0051 g $RuCl_3$ (Sigma Aldrich) were dissolved in 400 mL 10 % aq. MeOH solution. The suspension was then purged with nitrogen under stirring for 30 minutes to remove all oxygen from the solution. Following this, the solution was placed under a UV lamp for 5 hours. The photodeposited samples were centrifuged and dried at 60 °C in an electric oven.

4.2.2.2. H_2 evolution Under Visible Light

The hydrothermally made samples were tested for H_2 evolution under visible light (λ > 420 nm), with no additional co-catalyst, in aqueous methanol as sacrificial electron donor (**Fig. 4.5a-b**). For the sample where x = 0.05, hydrogen was detected after 1 hour of irradiation. This induction period has been attributed to the reduction of Rh^{4+} to Rh^{3+} prior to reduction of water, or to saturation of H_2 in water before the gas can be detected.[5] As the material in this study contains predominantly Rh^{3+}, the induction period can be attributed to the initial saturation of the water by H_2 before detection in

the gas phase is possible. The highest rate of H_2 production in the current study was found for the material where x = 0.05. When x > 0.05 the UV-Vis spectra (**Fig. 3.17b**) and XPS results (**Fig. 3.14a**) show the presence of Rh^{4+} surface species which inhibit the photocatalysis reaction due to the formation of inter-band d-states that act as charge-carrier recombination centres.[45]

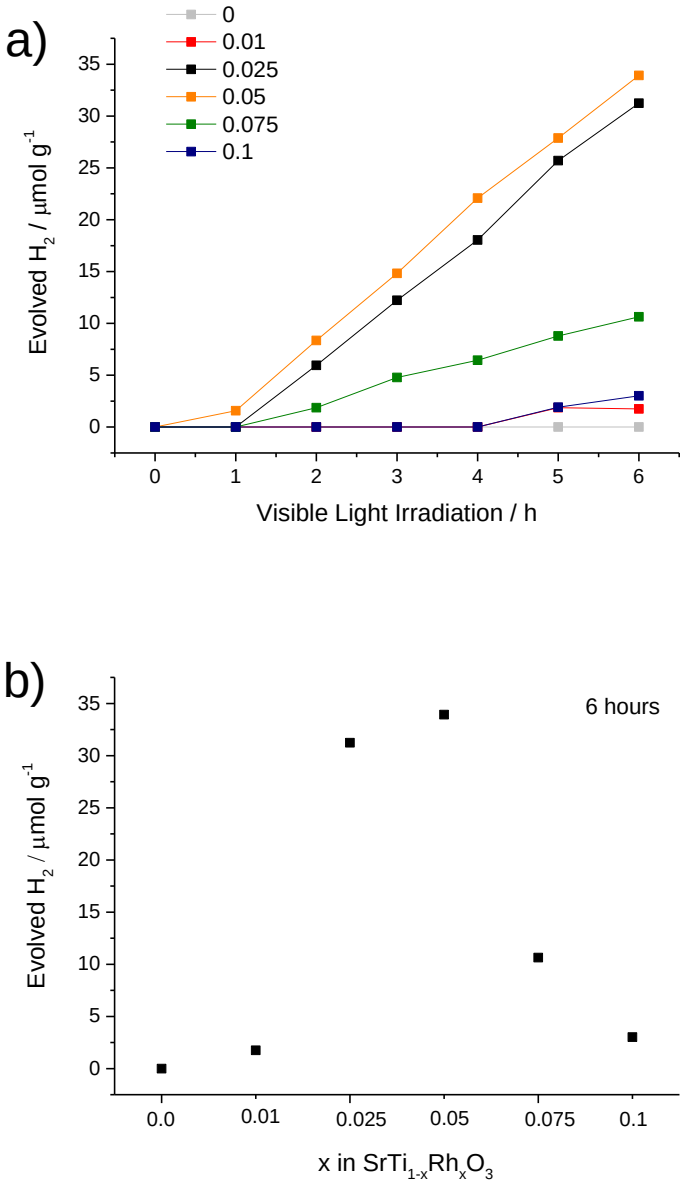

Fig. 4.5 (a) H_2 evolution reaction under visible light (λ > 420 nm) reaction of $SrTi_{1-x}Rh_xO_3$ (x = 0; 0.01; 0.025; 0.05; 0.075; 0.1) samples in a time scale of 6 hours; (b) Trend of H_2 evolution in the sixth hours using the as-made catalysts

To study the changes in Rh surface species, the sample with x = 0.05 was centrifuged after the H_2 evolution reaction and dried in an oven at 60 °C in static air. DRS (**Fig. 4.6**) and XPS (**Fig. 4.7a-b**) of the samples were compared before and after the photoreaction. The Kubelka-Munk function (**Fig. 4.6**) shows no significant difference between 300 and 500 nm, however the sample after photocatalytic testing shows an increase in the absorbance at $\lambda > 500$ nm. The colour of the sample also changed from yellow to greyish yellow.[46]

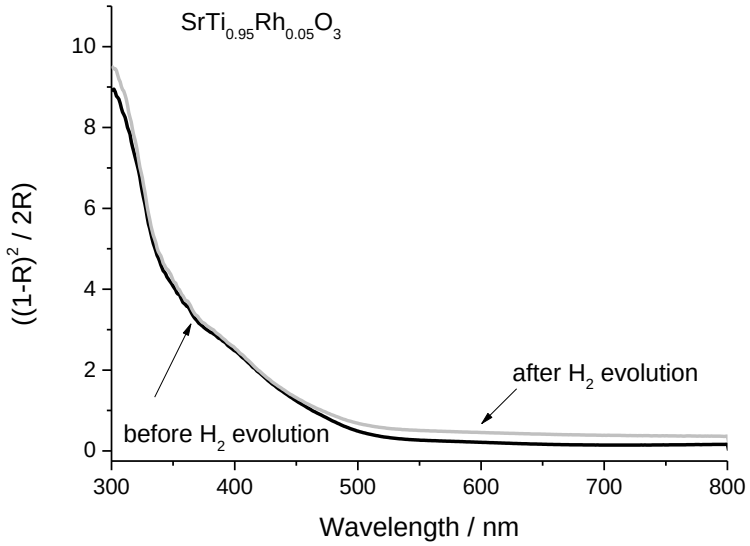

Fig. 4.6 Kubelka-Munk function of $SrTi_{0.95}Rh_{0.05}O_3$ samples before and after H_2 evolution reaction

For further investigation of Rh surface species after H_2 generation, the Rh 3d XPS was compared to the initial Rh states (**Fig 4.7a-b**). The sample after the photocatalytic reaction displays an extra shoulder with binding energy 307.6 eV matching that of the Rh metal standard [47] (**Fig. 2.4, Table 2.2, Table 4.5, Table 4.6**), indicating *in situ* surface photoreduction of rhodium states during the photocatalytic reaction. [46]

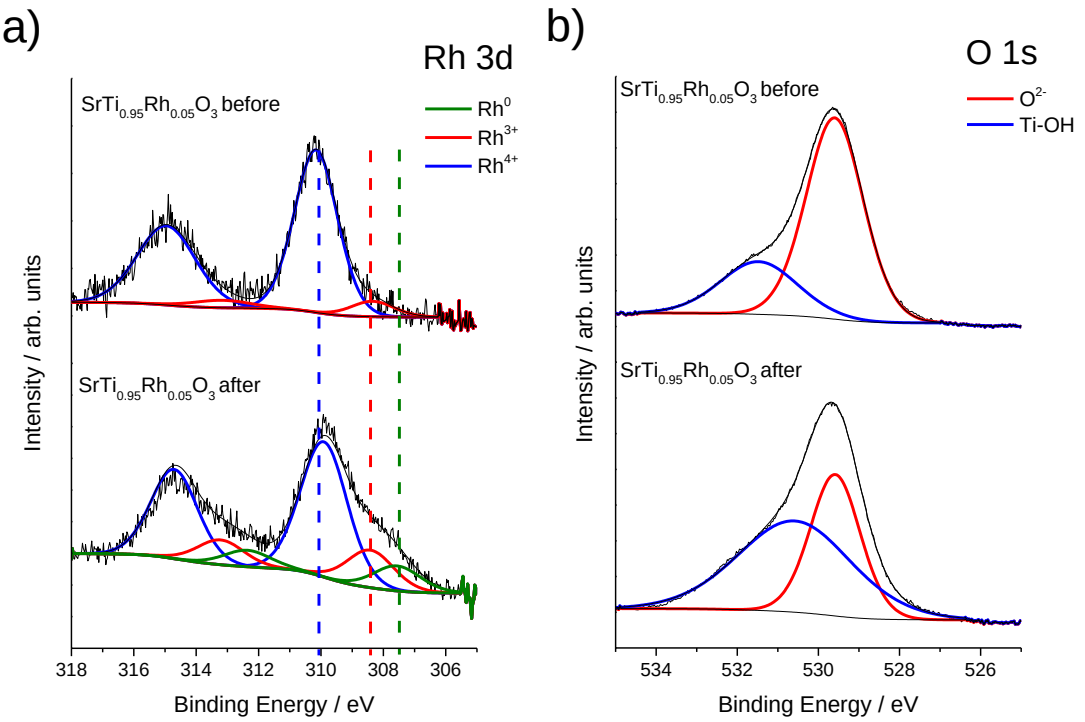

Fig. 4.7 (a) Fitted Rh 3d XPS spectrum of $SrTi_{0.95}Rh_{0.05}O_3$ before and after H_2 evolution reaction of the samples (Black line is the original data, the green line is the fit to the Rh^0, red line is the Rh^{3+} fit and blue line is the Rh^{4+} fit, Dotted lines are the fit to the rhodium standards, Rh metal and Rh_2O_3 (b) Fitted O 1s XPS spectrum of $SrTi_{0.95}Rh_{0.05}O_3$ before and after H_2 evolution reaction of the samples (Black line denotes the experimental data which is the superposition of O^{2-} species as red line and the -OH components as blue curve)

Tab. 4.5 XPS Fitting parameters of Rh^{4+} and Rh^{3+} 3d 3/2 and 5/2 spin orbit peaks for hydrothermally synthesised $SrTi_{1-x}Rh_xO_3$ sample with x = 0.05 content before H_2 evolution test reaction

	$SrTi_{0.95}Rh_{0.05}O_3$ **before reaction**					
	Rh^{4+} 3d 3/2	**Rh^{4+} 3d 5/2**	**Rh^{3+} 3d 3/2**	**Rh^{3+} 3d 5/2**	**Rh^0 3d 3/2**	**Rh^0 3d 5/2**
B. E. / eV	314.96	310.16	313.15	308.35	-	-
Area	398.6	604.0	37.7	57.1	-	-
FWHM	2.20	1.63	2.20	1.63	-	-

Tab. 4.6 XPS Fitting parameters of Rh^{4+} and Rh^{3+} 3d 3/2 and 5/2 spin orbit peaks for hydrothermally synthesised $SrTi_{1-x}Rh_xO_3$ sample with x = 0.05 content after H_2 evolution test reaction under visible light ($\lambda > 420$ nm)

	$SrTi_{0.95}Rh_{0.05}O_3$ **after reaction**					
	Rh^{4+} 3d 3/2	**Rh^{4+} 3d 5/2**	**Rh^{3+} 3d 3/2**	**Rh^{3+} 3d 5/2**	**Rh^0 3d 3/2**	**Rh^0 3d 5/2**
B. E. / eV	314.71	309.91	313.22	308.42	312.36	307.55
Area	540.0	818.2	150.0	227.2	99.7	151.1
FWHM	2.32	1.77	2.32	1.77	2.32	1.77

Photodeposited Rh metal and metal oxide nanoparticles have been shown to promote photocatalytic hydrogen production.[48] This metallic Rh may act as a co-catalyst in the hydrogen evolution reaction. Investigations are under way to determine if the Rh^0 is formed due to the photocatalytic reaction *i.e.* by the hydrogen, generated on the surface of the particles, or it is necessary for the hydrogen production and the cause of the initiation period observed.

The co-catalyst loading was also investigated on the x = 0.05 Rh sample when Ru^0 and Pt^0 PGMs were first photodeposited from their salts (**Chapter 4.2.2.1**) and thereafter

tested (**Fig. 4.8**). Samples with 0.5 wt% Pt^0 and 0.5 wt% Ru^0 seemed to have antagonistic effect with Rh^0 demonstrating less activity than the unloaded $SrTi_{0.95}Rh_{0.05}O_3$ compound. Although the sample with Pt loaded co-catalyst produced more H_2 in the first hour than the unloaded one. [46]

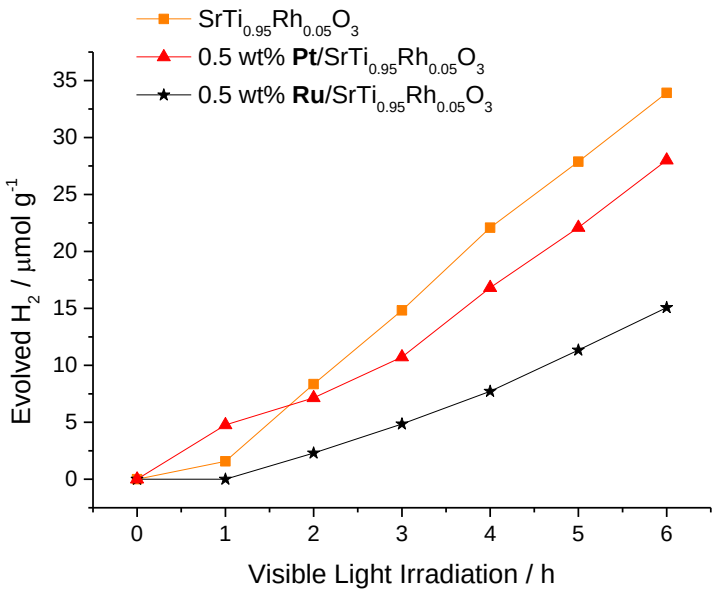

Fig. 4.8 H_2 evolution reaction under visible light (λ > 420 nm) reaction of $SrTi_{0.95}Rh_{0.05}O_3$ (orange line), 0.5 wt% Pt/$SrTi_{0.95}Rh_{0.05}O_3$ (red line) and 0.5 wt% Ru/$SrTi_{0.95}Rh_{0.05}O_3$ (black line) samples in a time scale of 6 hours

4.2.2.3. Methyl Orange Degradation and E. coli Inactivation Under Visible Light

Photocatalytic dye degaradation

The efficiency of as-made samples towards azo-dye degradation was tested. **Fig. 4.9a** and **b** show the photocatalytic activity in MO degradation reaction under visible light (λ > 420 nm). MO has been widely used as a probe for the photocatalytic oxidation of

dyes using UV light absorbing materials such as TiO_2. This is one of the few examples where it has been possible to photo-oxidise MO with visible light and the results show that $SrTi_{1-x}Rh_xO_3$ is remarkably active as a visible light photocatalyst leading to complete destruction of the dye.[46]

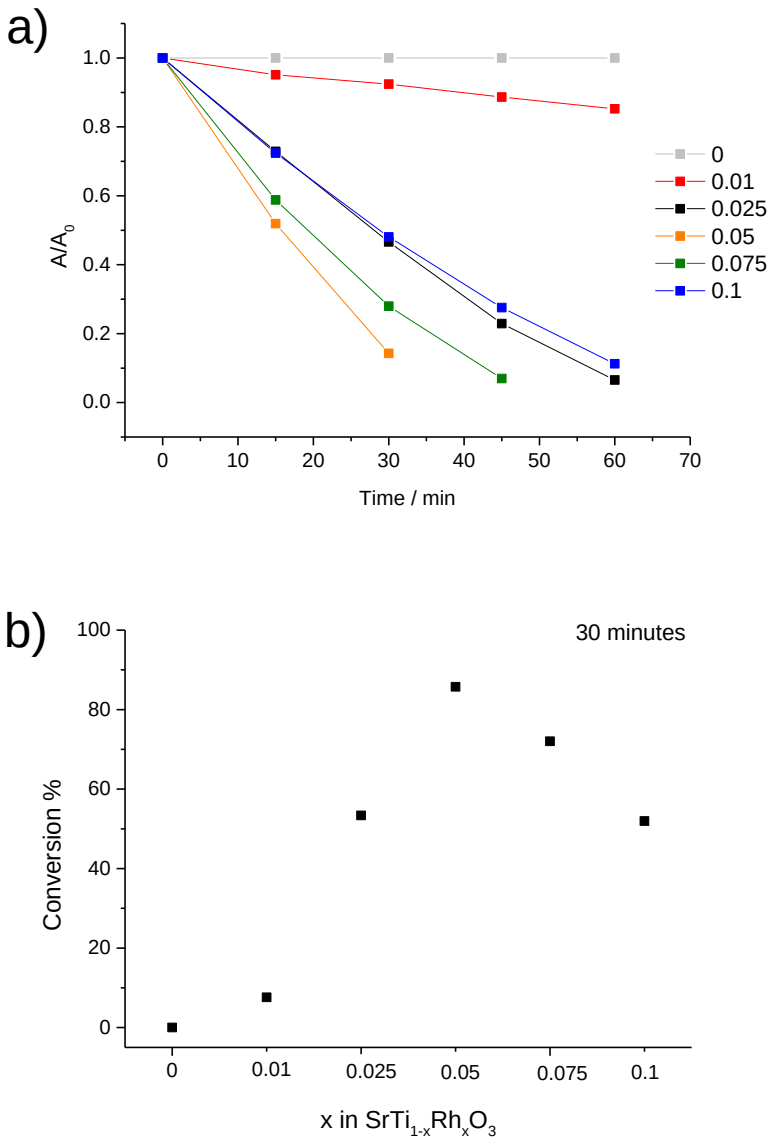

Fig. 4.9 (a) MO degradation under visible light reaction of $SrTi_{1-x}Rh_xO_3$ (x = 0; 0.01; 0.025; 0.05; 0.075; 0.1) samples in a time scale of 1 hour; (b) Trend of MO conversion after 30 minutes using the as-made catalysts

Four of the samples degraded 90 % of the MO in less than 1 h. The azo-dye degradation by $SrTi_{1-x}Rh_xO_3$ samples follows first order reaction kinetics. The $SrTi_{0.95}Rh_{0.05}O_3$ sample showed the best performance in photocatalytic activity. Within 30 minutes 86 % of MO was destroyed with a reaction rate 0.0649 min^{-1} (**Fig. 4.10**).

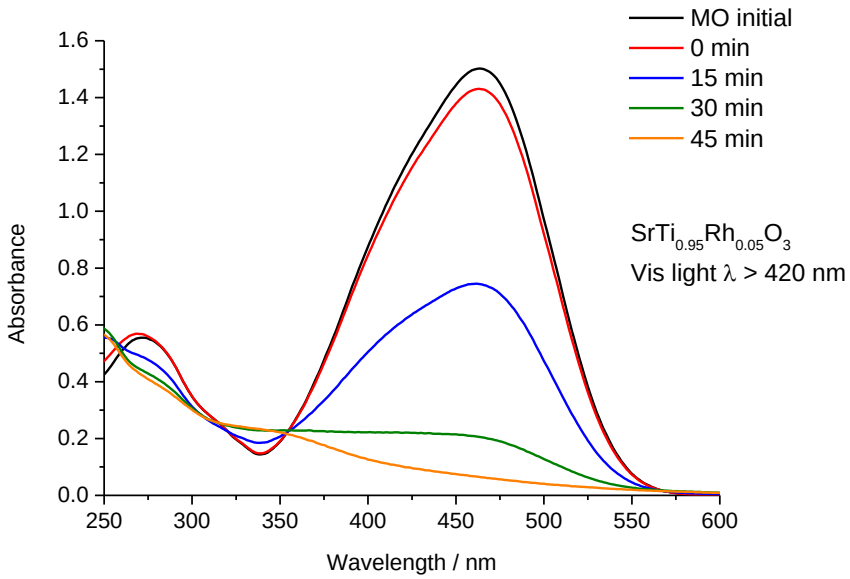

Fig. 4.10 MO degradation with a sample of $SrTi_{0.95}Rh_{0.05}O_3$ under visible light ($\lambda > 420$ nm) reaction (*MO initial* denotes the dye UV-Vis spectra prior to catalyst added; *0 min* is the absorbance spectra of dye after overnight stirring in dark with catalyst added; *15, 30, 45 min* are the UV/Vis spectra of the dye during destruction.

This can be attributed to the high surface area of the nanostructured acetic acid washed $SrTi_{1-x}Rh_xO_3$ sample and the Rh^{3+} oxidation state of species up to x = 0.05. Increasing the doping level x > 0.05 introduces Rh^{4+} which can act as a recombination site for the photogenerated charge carriers therefore suppresses the kinetic reaction rate. The parent compound showed no activity in MO degradation upon visible light exposure in a control experiment (**Fig. 4.11**).

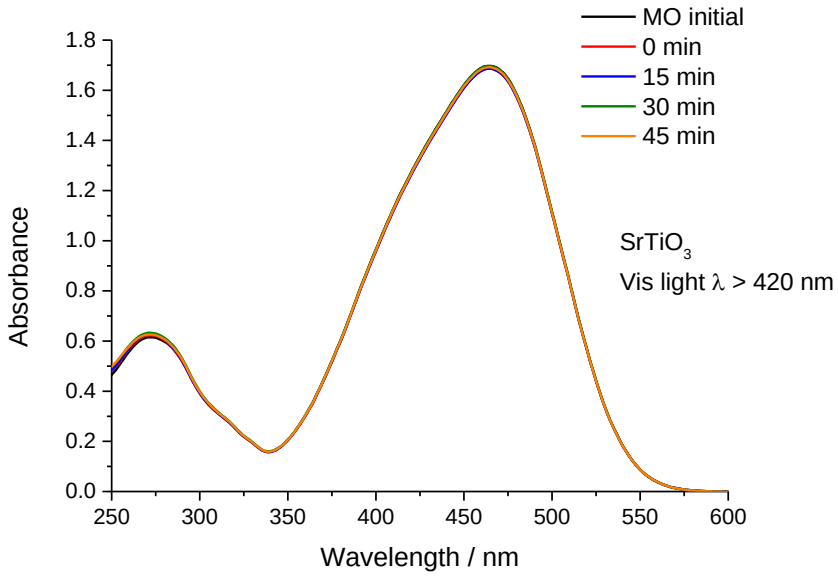

Fig. 4.11 MO degradation with a sample of $SrTiO_3$ under visible light (λ > 420 nm) reaction (*MO initial* denotes the dye UV-Vis spectra prior to catalyst added; *0 min* is the absorbance spectra of dye after overnight stirring in dark with catalyst added; *15, 30, 45 min* are the UV/Vis spectra of the dye during photoreaction

Photocatalytic treatment of bacteria

The as-synthesised perovskite compound which showed the highest activity in MO destruction was tested for the photocatalytic deactivation of *E. coli*. The suspension concentration was optimised to avoid any toxicity effect due to the photocatalyst. **Fig. 4.12a, b** and **c** show the absolute density of *E. coli* population in PBS suspension with $SrTi_{0.95}Rh_{0.05}O_3$ after sampling and plating them on LB agar under control light (**CL** – visible light exposure, no photocatalyst), dark (**D** – no light exposure, with photocatalyst) and light (**L** – visible light exposure, with photocatalyst) conditions. At the catalyst suspension concentrations of 1.0 and 0.5 % w/V, toxicity appeared after 180 min as the *E. coli* growth was inhibited even under dark condition compared to the control light sample when the catalyst was not present (**Fig. 4.12a and b).** At

photocatalyst suspension concentration of 0.1 % w/V, the **D** experiment shows similar population density to the **CL** indicating the photocatalyst is below the toxic limit for E. coli and any further effect is due to the photocatalytic activity of the material (**Fig. 4.12 c**). [46]

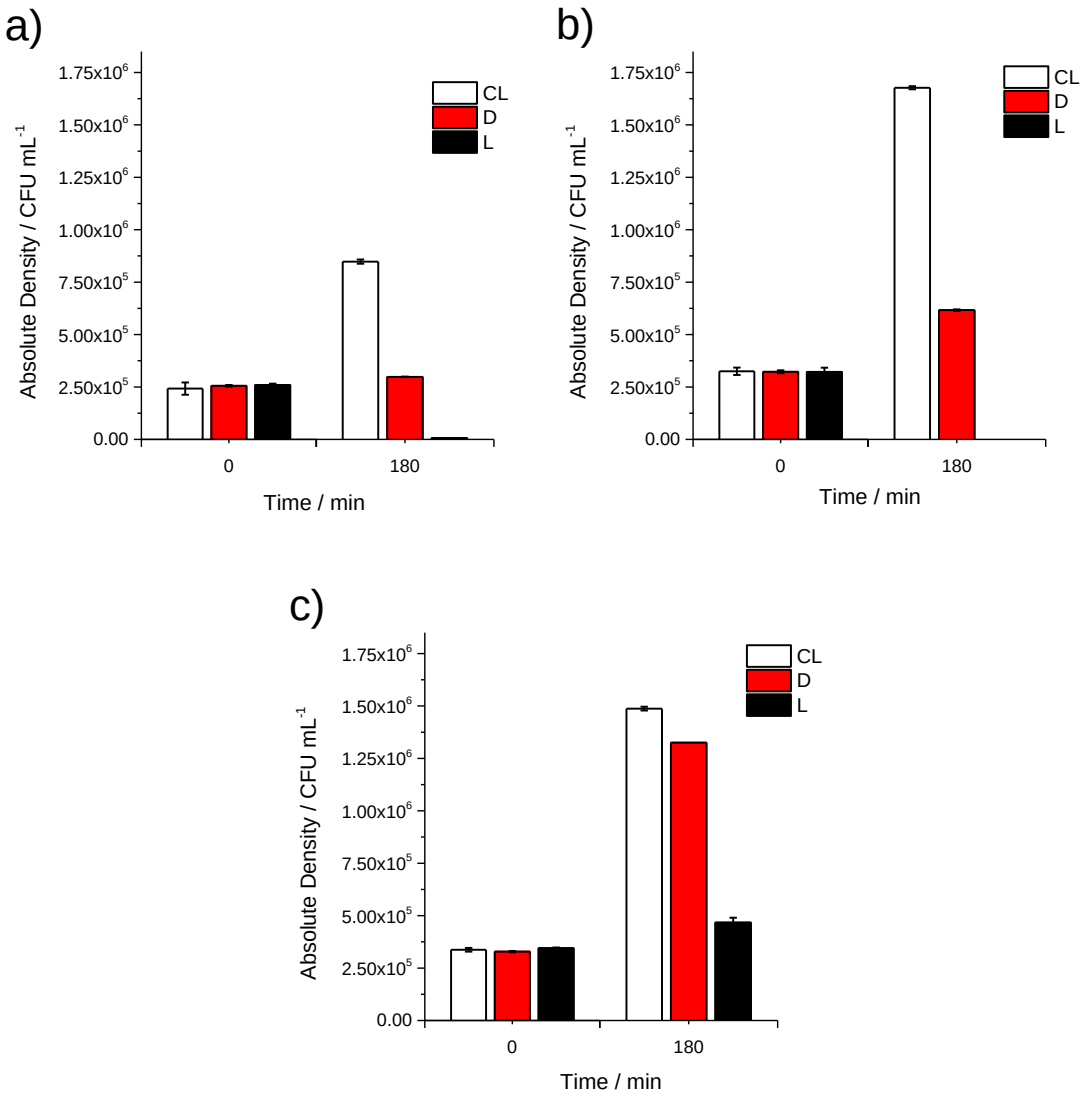

Fig. 4.12 Absolute density of *E. coli* population after 0 min and 180 min with catalyst concentrations of (a) 1% w/V of $SrTi_{0.95}Rh_{0.05}O_3$, (b) 0.5 % w/V of $SrTi_{0.95}Rh_{0.05}O_3$, (c) 0.1% w/V of $SrTi_{0.95}Rh_{0.05}O_3$ under control light (CL – white bars), dark (D – red bars) and light (L – black bars) conditions; 300 W Xenon lamp (λ > 420 nm); error bars denote the standard deviations of CFU ml^{-1} units for each experiments

ICP analysis of the supernatants was carried out in order to investigate the catalyst stability under the photocatalytic conditions. For this, the $SrTi_{0.95}Rh_{0.05}O_3$ catalyst was suspended in PBS buffer, stirred for 24 h in the dark, centrifuged at 10000 rpm for 10 min and the particles were filtered off with a d > 0.2 μm pore size syringe filter. The various suspension concentrations are shown in **Table. 4.7**.

Table 4.7 Strontium ICP results from $SrTi_{0.95}Rh_{0.05}O_3$ suspended in PBS at four different concentrations ¥, ¥ ¥

Photocatalyst Concentration (% w/V) *	**Dissolved Sr concentration (ppm) ¥ ¥**
0.05	2.502
0.1	5.023
0.5	17.576
1	24.683

* Freshly prepared catalyst suspension which was not used in experiment, no bacteria cells were added
¥ No rhodium was detected in any of the samples. ICP-AES detection limit for Rh = 100 ppb = 0.1 ppm = 0.1 μg/mL
¥¥ ICP-AES detection limit for Sr = 0.5 ppb = $5 \cdot 10^{-4}$ ppm = $5 \cdot 10^{-4}$ μg/mL

The measured data indicate no Rh in any of the supernatants however dissolved strontium was shown to increase with increasing amounts of catalyst in suspension from 0.05 – 1 % w/V respectively. *E. coli* appears to be resistant to strontium concentrations of up to 5.023 ppm. This concentration of strontium was consistent throughout all of the photocatalytic conditions used subsequently (**Table 4.8**) and comparable to the solubility of $SrCO_3$ at room temperature (11pm). The hydrothermally synthesised materials show improved stability over solid-state synthesised $SrTi_{1-x}Fe_xO_3$ at suspension concentration of 0.1 % w/V, where 49 ppm of Sr was detected in the supernatant and showed significant toxic effect to *E. coli* Gram negative bacteria.[38] This study shows that ~ 17 ppm of Sr can result in toxic effect

towards *E. coli* (**Fig. 4.12 b, Table 4.7**). Moreover, it should be also noted that the ICP detection limit for Rh is 0.1 ppm and the effective harmful concentration is reported to be three orders of magnitude greater.[49]

Table 4.8 ICP results of 0.1 % w/V $SrTi_{0.95}Rh_{0.05}O_3$ and 0.1 % w/V $SrTiO_3$ suspended in PBS at various photocatalytic reaction conditions, the blank PBS solution and the LB broth in PBS ¥, ¥¥

Rh content	Conditions	Sr / (ppm) ¥¥
0.05	Autoclaved cat. in PBS buffer + 24 h stirring in "Dark" + 2nd autoclaving, centrifuging, filtering off the particles †*	5.023
0.05	Autoclaved cat. in PBS buffer + 24 h stirring in "Light" + 2nd autoclaving, centrifuging, filtering off the particles †*	5.301
0.05	Autoclaved cat. in PBS buffer + 24 h stirring in "Dark" + Cells + 2nd autoclaving, centrifuging, filtering off the particles †**	6.545
0.05	Autoclaved cat. in PBS buffer + 24 h stirring in "Light" + Cells + 2nd autoclaving, centrifuging, filtering off the particles †**	4.749
N/A	PBS (=Phosphate Buffered Saline)	0.010
N/A	LB broth + PBS (5 µL LB broth in 5 mL PBS)	0.024
0	Autoclaved cat. in PBS buffer + 24 h stirring in "Dark" + Cells + 2nd autoclaving, centrifuging, filtering off the particles †***	6.655
0	Autoclaved cat. in PBS buffer + 24 h stirring in "Light" + Cells + 2nd autoclaving, centrifuging, filtering off the particles †***	7.220
0	Cat. in PBS buffer + 24 h stirring in "Dark" + no autoclaving, centrifuging, filtering off the particles *	6.030
0	Cat. in distilled water + 24 h stirring in "Dark" + no autoclaving, centrifuging, filtering off the particles *	5.677

† Autoclave: high pressure saturated steam at 121 °C, 15-20 min
* Freshly prepared catalyst suspension which was not used in experiment, no bacteria cells were added
** Tested in experiment with $SrTi_{0.95}Rh_{0.05}O_3$
***Tested in experiment with $SrTiO_3$
¥ No rhodium was detected in any of the samples. ICP-AES detection limit for Rh = 100 ppb = 0.1 ppm = 0.1 µg/mL
¥¥ ICP-AES detection limit for Sr = 0.5 ppb = $5 \cdot 10^{-4}$ ppm = $5 \cdot 10^{-4}$ µg/mL

To investigate the statistical effect on cell division/cell growth inhibition that takes place in the *E. coli* when exposed to the photocatalyst, culture samples were taken every 120 min over a six hour period using 0.1 % w/V $SrTi_{0.95}Rh_{0.05}O_3$ catalyst, under control dark (**CD** – no light exposure, no photocatalyst), control light (**CL** – visible light exposure, no photocatalyst), dark (**D** – no light exposure, with photocatalyst) and light (**L** – visible light exposure, with photocatalyst) conditions. The experiments were repeated three times and the data are shown representatively on **Fig. 4.13** and **Table 4.9**. [46]

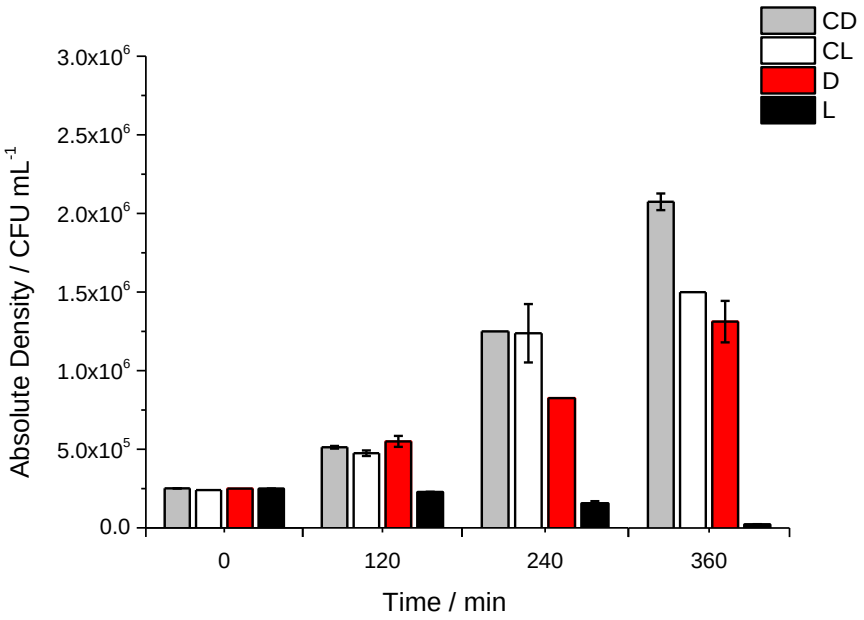

Fig 4.13 Representative absolute density time line measurement of *E. coli* population with concentration of 0.1% w/V of doped $SrTi_{0.95}Rh_{0.05}O_3$ under control dark, control light, dark and light conditions; 300 W Xenon lamp (λ > 420 nm); error bars denote the standard deviation of $CFUmL^{-1}$ units for each experiments

Table 4.9 *E. coli* absolute population density at T_0 and at T_{360} min with catalyst concentration of 0.1% w/V of $SrTi_{0.95}Rh_{0.05}O_3$ under control dark, control light, dark and light conditions; 300 W Xenon lamp (λ > 420 nm)

Conditions	T_0 Absolute density (CFU mL^{-1})	T_{360} Absolute density (CFU mL^{-1})
CD	2.51E+05	2.08E+06
CL	2.40E+05	1.50E+06
D	2.50E+05	1.31E+06
L	2.49E+05	2.25E+04

After two hours the absolute population density of *E. coli* in the **L** experiment exhibits a clear difference to the other conditions, showing no change in the number of colony forming units from the initial number, compared to the experiments **CD, CL** and **D** where significantly more CFUs are observed. After 6 hours the number of CFUs in the **L** experiment significantly decreases to 9% of the original cell numbers. As a comparison when no catalyst was added to the PBS suspension in **CD** experiment the number of CFUs increased by an order of magnitude.

As a control experiment the undoped $SrTiO_3$ was also tested under the same conditions, repeated three times (**Fig. 4.14** and **Table 4.10)**. There was no apparent change in CFUs, the **L** experiment suggesting an inhibition of cell growth/division rather than a deactivation of the cells. This combination of inhibition and photocatalytic deactivation makes the $SrTi_{0.95}Rh_{0.05}O_3$ containing material particularly effective in destroying *E. coli*.

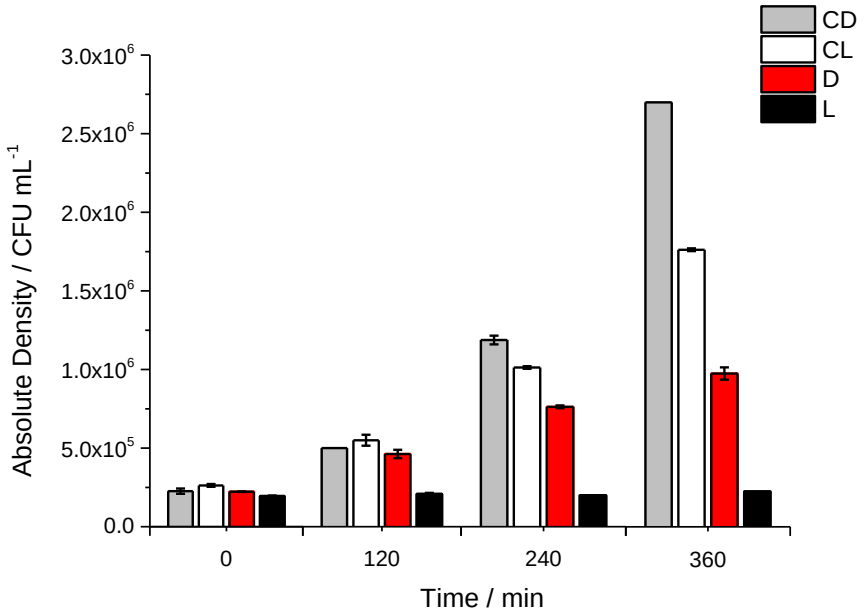

Fig. 4.14 Representative absolute density time reaction measurement of *E. coli* population with concentration of 0.1% w/V of parent $SrTiO_3$ under control dark, control light dark and light, conditions; 300 W Xenon lamp (λ > 420 nm); error bars denote the standard deviations of CFU mL^{-1} units for each experiments

Table 4.10 *E. coli* absolute population density at T_0 and at T_{360} min with catalyst concentration of 0.1 w/V% $SrTiO_3$ under control dark, control light, dark and light conditions; 300 W Xenon lamp (λ > 420 nm)

Conditions	T_0 Absolute density (CFU mL^{-1})	T_{360} Absolute density (CFU mL^{-1})
CD	2.26E+05	2.70E+06
CL	2.63E+05	1.76E+06
D	2.23E+05	9.75E+05
L	1.95E+05	2.25E+05

Although, looking through the CFU data, some questions might remain unanswered, hence some of the experimental factors will be further clarified. Samples were taken at every two hours and colony counting is strictly based on the statistics of bacteria being evenly dispersed through the medium when a sample is taken and only being counted on the agar plate if colony is formed, along with calculated standard deviation. To that, a reliable and countable appearance of the colony has to be optimised in order to avoid colonies' overlapping due to high population density, hence a series of dilution was applied and plated ($10^0 – 10^{-6}$). When plating, the time factor also has to be considered as *E. coli* bacteria is in the mid-growth phase when added to the photocatalyst suspension and the replication period only takes 20 minutes, therefore precise and rapid plating is essential. These are the factors that can be easily controlled by careful sampling and plating but what occurs to the bacteria if they form clusters on the photocatalyst particles? Would the number of bacteria cells decrease in solution when plated and could that lead to errors in colony counting methodology in a 6-hour-long deactivation?

In order to better understand the processes, Fluorescent Microscopy (**Section 2.10.5**) was used to visualise bacteria and the possible cell death. The LIVE/DEAD BacLight Bacterial Viability Kit utilises the mixtures of the SYTO®9 green-fluorescent nucleic acid stain and the red-fluorescent nucleic acid stain, propidium iodide. These stains differ both in their spectral characteristics and in their ability to penetrate into healthy bacterial cells. When both dyes (green-fluorescent SYTO®9 and red-fluorescent propidium iodide) are pre-mixed and added together to the cell culture, propidium iodide penetrates only into bacteria with damaged membranes, causing a reduction in the SYTO®9 stain fluorescence and stains the cells red. The deactivation of the cells by visible light activated $SrTi_{0.95}Rh_{0.05}O_3$ was visualised by fluorescent microscopy,

taken in the 6th hour of each experiment (**CD, CL, D, L**). In the control experiments (**Fig 4.15a, b**) the majority of cells are undamaged (fluorescing green). In the experiments containing photocatalyst (**Fig 4.15c, d**) only those exposed to light shows significant damaged cells (fluorescing red).[46]

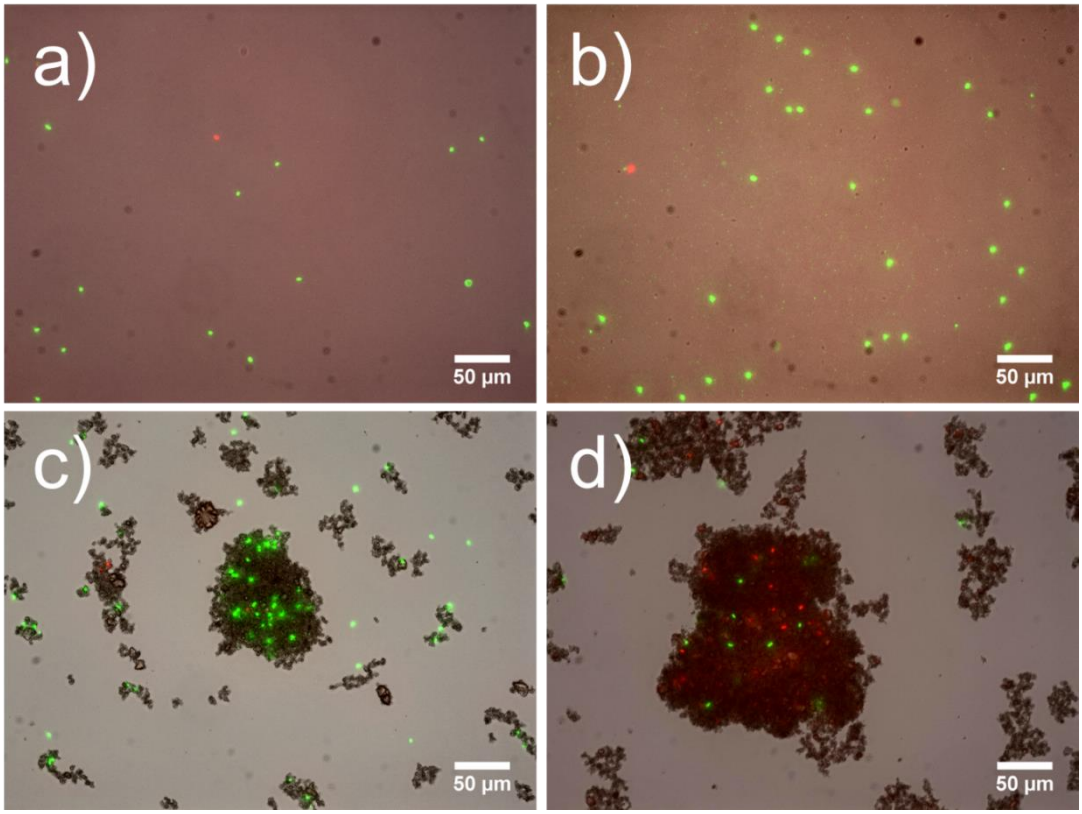

Fig. 4.15 *E. coli* cell population viability in the 6th hour of photocatalytic test detected by SYTO® 9 green fluorescent and Propidium Iodide red fluorescent nucleic acid stains (a) untreated cell in control dark and (b) control light experiments are viable (c) treated cells in dark experiment are intact (d) treated cells in light experiment are mostly damaged; Cat. 0.1% w/V $SrTi_{0.95}Rh_{0.05}O_3$; Light source 300W Xenon lamp (λ > 420 nm).

In the 6th hours of E. coli visualisation, it is also clear that bacteria is adhered to and clustered on the photocatalyt whereas only a limited number of E.coli cells are dispersed in solution (**Fig 4.15c, d)**. This confirms two facts: first a physical interaction between the bacteria and the catalyst particles, secondly bacteria population in solution

is very low in both **D** and **L** reactions under above mentioned conditions. With having analysed the fluorescent microscopy results too, these facts underestimate the number of cells considered during colony counting (**Fig. 4.13**), hence as a conclusion it could have led to errors in colony counting methodology. Furthermore it is also interesting that after cell death, cells remain attached and agglomerated on the catalyst, hence simple filtration of photo-active particles could remove harmful organisms as well, therefore catalyst can be called as "bioactive-filter" similarly to the well-known silver-deposited activated carbon fibers (ACF) [50] used in industrial processes such as drinking water filtration.

In conclusion, live cells attached to the photocatalyst in the **D** experiment suggests that the solid photocatalyst is not itself toxic to the *E. coli* and the survival rates observed are under-estimated in experiments containing photocatalyst as some potential CFUs are filtered along with the solid material. It is clear however that when exposed to visible light the photocatalyst is effective at deactivating *E. coli* (**Fig. 4.15d**) and works as an effective "bioactive-filter". It can also be concluded that in order to reliably monitor bacteria inactivation in solution, colony counting technique is necessary for direct estimation but data has to be supported by either SEM, TEM or Fluorescent Microscopy visualisation method for assured confirmation of a compound's anti-bacterial properties.

4.3. Conclusion and Future Prospects

HT-synthesised nanostructured $BaTi_{1-x}Rh_xO_3$ ($0.01 \leq x < 0.0.5$) compounds with Rh^{3+} oxidation state in the lattice were found active in water reduction upon visible light irradiation with no additional co-catalyst. H_2 generation activity was further improved when samples were loaded with various co-catalysts, in particular with Au^0 and NiO.

It is worth noting that as-synthesised $BaTi_{0.99}Rh_{0.01}O_3$ compound with higher surface area (6.8 – 7.5 m^2/g) and with NiO co-catalyst might be more efficient in overall water splitting reaction compared to the solid state synthesized material (2.0 m^2/g) reported by Maeda [11] when combined with PtO_x/WO_3.[11]

Novel simple one-step hydrothermal synthesis of $SrTi_{1-x}Rh_xO_3$, ($0 < x < 0.1$) with high surface area is described. When $x \leq 0.05$ the rhodium dopant is predominantly in the Rh(III) oxidation state in the bulk of the material resulting in a very efficient visible-light ($\lambda > 420$ nm) activated photocatalyst with multi-functionality – H_2 evolution from water, organic dye degradation and anti-microbial properties.

$SrTi_{0.95}Rh_{0.05}O_3$ with no co-catalyst loading is shown to produce H_2 from water at a rate of 6.5 µmol/g/h which seems less effective compared to the 1 wt% Pt^0-loaded $SrTi_{0.99}Rh_{0.01}O_3$ (literature data: 117 µmol/g/h for) [10] but was able to completely oxidise a 0.2 g/L solution of methyl orange within 30 minutes under visible light. It is also shown that $SrTi_{0.95}Rh_{0.05}O_3$ can act as an anti-microbial material to inhibit the growth of *E. coli* in aqueous suspension, completely deactivating the bacteria within 6 hours of visible light exposure.

4.4. References

1. *World Water Week, Stockholm, 2015*, http://weshare.unicef.org/C.aspx?VP3=SearchResult&ALID=2AM4080EJLV6&PBC=:2AM4080EJNYS:2AM4080EJLV6.
2. A. A. Krasnovsky and G. P. Brin, *Dokl. Akad. Nauk SSSR*, 1962, **147**, 656–659.
3. A. Fujishima and K. Honda, *Nature*, 1972, **238**, 37-38.
4. M. S. Wrighton, D. S. Ginley and P. T. Wolczanski, *PROC. NATL. ACAD. SCI. U. S. A.*, 1975, **72**, 1518-1522.
5. H. Kato, M. Hori, R. Konta, Y. Shimodaira and A. Kudo, *Chemistry Letters*, 2004, **33**, 1348-1349.
6. K. Iwashina and A. Kudo, *Journal of the American Chemical Society*, 2011, **133**, 13272-13275.
7. K. Maeda, *J. Photochem. Photobiol. C Photochem. Rev.*, 2011, **12**, 237-268.
8. C. C. Lo, C. W. Huang, C. H. Liao and J. C. S. Wu, *Int J Hydrogen Energy*, 2010, **35**, 1523-1529.
9. R. Konta, T. Ishii, H. Kato and A. Kudo, *J. Phys. Chem. B*, 2004, **108**, 8992-8995.
10. A. Kudo, R. Niishiro, A. Iwase and H. Kato, *Chem. Phys.*, 2007, **339**, 104-110.
11. K. Maeda, *ACS Applied Materials & Interfaces*, 2014, **6**, 2167-2173.
12. R. W. Matthews, *Water Research*, 1991, **25**, 1169-1176.
13. C. Galindo, P. Jacques and A. Kalt, *Journal of Photochemistry and Photobiology A: Chemistry*, 2000, **130**, 35-47.
14. C. Baiocchi, M. C. Brussino, E. Pramauro, A. B. Prevot, L. Palmisano and G. Marcì, *International Journal of Mass Spectrometry*, 2002, **214**, 247-256.
15. G. T. Brown and J. R. Darwent, *Journal of Physical Chemistry*, 1984, **88**, 4955-4959.
16. G. T. Brown and J. R. Darwent, *Journal of the Chemical Society, Faraday Transactions 1: Physical Chemistry in Condensed Phases*, 1984, **80**, 1631-1643.
17. J. R. Darwent and A. Lepre, *Journal of the Chemical Society, Faraday Transactions 2: Molecular and Chemical Physics*, 1986, **82**, 1457-1468.
18. A. Mills and G. Williams, *Journal of the Chemical Society, Faraday Transactions 1: Physical Chemistry in Condensed Phases*, 1987, **83**, 2647-2661.
19. C. Han, L. Ge, C. Chen, Y. Li, X. Xiao, Y. Zhang and L. Guo, *Applied Catalysis B: Environmental*, 2014, **147**, 546-553.
20. H. Zhang, H. Huang, H. Ming, H. Li, L. Zhang, Y. Liu and Z. Kang, *Journal of Materials Chemistry*, 2012, **22**, 10501-10506.
21. U. A. Joshi, J. R. Darwent, H. H. P. Yiu and M. J. Rosseinsky, *Journal of Chemical Technology & Biotechnology*, 2011, **86**, 1018-1023.
22. J. Cao, B. Luo, H. Lin and S. Chen, *Journal of Hazardous Materials*, 2011, **190**, 700-706.
23. G. Yang, Z. Jiang, H. Shi, T. Xiao and Z. Yan, *Journal of Materials Chemistry*, 2010, **20**, 5301-5309.
24. T. Tong, J. Zhang, B. Tian, F. Chen and D. He, *Journal of Hazardous Materials*, 2008, **155**, 572-579.
25. J. H. Clark, M. S. Dyer, R. G. Palgrave, C. P. Ireland, J. R. Darwent, J. B. Claridge and M. J. Rosseinsky, *Journal of the American Chemical Society*, 2011, **133**, 1016-1032.
26. S. C. Yan, Z. S. Li and Z. G. Zou, *Langmuir*, 2010, **26**, 3894-3901.
27. G. N. Schrauzer and T. D. Guth, *Journal of the American Chemical Society*, 1977, **99**, 7189-7193.
28. B. Kraeutler and A. J. Bard, *Journal of the American Chemical Society*, 1978, **100**, 2239-2240.

29. T. Matsunaga, R. Tomoda, T. Nakajima and H. Wake, *FEMS Microbiol. Lett.*, 1985, **29**, 211-214.
30. M. S. Wong, W. C. Chu, D. S. Sun, H. S. Huang, J. H. Chen, P. J. Tsai, N. T. Lin, M. S. Yu, S. F. Hsu, S. L. Wang and H. H. Chang, *Appl. Environ. Microbiol.*, 2006, **72**, 6111-6116.
31. Q. Li, Y. W. Li, P. Wu, R. Xie and J. K. Shang, *Adv Mater*, 2008, **20**, 3717-3723.
32. S. C. Hayden, N. K. Allam and M. A. El-Sayed, *Journal of the American Chemical Society*, 2010, **132**, 14406-14408.
33. P. Wang, B. Huang, X. Qin, X. Zhang, Y. Dai and M.-H. Whangbo, *Inorganic Chemistry*, 2009, **48**, 10697-10702.
34. I. Sondi and B. Salopek-Sondi, *J. Colloid Interface Sci.*, 2004, **275**, 177-182.
35. W. Wang, Y. Yu, T. An, G. Li, H. Y. Yip, J. C. Yu and P. K. Wong, *Environ. Sci. Technol.*, 2012, **46**, 4599-4606.
36. Y. Chen, A. Lu, Y. Li, L. Zhang, H. Y. Yip, H. Zhao, T. An and P.-K. Wong, *Environmental Science & Technology*, 2011, **45**, 5689-5695.
37. P. Wu, J. A. Imlay and J. K. Shang, *Biomaterials*, 2010, **31**, 7526-7533.
38. L. Zhang, P. Y. Tan, C. L. Chow, C. K. Lim, O. K. Tan, M. S. Tse and C. C. Sze, *Colloids Surf. A Physicochem. Eng. Asp.*, 2014, **456**, 169-175.
39. R. Asahi, T. Morikawa, T. Ohwaki, K. Aoki and Y. Taga, *Science*, 2001, **293**, 269-271.
40. J. Yuan, M. Chen, J. Shi and W. Shangguan, *Int J Hydrogen Energy*, 2006, **31**, 1326-1331.
41. M. I. Litter, *Applied Catalysis B: Environmental*, 1999, **23**, 89-114.
42. B. Kraeutler and A. J. Bard, *Journal of the American Chemical Society*, 1978, **100**, 4317-4318.
43. C. Gomes Silva, R. Juárez, T. Marino, R. Molinari and H. García, *Journal of the American Chemical Society*, 2011, **133**, 595-602.
44. Z. Zou, J. Ye and H. Arakawa, *J. Phys. Chem. B*, 2002, **106**, 13098-13101.
45. B. Kiss, C. Didier, T. Johnson, T. D. Manning, M. S. Dyer, A. J. Cowan, J. B. Claridge, J. R. Darwent and M. J. Rosseinsky, *Angewandte Chemie International Edition*, 2014, **53**, 14480-14484.
46. B. Kiss, C. Didier, T. D. Manning, H. E. Allison, A. W. Taylor, J. B. Claridge, J. R. Darwent and M. J. Rosseinsky, *in preparation*, 2015.
47. Z. Weng-Sieh, R. Gronsky and A. T. Bell, *J. Catal.*, 1997, **170**, 62-74.
48. K. Shimura, H. Kawai, T. Yoshida and H. Yoshida, *Chemical Communications*, 2011, **47**, 8958-8960.
49. B. Rosenberg, E. Renshaw, L. Vancamp, J. Hartwick and J. Drobnik, *J Bacteriol*, 1967, **93**, 716-721.
50. K. Y. Yoon, J. H. Byeon, C. W. Park and J. Hwang, *Environmental Science & Technology*, 2008, **42**, 1251-1255.

5. Chapter 5: Synthesis, Characterisation and Photocatalytic Application of $Y_2Ti_{2-x}Rh_xO_7$ Pyrochlore Structure

5.1 Introduction

The photocatalytic splitting of water by visible light using semiconductor materials has been proposed as a route to sustainable hydrogen generation.[1, 2] Of the systems available, Z-scheme photocatalysis offers several advantages over single particle photocatalysis or photoelectrocatalysis [3] The Z-scheme system is inspired by natural photosynthesis in which two separate photocatalysts are linked by a shuttle redox mediator. In an artificial Z-scheme, each of the water splitting half-reactions is performed separately on each of the catalysts. Z-scheme systems lower the energy required for photocatalysis (**Section 1.2.1**) as the valence and conduction band edges of the individual photocatalysts do not have to straddle the reduction potentials of H^+/H_2 and O_2/H_2O as they do for a single particle photocatalyst. In this way a wider range of visible light can be used. Importantly using the Z-scheme approach, water splitting can take place in a simple reactor without the requirement for potentially costly electrode connections and transparent conducting supports (see details in **Section 4.1**). The production of oxygen is a critical step in solar fuels production and is a requirement for any photocatalytic water splitting system. This half of the water splitting process is more challenging since it typically involves a four-electron process and powerful oxidizing species which can lead to the breakdown of the photocatalyst. It is also essential for photo-electrolysis. Whilst significant effort has been expended on developing visible light active hydrogen generating photocatalysts,[4] only a very limited number of stable, visible light active oxygen evolving photocatalysts are

known.[5] Monoclinic WO_3 has been extensively studied as an oxygen generating photocatalyst since 1962, [6, 7] and is generally used as the standard comparative material due to its commercial availability and reasonable performance. [8] However WO_3 has a relatively large band gap (2.6 eV) limiting its absorption of visible light to < 480 nm. Nanostructured $BiVO_4$ (E_g ~2.4 eV) [9] has been shown to photocatalytically generate oxygen under visible light irradiation and has a similar activity to WO_3.[10] Oxynitride perovskites have also displayed photocatalytic oxygen generation [11] but are less stable to photocorrosion than oxide materials unless •OH is removed *in situ* by the addition of La_2O_3.[12] Recently Ag_3PO_4 has been demonstrated as a highly efficient oxygen evolving photocatalyst [13, 14] though questions remain over its stability under reaction conditions.[15] Therefore to enable the development of an efficient Z-scheme for water splitting new stable, efficient, visible light active oxygen evolving photocatalysts are urgently required as highlighted in the recent review by Ma *et al.*[16]

The first reported photocatalyst for water splitting under ultraviolet (UV) radiation was TiO_2.[17] As a consequence, considerable attention has been given to titanium oxides, including the perovskite $SrTiO_3$ which also possesses photocatalytic activity for water splitting under UV irradiation.[18] Several substitutions for Ti have been evaluated in order to render these materials active under visible light,[19-22] with Rh reported as one of the most effective;[20] $SrTi_{1-x}Rh_xO_3$ with Pt co-catalyst in an aqueous CH_3OH solution is a highly-active hydrogen evolving photocatalyst under visible light, and has been used with $BiVO_4$ or with WO_3 in a Z-scheme to split water with visible light.[23] Calculations[24] suggest that Rh E_g states are located within the conduction band in $SrTi_{1-x}Rh_xO_3$, allowing visible light excitation from the Rh T_{2g} to generate delocalized electrons which evolve hydrogen, however the formation of Rh^{4+} inter-gap states, that act as a recombination centre for photoexcited carriers, can inhibit hydrogen evolution.

The $A_2B_2O_7$ pyrochlore structure (**Fig. 5.1**) consists of corner-sharing BO_6 octahedra with A cations in a 2+6 environment; there is one B-O-B angle which is around 135°.[25]

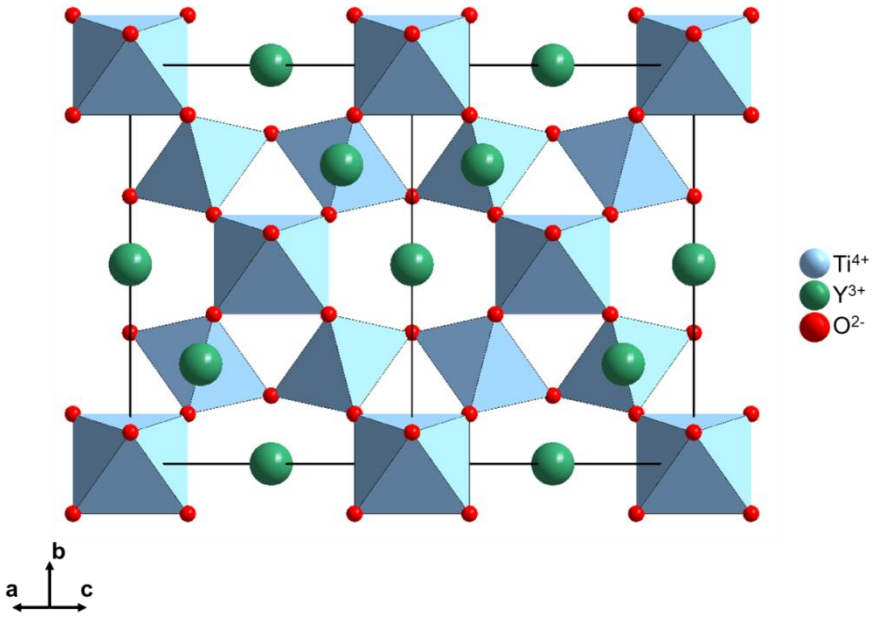

Fig. 5.1 Unit cell of the pyrochlore structure projected along the [101] direction, with the 6-coordinate Ti^{4+} sites represented by a network of blue corner-sharing octahedra, and Y^{3+} and O^{2-} ions represented by green and red spheres respectively

The rare-earth $R_2Ti_2O_7$ pyrochlores thus have some structural similarities with perovskite $SrTiO_3$, which also features a corner-sharing TiO_6 octahedral network but with angles much closer to 180°. Pyrochlore is an important ternary oxide type which sustains a range of functions and is extensively tuneable by substitution.[25] Abe *et al.* have shown that pyrochlore $Y_2Ti_2O_7$ with NiO_x co-catalyst can be successfully used as a photocatalyst for water splitting under UV light, with a band gap of 3.5 eV.[26] As this gap is much larger than that of $SrTiO_3$, (3.2 eV), the Rh-derived E_g states in $Y_2Ti_{2-x}Rh_xO_7$ may sit just below the conduction band edge and thus become localised, potentially acting as recombination states or becoming photocatalytically inactive to

hydrogen generation. The extensive chemical tuneability of pyrochlore suggests that suitable substitutions would enhance its photocatalytic properties and open up new directions in the synthesis of photocatalysts.

This chapter reports the phase-pure pyrochlore $Y_2Ti_{2-x}Rh_xO_7$ solid solution series and demonstrates its stable visible light activity as an oxygen evolving photocatalyst. Experiments in suspension establish this material as a promising candidate for inclusion in a Z-scheme, but we also note that $Y_2Ti_{2-x}Rh_xO_7$ is a potential photoanode.

5.2 Synthesis

5.2.1 Solid State Synthesis of $Y_2Ti_{2-x}Rh_xO_7$

Samples of $Y_2Ti_{2-x}Rh_xO_7$, with $0 < x < 0.2$, were prepared by solid-state reactions using a stoichiometric mixture of Y_2O_3 (Alfa-Aesar 99.99%), anatase TiO_2 (Sigma-Aldrich 99.7%, nanopowder) and Rh_2O_3 (Sigma-Aldrich 99.8%), according to the reaction:

$$Y_2O_3(s) + (2\text{-}x)\ TiO_2(s) + x/2\ Rh_2O_3(s) \rightarrow Y_2Ti_{2-x}Rh_xO_7(s) \qquad \textbf{(Eq. 5.1)}$$

Before weighing, powders of Rh_2O_3 and TiO_2 were dried overnight at 200 ºC while the powder of Y_2O_3 was dried overnight at 950 ºC. The mixture was ground with a mortar and pestle and pressed into a pellet (10 mm diameter). The pellet was placed in an alumina boat lined with platinum foil and fired for 12 h at 1300 ºC under ambient air. The obtained samples were ground, pelletized and annealed for a second time for 36 h at 1300 ºC. After the second annealing, XRD patterns confirmed the complete disappearance of the starting reactants. The powder of the undoped sample is white; all Rh-doped samples have a grey/purple colour.

5.2.2 Mechanical grinding and BET

Prior to co-catalyst loading and H_2 and O_2 evolution test reactions, all powder samples were ball milled using zirconium oxide balls in a zirconium oxide pot overnight in isopropanol (350 rpm for 12 hr) and dried at 110ºC. N_2 adsorption–desorption isotherms at 77 K were collected on a Tristar II porosimeter of Micromeritics. Before analysis the samples were degassed at 120°C and 10^{-3} mbar for 16 hr. The specific surface area was calculated applying the BET method in the range of relative pressure $0.05 < P/P_0 < 0.3$. The measured BET surface areas of the ball milled materials were 2.4-3.2 m^2/g.

5.2.3 Recyclability of the catalyst in test reactions

The long-term stability of the $Y_2Ti_{1.94}Rh_{0.06}O_7$ samples was also investigated for O_2 evolution. The experiment is set up as specified above. The $AgNO_3$ solution is periodically purged with N_2 gas in order to remove the evolved O_2. During purging, the Xenon lamp is turned off and the samples are covered in aluminium foil. The suspension was then irradiated periodically and the rate of O_2 gas was measured. The recyclability test of the catalyst was carried out 3 times.

5.2.4 Quantum Efficiency Calculations

For the Apparent Quantum Efficiency (AQE) determination, the number of incident photons emitted by the ozone-free Xenon 300 lamp supplied with 400(±5) nm, 450(± 5) nm band pass filters was determined by actinometry [27] (**Section 2.10.6**).

The AQE of $Y_2Ti_{1.94}Rh_{0.06}O_7$ was compared to that of commercially available WO_3. For the AQE calculation the following equation was used:[28]

$$AQE = \frac{4 * Number\ of\ O_2\ molecules}{number\ of\ incident\ photons} * 100\% \quad \textbf{(Eq. 5.2)}$$

For the AQE measurements, the conditions used were 0.1 g catalyst in 20 mL of 0.05 M aqueous $AgNO_3$ solution, however band pass filters were used instead of the full range of incident visible light. The experiments were repeated 3 times and the mean reported as the AQE.

5.2.5 Addition of co-catalyst to Solid State Synthesised $Y_2Ti_{2-x}Rh_xO_7$

In order to investigate the influence of co-catalyst addition, H_2 and O_2 evolution measurements were also carried out on samples loaded with various co-catalysts. The effect of Pt, Ru, NiO, RuO_2 and $Rh_{2-y}Cr_yO_3$ co-catalysts were investigated. [29-32]

For Pt metal, $Y_2Ti_{2-x}Rh_xO_7$ was loaded with 1 wt% Pt by photodeposition. 0.4 g of catalyst and 0.1050 g H_2PtCl_6 (8wt % Pt – Sigma Aldrich) were dissolved in 400 mL 10 % aq. MeOH solution. The suspension was then purged with nitrogen under stirring for 30 minutes to remove all oxygen from the solution. Following this, the solution was placed under a UV lamp for 5 hours. The photodeposited samples were centrifuged and dried at 60 ºC in an electric oven. [31]

For Ru metal, $Y_2Ti_{2-x}Rh_xO_7$ was loaded with 1 wt% Ru by photodeposition. 0.4 g of catalyst and 0.0082 g $RuCl_3 \bullet x\ H_2O$ (Sigma Aldrich) were dissolved in 400 mL 10 % aq. MeOH solution. The suspension was then purged with nitrogen under stirring for 30 minutes to remove all oxygen from the solution. Following this, the solution was placed under a UV lamp for 5 hours. The photodeposited samples were centrifuged and dried at 60 ºC in an electric oven.

For NiO loading the impregnation method was used. $Y_2Ti_{2-x}Rh_xO_7$ was loaded with 1 wt% NiO (the calculation was made for 1 wt% Ni metal content). 0.0198 g $Ni(NO_3)_2 \bullet 6\ H_2O$ (Sigma Aldrich) was dissolved in 4 mL MeOH solution. 0.4 g of catalyst was added to this solution and carefully mixed with a mortar and pestle. At 110 ºC, atmospheric pressure and vigorous stirring the MeOH was evaporated and the powder was annealed in air at 350 ºC for 3 h, with 5 ºC/min heating and cooling rates. [29]

For RuO_2 co-catalyst loading the impregnation method was applied. $Y_2Ti_{2-x}Rh_xO_7$ was loaded with 1 wt% RuO_2 (the calculation was made for 1 wt% Ru metal content). 0.0253 g $Ru_3(CO)_{12}$ (Sigma Aldrich) was dissolved in 4 mL THF. 0.4 g of catalyst was added to this solution and carefully mixed with a mortar and pestle. At 110 ºC, atmospheric pressure and vigorous stirring the THF was evaporated as under vacuum the $Ru_3(CO)_{12}$ sublimes. The resulted powder was annealed in air at 350 ºC for 1 h, with 5 ºC/min heating and cooling rates. [30]

For $Rh_{2-y}Cr_yO_3$ co-catalyst loading the impregnation method was applied. $Y_2Ti_{2-x}Rh_xO_7$ was loaded with 1 wt% Rh and 1.5 wt% Cr (the calculation was made for 1 wt% Rh metal and 1.5 wt% Cr metal contents). 0.0150 g $Na_3RhCl_6 \bullet 2\ H_2O$ (Sigma Aldrich) and then 0.0462 g $Cr(NO_3)_3 \bullet 9\ H_2O$ (Sigma Aldrich) were dissolved in 4 mL distilled water. 0.4 g of catalyst was added to this solution and carefully mixed with a mortar and pestle. At 110ºC, atmospheric pressure and vigorous stirring the water was evaporated. The resulting powder was annealed in air at 350 ºC for 1 h, with 5 ºC/min heating and cooling rates. [32]

5.3 Discussion 1 - Characterisation and Photocatalytic Application of Solid State Synthesised $Y_2Ti_{2-x}Rh_xO_7$

The powder XRD patterns of the $Y_2Ti_{2-x}Rh_xO_7$ samples, prepared by solid-state synthesis, with $0 \leq x \leq 0.2$, are shown in **Fig. 5.2** and **Fig. 5.3**.

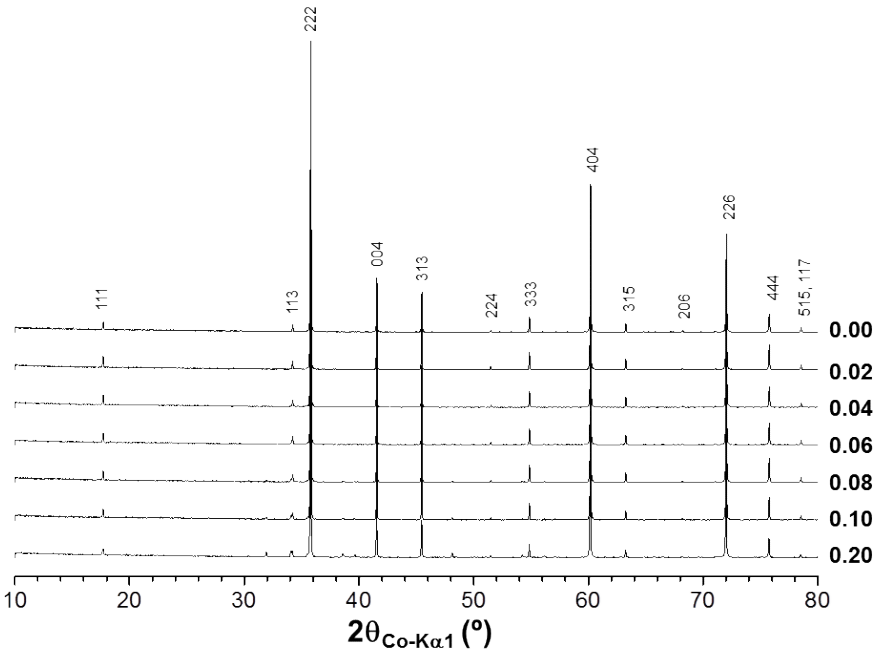

Fig. 5.2 Powder XRD patterns of $Y_2Ti_{2-x}Rh_xO_7$ with $0 \leq x \leq 0.2$ indexed to the cubic pyrochlore unit cell

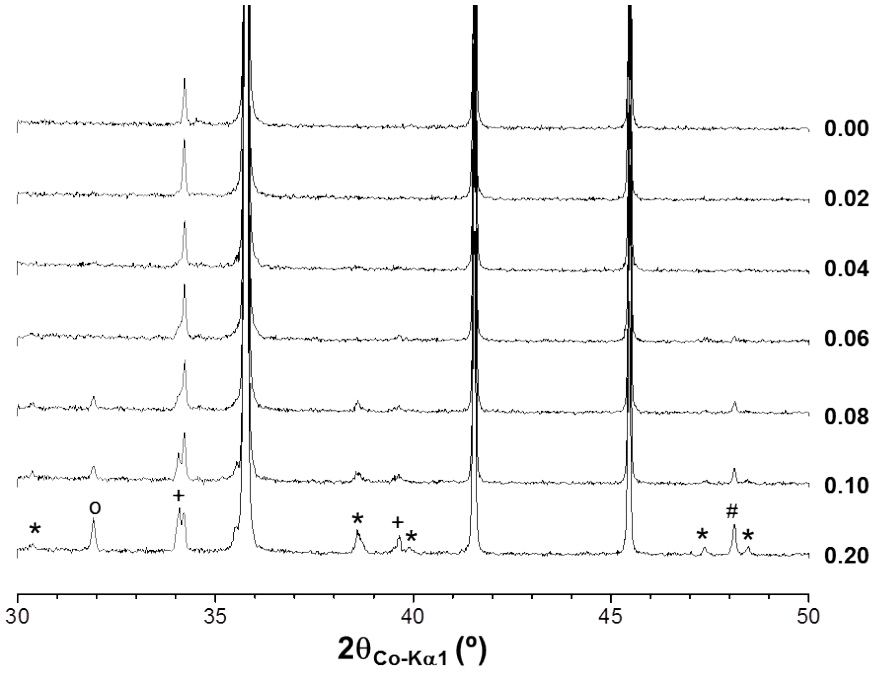

Fig. 5.3 Enlargement of the powder XRD patterns of $Y_2Ti_{2-x}Rh_xO_7$ with $0 \leq x \leq 0.2$ at the base of the peaks, showing impurities for $x > 0.06$. The main peaks ($x \geq 0$) denote the phase-pure cubic pyrochlore; impurities are indicated on the $x = 0.2$ doped sample: # Rh; o TiO_2; + Y_2O_3; * $YRhO_3$

All the samples contain a pyrochlore phase. However, as the comparison between **Fig. 5.2** and **Fig. 5.3** emphasizes, it is easy to miss crystalline impurities without a finer examination of the pattern. Non-pyrochlore peaks are observed for doping levels higher than x = 0.06, which have been assigned to Rh metal,[33] rutile TiO_2,[34] Y_2O_3 [35] and perovskite $YRhO_3$. [36] The presence of metallic rhodium results from conversion of Rh_2O_3 to the metal at temperatures above 1100 ºC.[37] This suggests that x = 0.06 is the maximum amount of rhodium that can be inserted into the pyrochlore $Y_2Ti_2O_7$; however one cannot exclude the presence of impurities that are not visible from XRD. A superior proof of Rh substitution into the pyrochlore structure is the evolution of the unit cell dimensions upon substitution (Vegard's Law [38]). An internal standard was thus added in order to permit precise and accurate lattice parameter determination. The unit cell parameter of the pyrochlore $Y_2Ti_{2-x}Rh_xO_7$ were derived from whole pattern

fitting using the Le Bail method. An example of the refinement profile is given in **Fig. 5.4**.

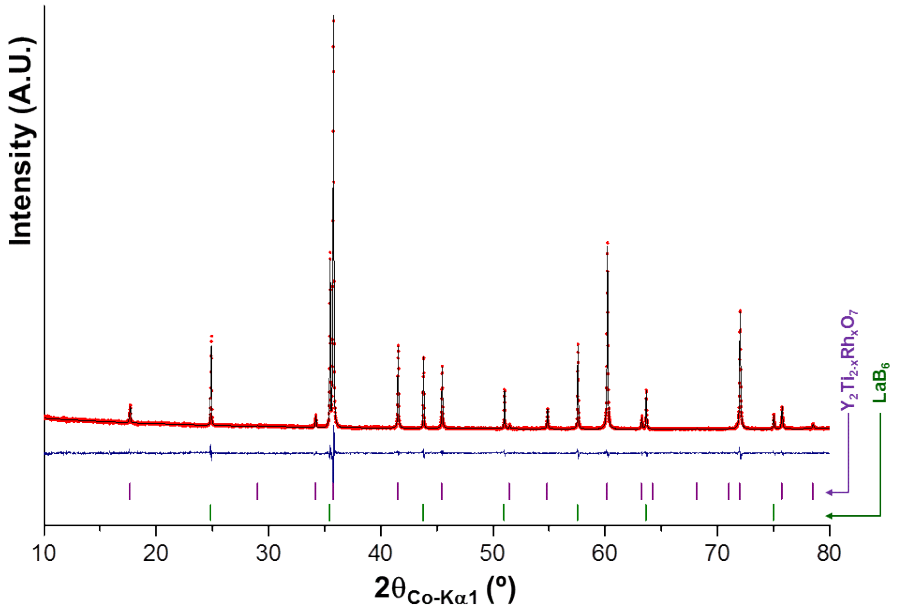

Fig. 5.4 Le Bail whole pattern fitting of $Y_2Ti_{1.98}Rh_{0.02}O_7$, with LaB_6 as an internal standard

The derived evolution of cell parameters with Rh concentration (**Fig. 5.5**) is linear to x = 0.08, after which the unit cell parameter is constant. This behavior confirms the insertion of rhodium into the pyrochlore structure at these concentrations.

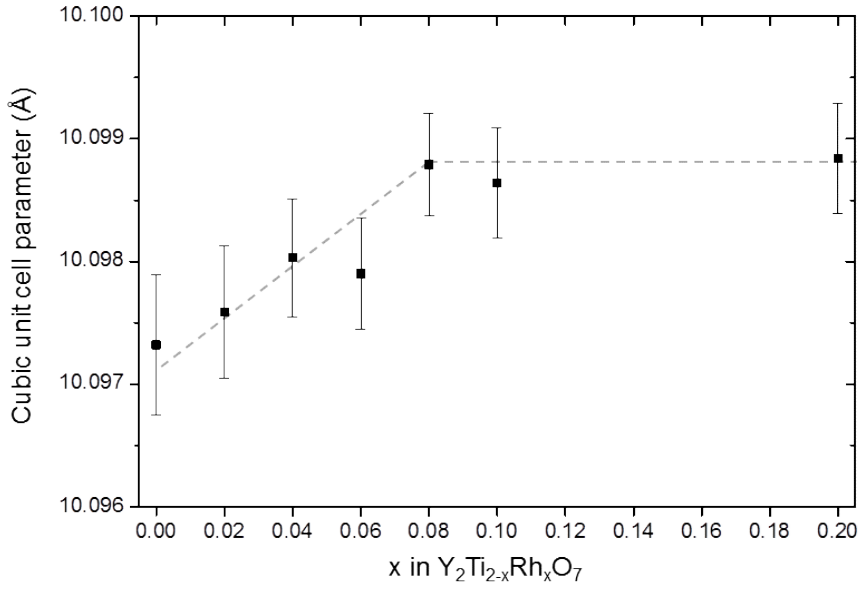

Fig. 5.5 Unit cell parameter of $Y_2Ti_{2-x}Rh_xO_7$ determined from whole pattern fitting using the Le Bail method, using LaB_6 internal standard. Error bars are 3 × e.s.d obtained from the refinement procedure, with Berar's factor included to ensure correlations are appropriately accounted for. Dashed lines are guides to the eye.

Since the x = 0.08 sample was not phase-pure, x = 0.06 is the maximum amount of Rh that can be substituted into $Y_2Ti_2O_7$ under the synthetic conditions used here. The ionic radii of Rh^{4+} (0.615 Å [39] or 0.60 Å [40] though the latter is based on values from a number of metallic oxides) and Ti^{4+} (0.605 Å) [40] are very close, whilst that of Rh^{3+} (0.665 Å) [40] is significantly larger. The unit cell parameter changes observed are expected to be comparatively small in any solid solution based on isovalent substitution, consistent with rhodium being present as Rh^{4+}. Substitution of Rh for Y is unlikely as the size difference between these cations is significant (1.019 Å for Y^{3+}),[40] and eight-fold or higher coordination for rhodium ions is very unusual. This substitution would also generate excess Y_2O_3 in the phase assemblage, which is not observed below the solubility limit (**Fig. 5.3**). The possibility of substitution of Rh for Y in the $Y_2Ti_2O_7$ pyrochlore can thus be safely excluded.

The Kubelka-Munk spectra, derived from the conversion of the diffuse reflection spectra, of $Y_2Ti_{2-x}Rh_xO_7$ ($0 \leq x \leq 0.06$) are shown in **Fig. 5.6**.

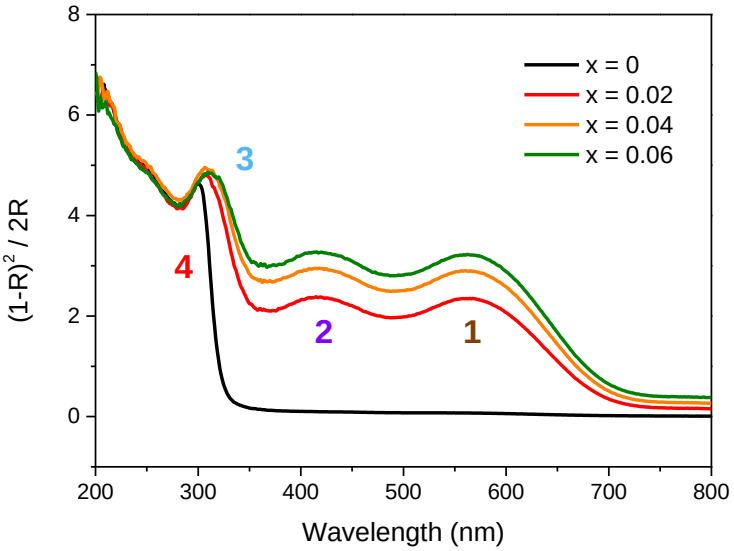

Fig. 5.6 Kubelka-Munk spectra of $Y_2Ti_{2-x}Rh_xO_7$ ($0 \leq x \leq 0.06$)

The parent $Y_2Ti_2O_7$ has a measured indirect band gap of 3.71 eV (**Fig. 5.7**) and does not absorb visible light. [26]

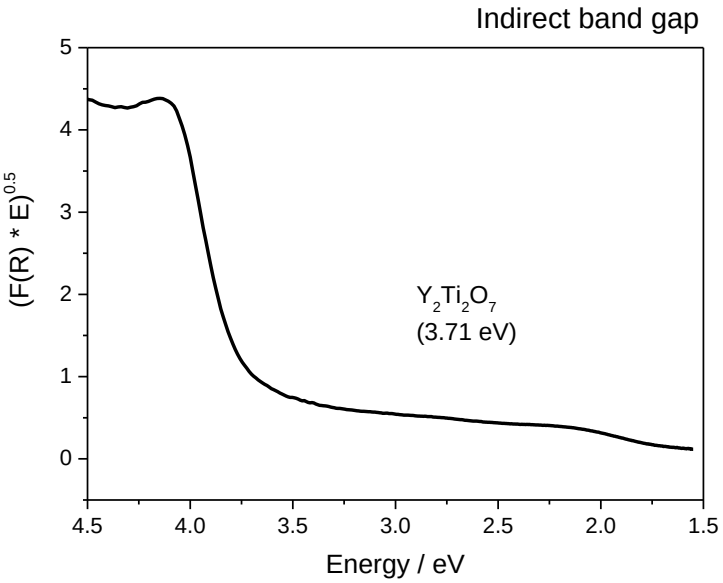

Fig. 5.7 Diffuse reflection spectra were converted to show the Indirect band gap plot vs. Energy. The Tauc methodology was used to determine the indirect band gap energy of $Y_2Ti_2O_7$.

Substitution of Rh into $Y_2Ti_2O_7$ produces significant changes in the spectral response, with a red-shift of the absorption edge, together with the presence of two entirely new visible absorption features, giving light absorption down to 700 nm (**Fig. 5.6**, **Fig. 5.8**).

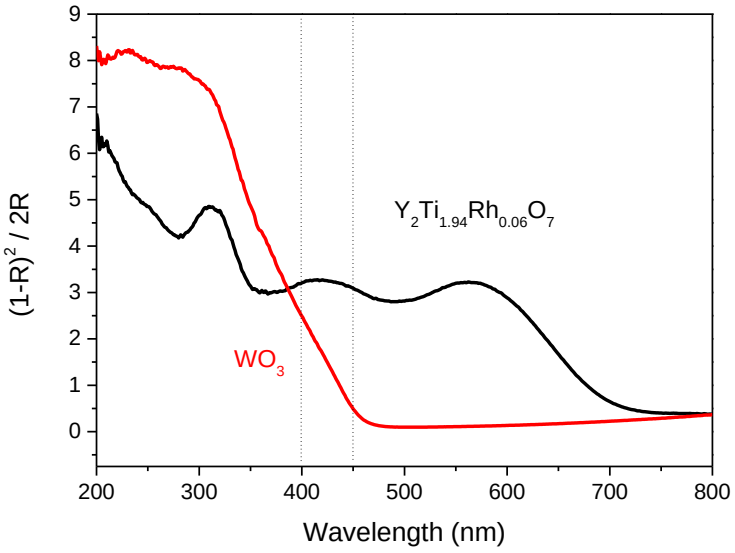

Fig. 5.8 Kubelka-Munk spectra of $Y_2Ti_{1.94}Rh_{0.06}O_7$ and WO_3. The dotted lines mark the wavelength at 400 and 450 nm

Visible absorption peaks in Rh^{4+} substituted $SrTiO_3$ are associated with d-d transitions between Rh states just above the valence band and to a Rh inter-gap state and the conduction band. [20, 24, 41] DFT calculations of the density of states (DOS) of $Y_2Ti_{1.75}Rh_{0.25}O_7$ (**Section 6.1** and **Fig. 5.9**) made by Matthew S. Dyer reveal that, in addition to the inter-gap and near valence band states, Rh d-states are also manifest just below the conduction band of $Y_2Ti_2O_7$ upon Rh substitution.

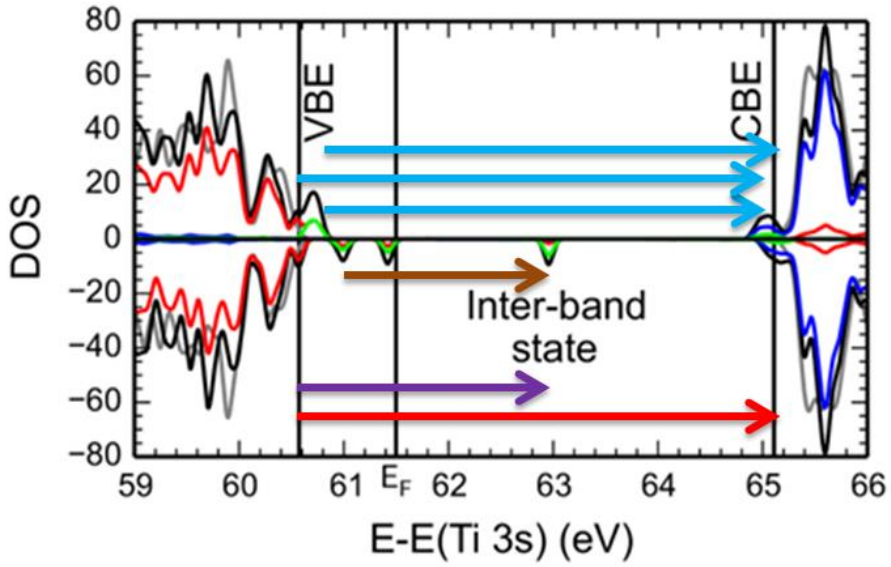

Fig. 5.9 The DOS of $Y_2Ti_2O_7$ (grey) and $Y_2Ti_{1.875}Rh_{0.125}O_7$ (black) are plotted along with the partial DOS projected onto the Ti 3d (blue), Rh 4d (green) and O 2p (red) orbitals of $Y_2Ti_{1.875}Rh_{0.125}O_7$ using the energy of the Ti 3s states as a common reference energy. The computed valence band edge (VBE) and conduction band edge (CBE) of $Y_2Ti_2O_7$ are indicated as vertical lines, along with the calculated Fermi energy of $Y_2Ti_{1.875}Rh_{0.125}O_7$

The computed DOS suggests that the lowest energy absorption feature (560 nm) results from a d-d transition from Rh d-states just above the valence band to the inter-gap state (**Fig. 5.6** N° 1, **Fig. 5.9** brown arrow), and that the feature at 420 nm is a transition from the valence-band-edge to inter-gap state (**Fig. 5.6** N° 2, **Fig. 5.9** purple arrow). The shift in absorption edge to lower energy cannot be attributed to a change in the fundamental O 2p – Ti 3d band gap, which remains almost unchanged in calculations (**Fig. 5.6** N° 4, **Fig. 5.9** red arrow). Rather a combination of transitions involving the localised Rh d-states just above the valence band, and those just below the conduction band have energies lower than the fundamental band gap, and effectively reduce the energy of the adsorption edge (**Fig. 5.6** N° 3, **Fig. 5.9** blue arrows). On this basis the spectra have been fitted to two Gaussian peaks, an exponential function for the Urbach

tail and a power-law dependant absorption edge (see **Section 6.2** for details, fitted by Alexander J. Cowan in collaboration with R. Treharne) with a red-shift of the absorption edge to 3.12 eV for x = 0.06 and a tail that extends into the visible. The visible light activity of $Y_2Ti_{2-x}Rh_xO_7$ arises from one or more of the transitions arising due to the incorporation of Rh and leading to absorption in the visible region.

The $Y_2Ti_{2-x}Rh_xO_7$ series were investigated as photocatalysts for the evolution of H_2 and O_2 using sacrificial reagents (CH_3OH and $AgNO_3$) with visible light. No H_2 evolution was detected under visible light illumination using a 300 W Xenon lamp with 420 nm cut-off filter for any material, with or without co-catalyst. The materials did however display visible light activity for O_2 generation**.**

The O_2 evolution rate, measured with a Clark electrode,[8, 42-44] for unloaded $Y_2Ti_{2-x}Rh_xO_7$ ($0 \leq x \leq 0.06$) is represented in **Fig. 5.10**.

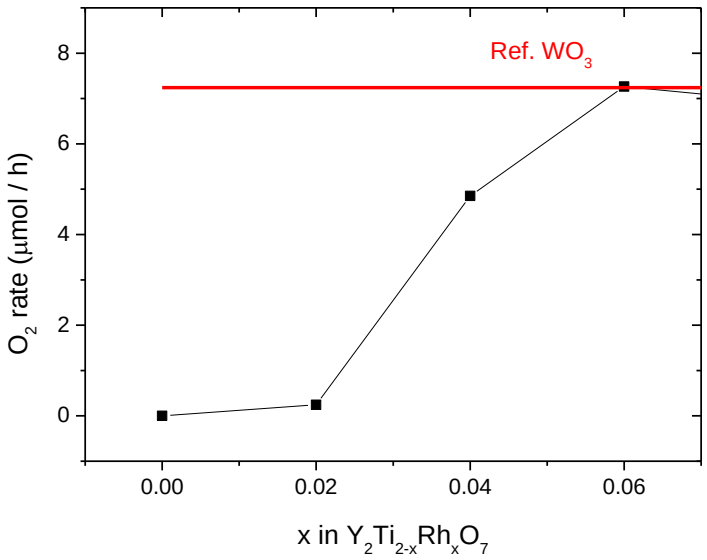

Fig. 5.10 Rate of O_2 generation using $Y_2Ti_{2-x}Rh_xO_7$ under visible light. 0.1 g of catalyst; no co-catalyst; 20 mL, 0.05 M $AgNO_3$(aq); 300 W Xe lamp (λ > 420 nm, < 2.95 eV)

The x = 0 and x = 0.02 materials did not show visible light activity. However, visible light photocatalytic O_2 evolution is observed for samples with $x \geq 0.04$. The activity increases up to x > 0.06 where it reaches a plateau $Y_2Ti_{1.94}Rh_{0.06}O_7$ displays excellent recyclability with no significant change in oxygen evolution rate over three cycles (**Fig. 5.11**).

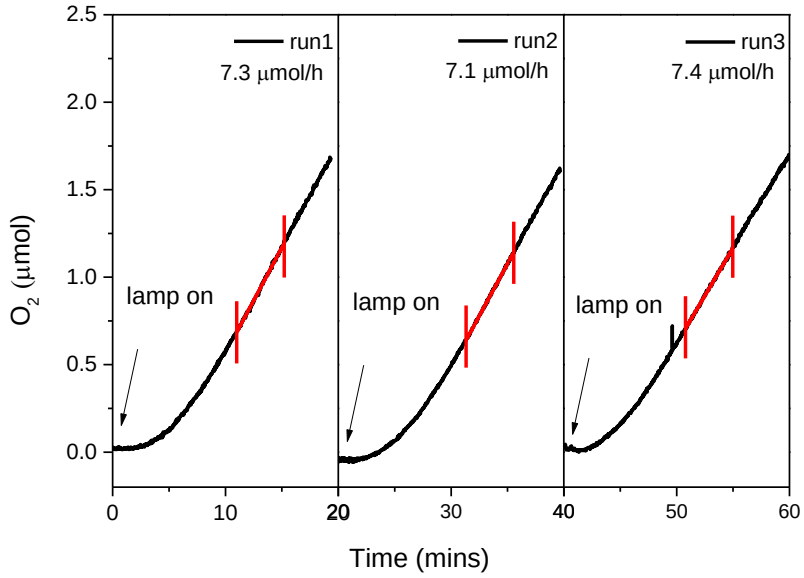

Fig. 5.11 Recyclability of $Y_2Ti_{1.94}Rh_{0.06}O_7$ oxygen evolution photocatalyst; Catalyst, 0.1 g; no co-catalyst; 20 mL 0.05 M $AgNO_{3(aq)}$; light source, 300 W Xe lamp λ > 420 nm cut-off filter. The red lines mark where the O_2 reaction rate was measured (μmol/min).

The samples were examined by SEM (**Fig. 5.12a-d**) and PXRD (**Fig. 5.13a-b**) before and after the photocatalytic measurements and no indication of photocorrosion was observed.

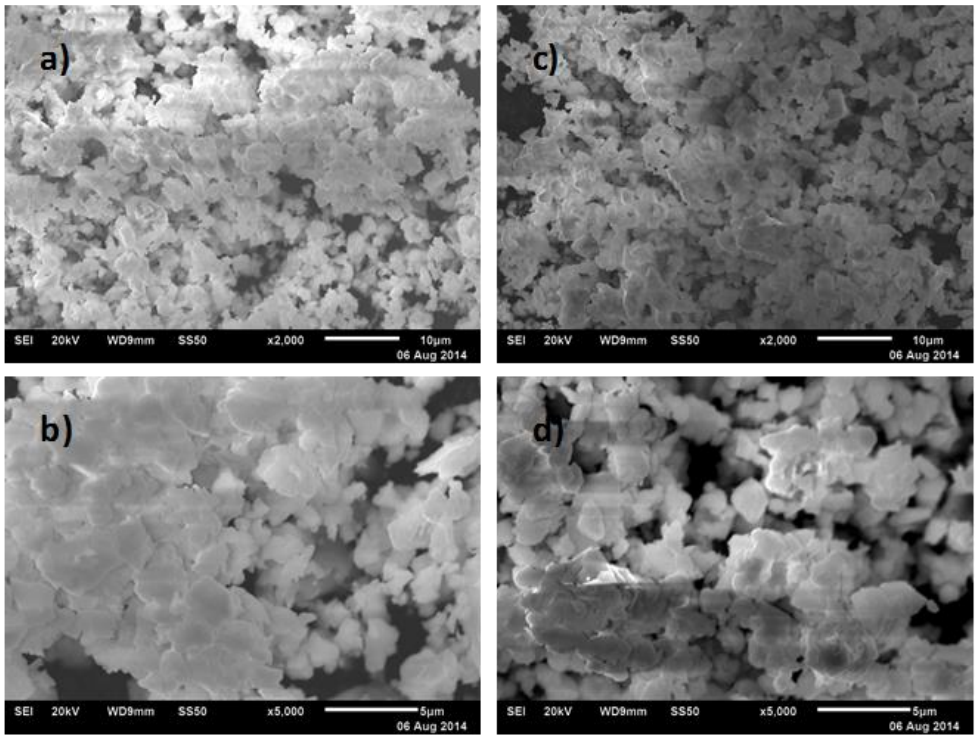

Fig. 5.12 SEM images of $Y_2Ti_{1.94}Rh_{0.06}O_7$ powder (a, b) before and (c, d) after water oxidation reaction.

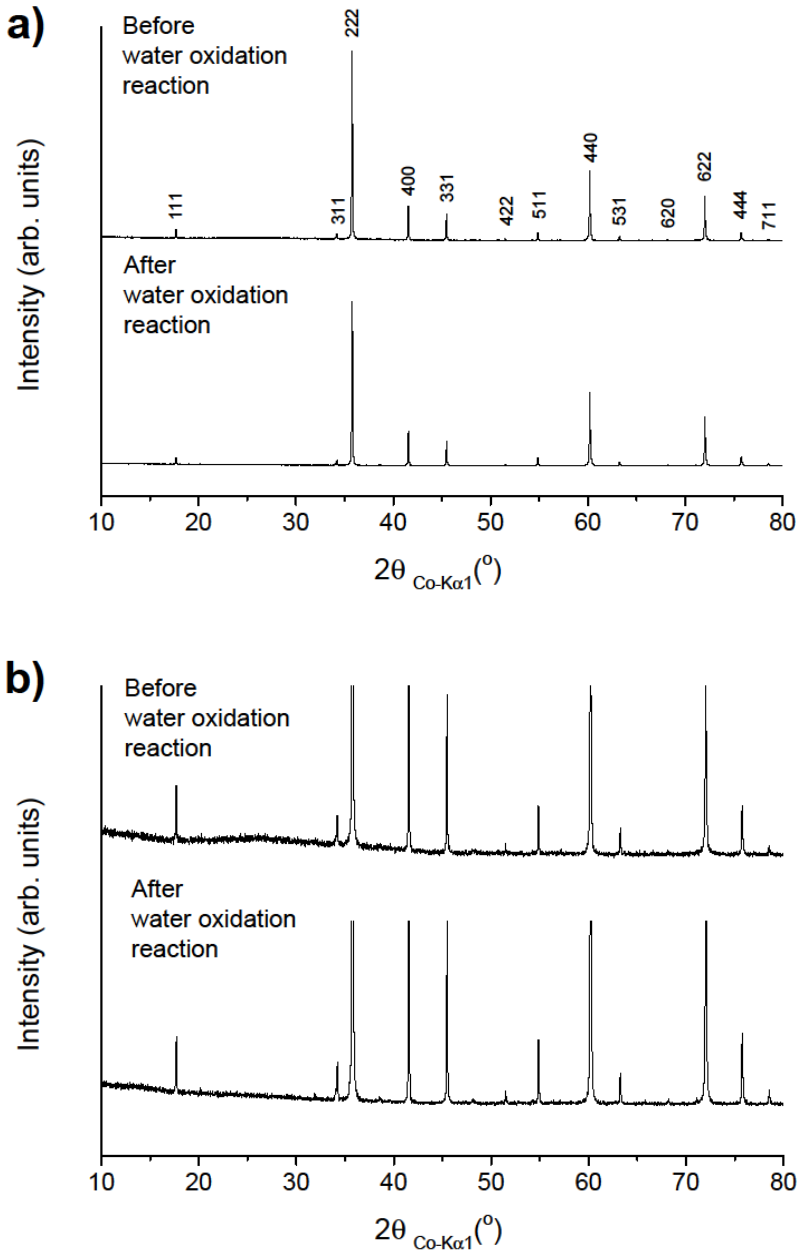

Fig. 5.13 Powder XRD patterns of (a) $Y_2Ti_{1.94}Rh_{0.06}O_7$before and after water oxidation reaction indexed to the cubic pyrochlore unit cell. (b) Enlargement of the powder XRD patterns of $Y_2Ti_{1.94}Rh_{0.06}O_7$ before and after water oxidation reaction at the base of the peaks.

Oxygen evolution rates for both WO_3, studied as a benchmark, and $Y_2Ti_{1.94}Rh_{0.06}O_7$ were confirmed by the widely used GC methodology using the same solution conditions as for the Clark electrode experiments and 400 ± 5 nm irradiation (**Fig. 5.14a-b**).

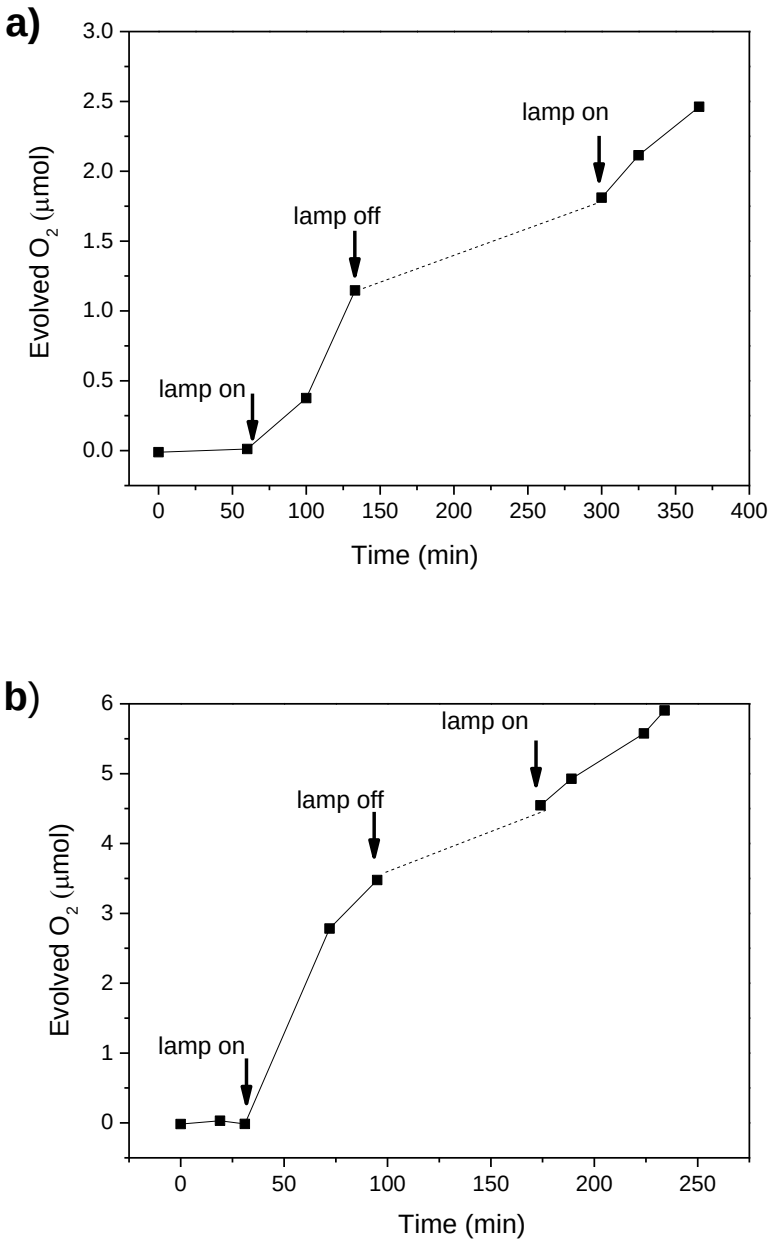

Fig. 5.14 GC measured O_2 evolution from (a) $Y_2Ti_{1.94}Rh_{0.06}O_7$ and (b) WO_3 using a 400(±5) nm band pass filter, 25 mg photocatalyst in 5 mL $AgNO_3$ (0.05 M), degassed with N_2, the experiments confirm that O_2 is formed during the photocatalysis measurements.

Turnover rates per unit mass (TOR_m) and per unit surface area (TOR_s) have been suggested as useful comparisons between photocatalytic materials. [45] TOR_m for $Y_2Ti_{1.94}Rh_{0.06}O_7$ and WO_3 are similar (73 and 72 µmol/g/h respectively, **Tab. 5.1**).

Tab 5.1 Turnover Rates (TOR) of WO_3 and $Y_2Ti_{1.94}Rh_{0.06}O_7$ (300 W Xenon lamp, λ > 420 nm, 0.1 g photocatalyst, 20 mL 0.05 M $AgNO_3$(aq))

Material	BET surface area (m^2/g)	TOR_m (μmol/g/h)[a]	TOR_s (μmol/m^2/h)[b]
WO_3	9.1	72	7.9
$Y_2Ti_{1.94}Rh_{0.06}O_7$	3.2	73	22.8

[a] TOR_m = O_2 evolution rate / catalyst mass
[b] TOR_s = O_2 evolution rate / catalyst surface area

However there was a significant difference in TOR_s. The commercial WO_3 nanopowder has a BET surface area of 9.1 m^2/g giving TOR_s = 7.9 μmol/m^2/h; $Y_2Ti_{1.94}Rh_{0.06}O_7$ has a surface area of 3.2 m^2/g giving TOR_s = 22.8 μmol/m^2/h (**Tab. 5.1**). This suggests that increasing the surface area of $Y_2Ti_{1.94}Rh_{0.06}O_7$ by using alternative synthetic methods may further increase the photocatalytic activity of the material. For example sol-gel routes for $Y_2Ti_2O_7$ have been reported by several groups.[46-48] Apparent quantum efficiency values are given in **Tab. 5.2**: $Y_2Ti_{1.94}Rh_{0.06}O_7$ is superior to WO_3 at 450 nm and comparable at 400 nm at the illumination conditions used.

Tab. 5.2 Apparent Quantum Efficiency (using the number of incident photons based on the actinometry measurement)

Apparent Quantum Efficiency	Wavelength (nm)	
	400 ± 5	450 ± 5
WO_3	54%	30%
$Y_2Ti_{1.94}Rh_{0.06}O_7$	53%	39%

The addition of co-catalysts for water oxidation is a widely employed approach to enhance photocatalytic activity. In addition to the pure catalysts the effect of five of the most widely studied co-catalysts (Pt^0, Ru^0, NiO, RuO_2, $Rh_{2-y}Cr_yO_3$), identified to enhance the photocatalytic activity of other oxides for hydrogen and/or oxygen

evolution, was investigated.[11] Protocols for co-catalyst loadings are provided in **Section 5.2.5**. Only the 1 % RuO_2 loaded $Y_2Ti_{1.94}Rh_{0.06}O_7$ showing a slight enhancement of the evolution rate (7.6 µmol/h) (**Tab. 5.3**, **Fig. 5.15**, **Fig. 5.16**).

Tab 5.3 Rates of photocatalytic oxygen evolution measured for $Y_2Ti_{1.94}Rh_{0.06}O_7$ using various co-catalysts

Photocatalyst	Co-catalyst	O_2 (µmol/h) [a]
$Y_2Ti_{1.94}Rh_{0.06}O_7$	unloaded	7.3
	1% Pt^0	7.0
	1% NiO_x	6.3
	1% Ru^0	2.0
	1% RuO_2	7.6
	1% $Rh_{2-y}Cr_yO_3$	6.7

[a] 0.1 g catalyst, 20 mL of 0.05 M aqueous $AgNO_3$ solution, 300 W Xe lamp with cut-off filter ($\lambda > 420$ nm).

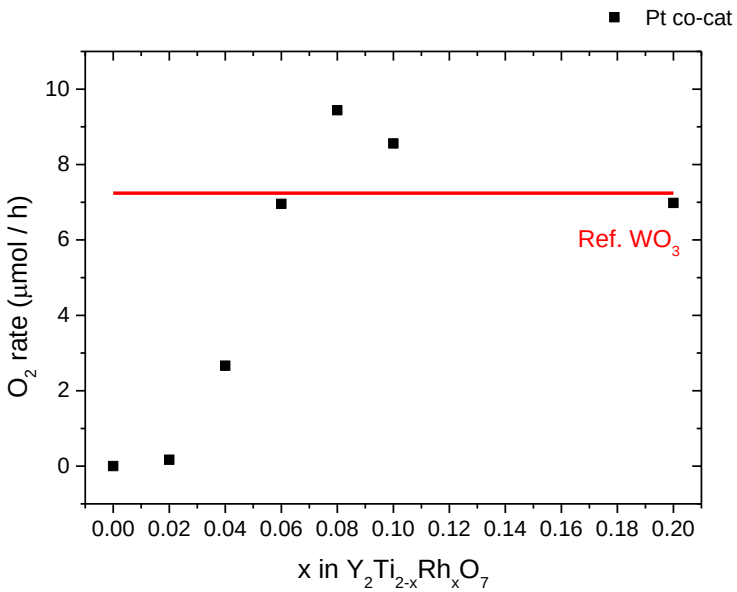

Fig. 5.15 Dependence of O_2 evolution activity of $Y_2Ti_{2-x}Rh_xO_7$ ($0 \leq x \leq 0.2$) upon the doping amount (black dots). Catalyst, 0.1 g; Pt^0 co-catalyst loading; solution, 20 mL of 0.05 M aqueous $AgNO_3$; light source, 300 W Xe lamp with cut-off filter ($\lambda > 420$ nm). The red line marks the O_2 evolution activity of a reference sample of WO_3.

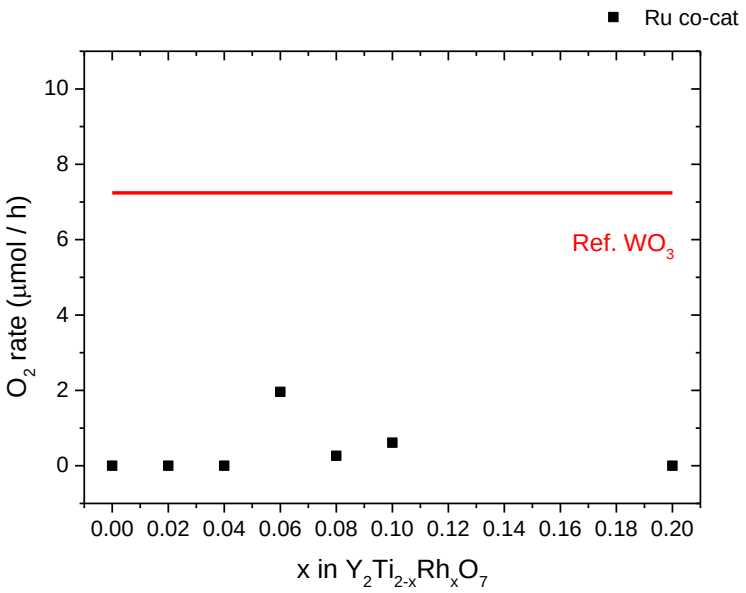

Fig. 5.16 Dependence of O_2 evolution activity of $Y_2Ti_{2-x}Rh_xO_7$ ($0 \leq x \leq 0.2$) upon the doping amount (black dots). Catalyst, 0.1 g; Ru^0 co-catalyst loading; solution, 20 mL of 0.05 M aqueous $AgNO_3$; light source, 300 W Xe lamp with cut-off filter ($\lambda > 420$ nm). The red line marks the O_2 evolution activity of a reference sample of WO_3.

Similarly an enhanced O_2 rate was reported for RuO_2/WO_3.[42] Interestingly Ru metal loading (**Fig. 5.16**) resulted in a large drop of the O_2 evolution activity. This inhibiting mechanism of Ru^0 in O_2 evolution has also been reported for Ru^0/WO_3.[42] It is in fact not uncommon for co-catalyst to reduce activity for O_2 evolution.[49, 50] Decreased photocatalytic activity in the presence of a co-catalyst is typically proposed to be due to increased electron-hole recombination losses, with either the co-catalysts themselves acting as recombination centres[49] or the deposition process leading to surface modifications and the formation of undefined recombination sites.

5.4. Introduction to Sol-gel Synthesised $Y_2Ti_{2-x}Rh_xO_7$ Samples

There have been several proposed routes for increasing the surface area of a material, in particular with sol-gel or with other words with Pechini-method (**Section 2.1.3**).[51] O. Merka and co-workers discussed the non-stoichiometric, excess amount of titanate precursor when synthesising the parent phase $Y_2Ti_2O_7$ with sol-gel method. Expectedly, they found that this excess Ti resulted in the appearance of TiO_2 rutile impurity at 27.5 2θ angle. The presence of TiO_2 impurity was further confirmed with DRS data showing red shift in the measured $Y_2Ti_2O_7$ indirect band gap value. Although, Pt-loaded samples containing stoichiometric Y:Ti ratios when calcined at 750 ºC for 4 h showed lower UV light activity in H_2 evolution compared to the composite materials containing excess of Ti (TiO_2).[46]

In comparison, M. Higashi and co-workers claimed the positive effect of access amount of Y in $Y_2Ti_2O_7$. Using the stoichiometric Y:Ti amount in parent compound according to their studies resulted in TiO_2 rutile impurities during calcination above 1000 ºC. Finally, they concluded that Y access is needed for the prevention of rutile impurity phase forming beside the main cubic pyrochlore structure.[48]

As the literature is controversial perhaps due to the inaccurate sample preparation in above detailed publications, in the following chapter the stoichiometric sample preparation will be described and a careful analysis will be conducted in order to affirm the syntheses of phase pure compounds.

5.5. Sol-gel Synthesis of $Y_2Ti_{2-x}Rh_xO_7$

Samples of $Y_2Ti_{2-x}Rh_xO_7$, with $0 < x < 0.08$, were prepared by sol-gel reactions using a stoichiometric mixture of 0.01 mol $Ti[OCH(CH_3)_2]_4$ (Sigma Aldrich, 99.999%), 0.01 mol $Y(NO_3)_3 \bullet 6\ H_2O$ (Sigma Aldrich 99.8%), x mol RhN_3O_9 (Sigma Aldrich, ~ 10%(w/w)) according to the rhodium loading amount, 0.4 mol Anhydrous Ethylene glycol (EG, Sigma Aldrich, 99.8%) and 0.3 mol Citric acid (CA, Sigma Aldrich, 99.5%).

In order to ensure all precursors went into solution while avoiding any precipitation reaction or sped up complexation, the order of adding each component is very important. It has to be noted that M. Higashi used a different order of adding precursors.[48] In his publication CA was added first then $Y(NO_3)_3$ but that results in that $Y(NO_3)_3$ is being dissolved at 130 ºC while Titanium-isopropoxide-EG-CA complex has been formed and esterification reaction has taken place .

First, the freshly opened Titanium-isopropoxide was added using a pipette into a 250 mL 3-neck round bottom flask under reflux. To this, EG solvent was added under vigorous stirring at room temperature. Crystals of $Y(NO_3)_3$ was added to this solution and the mixture was slowly heated up to 60 ºC to achieve complete solubility of all components. Then RhN_3O_9 was added to the doped material precursor solution with a pipette or left out when parent compound was synthesised. Once a clear solution was obtained for all A and B site cations, CA buffer was added in small portions under vigorous stirring with no additional solvent. At this point solution already appears as a viscous dense sol with an increased volume. Temperature is further being increased proportionally with desirable amount of CA up to 130 ºC. At ~130 ºC under vigorous stirring, the esterification reaction occurs and results in a viscous sol-gel with a

caramelised appearance. This transparent resin was transferred to an alumina crucible with a diameter of 15 cm and with a lid on and heated up in an electric oven to 360 ºC for 2 h under static air with 5 ºC/min heating and cooling rates. This process resulted in a light black solid mass with a visible porosity and a five-fold increased volume of the material. After homogenising this product with a mortar and pestle, powder sample was heated up to 1100 ºC for 6 h under static air with 5 ºC/min heating and cooling rates in an electric oven to form the pyrochlore. The produced fluffy samples were rehomogenised with a mortar and pestle before analysis. The resulted yield was 1.5 g, when 0.01 mol starting materials were used of Ti and Y precursors. Undoped sample is white and the rhodium doped samples have greyish purple colour.

5.6. Discussion 2 - Characterisation and Photocatalytic Application of Sol-gel Synthesised $Y_2Ti_{2-x}Rh_xO_7$

First the optimisation phase regarding the synthesis conditions of the sol-gel pyrochlore $Y_2Ti_{1.98}Rh_{0.02}O_7$ is discussed. For that, x = 0.02 Rh was inserted into $Y_2Ti_{2-x}Rh_xO_7$ structure and was examined with TGA analysis. The analysis was carried out on the produced black light mass described in (**Chapter 5.5**) which was previously synthesised at 130 ºC under vigorous stirring while esterification reaction took place. This viscous transparent resin was then heated up to 360 ºC in air while forming the black solid residue for thermogravimetric analysis (**Fig. 5.17**).

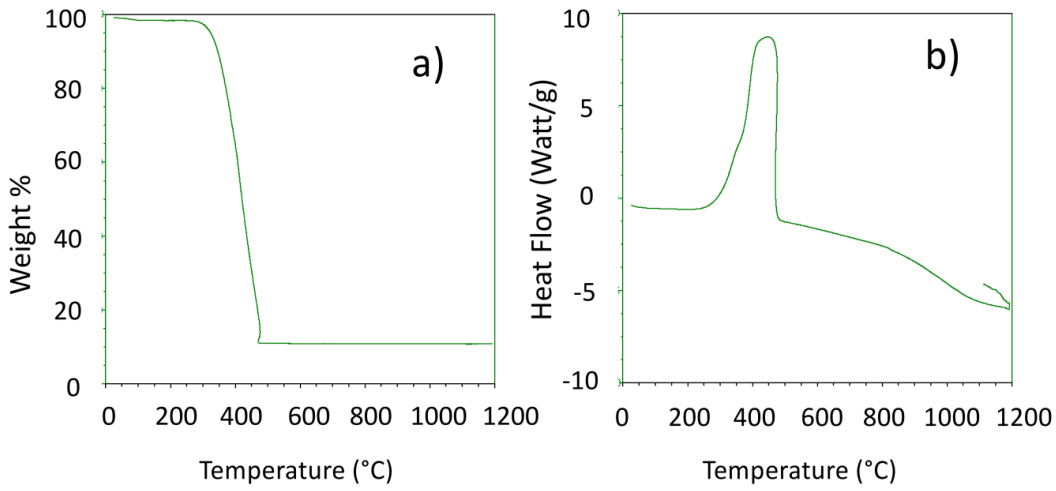

Fig. 5.17 Weight loss and DTA data of $Y_2Ti_{1.98}Rh_{0.02}O_7$ residue after heat treatment at 360 ºC for 2 hours; the sample was analysed in the range of 25 – 1200 ºC under constant air flow

The weight loss data show that up to 450 ºC, the removal of organic carbon originated from Titanium(IV) isopropoxide, Ethylene glycol and Citric acid, and the loss of nitrates from Yttrium(III) nitrate hexahydrate and Rhodium(III) nitrate hydrate solution took place. Data was confirmed by DTA analysis where the change in the heat flow suggests an exothermic reaction along with heat release. Above ca. 450 ºC no weight loss is detectable but sample remains amorphous if no further heat treatment in air occurs.

In order to form the pyrochlore structure, sample with x = 0.02 Rh in $Y_2Ti_{2-x}Rh_xO_7$ was examined at various calcination temperatures (1000; 1100 and 1200 ºC) (**Fig. 5.18**) in static air for 6 hours. All three patterns can be indexed to the cubic pyrochlore $Fd\bar{3}m$ space group with no apparent impurities.

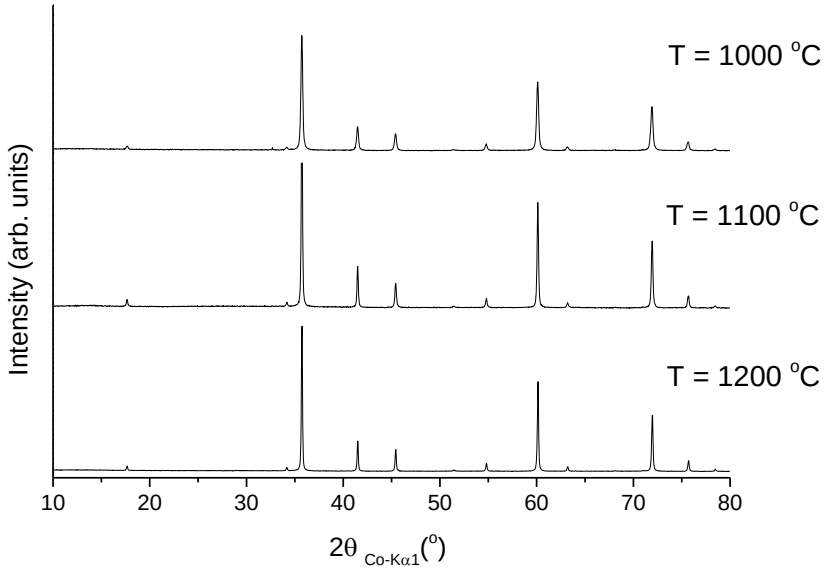

Fig. 5.18 Powder XRD patterns of the same batch of $Y_2Ti_{1.98}Rh_{0.02}O_7$ calcined at various temperatures (1000; 1100 and 1200 ºC) in air indexed to the cubic pyrochlore unit cell

However, the enlargement of the patterns reveals the [110] orientation of the rutile impurity phase at 32.6 2θ angle when sample calcined at 1000 ºC (**Fig. 5.19**) compared to the other two samples where T ≥ 1100 ºC heat treatment was applied. Evidently, higher calcination implies higher crystallinity of post-heat-treated samples.

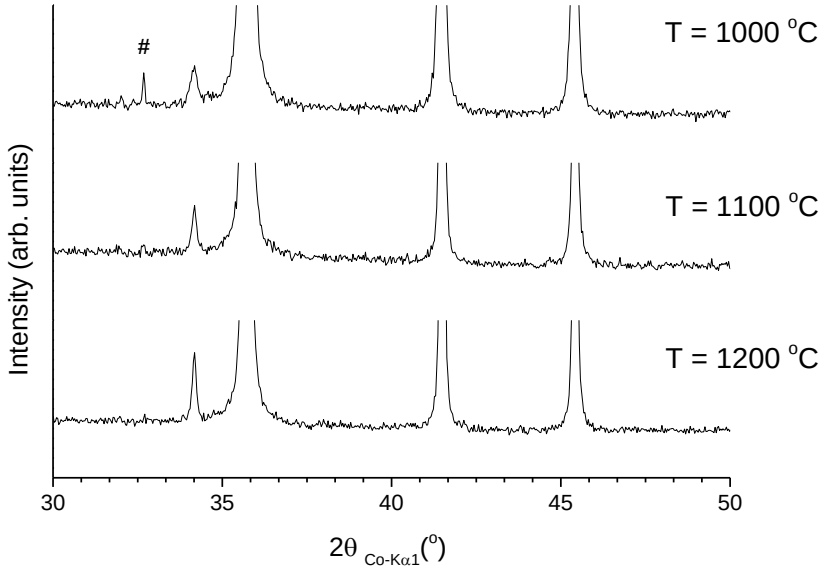

Fig. 5.19 Enlargement of the powder XRD patterns of the same batch of $Y_2Ti_{1.98}Rh_{0.02}O_7$ calcined at various temperatures (1000; 1100 and 1200 ºC) in air at the base of the peaks, showing impurities for T = 1000 ºC. The main peaks denote the phase-pure cubic pyrochlore; rutile impurity is indicated on the T = 1000 ºC sample: # TiO_2.

In addition, to investigate if any remaining organic residual was detected after firing the samples at 1100 ºC, CHN analysis was carried out on $Y_2Ti_{1.98}Rh_{0.02}O_7$ sample. As expected after high temperature firing sample contained negligible amount of C (0.02 %), 0.11 % H and 0% N confirming the weight loss and DTA results (**Fig. 5.17**).

SEM morphology study was performed on samples treated at various temperatures. Comparison is shown in **Fig. 5.20a-f**. Powder samples acquired at low magnification (400x) tend to form clusters with non-uniform particle size and shape (**Fig. 5.20a, c, e**) whereas images at higher magnification (10,000x) reveal the change in morphology due to heat treatment (**Fig. 5.20b, d, f**). Sample treated at 1000 ºC shows worm-like porous structure **(Fig. 5.20b)**. Increasing the temperature to 1200 ºC, a significant change in the morphology appears by the formation of bend and sintered sheets but with remaining visible porosity (**Fig. 5.20f**).

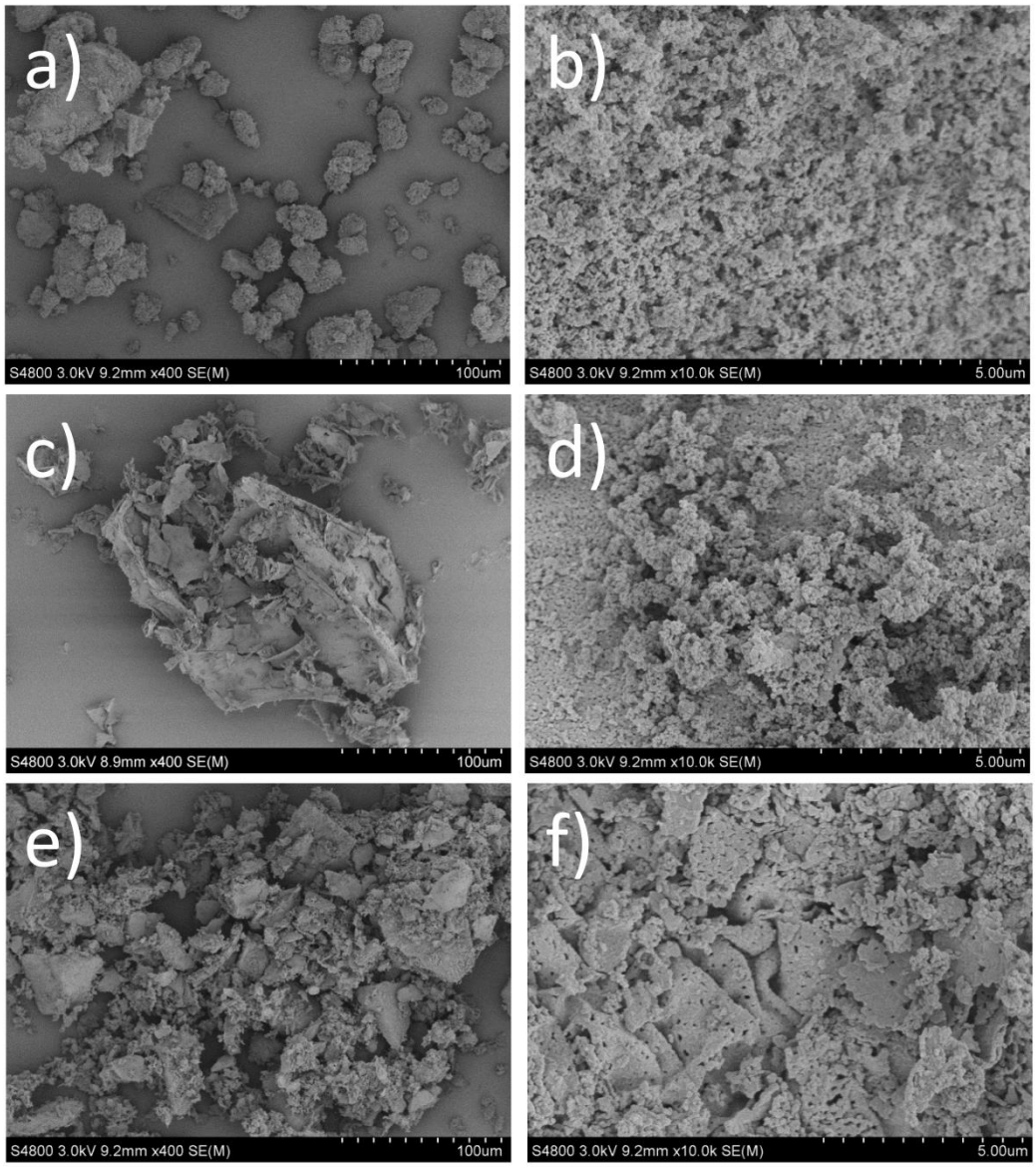

Fig. 5.20 SEM images of $Y_2Ti_{1.98}Rh_{0.02}O_7$ calcined at various temperatures (a-b) 1000 ºC; (c-d) 1100 ºC and (e-f) 1200 ºC in air

In conclusion, based on TGA, PXRD and CHN analyses, and SEM visualisation technique, secondary heat treatment of black residue at 1100 ºC for 6 hours under air results in a porous, phase-pure pyrochlore rhodium-doped yttrium titanate compound which can be used as an optimised template synthesis route for making the series of

$Y_2Ti_{2-x}Rh_xO_7$ with x = 0; 0.02; 0.04; 0.06 and 0.08 Rh doping (**Section 5.5**) and study the structure tunability using sol-gel route.

Using the optimized synthesis conditions mentioned above, the enlargement of the PXRD patterns of $Y_2Ti_{2-x}Rh_xO_7$ with x = 0; 0.02; 0.04; 0.06 and 0.08 Rh is shown in **Fig. 5.21**.

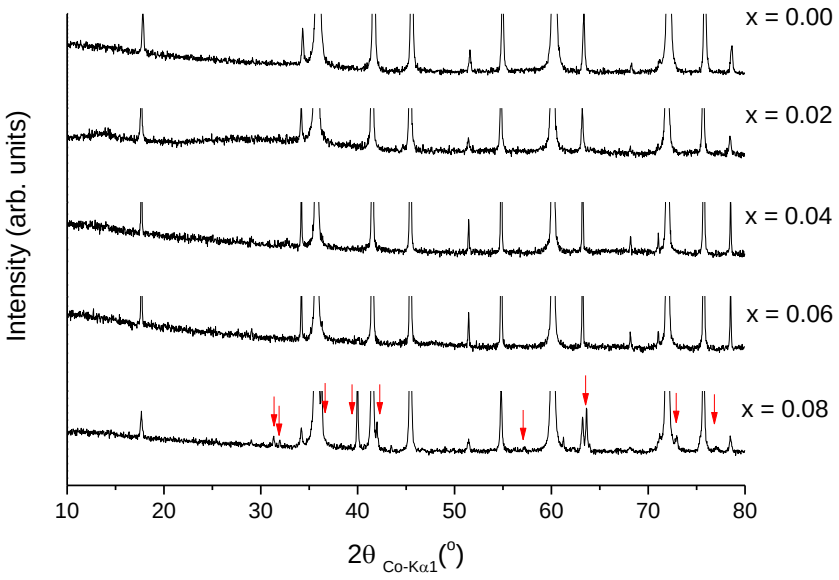

Fig. 5.21 Enlargement of the powder XRD patterns of sol-gel $Y_2Ti_{2-x}Rh_xO_7$ with x = 0; 0.02; 0.04; 0.06 and 0.08 Rh doping after calcination at 1100 °C in air at the base of the peaks, showing impurities for x = 0.08. The main peaks denote the phase-pure cubic pyrochlore; impurities are indexed with red arrows

Samples up to $x \leq 0.06$ show phase pure compounds (**Fig. 5.21**) when using sol-gel synthesis which is in a good agreement with solid-state synthesised samples where impurity appeared at x = 0.08 doping level (**Fig. 5.3**). Above the solubility limit of the solid solution when the lattice cannot be further expanded, distortion occurs in the structure along with detectable impurity phases. Impurities are identified in **Fig. 5.22** where the enlargement of the PXRD patterns for sol-gel samples with x = 0.06 and x

= 0.08 Rh are compared. Impurities on x = 0.08 sample appear for Y_2O_3 at 31.3 [100], 36.3 [101], for rutile TiO_2 at 32.0 [110], 42.0 [101], 63.6 [211], 77.3 [221] and for Rh_2O_3 at 40.0 [112], 57.2 [220], 73.0 [024] 2θ angles, respectively.

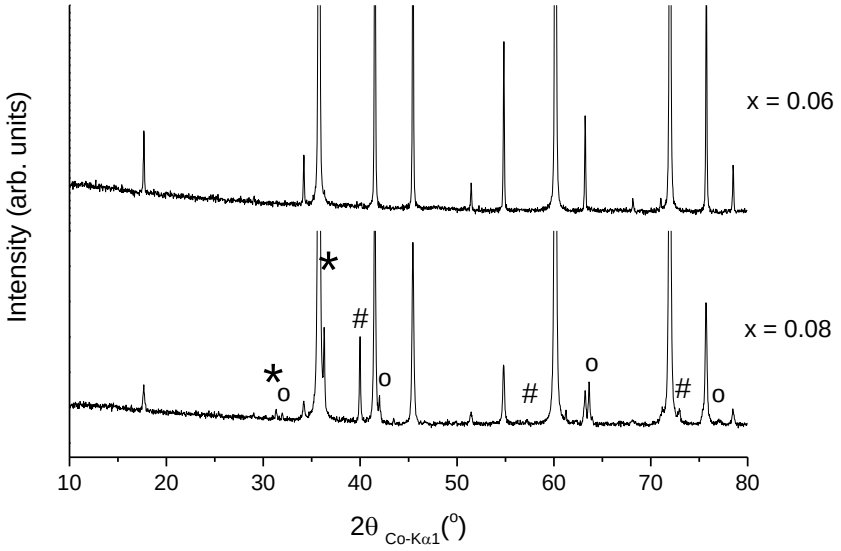

Fig. 5.22 Enlargement of the powder XRD patterns of sol-gel $Y_2Ti_{2-x}Rh_xO_7$ with x = 0.06 and 0.08 Rh doping after calcination at 1100 ºC in air at the base of the peaks, showing impurities for x = 0.08. The main peaks denote the phase-pure cubic pyrochlore; impurities are indexed with * Y_2O_3; o rutile TiO_2 and # Rh_2O_3

For accurate elemental composition determination, TEM EDAX analysis was used. Result for the x = 0.06 sample is shown on **Fig. 5.23**. The elemental analysis of the rhodium doped material matches with the expected $Y_2Ti_{1.94}Rh_{0.06}O_7$ composition, within accuracy of the machine for Ti, Y and Rh elements. The analysis also confirmed the chemical homogeneity of sample as no visible spread of the data points is obtained.

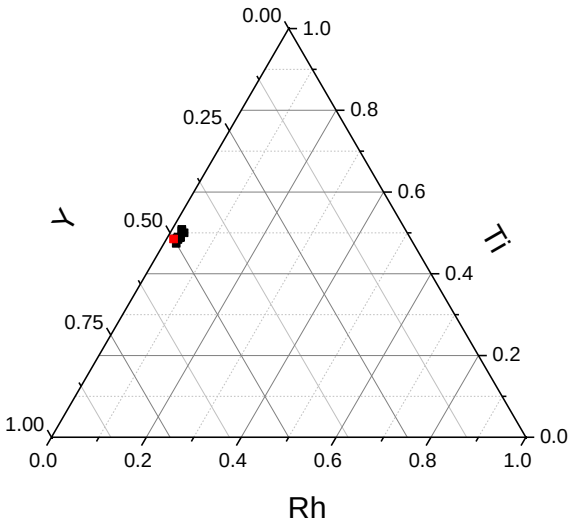

Fig. 5.23 TEM EDAX ternary diagram of sol-gel $Y_2Ti_{1.94}Rh_{0.06}O_7$ powder, black dots are the refined data based on elemental calibration of the electron microscope and red dot is the expected sample composition

In the next few paragraphs there will be a direct comparison of sol-gel and solid-state synthesised $Y_2Ti_{2-x}Rh_xO_7$ samples through SEM visualisation, BET surface area, DRS and O_2 evolution efficacy under visible light.

Morphology of sol-gel and solid-state synthesised samples was visualised with SEM and comparison is shown on **Fig. 5.24a-d**.

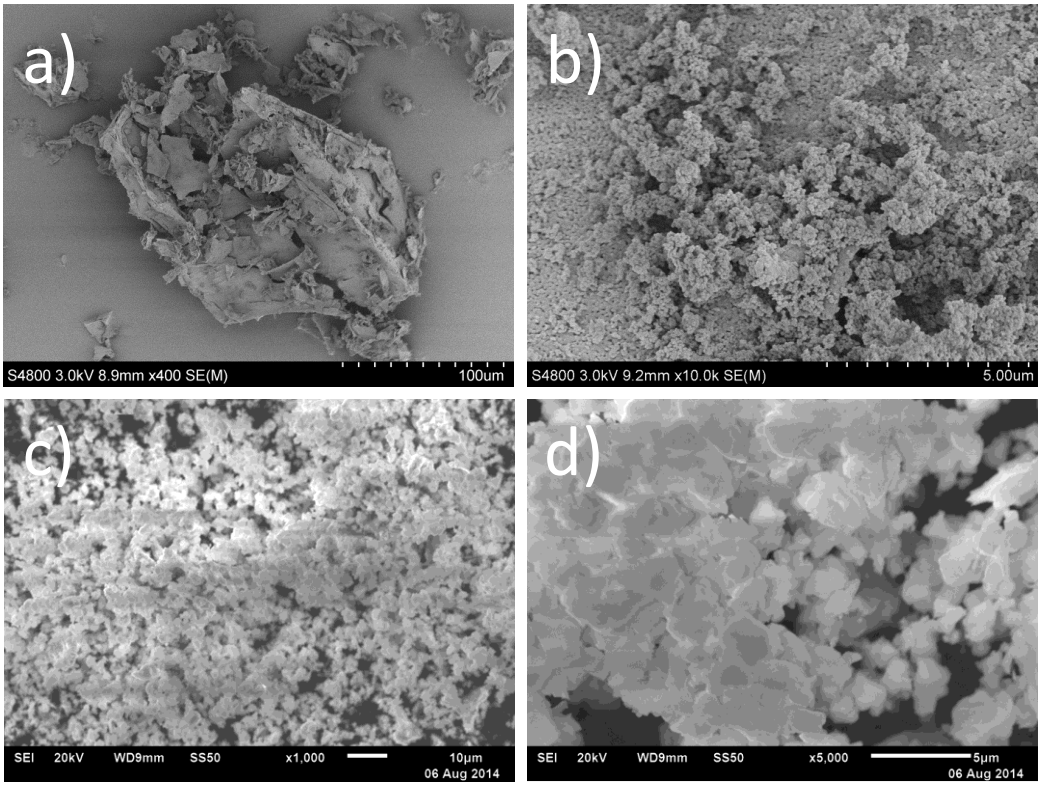

Fig. 5.24 SEM images of $Y_2Ti_{1.98}Rh_{0.02}O_7$ samples synthesized with (a-b) sol-gel method after calcination at 1100 ºC and with (c-d) solid-state method fired at 1300 ºC in air and ball milled

As explained earlier samples synthesised with solid state method, showed thin layers of equally ground particles after ball milling process (**Fig. 5.24c-d**) in comparison with sol-gel materials which exhibited a porous warm-like structure in particular at higher magnification (10,000x) with visible porosity (**Fig. 5.24a-b**). The primary particle size determined from the Scherrer equation gives 45-67 nm size for the sol-gel material.

Synthesising the compound with the alternative sol-gel route, the BET surface area for this material showed 16.0 m^2/g, a 5-fold increase in comparison with 3.2 m^2/g when sample was synthesised using the classic solid-state route (**Tab. 5.4**).

Tab 5.4 BET surface area comparison of solid state and sol-gel synthesised $Y_2Ti_{1.98}Rh_{0.02}O_7$ compounds

Synthesis Condition of $Y_2Ti_{1.98}Rh_{0.02}O_7$	BET Surface Area (m^2/g)
Solid state *	3.2
Sol-gel **	16.0

*1300 ºC for 12 h + 36 h in static air
** 360 ºC for 2 h; 1100 ºC for 2 h in static air

Kubelka-Munk spectra is shown in **Fig. 5.25** for the samples synthesised with sol-gel method with $0 \leq x \leq 0.06$ rhodium in $Y_2Ti_{2-x}Rh_xO_7$. Again, Ti substitution with Rh into $Y_2Ti_2O_7$ produces two new visible absorption bands at ca. 420 and 580 nm. Results confirm what was obtained earlier for solid-state samples (**Fig. 5.6**).

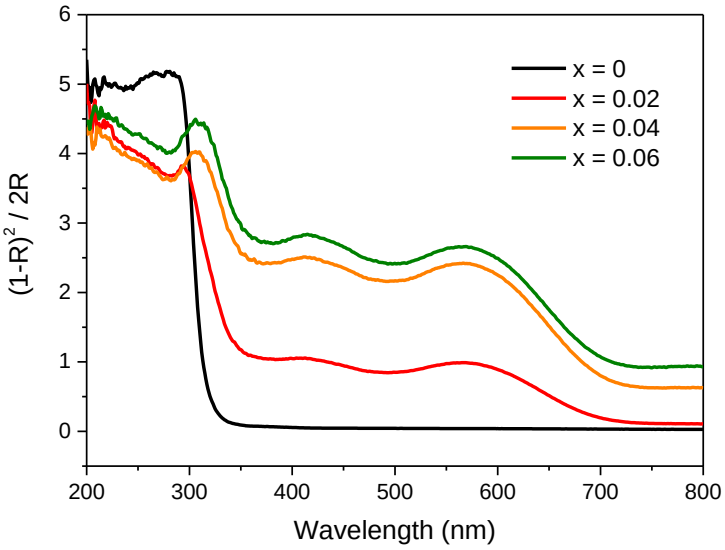

Fig. 5.25 Kubelka-Munk spectra of sol-gel $Y_2Ti_{2-x}Rh_xO_7$ ($0 \leq x \leq 0.06$)

The calculated indirect band gap for parent compounds synthesised by two different routes is shown in **Tab. 5.5**.

Tab 5.5 Indirect band gap comparison of solid state and sol-gel synthesised parent $Y_2Ti_2O_7$ compounds

Synthesis Condition of $Y_2Ti_2O_7$	Indirect Band Gap (eV)
Solid state *	3.71
Sol-gel **	3.75

*1300 ºC for 12 h + 36 h in static air
** 360 ºC for 2 h; 1100 ºC for 2 h in static air

Indirect band gap calculation gives 3.75 eV for the sol-gel parent material in comparison with SS compound which has a band gap of 3.71 eV. Owing to quantum confinement, typically nanostructures have larger band gaps than the corresponding bulk materials. As a result, the absolute position of CB and VB edges can be slightly shifted. Parent material does not absorb visible light as reported earlier (**Fig. 5.7** and **Tab 5.5**). [26, 52]

Phase pure samples synthesised with solid state and sol-gel methods were compared in O_2 generation reactions using the sacrificial electron acceptor silver-nitrate. Results for $Y_2Ti_{2-x}Rh_xO_7$ samples with $0 \leq x \leq 0.06$ rhodium are shown in **Fig. 5.26**. It is interesting that sol-gel samples when tested under visible light showed one order of magnitude less O_2 in comparison to the solid-state compounds. This is in contradiction with the expected results as it has been described in **Section 1.2.1** that "highly crystalline compounds with high surface area, small particle size and well defined morphology involving low density of defects are considered as good photocatalyst attributes if it is combined with good electronic properties". It is possible that recombination of separated holes and electrons occurred in the surface and resulted in smaller O_2 generation reaction rate for these particular sol-gel compounds. Further

investigation is needed to affirm such factors hence some possible ideas would be proposed in **Section 5.7**.

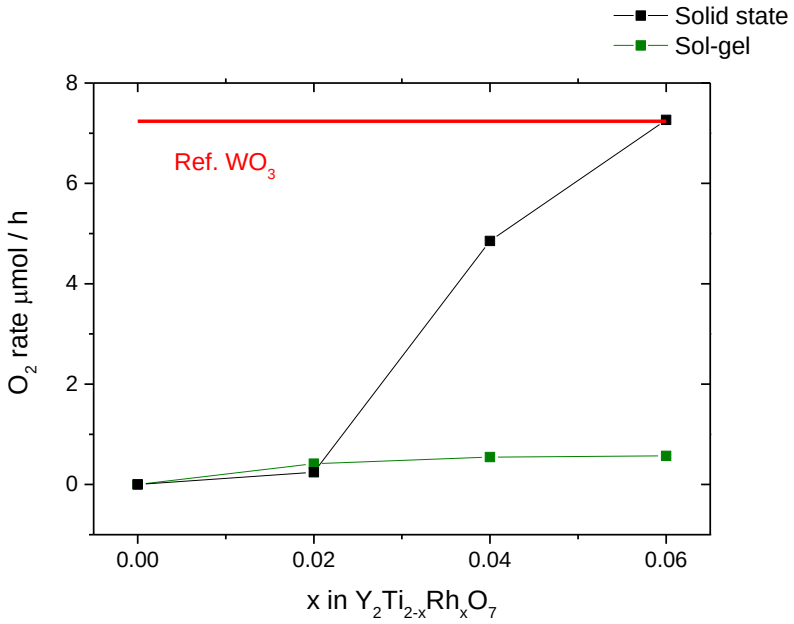

Fig. 5.26 Comparison of O_2 rate using solid-state and sol-gel $Y_2Ti_{2-x}Rh_xO_7$ compounds under visible light measured by O_2 electrode and optrode techniques, respectively. 0.1 g of catalyst; no co-catalyst; 20 mL, 0.05 M $AgNO_3$(aq); 300 W Xe lamp (λ > 420 nm, < 2.95 eV)

5.7. Conclusion and Future Prospects

In conclusion, advances in semiconductor materials for light-driven proton reduction to H_2 and for CO_2 reduction to carbon based fuels such as CH_3OH have led to an urgent requirement for improved, stable, visible light active water oxidation photocatalysts. Here it is demonstrated that $Y_2Ti_{2-x}Rh_xO_7$ ($0.04 \leq x \leq 0.06$) is an efficient visible light photocatalyst for the generation of oxygen from water in the presence of $AgNO_3$ electron scavenger without the need for a co-catalyst. In addition, highly crystalline solid state material in comparison with sol-gel samples were ten times affective in photoexcited O_2 evolution reactions which may be explained with less recombination site on the former's surface. This could be further investigated with Transient

absorption spectroscopy to trace the intermediate states in a photochemical reaction and the energy, charge or electron transfer processes. Application of such novel solid state material opens the pyrochlore structure class for wider use as a photoelectrode and in Z-schemes for solar fuels production. [52]

5.8. References

1. *The Hydrogen Economy: Opportunities, Costs, Barriers, and R&D Needs*, The National Academies Press, 2004.
2. *Report of the Basic Energy Sciences Workshop on Hydrogen Production, Storage and Use*, Argonne National Laboratory, 2004.
3. K. Maeda, *ACS Catal.*, 2013, **3**, 1486-1503.
4. F. Fresno, R. Portela, S. Suarez and J. M. Coronado, *J. Mater. Chem. A*, 2014, **2**, 2863-2884.
5. L. Yang, H. Zhou, T. Fan and D. Zhang, *Phys. Chem. Chem. Phys.*, 2014, **16**, 6810-6826.
6. G. V. Fomin, G. P. Brin, M. V. Genkin, A. K. Liubimova, L. A. Blumenfeld and A. A. Krasnovsky, *Dokl. Akad. Nauk SSSR*, 1973, **212**, 424–427.
7. A. A. Krasnovsky and G. P. Brin, *Dokl. Akad. Nauk SSSR*, 1962, **147**, 656–659.
8. W. Erbs, J. Desilvestro, E. Borgarello and M. Graetzel, *J. Phys. Chem.*, 1984, **88**, 4001-4006.
9. A. Walsh, Y. Yan, M. N. Huda, M. M. Al-Jassim and S.-H. Wei, *Chem. Mater.*, 2009, **21**, 547-551.
10. A. Kudo, K. Omori and H. Kato, *J. Amer. Chem. Soc.*, 1999, **121**, 11459-11467.
11. T. Hisatomi, J. Kubota and K. Domen, *Chem. Soc. Rev.*, 2014, **43**, 7520-7535.
12. T. Takata, G. Hitoki, J. N. Kondo, M. Hara, H. Kobayashi and K. Domen, *Res Chem Intermed*, 2007, **33**, 13-25.
13. Z. Yi, J. Ye, N. Kikugawa, T. Kako, S. Ouyang, H. Stuart-Williams, H. Yang, J. Cao, W. Luo, Z. Li, Y. Liu and R. L. Withers, *Nat. Mater.*, 2010, **9**, 559-564.
14. D. J. Martin, N. Umezawa, X. Chen, J. Ye and J. Tang, *Energy Environ. Sci.*, 2013, **6**, 3380-3386.
15. Y. Bi, S. Ouyang, J. Cao and J. Ye, *Phys. Chem. Chem. Phys.*, 2011, **13**, 10071-10075.
16. Y. Ma, X. Wang, Y. Jia, X. Chen, H. Han and C. Li, *Chemical Reviews*, 2014, **114**, 9987-10043.
17. A. Fujishima and K. Honda, *Nature*, 1972, **238**, 37-38.
18. K. Domen, S. Naito, M. Soma, T. Onishi and K. Tamaru, *J. Chem. Soc. Chem. Commun.*, 1980, 543-544.
19. H. Kato and A. Kudo, *J. Phys. Chem. B*, 2002, **106**, 5029-5034.
20. R. Konta, T. Ishii, H. Kato and A. Kudo, *J. Phys. Chem. B*, 2004, **108**, 8992-8995.
21. R. Niishiro, H. Kato and A. Kudo, *Phys. Chem. Chem. Phys.*, 2005, **7**, 2241-2245.
22. R. Asahi, T. Morikawa, T. Ohwaki, K. Aoki and Y. Taga, *Science*, 2001, **293**, 269-271.
23. Y. Sasaki, H. Nemoto, K. Saito and A. Kudo, *J. Phys. Chem. C*, 2009, **113**, 17536-17542.
24. S. Kawasaki, K. Akagi, K. Nakatsuji, S. Yamamoto, I. Matsuda, Y. Harada, J. Yoshinobu, F. Komori, R. Takahashi, M. Lippmaa, C. Sakai, H. Niwa, M. Oshima, K. Iwashina and A. Kudo, *J. Phys. Chem. C*, 2012, **116**, 24445-24448.
25. M. A. Subramanian, G. Aravamudan and G. V. Subba Rao, *Prog. Solid State Chem.*, 1983, **15**, 55-143.
26. R. Abe, M. Higashi, K. Sayama, Y. Abe and H. Sugihara, *J. Phys. Chem. B*, 2006, **110**, 2219-2226.
27. H. J. Kuhn, S. E. Braslavsky and R. Schmidt, *Pure Appl. Chem.*, 2004, **76**, 2105-2146.
28. X. B. Chen, S. H. Shen, L. J. Guo and S. S. Mao, *Chem. Rev.*, 2010, **110**, 6503-6570.
29. Z. Zou, J. Ye and H. Arakawa, *J. Phys. Chem. B*, 2002, **106**, 13098-13101.
30. K. Maeda, K. Teramura, H. Masuda, T. Takata, N. Saito, Y. Inoue and K. Domen, *J. Phys. Chem. B*, 2006, **110**, 13107-13112.
31. B. Kraeutler and A. J. Bard, *J. Amer. Chem. Soc.*, 1978, **100**, 4317-4318.

32. K. Maeda, K. Teramura, D. Lu, T. Takata, N. Saito, Y. Inoue and K. Domen, *J. Phys. Chem. B*, 2006, **110**, 13753-13758.
33. H. E. Swanson and R. K. Fuyat, *Natl. Bur. Stand. (U.S.), Circ. 539,*, 1953, **2**.
34. F. Schossberger, *Z. Kristallogr. Kristallgeom. Kristallphys. Kristallchem.*, 1942, **104**, 358-374.
35. Ľ. Smrčok and P. Ďuriš, in *X-Ray and Neutron Structure Analysis in Materials Science*, ed. J. Hašek, Springer, New York, Editon edn., 1989, pp. 375-378.
36. V. B. Lazarev and I. S. Shaplygin, *Russ. J. Inorg. Chem. (Engl. Transl.)*, 1978, **23**, 2614-2621.
37. *CRC Handbook of Chemistry and Physics*, 80th edn., CRC Press, 1999-2000.
38. A. R. West, *Solid Sate Chemistry and its Application*, 2nd edn., Wiley, Hoboken, 2013.
39. R. D. Shannon and C. T. Prewitt, *Acta Crystallogr., Sect. B*, 1969, **25**, 925-946.
40. R. Shannon, *Acta Crystallogr., Sect. A: Cryst. Phys., Diffr., Theor. Gen. Crystallogr.*, 1976, **32**, 751-767.
41. R. Niishiro, R. Konta, H. Kato, W.-J. Chun, K. Asakura and A. Kudo, *J. Phys. Chem. C*, 2007, **111**, 17420-17426.
42. J. R. Darwent and A. Mills, *J. Chem. Soc., Faraday Trans. 2*, 1982, **78**, 359-367.
43. Y. Zhang, J. Rosen, G. S. Hutchings and F. Jiao, *Catal Today*, 2014, **225**, 171-176.
44. N. M. Dimitrijevic, S. Li and M. Graetzel, *J. Amer. Chem. Soc.*, 1984, **106**, 6565-6569.
45. I. E. Wachs, S. P. Phivilay and C. A. Roberts, *ACS Catal.*, 2013, **3**, 2606-2611.
46. O. Merka, D. W. Bahnemann and M. Wark, *ChemCatChem*, 2012, **4**, 1819-1827.
47. O. Merka, O. Raisch, F. Steinbach, D. W. Bahnemann and M. Wark, *J Am Ceram Soc*, 2013, **96**, 634-642.
48. M. Higashi, R. Abe, K. Sayama, H. Sugihara and Y. Abe, *Chem. Lett.*, 2005, **34**, 1122-1123.
49. T. Sakata, K. Hashimoto and T. Kawai, *Journal of Physical Chemistry*, 1984, **88**, 5214-5221.
50. J. Yang, D. Wang, H. Han and C. Li, *Acc. Chem. Res.*, 2013, **46**, 1900-1909.
51. P. M. Pechini, Ceramic Dielectric Materials, U.S. Patent 3330697, Editon edn., 1967.
52. B. Kiss, C. Didier, T. Johnson, T. D. Manning, M. S. Dyer, A. J. Cowan, J. B. Claridge, J. R. Darwent and M. J. Rosseinsky, *Angewandte Chemie International Edition*, 2014, **53**, 14480-14484.

6. Appendix

6.1. Computational Details of $Y_2Ti_{2-x}Rh_xO_7$ Pyrochlore

Density functional theory (DFT) calculations were performed using the plane-wave based periodic DFT code VASP.[1] Valence-core electron interactions were modelled using the projector augmented wave method, [2] with semi-core s and p states treated as valence for Y and Ti, and semi-core p states for Rh. The screened hybrid density functional HSE06;[3] was used to avoid the underestimation of band gaps obtained using standard functionals. A plane-wave cut-off energy of 520 eV was used throughout, and unit cell vectors and atomic positions optimised until forces on atoms were below 0.01 eV/Å.[4]

Calculations of the parent compound $Y_2Ti_2O_7$ were performed in the 22 atom primitive unit cell with a 6×6×6 k-point grid. A single Ti atom within the 88 atom crystallographic unit cell was exchanged for Rh, to give a cell with composition $Y_{16}Ti_{15}RhO_{56}$, corresponding to the doped compound $Y_2Ti_{1.875}Rh_{0.125}O_7$. Calculations of the doped cell were performed with a 2×2×2 k-point grid.[4]

6.2. Optical properties of $Y_2Ti_{2-x}Rh_xO_7$ Pyrochlore

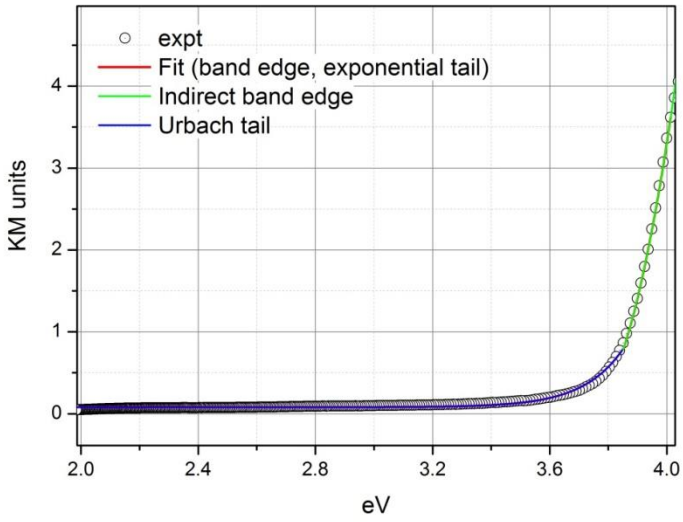

Fig. A1 The relative absorption spectrum of the un-doped $Y_2Ti_2O_7$ is well fitted to an indirect transition with a disorder induced tail to the band gap.

The un-doped $Y_2Ti_2O_7$ is found to be well fitted by a combination of a power law function to model the Tauc band gap for an indirect transition ($y = y_0 + A^{(x-x_g)^2}$) and an exponential function for the Urbach tail ($y = y_0 + A_1 e^{(-x/c)}$) which arises from the disorder induced optical features,[20] with a cut-off function to define the transition point between the two optical features . This yields an indirect band gap of 3.7 eV, **Fig. A1** which corresponds to the value obtained from a typical Tauc plot (**Fig. 5.7**).[4]

Rhodium doping leads to visible light absorption. Two clear bands, centred at *ca.* 2.1 and 2.9 eV are observed at all doping concentrations and the assignment of these is discussed on page 3 of the main text. The UV/Vis spectra of the Rh doped samples can be readily fitted to a combination of 2 Gaussian bands centred at *ca.* 2.1 and 2.9 eV

and the power law and exponential functions described above for the band gap and Urbach tail respectively. A representative fit of $Y_2Ti_{1.96}Rh_{0.04}O_7$ is shown in **Fig. A2**. Alternatively the doped material can also be adequately fitted to a combination of 2 Gaussian bands and power law type function, without the need for the inclusion of an Urbach tail, **Fig. A3**. This is not unexpected as although a disorder induced tail to the band gap transition would be expected to occur in these doped materials, given that it is present in the un-doped material as well, the presence of a large number of optical features leads to a very large number of fitting variables for this relatively small data set. Regardless, both **Fig. A2** and **Fig. A3** clearly show that doping leads to a shift in the band edge ($E_g \sim 3.17$ and 3.19 eV respectively) in addition to the presence of strong visible light absorption by either the 2.9 eV transition alone, or most likely a combination of the 2.9 eV feature with the band gap tail.[4]

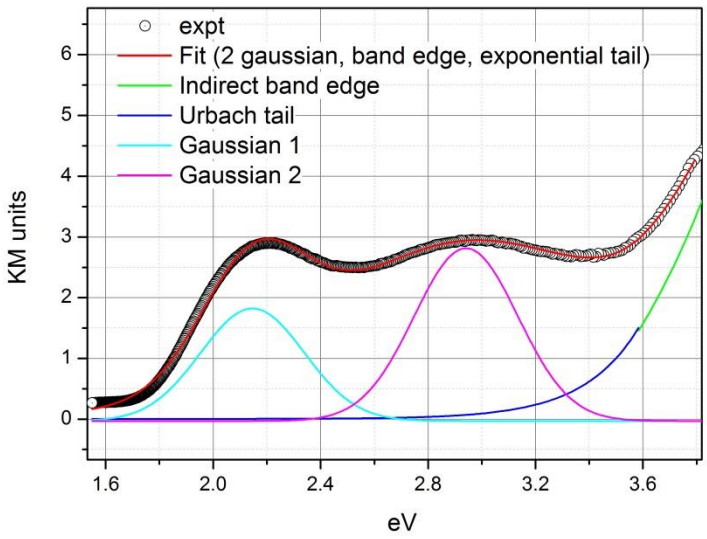

Fig. A2 Relative absorption spectrum of $Y_2Ti_{1.96}Rh_{0.04}O_7$ which can be well fitted to a combination of 4 functions modelling two visible light transitions (Gaussian) and an indirect band gap with a disorder induced tail.

Table A1 Fit parameters for optical spectra of $Y_2Ti_{2-x}O_7$ ($0 \leq x \leq 0.06$) fitting to two Gaussian curves, and exponential function for the Urbach tail and a power-law dependent absorption edge

	Rhodium content x in $Y_2Ti_{2-x}Rh_xO_7$							
	0	**±**	**0.02**	**±**	**0.04**	**±**	**0.06**	**±**
Xg	3.72076	0.00143	3.17093	0.0097	3.16844	0.03912	3.12325	0.02121
n	2	0	2	0	2	0	2	0
A	41.45448	0.44536	7.99197	0.20808	8.64527	0.74813	7.32375	0.35871
A1	3.63E-13	1.91E-13	7.81E-10	1.31E-09	4.30E-08	1.23E-07	1.86E-08	4.07E-08
Xu	-0.13604	0.00238	-0.16803	0.01256	-0.20632	0.03123	-0.1959	0.02226
y0	0.08029	0.00113	0.00375	0	0.03087	0.03734	0.02162	0
Xc	3.85125	0.00285	3.49888	1.08453	3.57382	0.9646	3.51198	0.39846
A2			1.64206	0	1.85122	0.05463	1.87733	0.0166
A3			2.34337	0.01386	2.84469	0.07506	3.18438	0.02966
xa			2.14681	0	2.14681	0	2.13575	0.00123
xb			2.94447	0.00629	2.94127	0.01847	2.92434	0.01213
w1			0.19458	0	0.19298	0.00301	0.186	0.0017
w2			0.51152	0.00321	0.55188	0.02974	0.58826	0.00581
Adj. R-Square	0.99835		0.99748		0.99756		0.99747	

Fitting to:

```
if (x > xc)
y = y0+ A*((x-Xg)^n) + A2*exp(-0.5*((x-xa)/w1)^2) + A3*exp(-0.5*((x-xb)/w2)^2);
if (x  < xc)
y = y0+ A1*exp(-x/Xu) + A2*exp(-0.5*((x-xa)/w1)^2) + A3*exp(-0.5*((x-xb)/w2)^2);
if (x = xc)
A = (A1*exp(-x/Xu))/((x-Xg)^n);
```

Where xc is the matching point between the Urbach tail and the indirect absorption edge; Xg is the position of the absorption edge; Xu is the decay constant for the Urbach tail; xa and xb are the centres of the two Gaussians; w1 and w2 are the widths of the two Gaussians; A, A1, A2 and A3 determine the heights of the various contributions; and y0 is a constant background.[4]

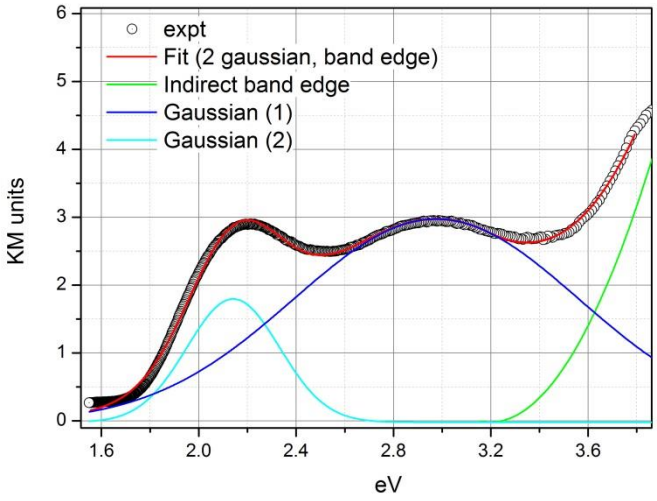

Fig. A3 Relative absorption spectrum of $Y_2Ti_{1.96}Rh_{0.04}O_7$ can also be fitted to a combination of 3 functions modelling two visible light transitions (Gaussian) and an indirect band gap without a disorder induced tail.

Table A2 Fit parameters for optical spectra of $Y_2Ti_{2-x}O_7$ ($0 \leq x \leq 0.06$) fitting to two Gaussian curves and a power-law dependent absorption edge

	Rhodium content x in $Y_2Ti_{2-x}Rh_xO_7$							
	0*	**±**	**0.02**	**±**	**0.04**	**±**	**0.06**	**±**
Xg	3.72	0.02	3.20	0.01	3.20	0.01	3.10	0.02
n	2.00	0.00	2.00	0.00	2.00	0.00	2.00	0.00
A	39.12	3.99	8.04	0.22	8.78	0.30	6.88	0.31
y0	0.18	0.16	-0.04	0.02	-0.02	0.03	0.13	0.03
A2	0.00	0.00	1.56	0.03	1.82	0.04	2.03	0.06
A3	0.00	0.00	2.42	0.02	3.00	0.03	3.17	0.03
xa	-	-	2.14	0.00	2.14	0.00	2.14	0.00
xb	-	-	2.97	0.00	2.98	0.00	2.95	0.01
w1	-	-	0.19	0.00	0.19	0.00	0.19	0.00
w2	-	-	0.56	0.02	0.59	0.02	0.54	0.02
--	--		--		--		--	
Adj. R-Square	0.99685		0.99745		0.99741		0.99735	

Fitting to:

if (x >Xg)

y = y0+ A*((x-Xg)^n) + A2*exp(-0.5*((x-xa)/w1)^2) + A3*exp(-0.5*((x-xb)/w2)^2);

```
if (x< Xg)
 y = y0+ A2*exp(-0.5*((x-xa)/w1)^2) + A3*exp(-0.5*((x-xb)/w2)^2);
```

*Fitted between 3.5-3.9 eV. Fitting parameters as in **Table A1**.

6.3. References

1. G. Kresse and J. Furthmüller, *Phys. Rev. B Condens. Matter Mater. Phys.*, 1996, **54**, 11169-11186.
2. G. Kresse and D. Joubert, *Phys. Rev. B Condens. Matter Mater. Phys.*, 1999, **59**, 1758-1775.
3. A. V. Krukau, O. A. Vydrov, A. F. Izmaylov and G. E. Scuseria, *J Chem Phys*, 2006, **125**.
4. B. Kiss, C. Didier, T. Johnson, T. D. Manning, M. S. Dyer, A. J. Cowan, J. B. Claridge, J. R. Darwent and M. J. Rosseinsky, *Angewandte Chemie International Edition*, 2014, **53**, 14480-14484.